DYNAMICAL STUDIES OF CRYSTALLINE POLYMERS

BY

INELASTIC NEUTRON SCATTERING

by

J.F. Twisleton, M.A.

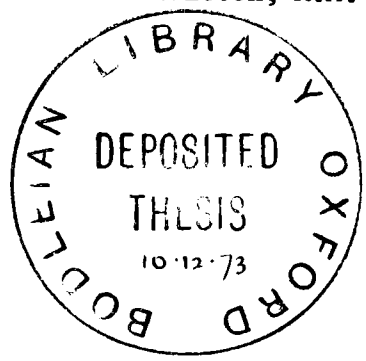

A thesis submitted for the degree of

Doctor of Philosophy

in the

University of Oxford

St. John's College,
Oxford.

July 1973.

Abstract

Experimental parameters of the interchain force field of polyethylene and polytetrafluoroethylene (P.T.F.E.) are measured by inelastic neutron scattering spectroscopy and provide some of the first anisotropic information about the forces between carbon chains in simple polymeric systems. Spectroscopic studies of polymers have long been restricted by the unavailability of samples with full single crystal texture and so the preparation of such a specimen of deuteropolyethylene reported here can be seen as a very significant development, one that is much exploited in this thesis.

Comparative studies of the low frequency incoherent neutron spectra of normal and deuteropolyethylene obtained by the time-of-flight method are described and facilitate assignment of the density of states function for external chain vibrations in the crystalline regions of this polymer. Some deficiencies in the existing Urey-Bradley interchain force models for polyethylene become apparent from these data.

Coherent acoustic features in the neutron time-of-flight spectra of isotropic and uniaxially oriented deuteropolyethylene are investigated. Dynamical structure factor calculations illustrate the predominant contribution of longitudinal acoustic phonons polarized along [ζζ0] in the isotropically averaged phonon spectrum. On this basis the observed singularities are assembled onto a dispersion curve which defines an elastic constant of the interchain force field, the first of such measurements. Persistence of anisotropic contributions within the isotropically averaged phonon spectrum is seen as a remarkable consequence of the anisotropy of the polyethylene unit cell and the high symmetry of the molecular basis therein, both of which act to simplify the dynamical structure factors. A technique for extracting anisotropic information about lattice vibrations from polycrystalline or partially oriented material is recognised and some criteria are established for the choice of suitable systems for further

investigations of this kind.

Preparation of a bulk specimen of deuteropolyethylene with full single crystal texture is reported. Biaxially oriented specimens are annealed at high pressure with a constraint on their shape following a recently devised procedure. Sudden cooling of the annealed material preserves the induced single crystal texture. Conditions of temperature, pressure and annealing time are adjusted to optimize the mosaic in the basal plane of the polymer as characterized by X-ray and neutron diffraction. The resulting specimens are assembled to give a target suitable for triple axis spectrometry which represents the closest approach to a single crystal of polyethylene yet achieved.

Triple axis neutron spectrometry is applied to this material and phonon measurements in the basal plane are described. Three acoustic slopes qualifying interchain phonons are reported together with two zone centre frequencies for external chain rotatory and translatory modes, assigned on the basis of dynamical structure factor calculations. These five parameters are combined with far infrared data and Raman data obtained in conjunction with the author to give a total of seven experimental parameters of the interchain force field of polyethylene, which are then used to test the available force models. Overall fits of 10 and 20% are provided to these data by two Urey-Bradley force fields, both of which include interactions between nearest neighbour nonbonded hydrogens only.

Calculations of the interchain phonon dispersion curves of deuteropolyethylene based on an atom-atom potential parameter model are reported. Intermolecular force constants are derived from an analytical 'six-exp' form for the potential between nonbonded atoms which reproduces a wide range of structural and thermodynamic data for the hydrocarbon system. This model fits the observed dynamical parameters within an average error of 5% which is significantly better than the fits obtained using the Urey-Bradley force fields. Moreover the close reproduction of the experimental elastic constants

gives support to the related elastic moduli perpendicular to the chain axis calculated from this model. Tensile elastic moduli calculated along the two crystallographic axes perpendicular to the chain axis in the orthorhombic cell are very similar in contrast with earlier predictions. The values of 8 and 9×10^{10} dyne cm^{-2} are moreover in very close agreement with an average interchain crystal modulus derived from bulk measurements. The basis of this derivation is a two phase 'sandwich' model of composite polyethylene in which the bulk stress is assumed to be homogeneous across alternate crystalline and amorphous layers. Such a model is consistent with present understanding of polyethylene morphology and is lent additional support by the agreement obtained here between interchain crystal moduli derived from macroscopic and microscopic sources.

Neutron time-of-flight spectra of P.T.F.E. exhibit coherent acoustic features strongly analogous to those observed in deuteropolyethylene. An acoustic slope for longitudinal acoustic phonons propagating along the $[\zeta 0 \bar{\zeta} 0]$ direction in the basal plane of hexagonal P.T.F.E. is derived from these data. The elastic constant c_{11} is evaluated from this slope and provides the first anisotropic information about the interchain force field of this polymer. Comparison of c_{11} with the elastic constant c_{33} derived from earlier measurements of acoustic phonons propagating within the chain itself is effected. A ratio $c_{33}:c_{11}$ of 8 compares with a figure of 22 for deuteropolyethylene also obtained in this work and highlights the greater anisotropy of the hydrocarbon force field. Other features in the time-of-flight spectra of P.T.F.E. suggest strong coupling between the lowest frequency intrachain torsional mode and the external chain vibrations, questioning the applicability of an isolated chain description of the internal vibrations of this molecule. Changes in the low frequency time-of-flight spectra at the $19^{\circ}C$ phase transition in P.T.F.E. are attributed to a decrease in external librational frequencies occurring parallel to the onset of dynamical disorder about the chain axis.

Acknowledgements

I should like to thank my supervisor, Dr. J.W. White, for his guidance and inspiration throughout this project and Drs. P.A. Reynolds, R.J. Young and C.P. Buckley for helpful discussions and advice about the experimental techniques of neutron inelastic scattering and the preparation of oriented polymers. I also thank Dr. N.G. McCrum for extending to me the facilities of his research group, Dr. R.W. Gray for assistance in the measurement of X-ray pole figures and Drs. G.S. Pawley and D.I. Marsh for the loan of their computer programs. Mr. H.A. Willis and Drs. J.S. King and H.W. Starkweather provided polymer specimens vital to this work.

Practical assistance from the staff at A.E.R.E. Harwell, A.E.K. Risø, Denmark and the Oxford University Computing Laboratory is gratefully acknowledged, especially that provided by Mr. G.E. Haines and Dr. J.K. Kjems. I am also grateful to the technical staff of the Physical Chemistry and Engineering Laboratories, Oxford University who constructed the die set and sample moulds employed in this work. Finally I think Mr. D. Kozlow for helping to draw some of the diagrams and Miss A.B. Onions, Oxford Typing Service Ltd., for typing this thesis.

Financial support from the Science Research Council and St. John's College, Oxford is gratefully acknowledged.

Publications

'Interchain force field of polyethylene by neutron scattering'.
J.F. Twisleton and J.W. White, 'Neutron Inelastic Scattering', Proceedings of Grenoble Symposium, IAEA, p. 301 1972.

'Phonons in crystalline deuteropolyethylene'.
J.F. Twisleton and J.W. White, 'Chemistry of the Organic Solid State', Proceedings of the 3rd International Symposium, p. 33 1972.

'Low frequency Raman spectra of single crystal textured polyethylene'.
R.T. Harley, W. Hayes and J.F. Twisleton, J. Phys. C, 6, 167 1973.

'Interchain force field and elastic constants of polytetrafluoroethylene'.
J.F. Twisleton and J.W. White, Polymer, 13, 40 1972.

Contents

Page

Chapter 6 (continued) Page

Chapter 9 (continued)

Preface

Polymer science has taken root in a wide range of scientific disciplines and so provides a valuable meeting place for those working in pure and applied research fields. Economic stimuli arising from the ever increasing role of plastics in the modern world have provoked intensive investigation of the microscopic origins of the fascinating bulk properties of polymers. From the chemists's point of view polymers are of intrinsic interest for several reasons. The anisotropy of the chemical binding and the symmetry of chain systems make them attractive molecular crystals for spectroscopic investigation. Moreover there are many parallels to be drawn with biological systems, so that information about such phenomena as hydrophobic bonds obtained from simple polymers is frequently transferable to more complicated relatives. Since polymers are usually composite, containing regions of order and disorder, they present interesting morphological problems which are related to the stereospecificity of chemical bonds and the range and polarity of intermolecular forces. Chemical intuition also assists in the interpretation of relaxation processes which are inferred from the visco-elastic behaviour of polymers. Many such phenomena appeal in some way to the chemical physicist for elucidation in terms of the structure and dynamics of constituent molecules.

Aspects of molecular structure which affect the bulk properties of polymers are well illustrated by a comparison of the two systems studied in this thesis, polyethylene and polytetrafluoroethylene (P.T.F.E.). In polyethylene the carbon skeleton has a planar zig-zag structure whereas P.T.F.E. exists as a helix because the planar structure would involve the energetically unfavourable eclipsing of fluorine atoms across the carbon-carbon bonds. Bulk textures differ strikingly. Electron microscopy of crystalline polyethylene shows that the chains fold every 100 Å or so to give a lamellar texture. In contrast fracture surfaces of P.T.F.E. show

chains extending up to lengths of 20,000 Å or more when examined in the same way. Chain folding in P.T.F.E. is not observed for the same reason that a helical structure is preferred. Moreover polyethylene melts to a mobile liquid whereas P.T.F.E. melts at much higher temperature to a state with the consistency of cheese. The persistence of the extended helical chains in the melt is thought to cause this remarkable behaviour and reflects the great stiffness of the helical conformation of P.T.F.E. Finally some understanding of the unique low frictional properties of P.T.F.E. which are not shared by polyethylene can be gauged from the almost cylindrical shape of this molecule which facilitates the process of interchain slippage under stress.

From these examples it is apparent that qualitative considerations of the shape and binding of constituent chain molecules can illuminate many aspects of polymer science. Most bulk properties though are sensitive to the intermolecular force field and it is here that quantitative information is lacking. The range and polarity of interchain forces play a central role in determining cohesive properties, particularly the fine details of polymer morphology, and primarily determine the dynamics in the low frequency region. Moreover information about these forces, especially those between nonbonded hydrogens, may have important biochemical applications. Information of this kind is at present very scant even for the simplest polymer, polyethylene, and it is a major experimental pursuit of this thesis to provide such data. Indeed present models for the interchain force field of this polymer are based upon dynamical information about interchain vibrations which is certainly insufficient to define the model parameters in a unique sense. A more promising approach employs thermodynamic and structural data from a range of related systems, distilling out a transferable analytical potential for the interactions between nonbonded atoms. Derivative properties of pseudopotentials constructed in this way are used in this thesis to reproduce the phonon dispersion curves for interchain vibrations in polyethylene.

One bulk property which particularly concerns this work is the elasticity, which, together with the physical strength and durability is responsible for some of the diverse applications of commercial polymers. Elastic moduli for tensile deformation of polymer chains are generally two orders of magnitude greater than the observed bulk moduli. This discrepancy is of great practical importance and reflects the relative ease of elastic deformations in the crystalline regions perpendicular to the chain axes and in the amorphous regions generally compared to those involving linear extension of the chains themselves. Resolution of these components of bulk elasticity is impaired by prevalent uncertainty about the relationship of crystalline and amorphous regions in the bulk texture of a polymer. Direct measurements of crystalline elastic constants are possible however since acoustic vibrations in the ordered regions are not heavily damped and can be characterized by various spectroscopic techniques. Acoustic phonon excitations correspond in the long wavelength limit to elastic deformations of the crystallites as a whole and phonon velocities can be related in this limit to the elastic constants. Such measurements are one object of this work and should define the crystalline moduli, which, together with the bulk moduli, facilitate an assessment of the all important role of the amorphous regions in determining the exceptional elastic properties of polymers.

What then are the facets of neutron scattering spectroscopy which recommend its application to some of the problems just outlined? In a quest for information about the range and polarity of the forces in a crystal it is the phonon dispersion curves for lattice vibrations that provide the most useful information. Full investigation of these curves requires an experimental technique that can excite lattice waves with frequencies and wavelengths spread over a wide region. Inelastic neutron scattering is ideally suited for this purpose since the neutron has a capacity for transferring sizeable quantities of both energy and momentum to a crystal. This capacity

arises from the massive nature of the neutron whereby particles with thermal energies have wavelengths comparable to the spacing of molecules in the solid state. Given then a polymer specimen with some anisotropy it should be possible to map out the dispersion curves using coherent neutron scattering techniques and so provide information about the forces in the crystalline regions where the phonons propagate. Acoustic phonon measurements should facilitate the calculation of elastic constants and enable the comparison between crystal and bulk moduli already discussed. Moreover even when the only available specimens are isotropic considerable information can often be extracted from the incoherent component of the inelastic neutron spectrum, which bears a close relationship to the density of states function for the target system. Selection rules for incoherent neutron scattering are very relaxed compared to those operative in electromagnetic spectroscopy so that many more density of states singularities are observable by this technique.

In summary the principal objective of this thesis is the measurement of anisotropic parameters of the interchain force field of two crystalline polymers, polyethylene and polytetrafluoroethylene. Such an objective was stimulated by the dearth of experimental information about these forces and the importance of such data in an evaluation of the anisotropy of binding in the crystalline regions of simple polymers and the relationship of this binding to overall bulk properties, in particular the elastic moduli. A major experimental problem was the preparation of polymer specimens with single crystal texture for optimum employment of the available neutron techniques. This was achieved for polyethylene which is most extensively treated in this thesis. After the background theory and experimental techniques have been outlined the experimental results are reported historically starting with neutron scattering studies of isotropic and uniaxially oriented polyethylene which prepare the ground for the more extensive measurements on the fully oriented material. Neutron scattering studies

of P.T.F.E. are described last since they were stimulated by certain aspects of the polyethylene work and, although less extensive,they provide a valuable complement to the hydrocarbon results.

Chapter 1

BINDING IN MOLECULAR CRYSTALS - THE PSEUDOPOTENTIAL

1.1 Introduction

The definition of a molecular crystal infers the virtual preservation of the gas phase shape and atomic binding of the constituent molecules on condensation to the solid. Intermolecular forces are weak and of short range in sharp contrast to the binding within metals and ionic crystals. The short range of the so-called 'Van der Waals' forces is an advantage which to some extent offsets the greater complexity of these systems. For example Kitaigorodskii has demonstrated quite clearly that molecular crystals are constructed according to the principle of close packing, which is a natural consequence of the short range of the forces [1-4]. The success of this principle encourages attempts to rationalise other properties of organic crystals and has led to the formulation of analytical pseudopotentials. Just as it is possible to give a qualitative explanation of the crystal structure of such systems by attaching Van der Waals radii to the bound atoms, parameters of the potential between nonbonded atoms may be introduced which fit not only the structure but also a variety of thermodynamic and spectroscopic data. Such parameters possess no absolute physical significance but provide an invaluable aid to the experimental scientist by linking the information available from structural and thermodynamic studies to a range of dynamical properties.

Paradoxically such a link is established only by assuming that lattice statics and lattice dynamics are dissociable. In other words observed crystal structures are in fact the configurations of minimum free energy, incorporating the energy of thermal motion as well as the crystal potential. Inevitably this contribution to the total free energy, which survives even at the absolute zero of temperature in the form of zero point vibrations, is overlooked in deriving the pseudopotential. Thus a crystal potential

is established on the basis of the observed structure and dynamical properties are later related to the curvature of this potential function at its minimum value. Such a procedure works well for low temperature crystal structures but is brought more into question as the thermal amplitude of molecular motion increases.

Since the prospects for ab initio calculations of intermolecular potentials are bleak the pseudopotential approach continues to be attractive. Although these empirically derived potentials are clearly approximate, their success in reproducing the observed crystal structures of related systems is a strong recommendation. Furthermore the number of parameters employed in the analytical formulation of pseudopotentials is small enough to ensure their adequate definition from experiment. In short this description is as yet the most efficient way of expressing the latent information about intermolecular forces contained in structural and thermodynamic data.

1.2 Analytical formulation of the pseudopotential

For a rigid molecule of known shape sitting on a lattice site the potential energy

$$\Phi = \Phi(a,b,c,\alpha,\beta,\gamma,\theta,\psi,\phi) \tag{1.1}$$

can be written as a function of the six lattice parameters and three Eulerian setting angles about suitable axes. The equilibrium crystal structure can be obtained by minimising the free energy, approximated to the potential energy, with respect to the nine parameters described. In practice an analytical form for the intermolecular potential is established and then used in the quest for the equilibrium structure where

$$\Phi_o = \varepsilon_o \tag{1.2}$$

$$\left[\frac{\partial\Phi}{\partial p_i}\right]_o = 0 \quad , \quad p_i = a,b \ldots \phi \tag{1.3}$$

and ε_o is the sublimation energy at absolute zero, or the nearest approach to it afforded by the potential model. The number of parameters is frequently reduced by constraining the minimisation procedure to reproduce the observed unit cell symmetry.

In choosing an analytical form for the potential two considerations arise. Firstly the form should have a reasonable physical basis. Secondly the number of parameters should be kept at a minimum if they are to be uniquely defined from experiment. Both these conditions are well met by the six-exp form

$$\Phi_{ij} = - \frac{A_{ij}}{r_{ij}^6} + B_{ij} \exp(-C_{ij} r_{ij}) \qquad (1.4)$$

for the potential between atoms i and j on neighbouring molecules, separated by a distance r_{ij}. The first term is the exact functional form expected for the potential between two free atoms attracted by an instantaneous dipole-dipole polarization - the Van der Waals attractive potential. The second term is the familiar result for the repulsive potential between two filled electron shells which is caused by the required antisymmetry of the total wave function for a two atom system. Summation of (1.4) over all pairs of nonbonded atoms gives the total crystal potential

$$\bar{\Phi} = \tfrac{1}{2} \sum_{i=1}^{N} \sum_{j=1}^{N} \left(- \frac{A_{ij}}{r_{ij}^6} + B_{ij} \exp(-C_{ij} r_{ij}) \right) \qquad (1.5)$$

Automatically excluding many body interactions, this summation implies a very serious simplification. Nevertheless consideration of many body corrections dramatically increases the number of parameters so it is preferred to strike the balance already referred to at this level, a fair price to pay for such a simple model.

1.3 Empirical derivation of potential parameters

Physical properties related to the crystal potential are enumerated in the next chapter. Of these properties the most widely accessible is the

crystal structure, which depends on the potential gradients with respect to various structural variables such as lattice parameters and setting angles. Pseudopotential parameters are generally obtained by adjusting the form of (1.4) for each pair potential until the minimum value of (1.5) corresponds to the observed crystal structure and heat of sublimation. In practice structural and thermodynamic data from a series of related molecular crystals are used in the fitting procedure and a transferable set of potential parameters is defined. Of such series the hydrocarbons have been thoroughly treated and several parameter sets are now available [3-13]. The quality of these parameters is very sensitive to the composition of the structural and thermodynamic data to which they are fitted. Three criteria are particularly important in the choice of molecular crystal for the fitting procedure:

[1] Molecular shape should be little affected by condensation to the solid. Such distortions will contribute to the crystal potential and weaken the basic assumption of rigid molecules.

[2] Low temperature structural data are essential since the contribution of thermal motion to the free energy is ignored in fitting the parameters.

[3] Special electrostatic forces such as hydrogen bonding, dipolar or quadrupolar interactions should be absent. Effects of this kind will lead to anomalous parameters since the six-exp analytical form cannot represent such forces.

For hydrocarbons [1] and [3] are well satisfied since intramolecular bonding changes little on condensation and the majority of compounds are nonpolar. However structural and thermodynamic data are less abundant for low temperature structures and so the parameters are frequently fitted to room temperature data. Thermal effects are then in a sense incorporated into the crystal potential. Specific accommodation of the potential parameter approach to the reproduction of high temperature crystal structures has been recently reported [14]. It would appear that provided the source

data is isothermal derived parameters retain transferability although their physical basis is undoubtedly weaker at higher temperatures [15-17].

1.4 Future directions

Recent developments in computer science facilitate molecular orbital energy calculations on relatively large molecules. Intermolecular potentials for some simple bimolecular systems have already been derived by the Hartree-Fock self consistent treatment and confirm the analytical form used for the repulsive potential in (1.4). Such calculations are incapable of reproducing the attractive component of the potential since they omit the electron correlation energy terms responsible for London type forces. In many cases work of this kind greatly assists the empirical methods for deriving potential parameters [18, 19].

Perhaps the most intractable defect of the atom-atom potential method is the inherent assumption of pairwise additivity [20]. In fact contributions from many body interactions are incorporated in the potential parameters extracted from experimental data so it is difficult to assess the implications of this assumption. Clearly analytical forms which allow for three and higher body interactions would be more suitable vehicles for a pseudopotential. In practice such potentials contain too many parameters to be a practical proposition in fitting to experimental data. For example the structure and phonon dispersion curves of solid argon have been successfully interpreted after the incorporation of Axilrod-Teller three body forces in the interatomic potential function [21-25]. Here the inclusion of three body interactions increases the number of potential parameters from two to eleven. Much more experimental data about molecular crystals are clearly required before such a refinement can be contemplated. For the moment the simple six-exp pair potential enjoys great popularity because, despite its clear deficiencies in principle, no other analytical form can presently improve on the reproduction of structural and thermodynamic parameters it provides.

References

[1] A.I. Kitaigorodskii and K.V. Mirskaya, Soviet Physics - Crystallography 6, 408 1961.

[2] idem, ibid., 9, 137 1964.

[3] A.I. Kitaigorodskii, Acta Cryst., 18, 585 1965.

[4] idem, J.Chim.Phys., 63, 6 1966.

[5] D.E. Williams, J.Chem.Phys., 43, 4424 1965.

[6] idem, ibid., 45, 3770 1966.

[7] idem, ibid., 47, 4680 1967.

[8] idem, J.A.C.S., 91, 1243 1968.

[9] idem, Acta Cryst. A25, 464 1969.

[10] idem, Trans.Amer.Cryst.Assoc., 6, 21 1970.

[11] idem, Acta Cryst. A27, 452 1971.

[12] G. Wobser and S. Blasenbrey, Kolloid-Z.u.Z.Polymere, 241, 985 1970.

[13] G. Wobser and P.C. Hägele, Ber.Bun.Ges., 74, 896 1970.

[14] D.E. Williams, Acta Cryst. A28, 84 1972.

[15] D.C. Wallace, 'Thermodynamics of Crystals', Wiley.

[16] W. Cochran, Rep.Prog.Phys., 26, 1 1963.

[17] G. Leibfried and W. Ludwig, Solid State Physics, 12, 276 1961.

[18] C.R.A. Catlow and M.R. Hayns, J.Phys.C., 5, 237 1972.

[19] V.I. Gaydaenko and V.K. Nikulin, Chem. Phys. Lett., 7, 360 1970.

[20] J.M. Dymond, M. Rigby and E.B. Smith, J.Chem.Phys., 42, 2810 1965.

[21] M.V. Bobetic and J.A. Barker, Phys.Rev. B2, 4169 1970.

[22] J.A. Barker, M.L. Klein and M.V. Bobetic, ibid., 4176 1970.

[23] M.L. Klein, J.A. Barker and T.R. Koehler, Phys.Rev. B4, 1983 1971.

[24] J.A. Barker, R.A. Fisher and R.O. Watts, ibid., 21, 657 1971.

[25] R.A. Fisher and R.O. Watts, Molecular Physics, 23, 1051 1972.

Chapter 2

LATTICE DYNAMICS OF CRYSTALLINE SOLIDS

2.1 Introduction and objectives

The quantization of crystal vibrations into so-called 'phonons' has been demonstrated from specific heat measurements and, more directly, microscopic phonon creation and annihilation experiments with e.g. neutrons, photons and electrons. These spectroscopic studies can provide the frequency, amplitude and polarization of lattice waves and it is the purpose of this chapter to relate these quantities to the range and polarity of crystalline forces. The full implications of phonon dispersion curve measurements will become clear when their relationship to both the microscopic force field and the macroscopic crystal properties is established. To this intent, the method of long waves will be briefly summarised using the formalism of Born and Huang [1]. The role of translational symmetry and the fundamental invariance of the potential energy upon symmetry transformation of the atomic displacements will be jointly emphasised in this treatment. Finally a series of integral and asymptotic properties of the phonon eigenfrequencies such as the density of states, specific heat and elastic constants will be examined.

2.2 Properties of the potential energy

Atomic positions in a crystal may be specified in two stages. The positions of the lattice points are defined as

$$\vec{x}(l) = l_1\vec{a} + l_2\vec{b} + l_3\vec{c} \qquad (2.1)$$

where $\vec{a}$, $\vec{b}$, $\vec{c}$ are vectors defining the unit cell and the index l, implying (l_1, l_2, l_3), defines the position of the cell itself. Introduction of an atomic basis on the lattice requires a second parameter $\vec{x}(k)$ specifying the position of the k-th atom in the cell. The total position vector is

then

$$\vec{x}\binom{l}{k} = \vec{x}(l) + \vec{x}(k) \qquad k = 1 \ldots n \tag{2.2}$$

Consider a small displacement from equilibrium of the k-th atom in the l-th cell

$$\vec{u}\binom{l}{k} = \delta\vec{x}\binom{l}{k} \tag{2.3}$$

with cartesian components

$$u_\alpha\binom{l}{k} \qquad \alpha = x, y, z$$

It is instructive to expand the potential energy $\bar{\Phi}$ about the equilibrium value $\bar{\Phi}_o$ in a Taylor serial expansion in such atomic displacements and to examine the physical significance of each coefficient.

$$\bar{\Phi} = \bar{\Phi}_o + \sum_{lk\alpha} \bar{\Phi}_\alpha\binom{l}{k} u_\alpha\binom{l}{k} \tag{2.4}$$

$$+ \frac{1}{2!} \sum_{lk\alpha} \sum_{l'k'\beta} \bar{\Phi}_{\alpha\beta}\binom{ll'}{kk'} u_\alpha\binom{l}{k} u_\beta\binom{l'}{k'}$$

$$+ \frac{1}{3!} \sum_{lk\alpha} \sum_{l'k'\beta} \sum_{l''k''\gamma} \bar{\Phi}_{\alpha\beta\gamma}\binom{ll'l''}{kk'k''} u_\alpha\binom{l}{k} u_\beta\binom{l'}{k'} u_\gamma\binom{l''}{k''}$$

$$+ \ldots.$$

[a] $\bar{\Phi}_o$ is the equilibrium potential energy and is of arbitrary magnitude. When defined with respect to the gaseous species (atoms or molecules) it is equated to the sublimation energy at 0^oK after corrections for zero point vibrational motion.

$$[b] \qquad \bar{\Phi}_\alpha\binom{l}{k} = \frac{\partial^2\bar{\Phi}}{\partial u_\alpha\binom{l}{k}} \tag{2.5}$$

If the potential energy is seen as a hyperfunction of all the atomic positions, the equilibrium structure will correspond to a minimisation

of this function with respect to all the parameters $\vec{x}(^{l}_{k})$. For small displacements from equilibrium, the first derivatives of Φ will be zero and so the second term in (2.4) is absent. As discussed in chapter 1, this condition for equilibrium can be used to obtain parameters of the potential from observed crystal structures.

$$[c] \qquad \Phi_{\alpha\beta}(^{ll'}_{kk'}) = \frac{\partial^2 \Phi}{\partial u_\alpha(^{l}_{k}) \partial u_\beta(^{l'}_{k'})} \tag{2.6}$$

For a harmonic solid the second differential of the potential energy with respect to atomic displacements determines the eigenvalues and eigenvectors of motion. Truncation of the Taylor series at this point effects the harmonic approximation where the potential becomes a hyperellipsoid parametrised by the atomic displacements.

$$[d] \qquad \Phi_{\alpha\beta\gamma}(^{ll'l''}_{kk'k''}) = \frac{\partial^3 \Phi}{\partial u_\alpha(^{l}_{k}) \partial u_\beta(^{l'}_{k'}) \partial u_\gamma(^{l''}_{k''})} \tag{2.7}$$

The third order differential term represents the first anharmonic contribution to the potential. Properties such as thermal expansion and anharmonic broadening of spectral features are determined by this and the higher terms in the potential expansion.

The range of thermodynamic, structural and spectroscopic properties determined by the crystal potential function is apparent. Conversely the situation is less tractable and many approximations are necessary if information from any of these experimental sources is to illuminate the potential function itself.

2.3 Reciprocal space formalism

Ccnsider a vector with the dimensions of inverse length associated with $\vec{x}(l)$

$$\vec{\tau}(h) = h_1 \vec{A} + h_2 \vec{B} + h_3 \vec{C} \tag{2.8}$$

where $\vec{A}$, $\vec{B}$ and $\vec{C}$ are reciprocal lattice vectors

$$\vec{a}.\vec{A} = \vec{b}.\vec{B} = \vec{c}.\vec{C} = 2\pi \tag{2.9}$$

A reciprocal lattice is defined by the components (h_1, h_2, h_3) of $\vec{\tau}(h)$, the so-called Miller indices. An important property of these vectors is the fact that the scalar product between a lattice vector and a reciprocal lattice vector is an integer times 2π, from (2.1)

$$\vec{x}(l).\vec{\tau}(h) = 2\pi(l_1h_1 + l_2h_2 + l_3h_3) \tag{2.10}$$

Properties of the crystal are often described using reciprocal vectors in a phase factor of the form

$$\exp(i\vec{q}.\vec{x}(l)) \tag{2.11}$$

where $\vec{q}$ is an arbitrary vector in the reciprocal lattice. Because atomic positions are periodic functions in a crystal, the range of $\vec{q}$ defining (2.11) is limited. Hence addition of a reciprocal lattice vector to $\vec{q}$ leaves the phase factor unchanged from (2.10)

$$\exp(i(\vec{q} + \vec{\tau}(h)).\vec{x}(l)) = \exp(i\vec{q}.\vec{x}(l)) \tag{2.12}$$

The Brillouin Zone is the smallest volume in reciprocal space which can be defined in such a way that points $\vec{q}$ within this volume can be related to all points in reciprocal space by addition of the vectors $\vec{\tau}(h)$.

The reciprocal space formalism concisely incorporates the simplifications afforded by translational symmetry to the theory of lattice dynamics. A further advantage will be seen in Chapter 3. The geometrical conditions prevalent in elastic and inelastic scattering processes from crystals are readily incorporated in the reciprocal lattice notation with consequent simplification.

2.4 Lattice Dynamics in the Harmonic Approximation

The crystal Hamiltonian may be constructed from (2.4) by incorporating the kinetic energy of the atoms and making the adiabatic approximation

$$H = \tfrac{1}{2} \sum_{lk\alpha} m_k \dot{u}_\alpha^2(^l_k) + \Phi_o + \tfrac{1}{2} \sum_{lk\alpha} \sum_{l'k'\beta} \Phi_{\alpha\beta}(^{l-l'}_{kk'}) u_\alpha(^l_k) u_\beta(^{l'}_{k'}) \qquad (2.13)$$

where m_k is the atomic mass and the dot signifies a time differential. The double index ll' is replaced by a single index l-l' in accord with translational symmetry and truncation of the potential expansion after the third term effects the harmonic approximation. Application of Lagrange's equation leads to an expression for the equation of motion of the atom (l,k) in the α-th polarization

$$m_k \ddot{u}_\alpha(^l_k) = - \sum_{l'k'\beta} \Phi_{\alpha\beta}(^{l-l'}_{kk'}) \, u_\beta(^{l'}_{k'}) \qquad (2.14)$$

Solution of these equations corresponds to finding the principal axes of the hyperellipsoid H, removing the cross terms of type $u_\alpha(^l_k)u_\beta(^{l'}_{k'})$ by a coordinate transformation. The coefficients of the normal coordinates are then related to the eigenvalues and the matrix of transformation generates the eigenvectors. Such a procedure for the 3N equations is facilitated by translational symmetry, introduced by the postulate of wave solutions

$$u_\alpha(^l_k) = \frac{1}{m_k^{\frac{1}{2}}} U_{k\alpha}(\vec{q}) \exp(i\vec{q}.\vec{x}(^l_k) - i\omega t) \qquad (2.15)$$

where $\vec{q}$ is the wave vector of the propagating wave, frequency ω and amplitude $U_{k\alpha}(\vec{q})$. Translational symmetry is automatically incorporated through $\vec{x}(^l_k)$, which is periodic since the wave has a physical significance only at the atomic sites.

Introducing (2.15) into (2.14) gives

$$\omega^2 U_{k\alpha}(\vec{q}) = \sum_{k'\beta} D_{\alpha\beta}(^{\vec{q}}_{kk'}) \, U_{k'\beta}(\vec{q}) \qquad (2.16)$$

where

$$D_{\alpha\beta}(\vec{q}_{kk'}) = \frac{1}{(m_k m_{k'})^{\frac{1}{2}}} \sum_{l} \bar{\Phi}_{\alpha\beta}(l_{kk'}) \exp\left(-i\vec{q}.(\vec{x}(^{o}_{k})-\vec{x}(^{l}_{k'}))\right) \qquad (2.17)$$

is an element of the dynamical matrix. These elements are constructed by spatial Fourier transformation of the interatomic force constants. Diagonalisation of the dynamical matrix yields $\omega_j^2(\vec{q})$ and $\vec{\zeta}_{k_j}(\vec{q})$, the frequency and amplitude vector of atom k moving in the j-th normal mode where

$$\vec{\zeta}_{kj}(\vec{q}) \equiv (U^j_{kx}(\vec{q}),\ U^j_{ky}(\vec{q}),\ U^j_{kz}(\vec{q})) \qquad (2.18)$$

There are 3n solutions for each $\vec{q}$ value where n is the number of atoms in the unit cell. These solutions are periodic in reciprocal space and may be completely defined by solving (2.17) for $\vec{q}$ values within the Brillouin Zone. As there are 3N such solutions, they are effectively continuous throughout the zone. The eigenvalues for a crystal with two atoms in the unit cell are shown in Fig. 2.1 for a particular symmetry direction.

Two types of classification are frequently applied to the dispersion curves $\omega_j(\vec{q})$:

[a] Acoustic and optical branches

In the limit of low $\vec{q}$ the eigenvalues separate into two regions. Three branches approach zero frequency with constant inclination or velocity whereas the remaining solutions approach constant values as $\vec{q}$ goes to zero. The former 'acoustic' branches become equivalent to sound waves generating elastic deformations in the crystal at low $\vec{q}$. The latter are named 'optical' branches because they are frequently observed by electromagnetic spectroscopy. Photon momentum is so small that only the longest wavelength crystal excitations are visible in optical spectroscopy. Thus only the zone centre $\vec{q}$ = 0 motion is directly observable and this subject to the rigorous selection rules of infrared and Raman spectroscopy.

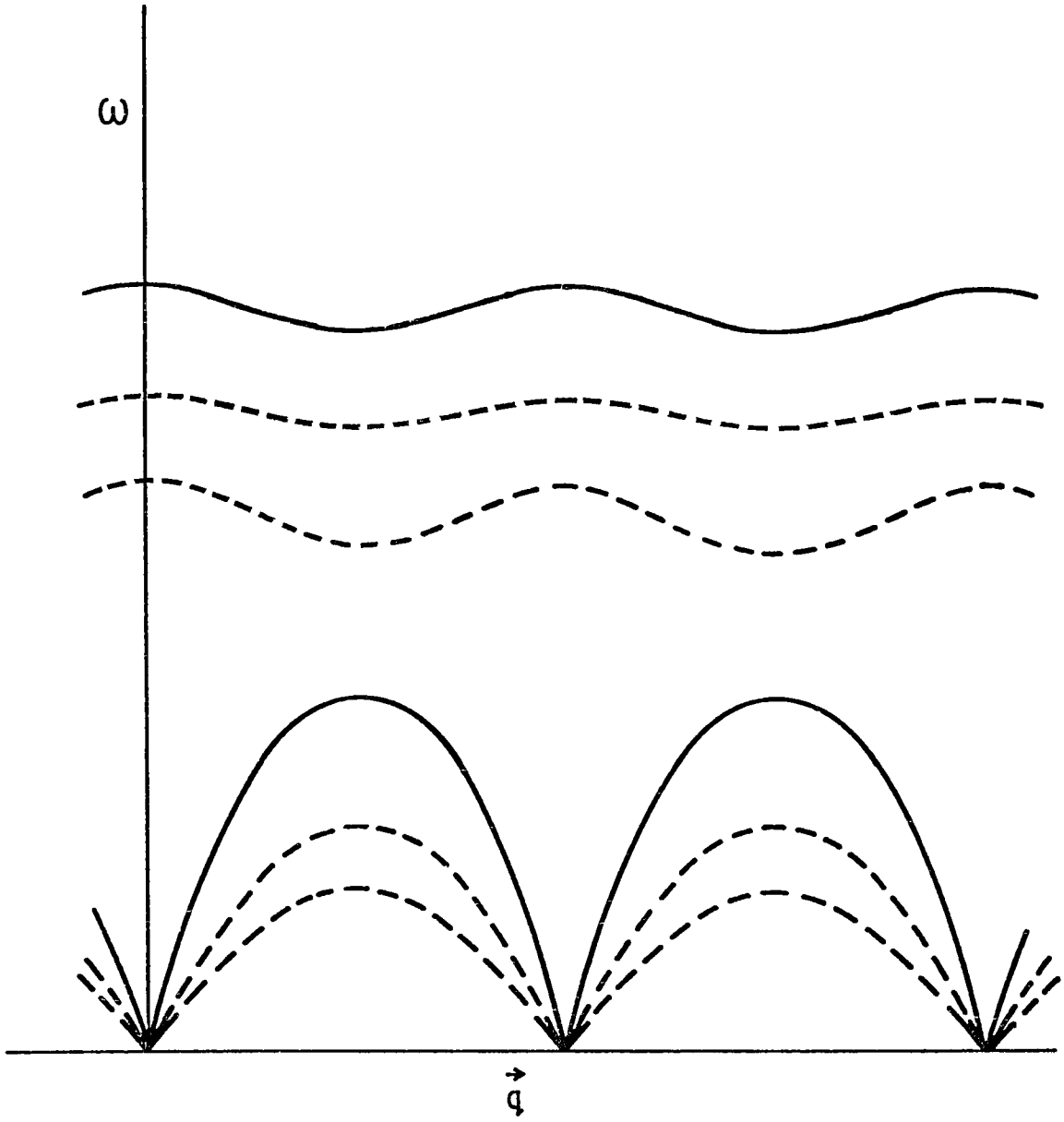

Fig. 2·1 Typical frequency solutions $\omega_j(\vec{q})$ along a symmetry direction in the Brillouin Zone for n = 2.

[b] Longitudinal and transverse polarization

Solution of the dynamical matrix for $\vec{q}$ values along certain symmetry directions causes a special simplification in the form of the eigenvectors $\vec{\zeta}_{kj}(\vec{q})$. For a wave propagating with wave vector $\vec{q}$, the atomic displacements can be along or perpendicular to $\vec{q}$, or in general a combination of both polarizations. In these special cases the solutions $\omega_j(\vec{q})$ correspond to pure longitudinal or transverse polarizations respectively. In Fig. 2.1 the full lines represent modes of longitudinal polarization and the broken lines those of transverse polarization. Even for an arbitrary direction of $\vec{q}$ the two lowest acoustic branches can be broadly classified as 'transverse' and the highest as 'longitudinal'. Modes of transverse polarization are generally of lower frequency than their longitudinal counterparts basically because the restoring forces for the shearing of planes of atoms are usually smaller than those for compression.

2.5 Symmetry properties of lattice phonons

Symmetry elements of a crystal can be catalogued and a space group defined. In a crystal the complete atomic basis of the unit cell may be generated from the asymmetric unit by applying suitable symmetry operations. The resulting space group combines the operations of a point group $\vec{\alpha}_n$ with generally nonprimitive translation operators $\vec{\tau}_n$ so that the transformation of atom $\vec{\rho}_i$ occurs as

$$\vec{R}_n\, X(\vec{\rho}_i) = \vec{\alpha}_n\, X(\vec{\alpha}_n.\vec{\rho}_i + \vec{\tau}_n) = \vec{\alpha}_n\, X(\vec{\rho}_j) \qquad (2.19)$$

where $\vec{R}_n$ is a symmetry operation of the space group. When $\vec{\tau}_n$ is a primitive lattice translation for all n the space group is called symmorphic. Conversely space groups containing nonprimitive translation operators are nonsymmorphic [2].

Dynamical properties of crystals are commonly parametrised by the wave vector $\vec{q}$ in the Brillouin Zone of the reciprocal lattice. Consequently the symmetry properties of $\omega^2(\vec{q})$ are determinable once the behaviour of $\vec{q}$

under group symmetry operations has been evaluated. A general polarisation of $\vec{q}$ in the Brillouin Zone reflects none of the space group symmetry. For certain symmetry directions however some of the elements of the space group belong to $\vec{q}$. A $\vec{q}$ group is then defined as the ensemble of space group operations $\vec{R}_n$ which transform the vector $\vec{q}$ as

$$\vec{\alpha}_n.\vec{q} = \vec{q} + 2\pi\,\vec{G} \tag{2.20}$$

where $\vec{G}$ is a reciprocal lattice vector. Since the eigenvalues are periodic in reciprocal space

$$\omega^2(\vec{q}) = \omega^2(\vec{q} + 2\pi\,\vec{G}) \tag{2.21}$$

and the transformations of the $\vec{q}$ group leave them invarient. All elements of this group form a subgroup of the space group of the crystal [2].

Three special considerations arising from symmetry affect the construction of dispersion curves:

[1] Modes of the same symmetry never cross. This is familiarly known as the non-crossing rule.

[2] The periodicity of $\omega^2(\vec{q})$ throughout reciprocal space infers that the frequency solutions must possess a continuity at the zone boundaries. When reflexion symmetry exists this function must have zero slope, i.e. a turning point at the boundary.

[3] Energy degeneracy of phonons with wave vectors $\vec{q}$ and $-\vec{q}$ introduces a concept known as time-reversal symmetry which prevails for all crystal space groups and can cause degeneracies additional to those required by spatial symmetry [2].

2.6 Integral properties of the dispersion curves

A range of bulk crystalline properties can be related to the eigensolutions of the dynamical matrix. Consider a thermodynamic property

$$T = \sum_{j,\vec{q}} f(\omega) \tag{2.22}$$

expressed as a sum over all allowed eigenvalues of the function $f(\omega)$. For example the vibrational energy of a crystal may be expressed as

$$E = \hbar \left\langle \sum_{j,\vec{q}} (n + \tfrac{1}{2})\omega_j(\vec{q}) \right\rangle_T \tag{2.23}$$

where the brackets represent a thermal average over the occupation number n. The large number of $\vec{q}$ values allowed in a crystal facilitates the replacement of the sum in (2.22) by an integral over the Brillouin Zone

$$T = \frac{V}{8\pi^3} \sum_j \sum_{B.Z} f(\omega) d^3q \tag{2.24}$$

with V the total volume of the crystal. A simplification of (2.24) is now desirable [3,4]

$$T = V \int f(\omega)g(\omega)d\omega \tag{2.25}$$

where the density of states function $g(\omega)$ is defined as

$$g(\omega) = \frac{1}{8\pi^3} \sum_j \int \frac{dS}{|\mathrm{grad}_q \omega|} \tag{2.26}$$

Integration in $\vec{q}$ space over the constant frequency surface elements dS of the group wave velocity $\mathrm{grad}_q\omega$ gives the number of $\vec{q}$ states at each frequency. This function is strongly dependent on the gradient of the eigensolutions $\omega_j(\vec{q})$ and increases in regions of $\vec{q}$ space where the dispersion curves are flat. Various singularities arise as $\mathrm{grad}_q\omega$ approaches zero and the integrand in (2.26) diverges. Van Hove [5] has classified these singularities which can be envisaged as maxima, minima and saddle points in the four dimensional functions $\omega_j(\vec{q})$ arising most often at symmetry sites such as the Brillouin Zone edges and centre.

The function $g(\omega)$ may be calculated from the experimental dispersion curves. Alternatively indirect information about the Van Hove singularities may be obtained from spectroscopic studies of polycrystalline material, as in Chapter 6. A whole range of thermodynamic properties can be rationalised

via $g(\omega)$, of which the specific heat at constant volume is the most important. Following from (2.23) and (2.25) the internal vibrational energy may be written

$$E = V\hbar \int \langle \omega . g(\omega) \rangle_T d\omega \tag{2.27}$$

and the temperature derivative expressed analytically in terms of the density of states once the thermal occupation factor is incorporated [4]

$$C_V = k \int \frac{(\hbar\omega/2kT)^2 g(\omega) d\omega}{\sinh^2(\hbar\omega/2kT)} \tag{2.28}$$

This result reduces to the classical limit of $3Nk$ as the temperature is raised to infinity.

2.7 Microscopic basis of elastic properties

For an elastic solid initially at equilibrium Hooke's Law can be expressed in tensor notation [1]

$$S_{\alpha\lambda} = \sum_{\beta\mu} C_{\alpha\lambda,\beta\mu} e_{\beta\mu} \tag{2.29}$$

where $S_{\alpha\lambda}$ is the α-component of a force applied to a surface with normal in the λ-direction. The constants $C_{\alpha\lambda,\beta\mu}$ are termed elastic constants and relate the stress in units of force/area to the strain in dimensionless units proper to a length ratio. Elements of the strain tensor $e_{\beta\mu}$ are constructed from elastic displacements u_β as follows [6,7]

$$e_{\beta\mu} = e_{\mu\beta} = \tfrac{1}{2}\left(\frac{\partial u_\beta}{\partial x_\mu} + \frac{\partial u_\mu}{\partial x_\beta}\right) \tag{2.30}$$

Since the force per unit volume is simply the divergence of the stress tensor, (2.29) and (2.30) can be combined to give equations of motion for elastic deformations

$$\rho \ddot{u}_\alpha = \sum_{\beta\lambda\mu} C_{\alpha\lambda,\beta\mu} \frac{\partial^2 u_\beta}{\partial x_\lambda \partial x_\mu} \tag{2.31}$$

and one possible solution of (2.31) is of interest in this treatment, that of a plane elastic wave

$$\vec{u} = \vec{u}' \exp(i\vec{q}.\vec{x}-i\omega t) \tag{2.32}$$

from which (2.31) reduces to

$$\rho\omega^2 u'_\alpha = (\sum_\beta \sum_{\lambda\mu} C_{\alpha\lambda,\beta\mu} q_\lambda q_\mu) u'_\beta \tag{2.33}$$

where ρ is the density of the medium. An immediate parallel between this macroscopic equation and that defining dynamical matrix elements in (2.16) is suggested. Born and Huang [1] have constructed (2.33) from (2.16) by expanding ω^2, $\vec{\zeta}_{kj}(\vec{q})$ and $D_{\alpha\beta}(_{kk'}^{\vec{q}})$ in powers of the wave vector $\vec{q}$. They stress that the derivation of elastic constants in this way, i.e. from the dynamical matrix elements in the low $\vec{q}$ limit, is only valid when the force constants $\Phi_{\alpha\beta}(_{kk'}^{l})$ in (2.17) are calculated for a configuration in which each nucleus is at equilibrium. The derivation of elastic constants from the velocity of acoustic waves is an important aspect of this thesis and now the parallel between (2.16) and (2.33) has been drawn it is convenient to relate the elastic constants defined here to the familiar bulk observables, the elastic moduli.

Following the notation of Voigt [8] the definition of $C_{\alpha\lambda,\beta\mu}$ can be simplified to a form $c_{\rho\sigma}$ where $\rho,\sigma = 1,2...6$ and

$$1 \equiv xx \quad 2 \equiv yy \quad 3 \equiv zz \quad 4 \equiv yz \quad 5 \equiv zx \quad 6 \equiv xy \tag{2.34}$$

Elastic moduli are the coefficients relating elastic deformations in or about particular directions to stresses applied to or about the same directions. As such they are usually evaluated from the compliance tensor elements $s_{\rho\sigma}$ where

$$e_\rho = \sum_\sigma s_{\rho\sigma} S_\rho \tag{2.35}$$

Elements of the compliance matrix are derived from the inversion of the elastic constant matrix defined in (2.29) taking note of the Voigt simplification (2.34). Bulk moduli can then be related to the reciprocals of diagonal elements in (2.35). In particular tensile moduli can be associated with $(s_{11})^{-1}$, $(s_{22})^{-1}$ and $(s_{33})^{-1}$ and shear moduli with $(s_{44})^{-1}$, $(s_{55})^{-1}$ and $(s_{66})^{-1}$. The number of independent elastic constants and moduli varies according to the crystal symmetry. Since the order of differentiation in (2.31) is immaterial it is clear that $c_{\rho\sigma}$ and $c_{\sigma\rho}$ must be identical, reducing the maximum number of elastic constants from 36 to 21. Further reductions are achieved only after inspection of the crystal space group.

References

[1] M. Born and K. Huang, 'Dynamical theory of crystal lattices', International series of monographs on Physics, Oxford 1954.

[2] D.J. Morgan in 'Solid State Theory - methods and applications', ed. P.T. Landsberg, Wiley 1969.

[3] J. De Launay, Solid State Physics, 2, 219, ed. F. Seitz and D. Turnbull, Academic Press 1956.

[4] J.E. Parrott in 'Solid State Theory - methods and applications', ed. P.T. Landsberg, Wiley 1969.

[5] L. van Hove, Phys. Rev. 89, 1189 1953.

[6] J.F. Nye, 'Physical properties of crystals: their representation by tensors and matrices', Oxford 1957.

[7] C. Kittel, 'Introduction to Solid State Physics', Wiley 1971.

[8] W. Voigt, Lehrbuch der Kristallphysik, Berlin 1910.

Chapter 3

NEUTRON SCATTERING FROM CRYSTAL EXCITATIONS

3.1 Introduction and objectives

In this chapter expressions for the scattering cross sections of various transition processes involving crystal excitations by cold neutrons are derived. Selection rules for absorption spectroscopy are simply obtained from symmetry arguments and the data provided by, for example, infrared spectroscopy are readily interpreted when only the eigenvalues of the dynamical equations are available by a comparison of calculated and observed energy levels. By contrast scattering experiments probe not only the discrete bound states of a system but also the continuous region of the energy spectrum and a different approach is necessary. Whereas the conservation of energy condition greatly simplifies analysis of absorption spectra, the arbitrary choice of incident beam energy and wave vector is responsible for the greater complexity of scattering theory, although enhancing the quantity of dynamical information available. Since scattering data are obtained as a set of intensity parameters over $(\vec{Q},\omega)$ space a proper treatment of such results involves a knowledge of the eigenfunctions of the Schrodinger equation. When this knowledge is not forthcoming various approximations must be made. Frequently a semiclassical approach is adopted, starting with the Green's function formalism and constructing time dependent correlation functions. Such a description is useful whenever the eigenstates of the target system are hard to define as in the case of anharmonic solids and the liquid state. As this thesis is primarily concerned with neutron scattering from bound vibrational states of a crystal in the harmonic approximation the correlation formalism will be only briefly treated and most attention will be given to an exact derivation of the inelastic neutron cross section, using the eigensolutions of the dynamical matrix described in Chapter 2.

3.2 Scattering in the Born approximation

The time independent Schrödinger equation describing the wave function of a neutron scattered by a fixed nucleus can be written

$$[-\frac{\hbar^2}{2m}\nabla^2 + V(\vec{r})]\psi(\vec{r}) = E\psi(\vec{r}) \tag{3.1}$$

where $V(\vec{r})$ defines the interaction potential between neutron and nucleus and m is the neutron mass. Introducing the scattered wave vector k (or $|\vec{k}|$) so that $k^2 = 2mE/\hbar^2$ and $U(\vec{r}) = 2mV(\vec{r})/\hbar^2$ gives a more suggestive equation

$$[\nabla^2 + k^2]\psi(\vec{r}) = U(\vec{r})\psi(\vec{r}) \tag{3.2}$$

in which $U(\vec{r})\psi(\vec{r})$ is seen as a perturbation on the Schrödinger equation for a free neutron. Solution of this differential equation proceeds by a transformation to an integral equation involving Green's functions, which are equally valid solutions of (3.2) describing the evolution of the system from $\psi(\vec{r})$ to $\psi(\vec{r}')$. Such functions can be defined by [1]

$$[\nabla^2 + k^2]G(\vec{r},\vec{r}') = -4\pi\,\delta(\vec{r}-\vec{r}') \tag{3.3}$$

and by virtue of the delta function solve (3.2) to give an integral equation containing the particular solution in integral form together with an arbitrary solution of the homogeneous equation for the free particle

$$\psi(\vec{r}) = \frac{1}{(2\pi)^{3/2}} e^{i\vec{k}\vec{r}} + \frac{1}{4\pi}\int G(\vec{r},\vec{r}')U(\vec{r}')\psi(\vec{r}')d^3r' \tag{3.4}$$

Choice of Green's function anticipates the analytical form of the second integral term in (3.4) which should correspond to a diverging spherical wave with amplitude determined by the nature of the scattering potential. In postulating a spherical wave form an assumption is made that the range of the potential is much less than the neutron wavelength

so that the scattering is isotropic. Under these circumstances a suitable solution of (3.3) is

$$G(\vec{r},\vec{r}') = \frac{e^{ik|\vec{r}-\vec{r}'|}}{|\vec{r}-\vec{r}'|} \tag{3.5}$$

which provides a basis for constructing the outgoing solutions of (3.4) in the limit of large r [1,2]

$$\psi(\vec{r}) \simeq \frac{1}{(2\pi)^{3/2}} \left[e^{i\vec{k}.\vec{z}} + \frac{e^{i\vec{k}'.\vec{r}}}{r} f(\vec{k},\vec{k}')\right] \tag{3.6}$$

where the scattering amplitude

$$f(\vec{k},\vec{k}') = \frac{(2\pi)^{3/2}}{4\pi} \int e^{-i\vec{k}'.\vec{r}'} U(\vec{r}')\psi(\vec{r}')d^3r' \tag{3.7}$$

and the direction of $\vec{k}$ has been defined so that (3.6) contains an incident plane wave polarized along $\vec{z}$ and outgoing spherical waves ($|\vec{k}'| = |\vec{k}|$) in the asymptotic limit. As a solution to (3.1) the integral equation (3.6) is unsatisfactory as it stands by virtue of the inclusion of the eigenfunction under the integral sign in (3.7). Replacement of $\psi(\vec{r}')$ by a plane wave effects an approximate solution of (3.7)

$$f(\vec{k},\vec{k}') \simeq \frac{m}{2\pi\hbar^2} \int e^{-i\vec{k}'.\vec{r}'} V(\vec{r}') e^{i\vec{k}.\vec{r}'} d^3r' \tag{3.8}$$

where the substitution of the plane wave is known as the first Born approximation and the matrix element of the potential is between wavefunctions qualifying the free neutron in its states before and after scattering within this approximation.

Starting from the wavefunctions of incident and scattered neutron wave packets the intensity distribution subsequent to scattering from a bound nucleus is simply derived. From (3.6) and the definition of the differential cross section for elastic scattering as the ratio of neutrons scattered into solid angle $d\Omega$ to the number incident over an equal time interval

$$\frac{d\sigma}{d\Omega} = \frac{r^2 \left| \frac{f(\vec{k},\vec{k}').e^{i\vec{k}'.\vec{r}}}{r} \right|^2}{\left| e^{i\vec{k}.\vec{z}} \right|^2} = |f(\vec{k},\vec{k}')|^2 \qquad (3.9)$$

What analytical form is appropriate for $V(\vec{r})$? This is the final obstacle to a calculation of the cross section via the scattering amplitude. In fact the assumption of isotropic scattering in the Born approximation restricts the choice of potential to the Dirac delta function

$$V(\vec{r}) = \frac{2\pi\hbar^2}{m} .b.\delta(\vec{r}) \qquad (3.10)$$

where the original value of $\vec{r}$ is at the bound target nucleus and b is a constant qualifying this nucleus and termed the scattering length [2]. Fermi justifies this potential on the grounds that although the neutron-nucleus interaction is very strong it is highly localised compared with the neutron wavelength. Introduction of (3.10) into (3.8) reduces the scattering amplitude to the scattering length and integration over the solid angle gives a total scattering cross section of $4\pi b^2$ for a single bound nucleus which is isotropic.

3.3 Coherent and incoherent scattering from atomic arrays

Consider a rigid assembly of chemically identical atoms with a variety of scattering lengths b_ν. There are two sources for such variations, the existence of spin on the target nucleus and the presence of more than one isotope. In the case of nonzero spin incident neutrons interact with spins parallel and antiparallel to the nucleus and the scattering amplitudes differ. Similarly isotopic impurities introduce a distribution of scattering lengths. Although these phenomena do not substantially affect the statics or dynamics or the array, the neutron cross section will be changed in consequence. Fermi's pseudopotential is rewritten

$$V(\vec{r}-\vec{r}_\nu) = \frac{2\pi\hbar^2}{m} b_\nu \delta(\vec{r}-\vec{r}_\nu) \qquad (3.11)$$

in which $\vec{r}$ and $\vec{r}_\nu$ are the neutron and atomic coordinate vectors respectively. Integration as in (3.8) gives an expression for the scattering amplitude which sums over all atomic sites

$$f(\vec{k},\vec{k}') = \frac{m}{2\pi\hbar^2} \sum_\nu \frac{2\pi\hbar^2}{m} b_\nu \delta(\vec{r}-\vec{r}_\nu) e^{i\vec{Q}.\vec{r}}$$

$$= \sum_\nu b_\nu e^{i\vec{Q}.\vec{r}_\nu} \qquad (3.12)$$

where $\vec{Q} = \vec{k}'-\vec{k}$ is the momentum transfer to the assembly.

From (3.9) the elastic cross section for a rigid array becomes

$$\frac{d\sigma}{d\Omega} = \left|\sum_\nu b_\nu e^{i\vec{Q}.\vec{r}_\nu}\right|^2 \qquad (3.13)$$

and this sum may be rewritten

$$\left|\sum_\nu b_\nu e^{i\vec{Q}.\vec{r}_\nu}\right|^2 = \sum_\mu \sum_\nu b_\mu b_\nu e^{-i\vec{Q}.\vec{r}_\mu} e^{i\vec{Q}.\vec{r}_\nu} \qquad (3.14)$$

An average scattering length can be defined as

$$\bar{b} = \frac{1}{N} \sum_\nu^N b_\nu \qquad (3.15)$$

and (3.14) can be rewritten so that

$$\frac{d\sigma}{d\Omega} = \sum_\mu \sum_\nu \{(b_\mu-\bar{b}).(b_\nu-\bar{b})+\bar{b}.(b_\mu-\bar{b})+\bar{b}.(b_\nu-\bar{b})+\bar{b}.\bar{b}\} e^{-i\vec{Q}.\vec{r}_\mu} e^{i\vec{Q}.\vec{r}_\nu} \qquad (3.16)$$

Summation over μ greatly simplifies (3.16) since the distribution of b's is random and the second and third terms disappear leaving two types of sum

$$\frac{d\sigma}{d\Omega}_{inc} = (\overline{b^2}-\bar{b}^2) \sum_\nu |e^{i\vec{Q}.\vec{r}_\nu}|^2 = N(\overline{b^2}-\bar{b}^2) \qquad (3.17)$$

$$\frac{d\sigma}{d\Omega}_{coh} = \bar{b}^2 \left|\sum_\nu e^{i\vec{Q}.\vec{r}_\nu}\right|^2 \qquad (3.18)$$

Physically (3.17) corresponds to a sum of intensities derived from the scattering amplitudes of each atom. In the limit of non-interfering amplitudes this would give the total cross section. By contrast (3.18) is constructed by addition or interference of atomic amplitudes to give a total amplitude and cross section. These two components are called the incoherent and coherent cross sections on the basis of their construction. Incoherent scattering from an array can be regarded as a straight summation of the individual atomic cross sections whereas coherent scattering is dependent upon the relative geometry (and motion for inelastic scattering) of the constituent atoms.

Experimentally (3.17) and (3.18) are best distinguished by their $\vec{Q}$ dependence. For an atomic array with long range order such a distinction is particularly dramatic. Consider an atomic crystal containing N unit cells and n chemically identical atoms in the basis. The position vector of the j-th atom in the i-th unit cell can be written

$$\vec{r}_\nu = \vec{\alpha}_i + \vec{\beta}_j \tag{3.19}$$

and the coherent cross section becomes [2]

$$\frac{d\sigma}{d\Omega}_{coh} = \bar{b}^2 \left|\sum_i^N e^{i\vec{Q}.\vec{\alpha}_i}\right|^2 \left|\sum_j^n e^{i\vec{Q}.\vec{\beta}_j}\right|^2 \tag{3.20}$$

Defining vectors $\vec{\tau}_i$ reciprocal to the lattice vectors α_i so that $\vec{\tau}_i.\vec{\alpha}_i$ is an integer, it is easily shown that the first sum in (3.20) reduces to a delta function and

$$\frac{d\sigma}{d\Omega}_{coh} = (2\pi)^3 \frac{N}{V} \bar{b}^2 \sum_i \left|\sum_j^n e^{i\vec{Q}.\vec{\beta}_j}\right|^2 \delta(\vec{Q}-2\pi\vec{\tau}_i) \tag{3.21}$$

where (3.21) has a value only when $\vec{Q}$ coincides with one of the reciprocal vectors $2\pi\vec{\tau}_i$. Such is the condition for Bragg scattering with elastic structure factor

$$F_i = \bar{b} \sum_j^n e^{2\pi i \vec{\tau}_i . \vec{\beta}_j} \qquad (3.22)$$

for a rigid lattice of chemically identical atoms in analogy with the standard X-ray result [3]. Thus coherent scattering from a crystal shows a remarkable $\vec{Q}$ dependence giving rise to the sharp reflexions observed in a diffraction pattern, whereas incoherent scattering gives a $\vec{Q}$ independent contribution $nN(\overline{b^2}-\bar{b}^2)$ to the cross section which provides no information about the relative disposition of atoms in the crystal.

3.4 Inelastic scattering and the space-time correlation formalism

Coherent elastic diffraction techniques provide important structural information since the diffraction pattern gives direct evidence of the target construction. The diffraction experiment effectively performs a Fourier analysis of the interatomic spatial distribution function, selecting in the case of a crystal the various reciprocal lattice vectors and providing intensity parameters, from which in principle the structure may be derived. By analogy inelastic scattering provides intensity contours in $(\vec{Q},\omega)$ space which reflect the Fourier components of the spatial and time distributions of the atoms.

In pursuit of this analogy a scattering amplitude can be defined for an inelastic process with energy transfer $\hbar\omega$ after (3.12)

$$f(\vec{k},\vec{k}',\omega) = \int dt\, e^{-i\omega t} \sum_\nu b_\nu \int d\vec{r}\,\delta(\vec{r}-\vec{r}_\nu(t)) e^{i\vec{Q}.\vec{r}}$$

$$= \int dt\, e^{-i\omega t} \sum_\nu b_\nu\, e^{i\vec{Q}.\vec{r}_\nu(t)} \qquad (3.23)$$

where the target nuclei have instantaneous positions $\vec{r}_\nu(t)$. After consideration of the flux in an energy range dE and angular range $d\Omega$ the differential cross section can be written [4,5]

$$\frac{d^2\sigma}{d\Omega dE} = \frac{k'}{k} \cdot \frac{1}{2\pi\hbar} \cdot |f(\vec{k},\vec{k}',\omega)|^2 \qquad (3.24)$$

in which the quantity $|f(\vec{k},\vec{k}',\omega)|^2$ is equivalent to the Van Hove scattering law $S(\vec{Q},\omega)$, a function characteristic of the scatterer and independent of purely experimental parameters [6]. This function can be written from (3.23) as the time Fourier transform of a correlation function

$$\frac{d^2\sigma}{d\Omega dE} = \frac{k'}{k} \cdot \frac{1}{2\pi\hbar} \cdot \int dt\ e^{-i\omega t} \sum_{\mu} \sum_{\nu} b_\mu b_\nu \left\langle e^{i\vec{Q}.\vec{r}_\mu(t)} e^{-i\vec{Q}.\vec{r}_\nu(0)} \right\rangle \qquad (3.25)$$

where the brackets indicate averaging over the various states of the target nuclei weighted by appropriate thermal occupation factors. Again by analogy with (3.17) and (3.18) this expression can be split into terms for coherent and incoherent scattering

$$\frac{d^2\sigma}{d\Omega dE}_{coh} = \frac{k'}{k} \frac{\bar{b}^2}{2\pi\hbar} \int dt\ e^{i\omega t} \sum_{\mu} \sum_{\nu} \left\langle e^{i\vec{Q}.\vec{r}_\mu(t)} e^{-i\vec{Q}.\vec{r}_\nu(0)} \right\rangle \qquad (3.26)$$

and

$$\frac{d^2\sigma}{d\Omega dE}_{inc} = \frac{k'}{k} \frac{(\overline{b^2}-\bar{b}^2)}{2\pi\hbar} \int dt\ e^{-i\omega t} \sum_{\nu} \left\langle e^{i\vec{Q}.\vec{r}_\nu(t)} e^{-i\vec{Q}.\vec{r}_\nu(0)} \right\rangle \qquad (3.27)$$

where for the moment an array of chemically identical atoms is assumed.

Correlation functions play an important role in scattering theory especially in regions where an exact formulation of the target dynamics is not possible. In such cases their behaviour in the classical limit can be used in the construction of approximate models [4,7]. However in the case of scattering from harmonic vibrations in a crystal it is simplest to express $\vec{r}_\nu(t)$ in a formalism of quantum mechanics and to construct the correlators in (3.26) and (3.27) accordingly.

3.5 Neutron scattering from single phonon excitations

Nuclear position vectors $\vec{r}_\nu(t)$ can be viewed as operators in the Heisenberg representation and decomposed for vibrational displacements into an equilibrium vector $\vec{\alpha}_\nu$ and a small oscillatory vector $\vec{u}_\nu(t)$ equivalent to (2.15)

$$\vec{r}_\nu(t) = \vec{\alpha}_\nu + \vec{u}_\nu(t) \tag{3.28}$$

From (3.23) the scattering amplitude may be rewritten

$$f(\vec{k},\vec{k}',\omega) = \int dt\, e^{-i\omega t} \sum_\nu b_\nu e^{i\vec{Q}.\vec{\alpha}_\nu} e^{i\vec{Q}.\vec{u}_\nu(t)} \tag{3.29}$$

and the problem reduces to a reformulation of $e^{i\vec{Q}.\vec{u}_\nu(t)}$ in terms of the available solutions of the dynamical equations (2.17) for harmonic lattice vibrations. This is achieved by means of the annihilation and creation operators $\hat{a}_{\vec{q}j}$ and $\hat{a}^+_{\vec{q}j}$ commonly used in the Heisenberg representation to express the quantization of an oscillator system. Furthermore these operators assist in the normalisation of the displacement vector (2.15) whose magnitude depends upon the number of phonons $n_{\vec{q}j}$ occupying a given normal mode so that [2,4]

$$E = N \sum_{\vec{q}j} (\hat{a}^+_{\vec{q}j}.\hat{a}_{\vec{q}j} + \hat{a}_{\vec{q}j}.\hat{a}^+_{\vec{q}j})\, \omega^2_j(\vec{q}) \tag{3.30}$$

where E is also equal to $\sum_{\vec{q}j} (n_{\vec{q}j} + \tfrac{1}{2})\hbar\omega_j(\vec{q})$. Using this formalism the expression (2.15) can be rewritten

$$\vec{u}_\nu(t) = M_\nu^{-\frac{1}{2}} \sum_{\vec{q}j} \{\hat{a}^+_{\vec{q}j} e^{-i\omega_j(\vec{q})t} e^{i\vec{q}.\vec{\alpha}_\nu} \vec{\zeta}_{\nu j}(\vec{q}) + \hat{a}_{\vec{q}j} e^{i\omega_j(\vec{q})t} e^{-i\vec{q}.\vec{\alpha}_\nu} \vec{\zeta}^+_{\nu j}(\vec{q})\} \tag{3.31}$$

in which $\vec{\zeta}^+_{\nu j}(\vec{q})$ is the conjugate of $\vec{\zeta}_{\nu j}(\vec{q})$ and

$$\sum_\nu \vec{\zeta}_{\nu i}(\vec{q}).\vec{\zeta}^+_{\nu j}(\vec{q}) = \delta_{ij} \tag{3.32}$$

from the derivation of 2.4. Introducing (3.31) into (3.29) gives [2]

$$f(\vec{k},\vec{k}',\omega) = \int dt\, e^{-i\omega t} \sum_\nu b_\nu\, e^{i\vec{Q}.\vec{\alpha}_\nu} \times$$

$$\prod_{\vec{q}j} \{1 + i\vec{Q}.(\hat{a}_{\vec{q}j} e^{-i\omega_j(\vec{q})t} e^{i\vec{q}.\vec{\alpha}_\nu} \vec{\zeta}_{\nu j}(\vec{q}) + \hat{a}^+_{\vec{q}j} e^{i\omega_j(\vec{q})t} e^{-i\vec{q}.\vec{\alpha}_\nu} \vec{\zeta}^+_{\nu j}(\vec{q}))M_\nu^{-\frac{1}{2}}$$

$$- \tfrac{1}{2}[\vec{Q}.(\hat{a}_{\vec{q}j} e^{-i\omega_j(\vec{q})t} e^{i\vec{q}.\vec{\alpha}_\nu} \vec{\zeta}_{\nu j}(\vec{q}) + \hat{a}^+_{\vec{q}j} e^{i\omega_j(\vec{q})t} e^{-i\vec{q}.\vec{\alpha}_\nu} \vec{\zeta}^+_{\nu j}(\vec{q}))]^2 M_\nu^{-1}$$

$$+ \ldots\ldots \} \tag{3.33}$$

Analysis of the terms in the expansion above illustrates the contribution of elastic, one-phonon and multiphonon processes to the total scattering amplitude. From (3.33) the inelastic cross section may be obtained using (3.24) with the useful simplification

$$\hat{a}^{+}_{\vec{q}j}.\hat{a}_{\vec{q}j} + \hat{a}_{\vec{q}j}.\hat{a}^{+}_{\vec{q}j} = \hbar(n_{\vec{q}j} + \tfrac{1}{2})/N\omega_j(\vec{q}) \qquad (3.34)$$

inferred from (3.30), and the approximate condensation of the expansion (3.33) to be discussed in 3.6

$$\prod_{\vec{q}j}\{1-|\vec{Q}.\vec{\zeta}_{\nu j}(\vec{q})|^2\frac{\hbar(n_{\vec{q}j}+\frac{1}{2})}{N\omega_j(\vec{q})M_\nu}\} \approx e^{-\sum_{\vec{q}j}|\vec{Q}.\vec{\zeta}_{\nu j}(\vec{q})|^2\frac{\hbar(n+\frac{1}{2})}{N\omega_j(\vec{q})M_\nu}} \approx e^{-2W_\nu} \qquad (3.35)$$

where W_ν is termed the Debye Waller factor. The product expression can be further simplified by integration over time to give a delta function in the energy transfer. For the coherent component of the scattering

$$\frac{d^2\sigma}{d\Omega dE}_{coh} = (2\pi)^3\sum_{\vec{q}j}\frac{k'}{k}.\delta(\hbar\omega\pm\hbar\omega_j(\vec{q})\sum_{\vec{\tau}}\delta(\vec{Q}\pm\vec{q}-2\pi\vec{\tau}).(n_{\vec{q}j}+\tfrac{1}{2}\pm\tfrac{1}{2}).|g_j(\vec{Q})|^2 \qquad (3.36)$$

where

$$g_j(\vec{Q}) = \sum_\nu(\frac{\hbar}{2M_\nu\omega})^{1/2}\bar{b}_\nu.\vec{Q}.\vec{\zeta}_{\nu j}(\vec{q}).e^{-W_\nu}e^{i\vec{Q}.\vec{\alpha}_\nu} \qquad (3.37)$$

and the phonon population $n_{\vec{q}j}$ is given by the Bose factor

$$n_{\vec{q}j} = (e^{\hbar\omega_j(\vec{q})/kT} - 1)^{-1} \qquad (3.38)$$

Two conservation conditions apply in the case of coherent scattering as set forward by the delta functions in the energy and the momentum transfer. The upper sign refers to creation, the lower sign to destruction of a single phonon. Expression (3.37) is called the <u>dynamical structure factor</u> on account of its resemblance to the elastic structure factor. In common with the latter it possesses a phase factor which is supplemented by a scalar product term involving the normal mode eigenvectors $\vec{\zeta}_{\nu j}(\vec{q})$.

Physically the dynamical structure factor can be viewed as the amplitude of the scattered neutron wave perturbed by encounter with a periodic array in turn distorted by the propagation of a single phonon.

Similarly the differential cross section for incoherent scattering in the one-phonon approximation becomes

$$\frac{d^2\sigma}{d\Omega dE_{inc}} = \sum_{\vec{q}j} \frac{k'}{k} \delta(\hbar\omega \pm \hbar\omega_j(\vec{q}))(n_{\vec{q}j} + \tfrac{1}{2} \pm \tfrac{1}{2}) \sum_{\nu} (\overline{b_\nu^2} - \overline{b_\nu}^2) |\vec{Q}.\vec{\zeta}_{\nu j}(\vec{q})|^2 \frac{2\hbar}{2M_\nu \omega} e^{-2W_\nu} \tag{3.39}$$

which is a straightforward summation of the properties of each atom, principally the eigenvector product $|\vec{Q}.\vec{\zeta}_{\nu j}(\vec{q})|^2$. Since there is no restriction on $\vec{q}$ for incoherent scattering, the scalar product term can be integrated over a constant frequency surface to remove the initial summation. The result is closely related to the density of states function described in 2.6. It has been shown that incoherent one-phonon scattering from polycrystals can be used to determine the density of states of cubic crystals containing atoms all of the same type provided the Debye Waller factors are very small [8]. For crystals of arbitrary symmetry containing different atoms the polycrystalline cross section depends upon the eigenvectors and so the experimental cross section must be viewed as the density of states function weighted by the amplitudes of the scattering atoms. For hydrogeneous samples this expression takes on a relatively simple form on account of the very high incoherent scattering length of hydrogen. To a good approximation the cross section can be written as a sum over the density of states weighted only by the hydrogen amplitudes [9]

$$\frac{d^2\sigma}{d\Omega dE_{inc}} = \frac{k'}{k} \cdot \frac{\hbar|\vec{Q}|^2}{4M\omega} \sum_{H} \frac{(\overline{b_H^2} - \overline{b_H}^2) e^{-2W_H}}{e^{\hbar\omega/kT} - 1} . G_H^{inc}(\omega) \tag{3.40}$$

where

$$G_H^{inc}(\omega) = \frac{M}{M_H} \cdot \frac{V}{(2\pi)^3} \cdot \frac{1}{3} \sum_j \int d\vec{q}\ |\vec{\zeta}_{Hj}(\vec{q})|^2 \delta(\omega - \omega_j(\vec{q})) \qquad (3.41)$$

with M the mass and V the volume of the unit cell. Expression (3.41) is valid for one-phonon excitations in a polycrystal by neutron energy gain and can be used to define an integral function

$$Z(\omega) = \sum_H G_H^{inc}(\omega) = \frac{4M\omega}{\hbar} \frac{\left(e^{\frac{\hbar\omega}{kT}} - 1\right)}{\overline{b_H^2} - \overline{b}_H^2} \lim_{Q^2 \to 0} \left[\left(\frac{d^2\sigma}{d\Omega dE} \right)_{inc} / Q^2 \right] \qquad (3.42)$$

whereby an extrapolation procedure is used to isolate the frequency dependent terms in (3.40) from the $\vec{Q}$ dependent Debye Waller factor term (3.35). Since $Z(\omega)$ is easy to define experimentally it provides a convenient basis for comparison of neutron spectra on account of its $\vec{Q}$ independence. Moreover recent work [9] has suggested that such amplitude weighted distribution functions may exhibit the same singularities as the true density of states function for several hydrogeneous molecular crystals.

3.6 Anharmonicity and multiphonon contributions to the neutron spectrum

Truncation of the phonon expansion (3.33) after inclusion of elastic and one-phonon scattering amplitudes is a reasonable approximation at low $\vec{Q}$ since the higher order multiphonon processes possess a $\vec{Q}$ dependence of successively higher order. The same argument applies to the derivation of the Debye Waller factor (3.35) which relies upon the predominance of one-phonon contributions in the inelastic spectrum. An important factor which can undermine the basis of both these approximate treatments is anharmonicity. In the case of a harmonic solid lattice phonons can be successfully described as infinite waves and the equations of motion solved accordingly. Introduction of anharmonicity leads to solutions of these equations which are finite in spatial extent and consequently in lifetime. Such a phenomenon

can be associated with phonon-phonon interactions and in the case of weak anharmonicity perturbation theory can be employed in the calculation of the energy width of phonon excitations starting from the infinite wave solutions. Such calculations have shown that the multiphonon component of the inelastic cross section is increased on the introduction of anharmonicity and the neglected contributions to the Debye Waller factor are no longer negligible [10]. From these brief considerations it is apparent that an exact theoretical interpretation of the inelastic neutron cross section is approachable only in the harmonic approximation, which to a large extent restricts the choice and in particular the temperature of scattering experiments.

3.7 Relationship of inelastic neutron scattering to other spectroscopic techniques

From the theory outlined in this chapter two practical courses are suggested. Coherent neutron scattering experiments on single crystals facilitate the complete mapping of the dispersion surfaces $\omega_j(\vec{q})$ and in principle give information about the eigenvectors for atomic vibrations. By contrast incoherent scattering techniques when applied to polycrystalline materials can provide a frequency distribution function which is an integral property of the dispersion curves closely related to the density of states. Comparison with X-ray and Raman scattering techniques should begin with the observation that photons with very high incident energy are needed to probe $\vec{q}$ right into the Brillouin zone and at such incident energies the low energy vibrational excitations in question would be unresolvable. Some information away from the zone centre is available from these sources as also from ultra violet fluorescence and phospherence studies, but it is often hard to define the $\vec{q}$ vector of the vibrational excitations. Neutron scattering is ideally suited for the investigation of phonon dispersion curves on account of the neutron's capacity for transferring sizeable

quantities of momentum in conjunction with the excitation of vibrational modes in the thermal energy region. Moreover the rigorous selection rules operating for transitions induced by electromagnetic radiation as in infrared and Raman techniques are greatly relaxed in neutron scattering spectroscopy. Although this makes neutron spectra more complicated, intensities are more readily calculated using dynamical models than, for example, in Raman scattering spectroscopy where some knowledge of the electronic structure is required. In conclusion it should be mentioned that although the amount of information derivable in principle from inelastic neutron scattering is much greater than for these optical techniques the rate of data collection is down by a factor of up to 10^{10}. Consequently neutron experiments are expensive and a major aspect of their design is the maximisation of the count rate.

References

[1] E. Merzbacher, 'Quantum Mechanics', Second Edition, Wiley 1970.

[2] P.A. Egelstaff, 'Thermal neutron scattering', Academic Press 1965.

[3] G.E. Bacon, 'Neutron diffraction'. Oxford 1962.

[4] I.I. Gurevich and L.V. Tarasov, 'Low-energy neutron physics', North-Holland 1968.

[5] B.N. Brockhouse in 'Phonons in perfect lattices and in lattices with point imperfections', ed. R.W.H. Stevenson, Scottish Universities Summer School 1965.

[6] L. van Hove, Phys. Rev. 95, 249 1954.

[7] G. Vineyard, Phys. Rev. 110, 999 1958.

[8] F. Gompf, H. Lau, W. Reichardt and J. Salgado, 'Neutron Inelastic Scattering', IAEA, Grenoble, 137 1972.

[9] G.S. Pawley, P.A. Reynolds, J.K. Kjems and J.W. White, Solid State Commun. 9, 1351 1971.

[10] A.A. Maradudin and P.A. Flinn, Phys. Rev. 129, 2529 1963.

Chapter 4

EXPERIMENTAL METHODS OF NEUTRON SCATTERING SPECTROSCOPY

4.1 Introduction

In a typical inelastic scattering process the speed of an incident neutron changes as it encounters the target nuclei. This speed change can be resolved into changes in both velocity and direction. The function of a neutron spectrometer is to collect these two labels for each neutron scattering event and, from the summation of all such processes, to evaluate the probability of particular energy and momentum changes. From the resulting histogram of scattered intensity in $(\vec{Q},\omega)$ space some of the quantities described in the last chapter can be evaluated. Essential features of most spectrometers are:

[1] An incident beam of neutrons focused in both energy and momentum to define a constant vector $\vec{k}$

[2] Facilities for energy and momentum analysis of the scattered neutrons and the definition of $\vec{k}'$ or at least $|\vec{k}'|$

From a knowledge of these two quantities the scattering can be mapped over a suitable area in $(\vec{Q},\omega)$ space where

$$\frac{\hbar^2}{2m}\left(|\vec{k}'|^2 - |\vec{k}|^2\right) = \hbar\omega \qquad (4.1)$$

$$\vec{k}' - \vec{k} = \vec{Q} \qquad (4.2)$$

and the relationship between (4.1) and (4.2) is known as the instrumental dispersion curve. It is the form of this relationship that mainly qualifies our choice of neutron spectrometer.

4.2 Choice of neutron spectrometers in this work

Available spectrometers can be broadly grouped into two categories on the basis of their applicability to the analysis of coherent and incoherent scattering respectively. The conservation condition on the momentum

transfer vector in coherent scattering facilitates the observation of single phonon events. For a successful experiment of this kind both $\vec{Q}$ and $2\pi\vec{\tau}$ must be spatially defined and this is most generally achieved in triple axis spectrometry using single crystals. In such experiments scattered neutrons are analysed by Bragg reflexion from an analyser crystal, which maps the outgoing wave vector $\vec{k}'$ with the highest possible resolution. By way of contrast incoherent scattering is subject only to an energy conservation condition, so that little extra information is obtained from single crystal experiments. Here the spatial anisotropy of both $\vec{Q}$ and $2\pi\vec{\tau}$ are best relaxed and so polycrystalline targets and counters with large solid angle are preferred. Time-of-flight experiments fall into this second category in which lower selectivity in the detection techniques affords enhancement in the rate of data collection. Of the two techniques outlined triple axis spectrometry by its application to phonon dispersion curve measurements is the more rewarding experimentally, although the higher resolution restricts the observed count rate in this case.

What sort of experiments can aid dynamical studies of polymers? On account of the large mosaic spreads normally encountered here the distinction between triple axis and time-of-flight spectroscopy just described becomes vaguer and both methods have their advantages. Ideally a spectrometer which matches its $\vec{Q}$ resolution to the sample mosaic is required for coherent scattering studies of a polymer. In practice both the techniques described will be used since they can both accommodate towards the interim rite, in the former case by relaxing the collimation and in the latter case by restricting the solid angle of detection. Both these accommodations are subject to the general principle of obtaining the maximum neutron count rate at the minimum expense to the energy resolution.

4.3 Time-of-flight spectrometry

In this method thermal neutrons are selected by mechanical choppers to give a monochromatic beam. After being scattered the neutrons travel

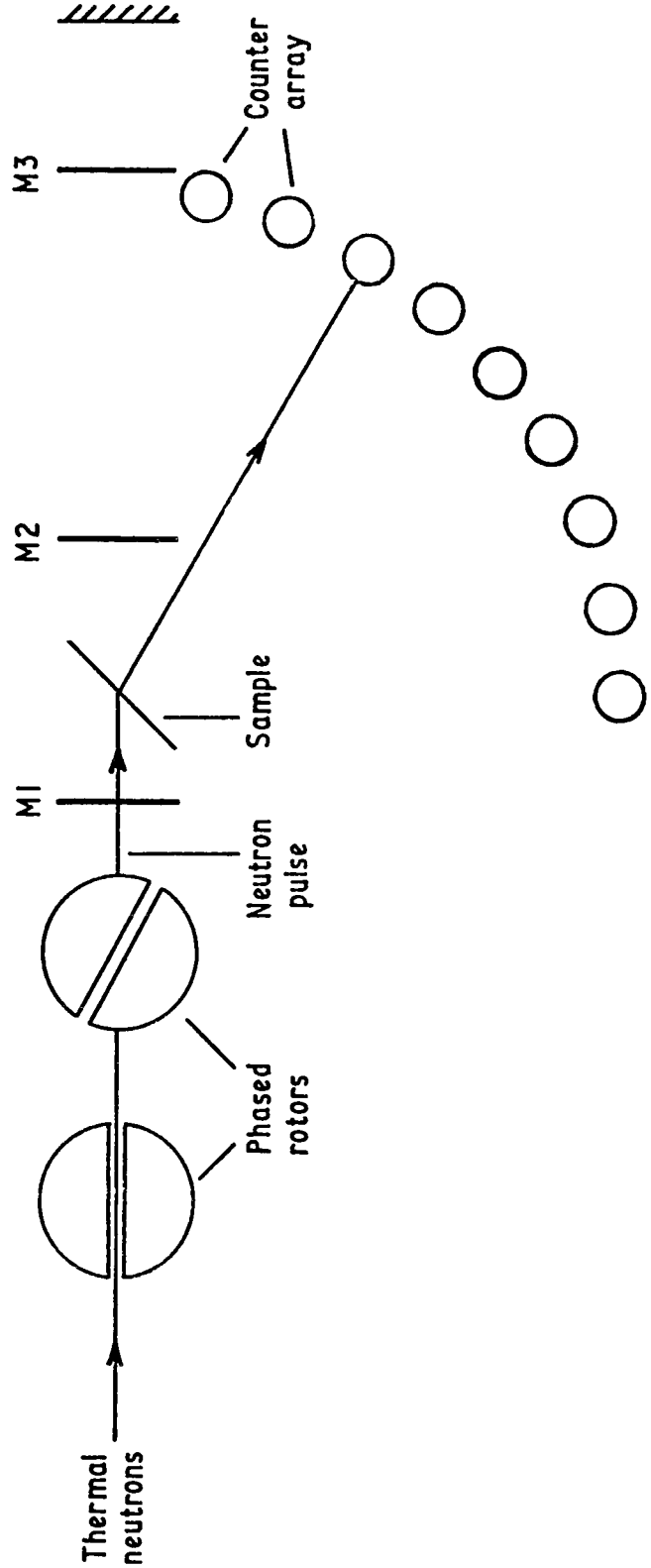

Fig. 4·1 Schematic illustration of the neutron time-of-flight spectrometer.

in bursts to a counter bank, arriving at times inversely proportional to their velocity. Energy analysis of the scattered neutrons is simply achieved from the time-of-flight.

4.3.1 Instrumental description

Experiments were performed on the 4H5, 6H and 7H time-of-flight spectrometers of the DIDO and PLUTO reactors at A.E.R.E. Harwell [1, 2]. A schematic illustration of the time-of-flight experiment is shown in Fig. 4.1 and a vertical cross section of the 6H machine is detailed in Fig. 4.2. It is most profitable to describe the construction of 6H first with reference to Fig. 4.2 and then to qualify this description for the other spectrometers.

Inpile neutrons from the heavy water moderator pass down the 6H beam tube and through a beryllium filter, cooled to liquid nitrogen temperatures, which removes all wavelengths less than 3.96 Å by diffraction and also serves to increase the thermal neutron flux by cooling [2]. After collimation the neutrons are monochromated by two high speed rotors, phased so that only neutron groups with velocities within narrow limits do not 'see' the rotors and pass on unimpeded (Fig. 4.1). The neutron wavelength produced depends on the rotor period and slot curvature [3]. Peak flux occurs at 4.22 Å, for which the rotor period is 2208 μsec, the burst time 20 μsec and the wavelength resolution about 5% FWHM ($\Delta\lambda/\lambda$). Monochromatic neutrons are then incident upon the sample from which they diffract and pass on to the detectors, arriving at times inversely proportional to their velocity, hence energy - the basis of the time-of-flight spectrometer.

Samples cover the 2" x 1" beam and are usually inclined at 45° to the incident radiation. Powder specimens are mounted in aluminium foil, suitable on account of its high transmission for thermal neutrons. Automatic cycling of up to three samples is possible, one of which is normally a vanadium plate. Some measure of the sample transmission is provided by a series of

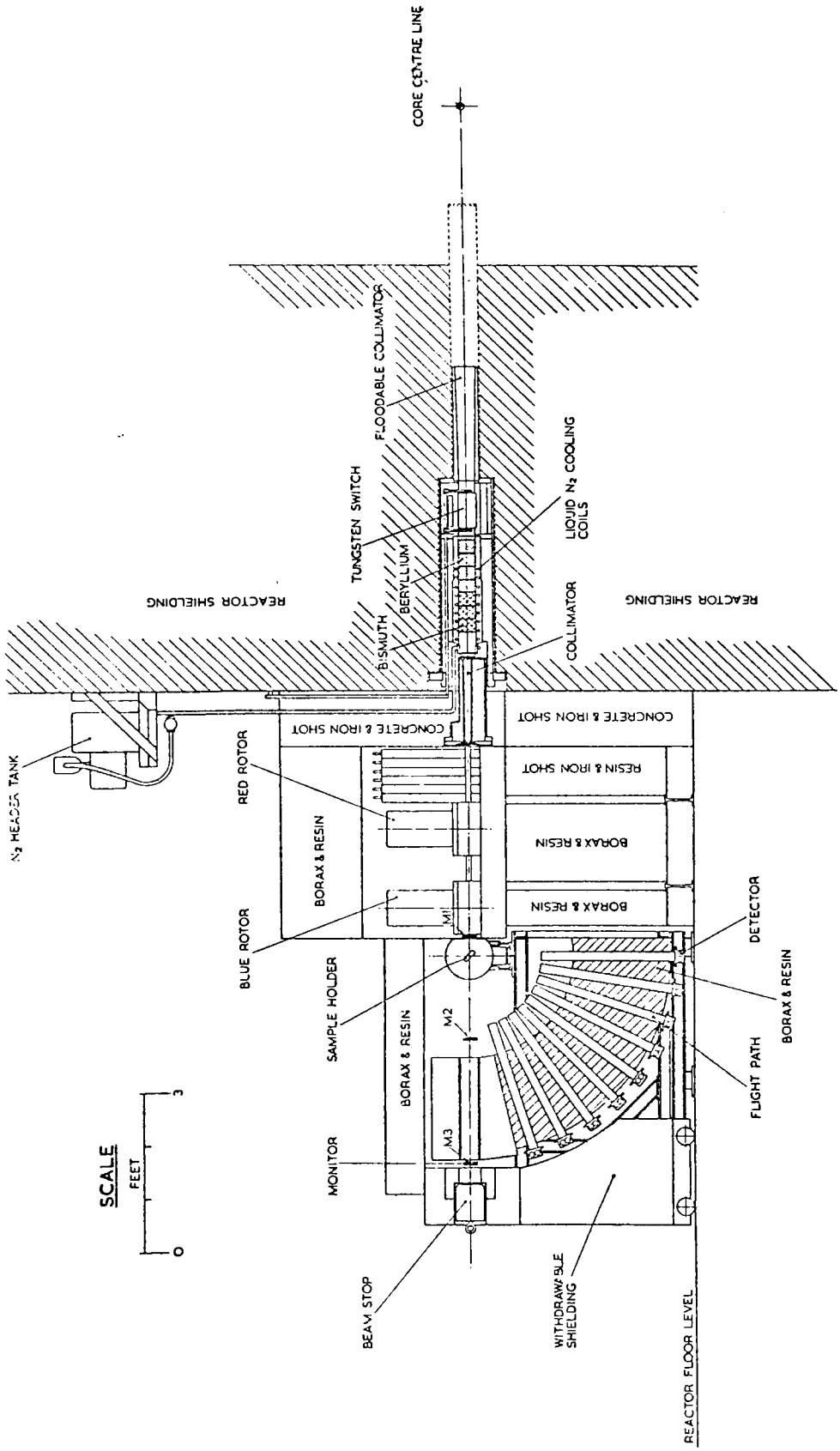

Fig.4·2 A.E.R.E. R6246. FIG.1. VERTICAL SECTION OF THE 6H TIME-OF-FLIGHT SPECTROMETER.

fission counters (M1, M2, M3) placed along the flight path to monitor the beam flux and velocity. The counter bank extends over a wide solid angle (Fig. 4.2) and incorporates two atmosphere BF_3 detectors, absorbing neutrons by the $^{10}B(n, \alpha)^{7}Li$ reaction to give α particles detectable on a proportional counter. A PDP8 computer is used to store the data in the form of counts/time-of-flight for counter banks at each scattering angle [4]. Experiments can be monitored by a closed circuit TV system which displays the sorted data throughout the run. Typical solid spectra contain one very strong peak from elastic (usually incoherent) scattering and a series of weaker peaks corresponding to inelastic transitions with neutron energy gain. Strong analogy with the anti-Stokes Raman scattering spectra is evident.

An inpile liquid hydrogen moderator distinguishes the 4H5 spectrometer from 6H. In consequence the flux is greater at longer wavelengths since the neutrons are colder. Disadvantages of 4H5 are a higher background level and the irregular disposition of counters caused by the construction of the reactor shell. The 7H spectrometer or phonon arc is complementary to both 6H and 4H5. Here a liquid nitrogen cooled MgO filter provides neutrons of shorter wavelength (1-4 Å) and counters are arranged in an arc so that a single scattering plane is defined. Two sorts of detector are employed, scintillation counters and the more efficient He^3 counters, a total of thirty in all, situated at 2^{o} intervals about an arc in a horizontal plane. The unique facility of the phonon arc is the solid angle of detection, restricted within a plane and as such ideally suited for experiments on oriented polymers (see Fig. 7.2). On the debit side counting rates are low and background levels high compared to the other spectrometers. A similar phonon arc is occasionally available as an alternative counter array on the 4H5 spectrometer.

4.3.2 Calibration of the time-of-flight

For each neutron pulse the arrival times at both the monitors and the counters are recorded and stored as a number of 6 μsec channels in a multi-channel analyser. The incident neutron velocity is calculated from the channel separation between the M1 and M3 monitors since only unscattered neutrons pass on to M3

$$V_o = \frac{d_{13}}{6(C_3-C_1)} \text{ metre/μsec} \qquad (4.3)$$

where d_{13} is the physical separation of the monitors and C_1, C_3 their time channels. Since the inelastic scattering can only be calibrated when the time channel for the arrival of elastically scattered neutrons is known, it is necessary to fix the sample on a timescale zeroed at the rotors

$$C_s = C_1 + (C_3-C_1) \cdot \frac{d_{1s}}{d_{13}} \qquad (4.4)$$

where d_{1s} is the M1-sample distance. After subtracting the sample time channel from the counter channel the time-of-flight of scattered neutrons can be directly compared. Once the time-of-flight for elastically scattered neutrons is established, the energy scale can be calibrated. Vanadium is commonly used to fix the time channel C_v for elastic scattering since it has the virtues of a purely incoherent cross section, well shaped elastic peaks and the minimum of inelastic scattering. The ratio of scattered neutron velocities for inelastic and elastic scattering is then

$$\frac{v}{v_o} = \frac{C_v - C_s}{C - C_s} \qquad (4.5)$$

and for the reciprocal velocities

$$\tau = \tau_o \frac{(C - C_s)}{C_v - C_s} \qquad (4.6)$$

with τ the reciprocal of v. A reciprocal velocity scale is preferred in the early stages of data analysis since τ relates linearly to the time

channel C in which the counts are stored. The parameters C_s, C_v and τ_o are calculated from the stored experimental data in the programme PRESCAT [5].

4.3.3 Energy analysis and the (Q,ω) track

From De Broglie the reciprocal velocities τ and τ_o are inversely proportional to the related wave vectors. Using (4.1) the energy transfer $\hbar\omega$ is expressed as

$$\hbar\omega = \frac{m}{2}\left(\frac{1}{\tau^2} - \frac{1}{\tau_o^2}\right) \tag{4.7}$$

where m is the neutron mass. This quantity is generally positive in cold neutron experiments since the incident energies of around 30 cm^{-1} are much less that kT (206 cm^{-1} at 298°K) and the neutron prefers to gain energy from the sample or to upscatter. Data collection at constant scattering angle θ over a wide arc relaxes the spatial anisotropy of $\vec{Q}$, which now loses its vector subscript

$$Q^2 = \left(\frac{m}{\hbar}\right)^2\left(\frac{1}{\tau_o^2} + \frac{1}{\tau^2} - \frac{2}{\tau_o\tau}\cos\theta\right) \tag{4.8}$$

The instrumental dispersion curve or (Q,ω) track for upscattering can be constructed from (4.7) and (4.8) and is found to be a function of τ_o and θ alone

$$Q = \sqrt{2}\left(\frac{m}{\hbar}\right)\left(\frac{1}{\tau_o^2} + \frac{\hbar\omega}{m} - \frac{1}{\tau_o}\left(\frac{1}{\tau_o^2} + \frac{\hbar\omega}{m}\right)^{1/2}\cos\theta\right)^{1/2} \tag{4.9}$$

In Fig. 4.3 this relationship is drawn out for three wavelengths at a constant scattering angle of 27°, from which it can be seen that the locus approaches a constant Q scan at short wavelengths where $\hbar\omega << \tau_o^{-2}$.

4.3.4 Normalisation of the scattered intensity

The observed counts depend on a variety of instrumental factors and

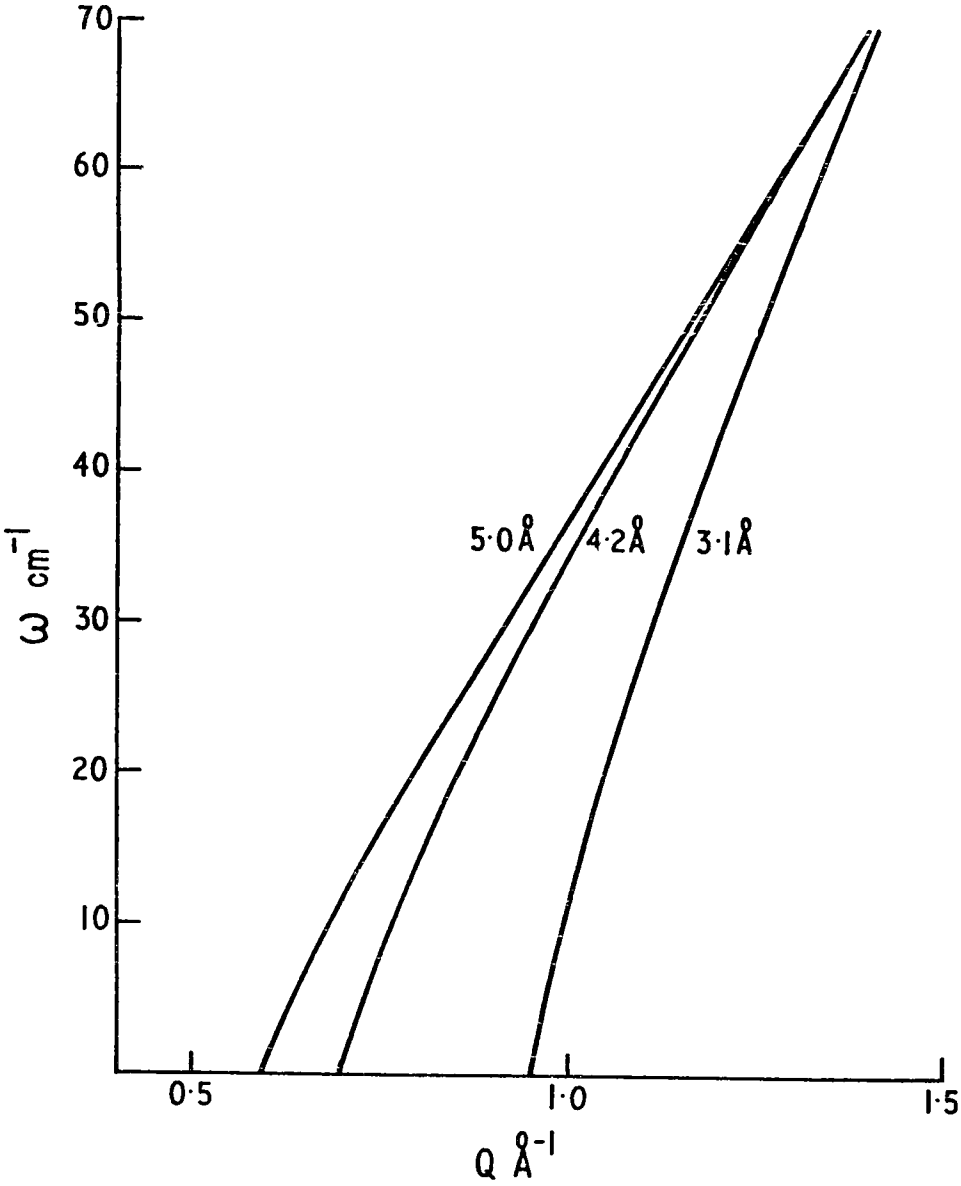

Fig. 4·3 Instrumental (Q,ω) tracks for the time-of-flight spectrometer at a constant scattering angle of 27^0 as a function of neutron wavelength.

it is desirable to remove as many of these as possible to give absolute significance to the data. In each experiment the sample alternates in the beam with a blank can and a vanadium plate. After subtraction of the background can data the sample counts are normalised using the vanadium counts at each scattering angle. A correction factor for counter efficiency is also included [6].

A differential cross section for the time-of-flight spectrum may be defined as the probability an incident neutron has of being scattered through solid angle Ω and to time-of-flight τ by one sample molecule. When there are n incident neutrons and N molecules, the scattered counts less the background are

$$N_s = \alpha \left(\frac{d^2\sigma}{d\Omega d\tau}\right)_s \qquad \alpha = n\Omega\varepsilon_\tau N\Delta \tag{4.10}$$

where ε_τ is the counter efficiency, Δ the time channel width in μsec and Ω the total counter solid angle. For vanadium the integrated elastic peak counts are

$$N_V = \beta\left(\frac{d\sigma}{d\Omega}\right)_V \qquad \beta = n\Omega\varepsilon_{\tau_o} N' \tag{4.11}$$

since almost all the scattering is elastic here. From (4.10) and (4.11) the absolute sample cross section is

$$\left(\frac{d^2\sigma}{d\Omega d\tau}\right)_s = \frac{N_s \varepsilon_{\tau_o} N'}{N_V \varepsilon_\tau \Delta N} \left(\frac{d\sigma}{d\Omega}\right)_V \tag{4.12}$$

where the dependence on flux size has gone and $\left(\frac{d\sigma}{d\Omega}\right)_V$ is well approximated by the square of the incoherent scattering length of vanadium. From (4.7) this result is readily transformed to give the more familiar form

$$\left(\frac{d^2\sigma}{d\Omega dE}\right)_s = \left(\frac{d^2\sigma}{d\Omega d\tau}\right)_s \frac{1}{\hbar}\frac{d\tau}{d\omega} = \left(\frac{d^2\sigma}{d\Omega d\tau}\right)_s \frac{\tau^3}{m\hbar^2} \tag{4.13}$$

and the scattering law of (3.24)

$$S(Q,\omega) = \frac{d^2\sigma}{d\Omega d\tau} \cdot \frac{\tau^4}{\tau_o} \cdot \frac{2\pi}{m\hbar} \qquad (4.14)$$

Counts in each time channel were scaled by the factors in (4.12) and (4.14) by the program CIRCA developed by Cocking and Heard [7]. After these corrections the absolute cross section is only accurate to about 20% since there are several experimental parameters that are hard to evaluate, of which the most prominent are

[1] Multiple scattering processes

[2] Sample absorption

[3] Uncertainty in ε_τ

In [1] neutrons experience more than one scattering event on transit through the sample. Hence the measured cross section is really a sum over all scattering processes, single and multiple. For an incoherently scattering solid the time-of-flight spectrum is dominated by the elastic peak. Here secondary processes will come mainly from elastic-elastic and elastic-inelastic scattering and so, although the absolute intensities are renormalised, no new peaks are observed in the spectra. It can be shown that multiple scattering makes a sizeable contribution at low scattering angles and high energy transfers [8, 9] but a full evaluation of [1] is only possible when there is some prior knowledge of $S(Q,\omega)$. In practice the sample size is adjusted so that only 10% of the incident neutrons are scattered, which reduces the higher order processes to the same fraction of the total scattering.

Neutron absorption can be a powerful rival to scattering processes especially since the relevant cross section is much larger for longer wavelength neutrons. As the magnitude of [2] depends strongly on the time-of-flight it is very difficult to correct the cross section without a first approximation to the true form of $S(Q,\omega)$. It is however possible to correct the vanadium data since the scattering is almost wholly elastic here. Finally [3] presents a similar problem since the ease of neutron

capture by the counters is very sensitive to the neutron velocity, slow neutrons being captured more easily than fast neutrons.

At present the information provided by absolute intensities has only been employed in work on systems where the dynamical models are of sufficient quality to assist the resolution of these factors. Fortunately in this work absorption cross sections are small and the extent of multiple scattering was reduced by the construction of samples with high transmission. Also the quest for singularities both in the coherent and incoherent neutron spectrum is little affected by these intensity factors, although the amount of information extractable from the data in principle is reduced on their account.

4.3.5 Resolution

In the time-of-flight spectrometer energy and momentum resulution are correlated since at constant scattering angle both quantities are related to the spread in τ. The observed cross section can be written as a convolution

$$\left(\frac{d^2\sigma}{d\Omega d\tau}\right)_{obs} = \int \left(\frac{d^2\sigma}{d\Omega d\tau}\right)'_{true} R(\tau-\tau')d\tau' \qquad (4.15)$$

where the resolution function can be successfully approximated to a Gaussian profile [10, 11]

$$R(\tau) = \frac{1}{\sqrt{2\pi\sigma^2(\tau)}} \exp(-\tau^2/2\sigma^2(\tau)) \qquad (4.16)$$

There are four distinct contributions to $\sigma(\tau)$

[1] From the burst time of the rotors, usually about 20 μsecs

[2] Finite sample size causes a spread in the total path length of scattered neutrons and contributes to $\sigma(\tau)$

[3] A strong contribution proportional to the flight path since the original wavelength spread is exaggerated when measured at later times-of-flight

[4] Finite detector size makes a small contribution.

Of these factors [1] and [3] are predominant and can be quantified by examining the time-of-flight distribution of the incident neutrons along the flight path using the monitor data. For each neutron pulse the variance σ_x^2 of the arrival time at a point x along the unimpeded flight path can be expressed [10]

$$\sigma_x^2 = \sigma_t^2 + x^2\sigma_{\tau_o}^2 \tag{4.17}$$

where x is measured from the rotor midpoint, σ_t^2 is the variance of the mean arrival time at x caused by the finite burst time and $\sigma_{\tau_o}^2$ the variance of the incident reciprocal velocities. From the time channel distributions at M1, M2 and M3 a plot of σ_x^2 against x^2 can be constructed and the variance parameters of σ_t^2 and $\sigma_{\tau_o}^2$ evaluated. Royston [10] has expressed $\sigma^2(\tau)$, the variance in reciprocal velocity τ of scattered neutrons on arrival at the counters as

$$\sigma^2(\tau) = \sigma_t^2 + [x_s + (x_c - x_s)\,(\frac{\tau}{\tau_o})^3]^2\sigma_{\tau_o}^2 \tag{4.18}$$

where x_s and x_c are the distances of sample and counters from the rotor midpoint. An additional factor which affects $\sigma^2(\tau)$ is the spread in path lengths for scattered neutrons caused by the finite beam size and sample dimensions, which is minimised only when the sample is perpendicular to the incident beam. In these experiments a setting angle of 45^o was preferred, since the optimum configuration cuts down the flux in the higher angle counters.

Energy and momentum resolution functions can be readily constructed once $\sigma^2(\tau)$ has been calculated. In Fig. 4.4 the energy resolution FWHM in cm^{-1} is shown as a function of neutron energy transfer for two counters of 6H, calculated for a sample inclination of 45^o to an incident beam of 4.22 Å neutrons [12]. The contribution of factor [3] is important only

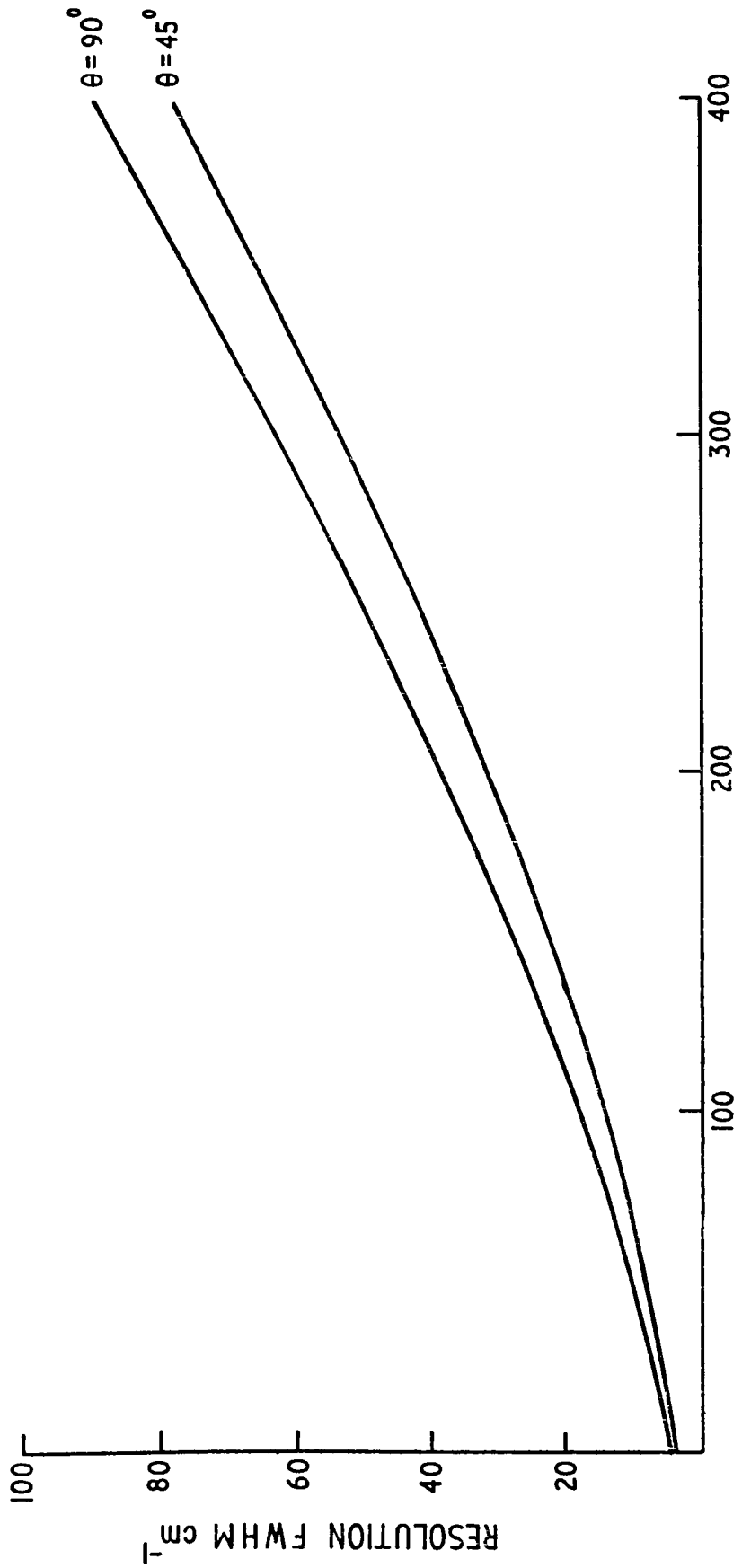

Fig. 4·4 Resolution as a function of energy transfer for incident 4·22 Å neutrons on the 6H spectrometer.

at low energy transfers and at higher energy the resolution is determined mainly by the burst time and sample geometry. Some accommodation of the resolution can be achieved by changing the rotors and hence the burst time or by adjusting the beam size and sample geometry. Improvements in the resolution are then most effective at the higher energy transfers (>200 cm^{-1}). In practice the loss in flux caused by such changes is much more dramatic than the gain in resolution and so a compromise must weigh especially on the side of flux in low temperature studies, since the Boltzman factor reduces the observed count rate for upscattering and greatly lengthens the run time, which is ideally 24 hours.

4.4 Triple axis spectrometry

Mapping of the dispersion curves for lattice phonons provides anisotropic dynamical information about a crystal and is the particular function of triple axis spectrometry [13, 14]. Such information is derived from coherent one phonon scattering processes observed throughout the Brillouin Zone and subject to the conservation laws

$$\vec{Q} = 2\pi\vec{\tau} + \vec{q} \tag{4.19}$$

$$\hbar\omega = \hbar\omega_j(\vec{q}) \tag{4.20}$$

where $\vec{q}$ is the propagation wave vector of a phonon in the j-th branch of the crystal dispersion curves.

Experimentally both $\vec{Q}$ and $2\pi\vec{\tau}$ must be spatially defined and this is the case in triple axis experiments on single crystals. In such experiments energy analysis is achieved by Bragg scattering and so $\vec{Q}$ and $\hbar\omega$ can be independently varied to satisfy (4.19) and (4.20) simultaneously. Instrumental $(\vec{Q},\omega)$ tracks are made through the four dimensional $\omega_j(\vec{q})$ space and the coherent spectrum exhibits a singularity whenever these tracks intersect a dispersion surface.

Observed intensities are related to the dynamical structure factor

$g_j(\vec{Q})$ of (3.37) in which the orientation of $\vec{Q}$ with respect to the atomic amplitude vectors $\vec{\zeta}_{\nu j}(\vec{q})$ plays an important role in determining the relative contribution of normal modes to the spectrum. Consequently $\vec{q}$ is excited from different reciprocal lattice points in a bid to maximise (3.37) for each branch of the dispersion curves. In planning such scans a dynamical model provides invaluable assistance.

4.4.1 Instrumental description

A schematic illustration of the triple axis spectrometer is shown in Fig. 4.5 together with the scattering diagram in reciprocal space. Inpile radiation is collimated and incident upon a monochromator crystal which defines the first axis. After Bragg reflexion the outgoing radiation is filtered to remove higher order contamination and monitored by a fission chamber. Monochromatic neutrons then pass on to the sample and are scattered about the second axis. The analyser assembly rotates about this axis, selecting the diffracted neutrons within a solid angle defined by the sample-analyser collimation. Energy analysis of the scattered neutrons is achieved at the analyser crystal which lies on the third axis and the neutrons pass down a collimator into the detector. Four angles are defined in all: θ_m and θ_A determine the energy of incident and outgoing neutrons, ϕ and ψ the size of $\vec{Q}$ and its orientation on the reciprocal lattice of the sample. All these parameters can be changed automatically and so it is possible to program the machine to perform scans in $(\vec{Q},\omega)$ space once the sample orientation has been defined [14]. In this fashion the parameters $(\vec{q}, \omega_j(\vec{q}))$ can be determined for single phonon excitations by simply fixing $\vec{Q}$ at various points in reciprocal space and analysing the energies of scattered neutrons - the 'constant $\vec{Q}$' method.

Experiments were performed using the TAS II triple axis facility on the DR3 reactor of the Danish Atomic Energy Commission, Risø. Although this spectrometer is essentially identical to those at A.E.R.E. Harwell, the Danish facilities were preferred since they offered a selection of

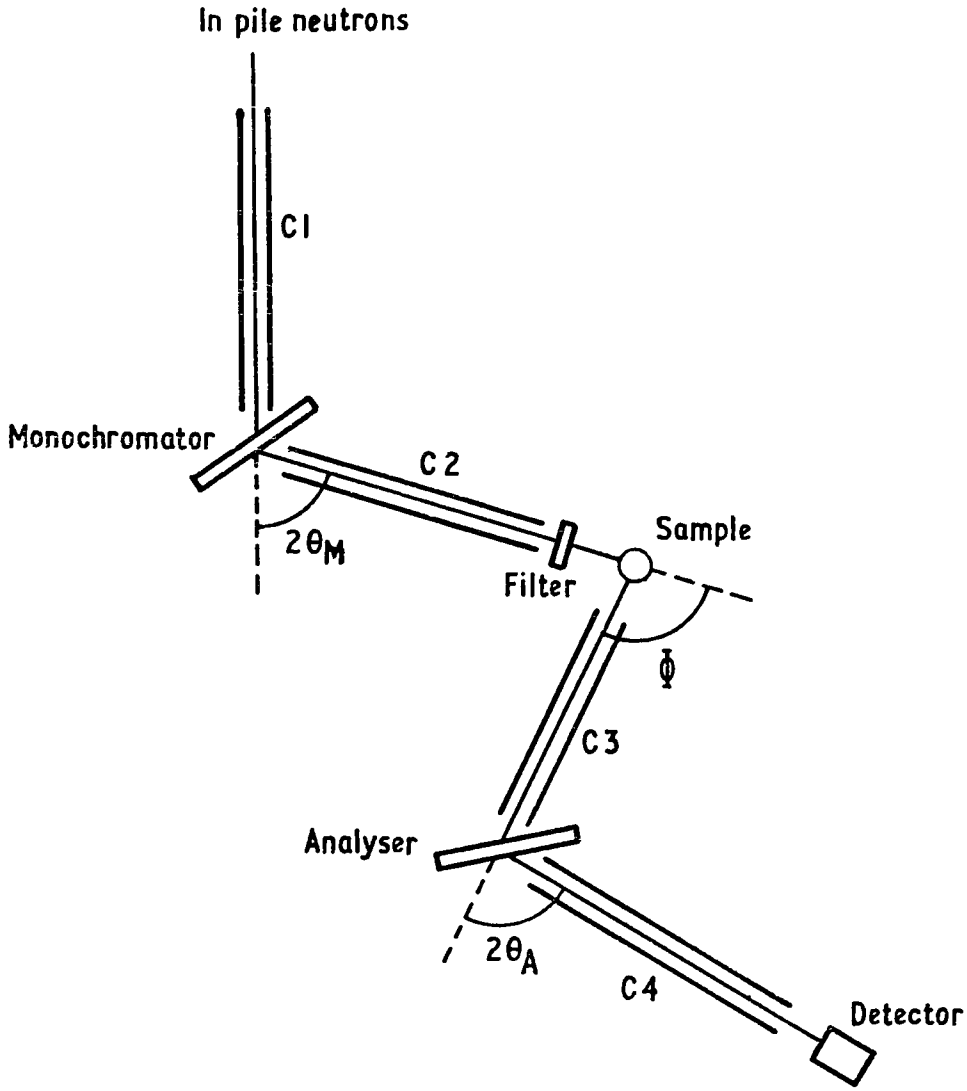

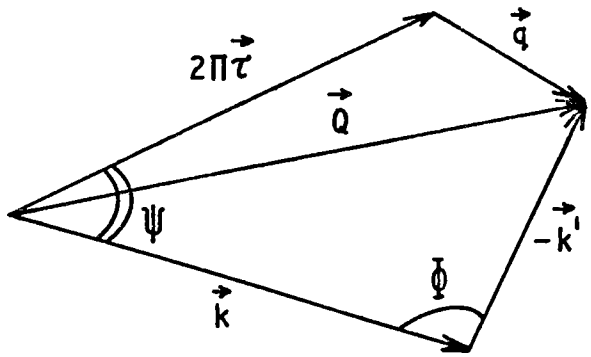

Fig. 4·5 Schematic illustration of the triple axis neutron spectrometer with the scattering diagram in reciprocal space.

pyrolytic graphite specimens ideally suited to this work. Besides providing a higher incident flux on account of their reflectivity and the virtual absence of double Bragg scattering [15], pyrolytic graphite monochromation and analysis could be easily relaxed by choice of specimens with large mosaic. Such a relaxation in the resolution was essential for the work on oriented polyethylene on account of the large mosaic which greatly reduced the count rate observed for phonon excitations.

On TAS II incident neutrons were reflected off the [002] planes of a graphite monochromator, which was curved vertically to focus the outgoing radiation upon the smaller sample. A graphite filter placed on the sample side of the monochromator reduced the second order scattering from [004] by a factor of 5000 giving an essentially clean beam of wavelength 2.40 Å. Energy analysis employed the [002] planes of a graphite analyser and neutrons were detected about the third axis by a standard two atmosphere He^3 counter. An online computer was used to calculate a sequence of settings for the angular parameters consistent with the desired $(\vec{Q},\omega)$ scan. The output data were printed out at a teletype so that once the crystal was mounted properly and all the zero angles were determined, the machine could be left under automatic control. For the constant $\vec{Q}$ scan normally used in this work, the output was in the form counts/energy transfer for each point in reciprocal space.

4.4.2 Resolution and optimization of the count rate

Since the experimental parameters $\vec{Q}$ and $\hbar\omega$ can be independently varied in a triple axis experiment the observed cross section is a convolution of the true cross section with a two dimensional resolution function

$$\left(\frac{d^2\sigma}{d\Omega dE}\right)_{obs} = \int \left(\frac{d^2\sigma}{d\Omega dE}\right)_{true} R(\vec{Q},\omega)\, d\vec{Q}\, d\omega \qquad (4.21)$$

where $R(\vec{Q},\omega)$ represents the uncertainty of an experimental location $(\vec{Q},\omega)$. Contours of the resolution function at constant amplitude define an ellipsoid since $\vec{Q}$ is restricted to a plane in the experiment. The energy and $\vec{Q}$ resolution are then determined by the shape of this ellipsoid

and its orientation with respect to the dispersion surfaces $\omega_j(\vec{q})$. A typical constant $\vec{Q}$ experiment in which the $(\vec{Q},\omega)$ locus lies along the energy axis is represented in Fig. 4.6. In the diagram $\vec{q}$ is measured from a reciprocal lattice point and a two dimensional surface $\omega_j(q_x,q_y)$ is drawn in for an acoustic branch of the dispersion curves. Clearly the energy resolution of each phonon excitation depends upon the profile presented by the resolution function at the point of intersection with the dispersion surface. When the focusing is poor intersection occurs over a wide range of $(\vec{Q},\omega)$ across the ellipsoid and excitations are correspondingly broad. Focusing of a triple axis spectrometer [16] is a matter of adjusting the orientation of the resolution ellipsoid to match the slope of the dispersion surface hence minimising the integration track of (4.21).

Experimental contributions to $R(\vec{Q},\omega)$ can be enumerated under three heading

[1] Collimation in the monochromator and analyser system which defines the angular spread in $\vec{k}$ and $\vec{k}'$

[2] Mosaic in the monochromator and analyser crystals operating in a similar fashion to the collimation

[3] For very relaxed collimation, the sample size and orientation with respect to $\vec{k}$ and $\vec{k}'$

Each of these contributions leads to a finite resolution along the instrumental track by defocusing $\vec{k}$ and $\vec{k}'$. Cooper and Nathans (17) provide an analytical expression for the resolution function in terms of [1] and [2]. Assuming that each contribution is the FWHM of a Gaussian probability function, the resolution function is constructed by resolving these components along the instrumental $(\vec{Q},\omega)$ track and summing them to define the exponent of a Gaussian function

$$R(\vec{Q},\omega) = R_o \exp(-\sum_{i=1}^{3}\sum_{j=1}^{3} \alpha_{ij} X_i X_j) \qquad (4.22)$$

where X_i define small displacements in energy and momentum transfer from the experimental setting caused by finite resolution. Triple axis

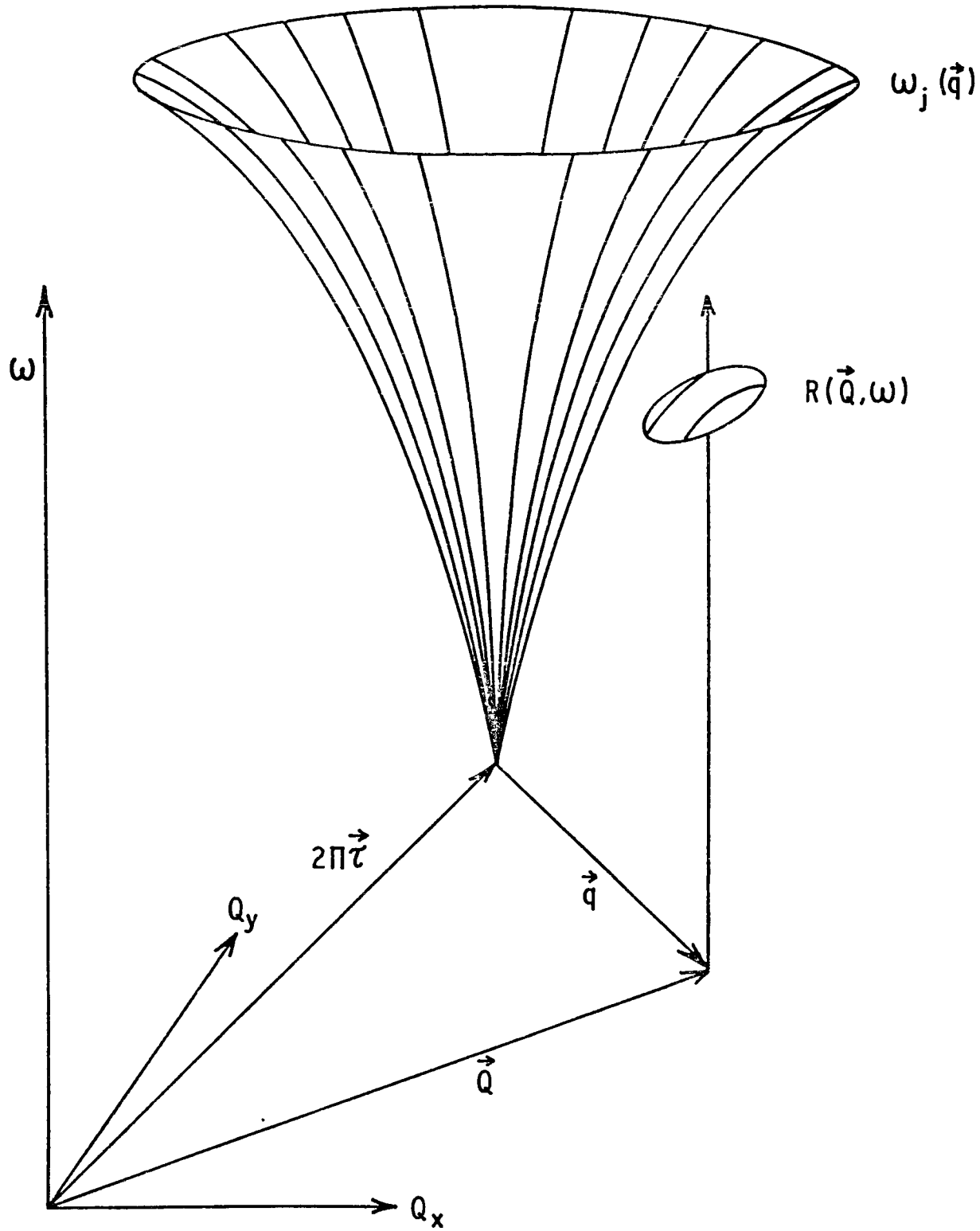

Fig. 4·6 Intersection of the resolution ellipsoid $R(\vec{Q},\omega)$ with an acoustic dispersion surface $\omega_j(\vec{q})$. Energy analysis is at constant $\vec{Q}$.

experiments confine $\vec{Q}$ to a single plane and so there are only three components of the resolution to be considered, two for the $\vec{Q}$ vector and one for the energy transfer. The resolution ellipsoid is defined by the exponent of (4.22) which is fixed for a contour of constant intensity. An experimental check on the calculated resolution function is made possible in the region of a Bragg peak which being a delta function in $(\vec{q},\omega)$ space adopts an experimental profile identical to $R(2\pi\vec{\tau},0)$. Such measurements confirm that the resolution function closely resembles a Gaussian and is almost exactly predicted by the calculations. The successful computation of $R(\vec{Q},\omega)$ from well defined instrumental parameters such as collimation angles, mosaic spread etc. is in sharp contrast to the situation in time-of-flight spectrometry, where there are many ill-defined factors influencing the resolution.

Among factors affecting the count rate other than the resolution, sample size and mosaic are prominent. With present incident fluxes the specimen dimensions are a critical factor affecting the feasibility of experiments. An additional factor is temperature. The reduced count rate from inelastic excitations at low temperatures is partially offset in triple axis experiments by analysing the neutron energy loss spectrum.

How far can triple axis spectrometry accommodate to samples with large mosaic spread? This is a question which is to a large extent answered by the results of Chapter 10. Mosaic blurs the reciprocal lattice points into arcs so that the resolution ellipsoid depicted in Fig. 4.6 encounters a continuous spectrum of dispersion surfaces $\omega_j(\vec{q})$ in its vertical transit. Since the wave vector $\vec{q}$ loses some definition, phonon excitations are broader in frequency and in some cases average out completely. Of practical importance is the fall in count rate which is frequently prohibitive. To offset this some relaxation in the $\vec{Q}$ resolution is inevitable so that data can be collected over a wider solid angle. In practice a balance must be struck between count rate and energy

resolution since the latter deteriorates as the collimation is relaxed.

References

[1] D.H.C. Harris, S.J. Cocking, P.A. Egelstaff and F.J. Webb, 'Inelastic neutron scattering in Solids and Liquids', IAEA, Vienna, Vol. I, 107 1963.

[2] L.J. Bunce, D.H.C. Harris and G.C. Stirling, A.E.R.E. Res. Rep., R-6246 1970.

[3] S.J. Cocking, A.E.R.E. Res. Rep., R-4920 1970.

[4] J.W. Hall, A.E.R.E. Res. Rep., R-5962 1968.

[5] G.D. Wignall, A.E.R.E. Res. Rep., M-1928 1967.

[6] S.J. Cocking and F.J. Webb, A.E.R.E. Res. Rep., R-5168 1967.

[7] S.J. Cocking and C.R.T. Heard, A.E.R.E. Res. Rep., R-5016 1965.

[8] S.J. Cocking, D.Phil. thesis, University of London 1967.

[9] P.A. Reynolds, D.Phil. thesis, University of Oxford 1972.

[10] R.J. Royston, Nucl. Inst. and Meth., 30, 184 1964.

[11] S. Komura and M.J. Cooper, J. Appl. Phys.(Jap.), 9, 866 1970.

[12] M.B.M. Harryman and J.B. Hayter, private communication.

[13] B.N. Brockhouse in 'Phonons in perfect lattices and in lattices with point imperfections', Scottish Universities Summer School 1965, ed. R.W.H. Stevenson, Oliver and Boyd 1966.

[14] D.H. Saunderson, C. Duffill and R.I. Sharp, A.E.R.E. Res. Rep. R-4895 1965.

[15] T. Riste in 'Instrumentation for neutron inelastic scattering research', Panel proceedings series, IAEA, Vienna 1970.

[16] G.E. Peckham, D.H. Saunderson and R.I. Sharp, J. Appl. Phys.(Brit.), 18, 473 1967.

[17] M.J. Cooper and R. Nathans, Acta Cryst., 23, 357 1967.

Chapter 5

INTRODUCTION TO THE SCIENCE OF POLYETHYLENE

5.1 Polyethylene morphology

For molecules as large as polyethylene, condensation into the solid can occur in a variety of ways on account of the uneasy balance between the pronounced tendency to disorder, on the one hand, and the gain of potential energy on the formation of an ordered structure, on the other hand. Under normal conditions it is the fastest route that determines the final morphology. In consequence polyethylene is a composite solid containing regions of high order and yet exhibiting such phenomena as viscoelastic behaviour generally attributed to random chain structures.

One of the remarkable features of historical development in the field of polymer morphology is the hierarchy of order which has been slowly revealed to the crystallographer. Thus the order exhibited within the microcrystal or unit cell and characterised by the first crystallographic studies is embraced by the longer range order of the lamellae, which in turn contribute towards the several bulk textures of polyethylene. This hierarchy provides a convenient basis for this brief review.

5.1.1 The microcrystal

The existence of crystalline regions within polyethylene was first demonstrated by Bunn [1] who observed discrete reflexions in the wide angle X-ray diffraction pattern. From this evidence it became clear that the ordered regions of polyethylene contain parallel arrays of planar zig-zag chains stacking in an orthorhombic lattice with two chains in each unit cell (Fig. 5.1). The lattice c-parameter includes the monomeric C_2H_4 unit of the chain indicating a persistence of the planar, linear chain at least to lengths where end-effects will not be reflected in the lattice parameters. However the Bragg reflexions were broadened in

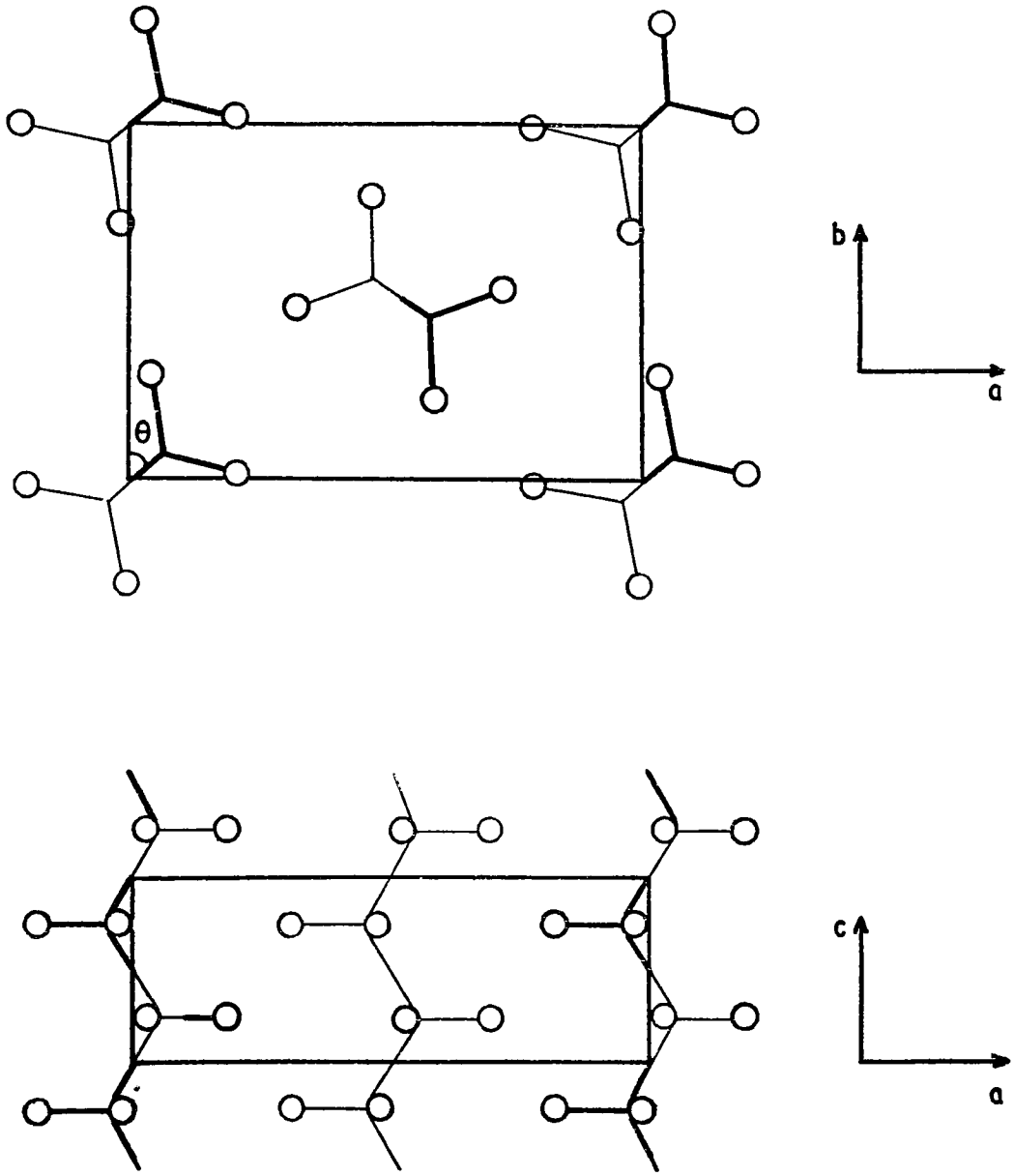

Fig. 5·1 Unit cell of polyethylene viewed along and perpendicular to the chain axis.

such a way as to indicate crystallite sizes of only a few hundred angstroms. Further inspection of the diffraction pattern revealed the so-called 'amorphous haloes' representing an ill-defined stacking of a fraction of the chain molecules.

5.1.2 The lamella

Crystallization of polyethylene from dilute aromatic solvent solutions to give lamellar 'single-crystals' was reported simultaneously by Keller [2], Till [3] and Fischer [4] in 1957. Low angle X-ray diffraction work coupled with electron microscopy showed that the chain axes are normal to the faces of the platelets or lamellae which are only c. 100 Å thick. Since the molecular length of a polyethylene molecule can be around 10^5 Å, the only possible explanation of 'single-crystals' is the folding of chains at the surface of the platelets. The lamellae are built up by growth along defined prism faces to give plates of thickness equal to the fold length such that the chains are perpendicular to the basal plane of the lamellae. Folding occurs in the crystallographic [010] direction and the lateral dimensions of the lamellae are of the order of thousands of angstroms (see Fig. 8.1). Although the thermodynamics of crystallization indicate that a fully extended chain polymer crystal has the lowest free energy, it is clear that chain folding occurs because in this way crystallization can proceed faster [5, 7].

5.1.3 Composite polyethylene

In bulk polyethylene the lamellae are tied together in a variety of ways and it is the tie molecules which introduce a new unknown, the amorphous region. Much controversy surrounds the specific nature of interlamellar linkages and it is sufficient to state that a model distinguishing separate 'crystalline' and 'amorphous' phases is now widely accepted [6]. In this work three forms of polyethylene are investigated with bulk textures determined primarily by the mode of crystallization:

[1] Single-crystal mats are obtained by bulk deposition from solution and are agglomerations of lamellae possessing no macroscopic orientation. A 'sandwich' model in which amorphous layers including chain folds separate the ordered lamellae has been suggested from electron microscopic studies of single-crystals [6, 7].

[2] Melt crystallized polyethylene has an increased proportion of ties between lamellae which has been associated with the observed mechanical cohesion [8, 9]. The growth of spherulites on melt crystallization involves a radially symmetric deposition of the basic lamellae units twisted about an axis parallel to the spherulitic radius [6, 10-13].

[3] High pressure crystallization (>5 kbar) of polyethylene melts yields a brittle powder of high crystallinity in which the chains are highly extended [14-18]. Examination of fracture surfaces reveals the presence of broad lamellae extending almost throughout the solid, representing the closest approach to the thermodynamically stable state of solid polyethylene yet attained. Unfortunately although the chains can be very well aligned in this material no preferred orientation is obtained perpendicular to the chain axis.

The process of crystallization from melt or solution cannot be exploited to produce a specimen of polyethylene with bulk anisotropy under normal conditions. Instead attention is diverted to the unique flow properties of long chain compounds which facilitate orientation by purely mechanical means. For rubber or elastomers in general a degree of orientation can be produced reversibly on application of a static deformation. In the absence of cross-linking, the simpler synthetic polymers are aligned almost exclusively by dynamic processes applied to the melt or solid. Such plastic deformations are achieved by drawing, rolling or extruding the isotropic solid or melt [19]. The principal effect of these processes is the institution of a fibrous texture in which the chain axes

are aligned, although recent developments have facilitated orientation of the other crystallographic directions and are reported later in this thesis [5, 20].

5.2 Vibrational analysis of polyethylene

In a polymer the unique axis adopted by the chains on crystallization suggests that the crystal binding forces will be highly anisotropic. For polyethylene the relative strengths of forces within and between the chains are such that the dynamical model most frequently adopted is that of a two-dimensional molecular crystal in which coupling between internal and external chain vibrations is excluded. The success of an isolated chain model in predicting the observed intrachain vibrational frequencies justifies this assumption. Historically the sophistication of dynamical models of the polyethylene lattice has evolved with experiment. Earliest information came from near infrared and Raman spectroscopy, from which a force field was derived for a single chain. Observation of crystal field splittings in these spectra encouraged a perturbation treatment of the first force field. More recent refinements have been geared to the rather frugal experimental information directly relevant to the interchain force field. The measurement of phonon dispersion curves for external chain vibrations reported in this thesis dramatically alters the situation by providing a firm empirical basis for model calculations. In this section the present dynamical models are reviewed to provide the background information required for an appreciation of the author's own contribution.

5.2.1 Internal dynamics of the polyethylene chain

Spectroscopic studies of the long chain hydrocarbon series provide a wealth of dynamical information all of which is transferable to polyethylene itself, in which selection rules for electromagnetic radiation are more rigorously upheld. Schachtschneider and Snyder [21, 22] fitted a 35 parameter valence force field to the assigned infrared and Raman

frequencies of n-paraffin homologues up to $C_{14}H_{30}$. A least squares perturbation method was employed and a total of 270 observed frequencies were reproduced to within an average error of 0.25%. The same experimental data were also fitted to a Urey-Bradley force field by Tasumi, Shimanouchi and Miyazawa in an extension of the earlier work by Snyder [21, 23, 24]. Making full use of the intrinsic symmetry of chain compounds, they calculated the vibrational frequencies of an isolated infinite chain as a function of a parameter related to the phonon wavevector in a crystal. This parameter represented the phase lag between a set of oscillators coupled to give the normal vibrations of an infinite chain. Agreement with Schachtschneider and Snyder was good, lending strong support to the postulated transferability of force constants among the n-paraffins and polyethylene.

Piseri and Zerbi [25] developed a general method for computing the normal mode vibrations of isolated, extended polymer chains and their results for polyethylene are shown in Fig. 5.2(a), derived from the earlier valence force field [22]. Calculated acoustic and optical normal modes are well separated in frequency, with the lowest branches corresponding to cooperative chain stretching and torsional motion, ν_5 and ν_9 respectively. The absence of a restoring force to overall axial rotation lends acoustic character to the ν_9 mode, which evolves into a free rotation at zero wavevector.

Tasumi and Shimanouchi [26] repeated their calculation for chain molecules in an orthorhombic lattice, including an intermolecular potential but solving only for intrachain phonons. Crystal field splittings of the chain modes were predicted, with mixing of the lowest acoustic branches to give intercepts at zero wave vector corresponding to purely external vibrations. In Fig. 5.2(b) dispersion curves for intrachain phonons split by the crystal field into a (solid line) and b (broken line) polarizations are shown for comparison with the isolated chain model. Only one acoustic branch remains in the extended zone scheme of Fig. 5.2(b), corresponding

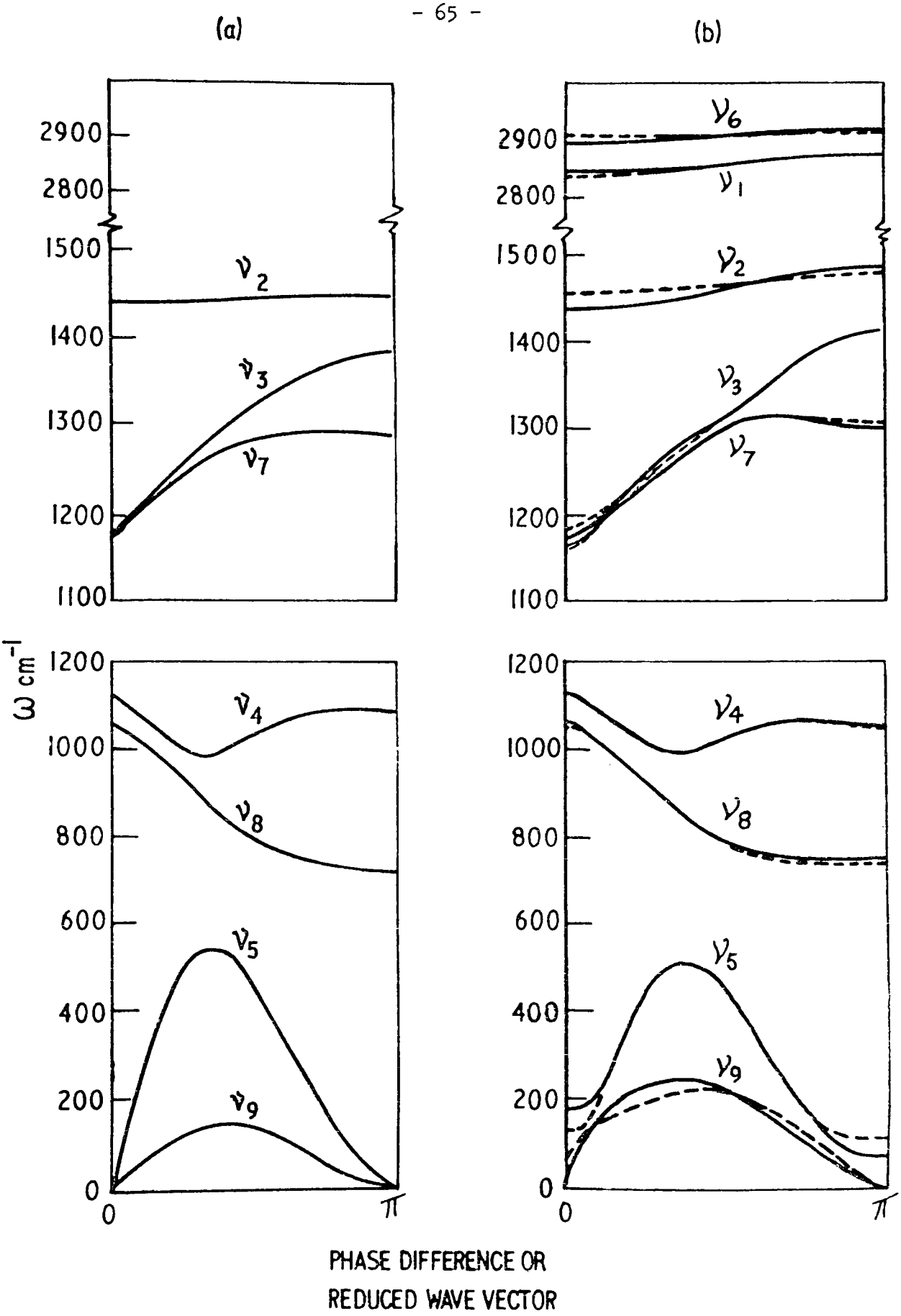

Fig. 5·2 Comparison of theoretical dispersion curves for chain axis modes in polyethylene : (a) calculated assuming an isolated chain [25]; (b) calculated using a Urey-Bradley molecular force field and four intermolecular H-H force constants [26]

to accordionlike chain deformations of longitudinal polarization. Schaufele and Shimanouchi [27] have observed such acoustic vibrations in the Laser Raman spectrum of long chain hydrocarbons, assembling a dispersion curve which is in good agreement with the calculations. Similar measurements by coherent neutron scattering are discussed later [74].

5.2.2 Experimental parameters of the interchain force field

The refined state of the intrachain potential is a consequence of the extensive spectroscopic information about the normal modes of vibration. By way of contrast there is very little information to date about the interchain force field available from spectroscopy. Consequently a prime deficiency of present models for the force field is found in the overall reliance upon thermodynamic data such as specific heat, which in no way reflect the anisotropy of such forces. And so before considering these models it is important to enumerate the experimental parameters on which they are based if a true appreciation of their limitations is to be achieved.

[1] Specific Heat

Wunderlich [28, 29] obtained the specific heat of 100% crystalline polyethylene at low temperatures by extrapolating data from samples of different crystallinity. Later work on single-crystals confirmed his results. The general features of the temperature variation are a Debye type T^3 law below $9^{\circ}K$ which changes to an approximately linear law valid up to $70^{\circ}K$. This behaviour has been interpreted by combining three dimensional and one dimensional Debye models with different cut-off frequencies [30]. These two parameters are a crude index of the relative strength of chain and interchain forces but little more. As an integral property of the density of states of the crystal, specific heat data provide a valuable boundary condition upon dynamical calculations as will be shown later.

[2] Near infrared and Raman splittings

Snyder observed splittings in the progression bands of n-paraffin infrared spectra from which he calculated some intermolecular force constants [21]. His assignments were later revised and extended by Tasumi and Shimanouchi who based their interchain force field upon these splittings [26]. Recent laser Raman studies by Boerio and Koenig have revealed a series of splittings unresolved in previous Raman work [31-33]. In principle careful observation of the polarization of doublet components can lead to anisotropic information about the crystal field itself. For example the CH_2 rocking mode in polyethylene has a higher component at 731 cm^{-1} polarized along the a-axis and a lower component along the b-axis at 720 cm^{-1}. In practice it has proved very difficult to extract this information without some prior knowledge of the interchain force field.

[3] Far infrared studies

Early far infrared work on the n-paraffin series demonstrated the existence of a band at 71 cm^{-1} occurring only in the orthorhombic and monoclinic phases where there are two chains in the unit cell [34-36]. The invariance of this band frequency with chain length and its shift on deuteration were consistent with assignment to one of the two infrared active translatory lattice modes. Krimm and Bank [37, 38] confirmed assignment to the $\Gamma_6(B_{1u})$ translatory zone centre mode by dichroism studies on machine extruded polyethylene with some preferred a-axis orientation. Almost simultaneously, Dean and Martin [39, 40] made the same assignment from polarized spectra of single crystals of $C_{23}H_{48}$. The same authors observed a weak band at 109.5 cm^{-1} in the far infrared spectrum of polyethylene at 2°K and suggested an assignment to the $\Gamma_8(B_{2u})$ translatory zone centre mode on the basis of early model predictions.

[4] Raman studies

Low frequency Laser Raman spectra for polyethylene have been reported

by several workers and there is some confusion about the assignment of lattice modes. Two Raman active external modes are expected, corresponding to overall molecular librations about the chain axis with differing phase. Kitagawa [41, 42] reports Raman lines at 122 and 167 cm^{-1} obtained by Schaufele for room temperature polyethylene but only comments on the proximity of the lower line to his calculated $\Gamma_3(B_{3g})$ mode frequency. Wu and Nicol [43] have assigned bands at 131.5 and 137.5 cm^{-1} in isotropic samples of $C_{23}H_{48}$ and $C_{44}H_{90}$ at 77°K to $\Gamma_3(B_{3g})$ and $\Gamma_1(A_g)$ modes respectively on the basis of the pressure dependence of these lines. Recently Harley, Hayes and Twisleton [44] have made Laser Raman measurements on polyethylene samples of single crystal texture prepared by the present author and of sufficient anisotropy to allow determination of band polarisations. Two prominent features were observed at 108.0 and 136.5 cm^{-1} in the 77°K data and their dichroism confirmed assignment to modes of B_{3g} and A_g symmetry respectively. Although the higher band is in agreement with the data of Wu and Nicol, the assignment of the B_{3g} mode by these authors is brought into question by the later work.

[5] Elastic moduli

In the long wavelength limit phonon propagation corresponds to elastic deformation of a crystal as discussed in 2.7. Dynamical matrix elements are then related to the crystalline elastic constants which constitute the elastic moduli and determination of the latter can provide useful information about the force field. In polyethylene the relationship between crystalline and bulk elastic moduli is complicated by the presence of amorphous regions. Ito, Sakurada and Nakumae [45] have reported elastic moduli transverse to the chain axis, derived from changes in the X-ray diffraction pattern of polyethylene induced by the application of bulk stress perpendicular to the draw direction of an uniaxially oriented specimen. Crystalline moduli for compression in the a and b directions

of 3.2 and 3.9 x 10^{10} dyne cm^{-2} are quoted, resting on the assumption of homogeneous stress throughout the composite material. Buckley [46] has derived an 'average' elastic modulus in the ab plane of 8.0 x 10^{10} dyne cm^{-2} with the same assumption. Here the lamellar texture of the uniaxially oriented material was thoroughly investigated and this morphological evidence was used to justify a two phase 'sandwich' model for the composite material. This model was employed in the interpretation of viscoelastic phenomena and particularly in the extraction of tensile elastic moduli from such data (see 10.4.1). It appears that Buckley's interchain modulus has a stronger empirical basis than the earlier values of Ito et al. which are derived from a macroscopically applied stress and microscopically determined strains without considering the role of the amorphous regions [45, 46]. As yet the unavailability of fully oriented polyethylene has restricted the scope of elastic moduli measurements perpendicular to the chains and only a qualitative test of the dynamical models is possible using the present experimental data.

5.2.3 Model force fields for polyethylene

Several force fields have been constructed independently for polyethylene. Most incorporate the intrachain force field described in 5.2.1 with slight modifications, but in their approach to the interchain force field they group into two categories. In the first approach nonbonded interactions between neighbouring chains are quantified using some form of analytical potential derived empirically. Alternatively a fit to some of the experimental data just described is achieved using a model with several independent parameters all related to the nonbonded interactions between hydrogen atoms on neighbouring molecules.

[1] Analytical potential models

Enomoto and Asahina [47] used a modified Urey-Bradley force field in the first calculation of external vibrational modes in polyethylene [48].

Intermolecular force constants between methylene groups taken as one unit were estimated from the Lennard-Jones potential function of methane [49]. Poor agreement with the assigned zone centre modes was obtained. Later work by Kitagawa and Miyazawa again treated the methylene groups as single dynamical units [42, 50]. Intermethylene force constants were derived by fitting to low temperature specific heat data, but the intermolecular potential of methane again provided a guiding influence on the fitting procedure and the resulting constants closely resembled those of Enomoto and Asahina.

Odajima and Maeda [51] have calculated the elastic constants of polyethylene using various analytical pair potentials for nonbonded interactions between atoms on neighbouring chains. Two sets of H-H, C-H and C-C potentials were used. each of which reproduced the observed 77°K lattice parameters to 3% [52, 53]. Tensile elastic moduli of 5.9 and 9.1 $\times 10^{10}$ dyne cm^{-2} were derived for the a and b directions using the hydrocarbon potential parameters of Kitaigorodskii [53]. As the dynamical matrix was solved only in the long wavelength limit, Odajima and Maeda provide no information about the phonon dispersion curves other than the related elastic constants. More recently Williams [54-56] has refined the potential parameters for nonbonded interactions in hydrocarbons by the methods described in Chapter 1, obtaining much closer reproduction of the observed crystal structure of polyethylene. Full dynamical calculations based on these improved parameter sets are reported later in this thesis.

[2] Independent parameter models

The most established force fields are based on the assumption that the interchain potential can be expressed in terms of short range repulsions between nonbonded hydrogen atoms. Four H-H interactions are considered as in Fig. 5.3 and harmonic force constants are defined. A fit is then made to some of the parameters described in the last section.

Tasumi and Shimanouchi [26] fitted intermolecular force constants to

observed near infrared band splittings by a perturbation treatment described earlier, solving the dynamical matrix for chain phonons only. Interchain phonon dispersion curves have been calculated by Marsh and Martin using this force field [57]. Further refinements were made by Tasumi and Krimm who repeated these calculations, fitting also to the $\Gamma_6(B_{1u})$ mode assigned in the infrared spectrum [58]. These authors also provided a force field for the low temperature crystal structure.

Full phonon dispersion curves for all symmetry directions were recently calculated by Kitagawa and Miyazawa [60]. A four parameter interchain potential was used in conjunction with the intrachain force field of Schachtschneider and Snyder, adjusted by a change in the force constant for internal rotation. Intermolecular force constants were varied to fit the specific heat data below $10^{o}K$, the band splitting of methylene rocking and scissoring vibrations and finally the B_{1u} symmetry lattice mode. The resulting force field was used to calculate the elastic moduli, density of states and amplitude weighted frequency functions for comparison with incoherent neutron spectra [42, 59].

[3] Objectives for refining the force field

From this brief survey of existing models for the lattice dynamics of polyethylene an appreciation of the weak empirical basis of the available interchain force fields is obtained. This weakness is particularly striking in the second type of calculation in which four H-H force constants are independently fitted to the available experimental data. In this case the number of variable force constants greatly exceeds the available anisotropic parameters of the force field. The approach of Odajima and Maeda is more promising since some empirical foundation for the atom pair potential calculation is provided by its approximate reproduction of the observed crystal structure. By contrast the transferable potential parameters of Williams for hydrocarbons reproduce the structural and thermodynamic properties of polyethylene to a high degree of accuracy.

In Chapter 9 phonon dispersion curves for the interchain vibrations of polyethylene will be calculated using these parameters.

5.3 Neutron Scattering from polyethylene

The lattice dynamics of polyethylene has been widely studied by inelastic neutron scattering techniques over the last ten years [61, 62, 63]. The extensive literature on this subject reflects developments within polymer science as well as in the experimental techniques. In this section progress to date is reviewed historically and the state of the field clarified prior to presenting the author's own contribution.

5.3.1 Scattering from isotropic polyethylene

Danner, Safford, Boutin and Berger [64] measured the neutron time-of-flight spectra of an isotropic sample of crystalline polyethylene at 100^0K. Complementary down-scattering measurements were performed by Myers, Donovan and King on the same sample [65]. In both sets of data two strong singularities were observed at 200 and 550 cm^{-1}. Comparison with the normal mode calculation of Tasumi, Shimanouchi and Miyazawa [23] for an isolated, extended chain suggested assignment to ν_9 and ν_5 chain torsional and stretching deformation modes respectively. For such modes a prominent singularity is expected in the density of states and neutron spectrum at the maximum frequency of each branch (see Fig. 5.2). Additional spectral features below 190 cm^{-1} were attributed to lattice modes but some difficulty arose in the assignment of broad peaks between 200 and 500 cm^{-1}. As the extended chain calculations show that there is no mode which might give a singularity in this region, initial assignment to the libration of chain segments in the amorphous regions was made [64]. The observation of the same broad peaks in the spectra of single-crystal mats by Boutin, Prask and Trevino definitely discounted this theory as Safford and Naumann accept in their review [61, 66]. Assignment to multiphonon transitions was deterred by early calculations which underestimated the intensity of such contributions [67].

Safford, Naumann and Simon [68] reported higher resolution time-of-flight studies of isotropic polyethylene at temperatures between 200 and 350°K. As many as eight weak peaks were noted in the region 200-500 cm^{-1}. An assignment of five singularities below 190 cm^{-1} to the zone centre lattice frequencies was inferred on the basis of a comparison with the calculated values of Tasumi and Shimanouchi [26]. Deficiencies of such an assignment will be discussed later. The overall inconsistency of the room temperature data from various sources [64, 65, 68] reflects to a large extent the difficulties encountered in the location of singularities in neutron spectra which are broadened by the effects of anharmonicity and multiphonon transitions. Both these effects are suppressed at low temperatures.

5.3.2 Scattering from oriented specimens

Myers, Summerfield and King [69] reported the first experiments on oriented polyethylene using triple axis spectrometry. Experiments with the momentum transfer vector parallel (||) and perpendicular ($\perp$) to the chain axis were performed at 100°K on a hot drawn Marlex filament with a c-mosaic of 4° FWHM. The skeletal stretching mode at 525 cm^{-1} had || and the 190 cm^{-1} torsional mode a mixed ($\perp$,||) polarization. Calculations of the hydrogen amplitude weighted frequency distribution by Kitagawa and Miyazawa facilitated a direct comparison between theoretical and experimental neutron spectra [70]. The anisotropy observed gave qualitative agreement with the calculated frequency distribution (Fig. 5.3) confirming the earlier assignment of ν_5 and ν_9 modes.

Trevino [71] performed similar experiments at room temperature using the time-of-flight method and observed a similar dichroism for the principal features. A reassignment of the torsional peak to a higher frequency singularity was proposed with ensuing controversy [42]. Subsequent calculations by Kitagawa finally dismissed this postulate and confirmed the

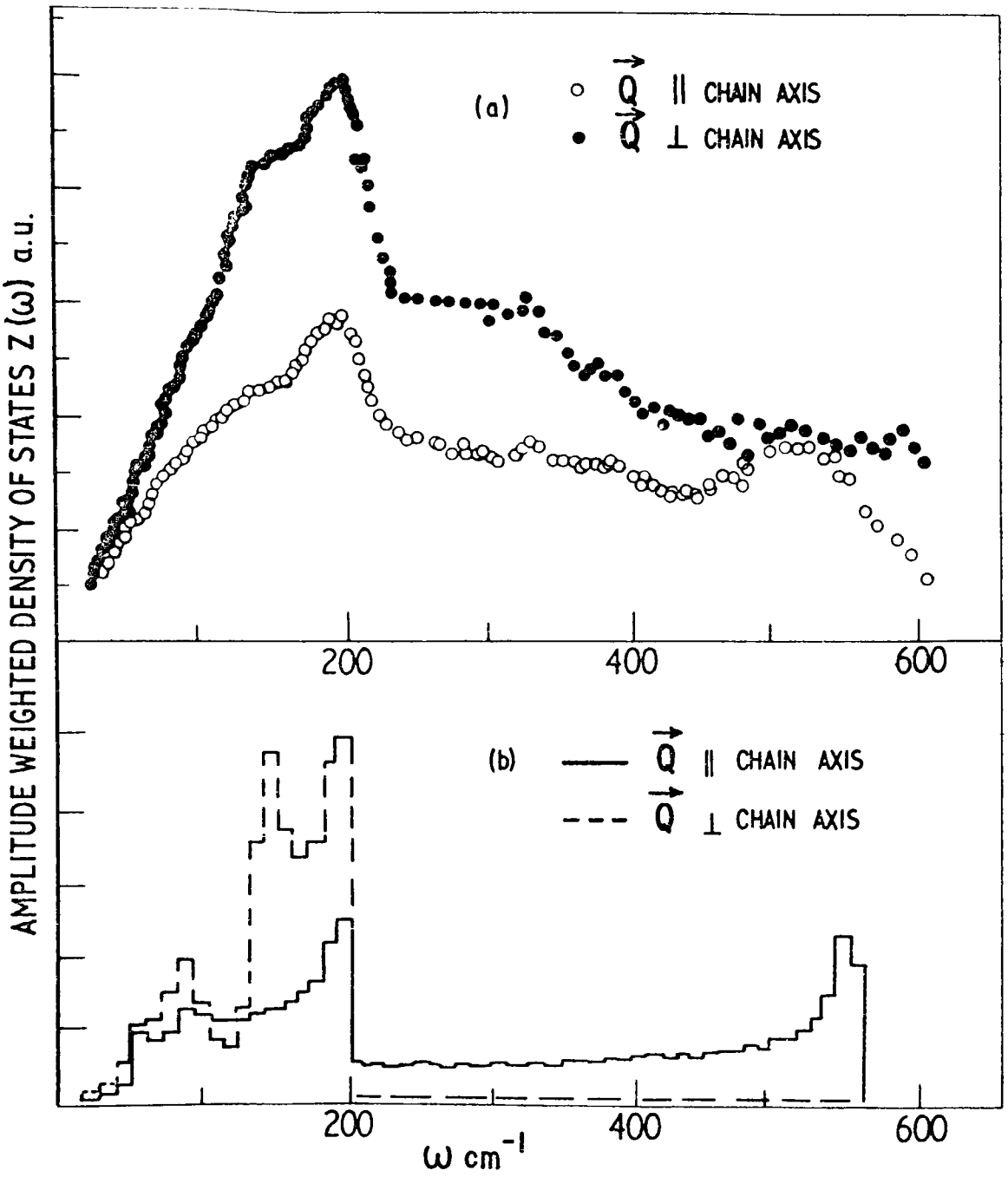

Fig. 5·3 Density of states functions, Z(ω), weighted by hydrogen amplitudes polarized along and perpendicular to the chain axis of uniaxially oriented polyethylene: (a) derived from triple axis dichroism studies [69]; (b) calculated from the force field of Kitagawa and Miyazawa [70].

importance of multiphonon contributions in the frequency region 200-500 cm^{-1}.

Most recent measurements by Myers and Randolph have employed a combination of down-scattering techniques with a phased chopper neutron velocity selector [72]. Longitudinal and transverse polarized spectra were reported at 300, 77 and 4°K. The principal singularities were at 45(||), 97(⊥), 125(⊥), 199(⊥,||) and 524(||) cm^{-1} for the 77°K data. Calculations by Lynch and Summerfield in which the phonon wavevector was restricted to be along the chain axis were used to interpret the data [73]. The lowest three peaks were assigned to zone centre Γ_2, Γ_8 and Γ_3 singularities of A_u, B_{2u} and B_{3g} symmetry respectively. Weaker features at 75 and 186 cm^{-1} were tentatively assigned to the remaining Γ_6 and Γ_1 singularities of B_{1u} and A_g symmetry (see 9.4.4.1). The amplitude weighted density of states function derived for the 4°K data in the one-phonon approximation was used to calculate the low temperature specific heat. Comparison with Wünderlich's experimental data afforded good agreement below 50°K [28]. The divergence of calculated and experimental specific heat above 50°K was attributed to the extensive contribution of multi-phonon scattering processes for neutron energy transfers in excess of 100 cm^{-1}. This conclusion is corroborated by Kitagawa who calculates the two-phonon contribution to the neutron spectrum as a slowly rising function of frequency which peaks at 240, 340 and 380 cm^{-1} in N.P.E. at 77°K [42].

5.3.3 Scattering from deuteropolyethylene

Triple axis down-scattering studies of isotropic and c-oriented deuteropolyethylene at 78°K have been reported by Lynch, Summerfield, Feldkamp and King [73]. Amplitude weighted frequency functions were obtained in the incoherent one-phonon approximation and contained two well defined peaks at 105 and 165 cm^{-1}, both of which appeared to have mainly perpendicular polarization. The higher energy peak corresponded

exactly with the ν_9 singularity calculated by both Tasumi and Krimm and these authors for deuteropolyethylene [58, 73]. The peak at 105 cm^{-1} was assigned to the zone centre $\Gamma_3(B_{3g})$ singularity on the basis of the calculations. A poorly defined shoulder at 70 cm^{-1} was tentatively assigned to translatory lattice vibrations. No lower energy features were resolved but a broad peak at 270 cm^{-1} was assigned to a two-phonon scattering process. The apparent absence of coherent inelastic singularities in the low frequency spectra is notable.

A major breakthrough in the application of neutron scattering techniques to polymer dynamics has been reported by Feldkamp, Venkataraman and King who have applied triple axis techniques to a c-oriented sample of deuteropolyethylene [74]. Exploiting fully the limited anisotropy available, they made direct observations of the predominantly longitudinal, acoustic skeletal vibrations throughout the zone. Constant energy and momentum transfer scans from the strong [002] reflexion along [00q_c] were performed on a sample with c-mosaic 9° FWHM and isotropic a and b poles. Their results are shown in Fig. 5.4 superimposed upon the calculated ν_5 and ν_9 branches of Lynch [73]. Calculated dynamical structure factors anticipate the cross over from ν_5 to ν_9 observed in the data at high q_c. The maximum observed frequency is 452 cm^{-1} which is 7% lower than the calculated value [58, 73].

This experimental work provides the first anisotropic information about the forces in polymers from neutron scattering and a major purpose of this thesis is to provide complementary data for interchain phonon excitations.

5.3.4 Summary and objectives

The singularities in the incoherent neutron spectra between 150 and 600 cm^{-1} are now well understood. At lower frequencies the situation is not so clear. The poor definition of much of the room temperature data

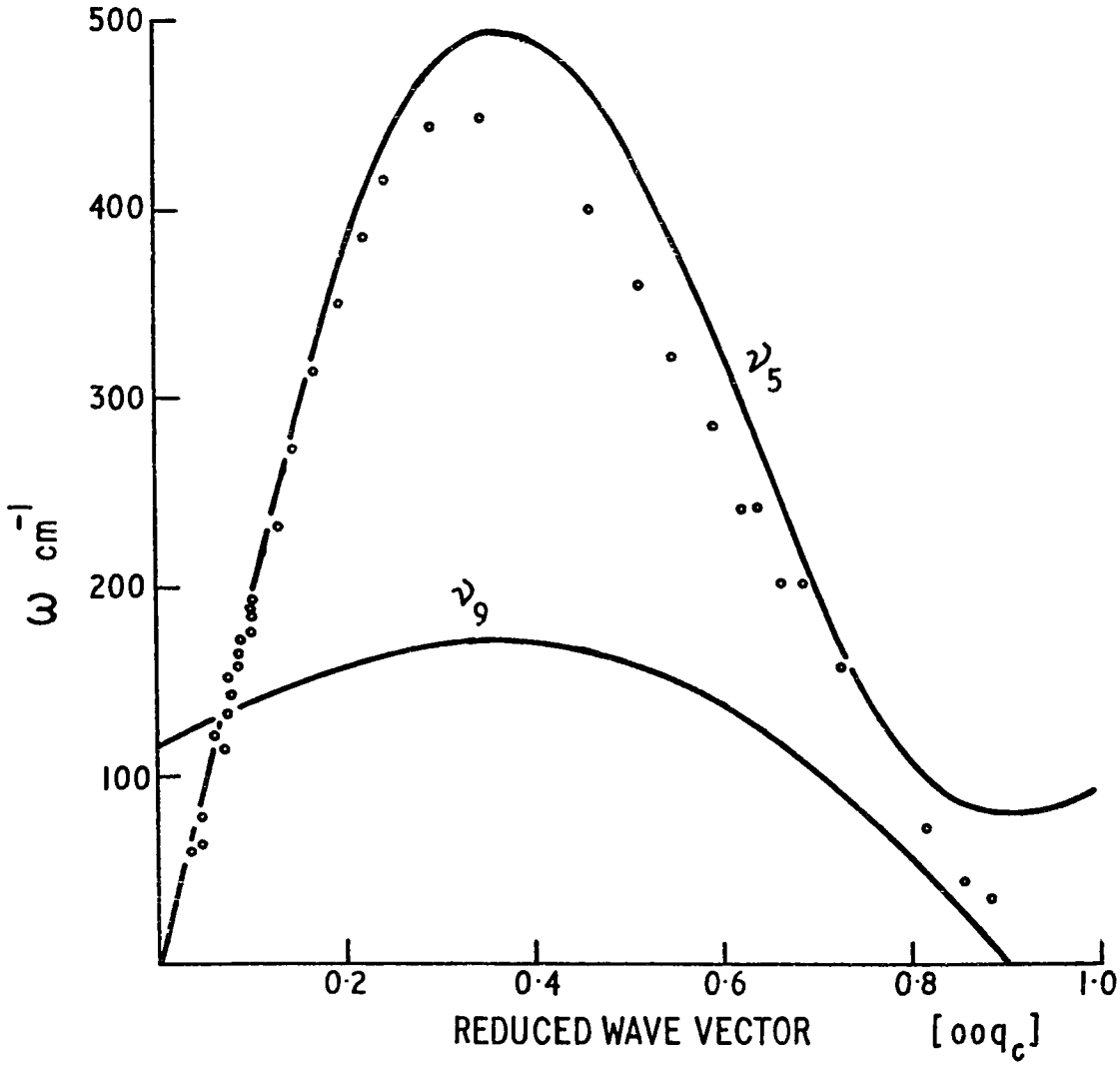

Fig. 5·4 Experimental data for LA phonons polarized along the chain axis of D.P.E. from Feldkamp et al. compared with the model predictions of Lynch for ν_5 and ν_9 normal modes [73,74].

is seemingly a consequence of the anharmonic broadening and multiphonon transitions facilitated at higher temperature. The inconsistency of data supplied for this region by various workers reflects the difficulties involved in locating such broad singularities. More progress has been made at lower temperatures where singularities sharpen up. However the assignments of Myers and Randolph are mostly tentative and based on a set of calculated zone centre frequencies.

In fact the critical points in the amplitude weighted density of states come from many other parts of the Brillouin Zone besides the zone centre frequencies. In principle a complete understanding of the low frequency density of states will only arise when anisotropic information about the dispersion curves for interchain vibrations becomes available, from which all the singularities will be calculable. Such information has been unavailable to date because of the experimental difficulties encountered in the preparation of fully oriented polyethylene.

From these considerations and in recognition of the potential of coherent scattering methods, two practical courses were adopted in this work, both of which promised an extension of the information available to date about the forces between the chains in polyethylene:

[1] Complementary neutron time-of-flight experiments on deuteropolyethylene to the down-scattering work of Lynch et al. with full exploitation of recent improvements in both the flux and resolution of time-of-flight spectrometers.

[2] Preparation of deuteropolyethylene samples of single crystal texture and measurement of phonons propagating in the basal plane of the polymer by triple axis techniques.

References

[1] C.W. Bunn, Trans. Far. Soc., 35, 482 1939.

[2] A. Keller, Phil. Mag., 2, 1171 1957.

[3] P.H. Till, J. Poly. Sci., 24, 301 1957.

[4] E.W. Fischer, Z. Naturforsch., 12A, 753 1957.

[5] A. Keller, Physics Today, 23, 5, 42 1970.

[6] E.W. Fischer and G.F. Schmidt, Angew. Chem., 74, 551 1962.

[7] P.H. Geil, 'Polymer single crystals', Wiley 1963.

[8] H.D. Keith, F.J. Padden and R.G. Vadimsky, J. Poly. Sci. A2, 4, 267 1966.

[9] R.G. Vadimsky, H.D. Keith and F.J. Padden, J. Poly. Sci. A2, 7, 1367 1969.

[10] T. Okada and L. Mandelkorn, J. Poly. Sci. A2, 5, 239 1967.

[11] E.W. Fischer, H. Goddar and G.F. Schmidt, J. Poly. Sci. B, 5, 619 1967.

[12] E.W. Fischer, F. Kloos and G. Lieser, J. Poly. Sci. B, 7, 845 1969.

[13] E.W. Fischer and F. Kloos, J. Poly. Sci. B, 8, 685 1970.

[14] B. Wunderlich and T. Arakawa, J. Poly. Sci. A, 2, 3697 1964.

[15] P.H. Geil, F.R. Anderson, B. Wunderlich and T. Arakawa, ibid., 3707 1964.

[16] D.V. Rees and D.C. Bassett, J. Poly. Sci. A2, 9, 385 1971.

[17] Idem, Nature, 219, 368 1968.

[18] Idem, J. Poly. Sci. B, 7, 273 1969.

[19] T. Seto and T. Hara, Rept. Prog. Poly. Phys. Jap., 9, 207 1966.

[20] W. Glenz, A. Peterlin and W. Wilke, J. Poly. Sci. A2, 9, 1243 1971.

[21] R.G. Snyder, J. Mol. Spectry., 7, 116 1961.

[22] J.H. Schachtschneider and R.G. Snyder, Spectrochim. Acta, 19, 117 1963.

[23] M. Tasumi, T. Shimanouchi and T. Miyazawa, J. Mol. Spectry., 9, 261 1962.

[24] idem, ibid., 11, 422 1963.

[25] L. Piseri and G. Zerbi, J. Chem. Phys., 48, 3561 1968.

[26] M. Tasumi and T. Shimanouchi, J. Chem. Phys., 43, 1245 1965.

[27] R.F. Schaufele and T. Shimanouchi, J. Chem. Phys., 47, 3605 1967.

[28] B. Wunderlich, J. Chem. Phys., 37, 1221 1962.

[29] B. Wunderlich, J. Poly. Sci. C1, 41 1963.

[30] V.V. Tarasov, J.A.C.S., 80, 5052 1958.

[31] F.J. Boerio and J.L. Koenig, J. Chem. Phys., 52, 3425 1970.

[32] R.G. Brown, J. Chem. Phys., 38, 221 1963.

[33] J.R. Nielsen and A.H. Woollett, J. Chem. Phys., 26, 1391 1957.

[34] S. Krimm, Adv. Poly. Sci., 1, 103 1960.

[35] J.E. Bertie and G.E. Whalley, J. Chem. Phys., 41, 575 1964.

[36] R.V. McKnight and K.D. Möller, J. Opt. Soc. Am., 54, 132 1964.

[37] S. Krimm and M.I. Bank, J. Chem. Phys., 42, 4059 1965.

[38] S. Krimm and M.I. Bank, J. Appl. Phys., 39, 4951 1968.

[39] G.D. Dean and D.H. Martin, J. Chem. Phys. Lett., 1, 415 1967.

[40] G.D. Dean, Ph.D. thesis, University of London 1969.

[41] T. Kitagawa and T. Miyazawa, Rep. Prog. Poly. Phys. Jap., 11, 219 1968.

[42] T. Kitagawa, D.Sc. thesis, Osaka University 1968.

[43] C.K. Wu, Dept. of Chemistry, University of California, private communication.

[44] R.T. Harley, W. Hayes and J.F. Twisleton, J. Phys. C, 6, 167 1973.

[45] I. Sakurada, T. Ito and K. Nakamae, J. Poly. Sci. C, 15, 75 1966.

[46] C.P. Buckley, D.Phil. thesis, Oxford University 1972.

[47] S. Enomoto and M. Asahina, J. Poly. Sci. A2, 3523 1964.

[48] H.C. Urey and C.A. Bradley, Phys. Rev., 38, 1969 1930.

[49] T.L. Hill, J. Chem. Phys., 16, 399 1948.

[50] T. Kitagawa and T. Miyazawa, Polymer Letters, 2, 395 1964.

[51] A. Odajima and T. Maeda, J. Poly. Sci. C, 15, 55 1966.

[52] S. Kimel, A. Ron and D.F. Hornig, J. Chem. Phys., 40, 3351 1964.

[53] A.I. Kitaigorodskii and K.V. Mirskaya, Kristallografiya, 9, 174 1964.

[54] D.E. Williams, J. Chem. Phys., 43, 4424 1965.

[55] idem, ibid., 45, 3770 1966.

[56] idem, ibid., 47, 4680 1967.

[57] D.I. March and D.H. Martin, J. Phys. C, 5, 2309 1972.

[58] M. Tasumi and S. Krimm, J. Chem. Phys., 46, 755 1967.

[59] T. Kitagawa and T. Miyazawa, Bull. Chem. Soc. Jap., 43, 372 1970.

[60] idem, Jap. Polym. J., 1, 471 1970.

[61] G.J. Safford and A.W. Naumann, Adv. Poly. Sci., 5, 1 1967.

[62] S. Trevino and H. Boutin, J. Macromol. Sci. (Chem.) A1 (4), 723 1967.

[63] J.W. White in 'Polymer Science', ed. A.D. Jenkins, North-Holland 1972.

[64] H.R. Danner, G.J. Safford, H. Boutin and M. Berger, J. Chem. Phys., 40, 1417 1964.

[65] W. Myers, J.L. Donovan and J.S. King, J. Chem. Phys., 42, 4299 1966.

[66] H. Boutin, H. Prask, S.F. Trevino and H. Danner, 'Neutron inelastic scattering', IAEA, Bombay, 2, 407 1965.

[67] G.C. Summerfield and J.D. Erickson, Bull. Am. Phys. Soc., 9, 623 1964.

[68] G.J. Safford, A.W. Naumann and F.T. Simon, J. Chem. Phys., 45, 3787 1966.

[69] W.R. Myers, G.C. Summerfield and J.S. King, J. Chem. Phys., 44, 184 1965.

[70] T. Kitagawa and T. Miyazawa, J. Chem. Phys., 47, 337 1967.

[71] S.F. Trevino, J. Chem. Phys., 45, 757 1966.

[72] W.R. Myers and P.D. Randolph, J. Chem. Phys., 49, 1043 1968.

[73] J.E. Lynch Jr., G.C. Summerfield, L.A. Feldkamp and J.S. King, J. Chem. Phys., 48, 912 1968.

[74] L.A. Feldkamp, G. Venkataraman and J.S. King, 'Neutron inelastic scattering', IAEA, Copenhagen, 2, 159 1968.

Chapter 6

NEUTRON SCATTERING STUDIES OF ISOTROPIC NORMAL AND DEUTEROPOLYETHYLENE

6.1 Introduction

Time-of-flight experiments on isotropic normal and deuteropolyethylene using cold neutrons were expected to provide information about the low frequency density of states inaccessible to triple axis spectrometry on account of the inferior resolution in this region [1]. The observation of sharp coherent inelastic excitations in the time-of-flight spectra of polycrystalline deuteropolyethylene provided an exciting stimulus. Very little anisotropic information is available about interchain forces in polymers, primarily as a consequence of the dearth of fully oriented specimens, and so the provision of such information by a polycrystalline sample excited our interest. Consequently, after a discussion of the characteristics of the polymers employed, this chapter deals first with the interpretation of these coherent inelastic excitations and then moves on to consider the assignment of singularities in the incoherent neutron spectrum on the basis of well resolved data for both normal and deuteropolyethylene.

6.2 Sample characteristics

[a] Deuteropolyethylene

Deuteropolyethylene (D.P.E.) was obtained from Merck, Sharp and Dohme (Canada) both as a powder and in the form of a moulded sheet. The polymer is prepared by Ziegler catalysis using ethylene-D_4 starting material [2]. Consequently the molecular weight is rather high, values of 1.2×10^5 and 4.8×10^5 for number and weight averages have been determined by the P.S.C.C., Shropshire indicating a molecular length of about 10^4 Å. The minimum deuterium content is quoted as 98%, a figure confirmed by near infrared spectra which show the great predominance of the deuterium

stretching and bending modes over those for hydrogen. The absence of methyl-D_3 and carbonyl features in these spectra is a further testimony to the absence of branching and degradation in the source material. Microcalorimetric studies revealed a broad melting point around 130°C typical of normal polyethylene (N.P.E.) of this molecular weight. Density measurements were obtained by weighing the moulded specimens in pure ethanol and air employing Archimedes' principle. A crystalline density ρ_c of 1.006 gm cm^{-3} is calculable from the crystal structure [3] and an amorphous density ρ_a of 0.8534 gm cm^{-3} has been estimated for N.P.E. by extrapolation from the melt [4]. Assuming a simple two phase model, the mass fraction crystallinity χ_M may be estimated from the density ρ of any sample using the formula

$$\chi_M = \frac{100(\rho-\rho_a)}{\rho_c-\rho_a} \cdot \frac{\rho_c}{\rho} \qquad (6.1)$$

Values of 1.149 and 0.975 gm cm^{-3} for ρ_c and ρ_a led to a crystallinity of 71% for the moulded slab of D.P.E. density 1.093 gm cm^{-3} at 25°C. The major approximation in this derivation is the neglect of sample voids which affect the bulk density.

[b] Normal polyethylene

Initial experiments were performed on the commercial linear polymer Rigidex 2 as this was immediately available. Moulded sheets of the required thickness were prepared by compression of the granular product under heated patens. The weight average molecular weight was about 1.7 x 10^5 and the polydispersity M_W/M_N between 12 and 20. Crystallinity was found to be 70% which is high for a commercial product. No details about antioxidants and other additives were available but the proportion of such impurities was expected to be small.

Single-crystal mats of linear polyethylene crystallized from toluene solution were provided by Dr. C.P. Buckley, Oxford Engineering Department.

These were ground up for use and were 80% crystalline.

Very highly crystalline polyethylene was obtained from Dr. R.J. Young of Cambridge Metallurgy Department in the chain extended form. The sample was made by annealing drawn polyethylene at 228°C and 4.1 kbar pressure for 15 mins. The density of 0.990 gm ml^{-1} led to an estimated crystallinity of 91%. This material was remarkable for its inorganic appearance and a tendency to crumble on handling, clear indications of a highly crystalline composition.

6.3 Neutron diffraction studies of deuteropolyethylene

Neutron diffraction data were obtained from predominantly coherent scattering D.P.E. using the Badger 2 powder spectrometer at A.E.R.E. Harwell. An incident neutron wavelength of 1.130 Å from a Pb [110] monochromator was employed for experiments on the isotropic powder and slab at 77 and 298°K. The low temperature data are shown in Fig. 6.1. As the cross section of deuterium is only 71% coherent there is a sizeable background from incoherent scattering. The anisotropy of the polyethylene unit cell leads to a predominance of [hk0] reflections at low Q, in particular the [110] and [200] reflexions. Elastic structure factors were calculated using the 77°K lattice parameters of Swan [5], the atomic coordinates of Teare [6] and one elastic Debye Waller factor of 0.020 $Å^2$ estimated for an isotropic sample from the data of Myers and Randolph [7]. The elastic cross section for a cylindrical sample is related to the structure factor F_{hkl} as follows

$$\left(\frac{d\sigma}{d\phi}\right)_{hkl} = \frac{A\left|F_{hkl}\right|^2 \exp(-\alpha_{hkl}Q^2)}{\sin\phi \ \sin 2\phi} \qquad (6.2)$$

where ϕ is the scattering angle, α_{hkl} the Debye Waller factor and A an arbitrary constant [8]. The agreement with experiment is good as Fig. 6.1 illustrates, confirming within experimental error the parameters of Swan and Teare

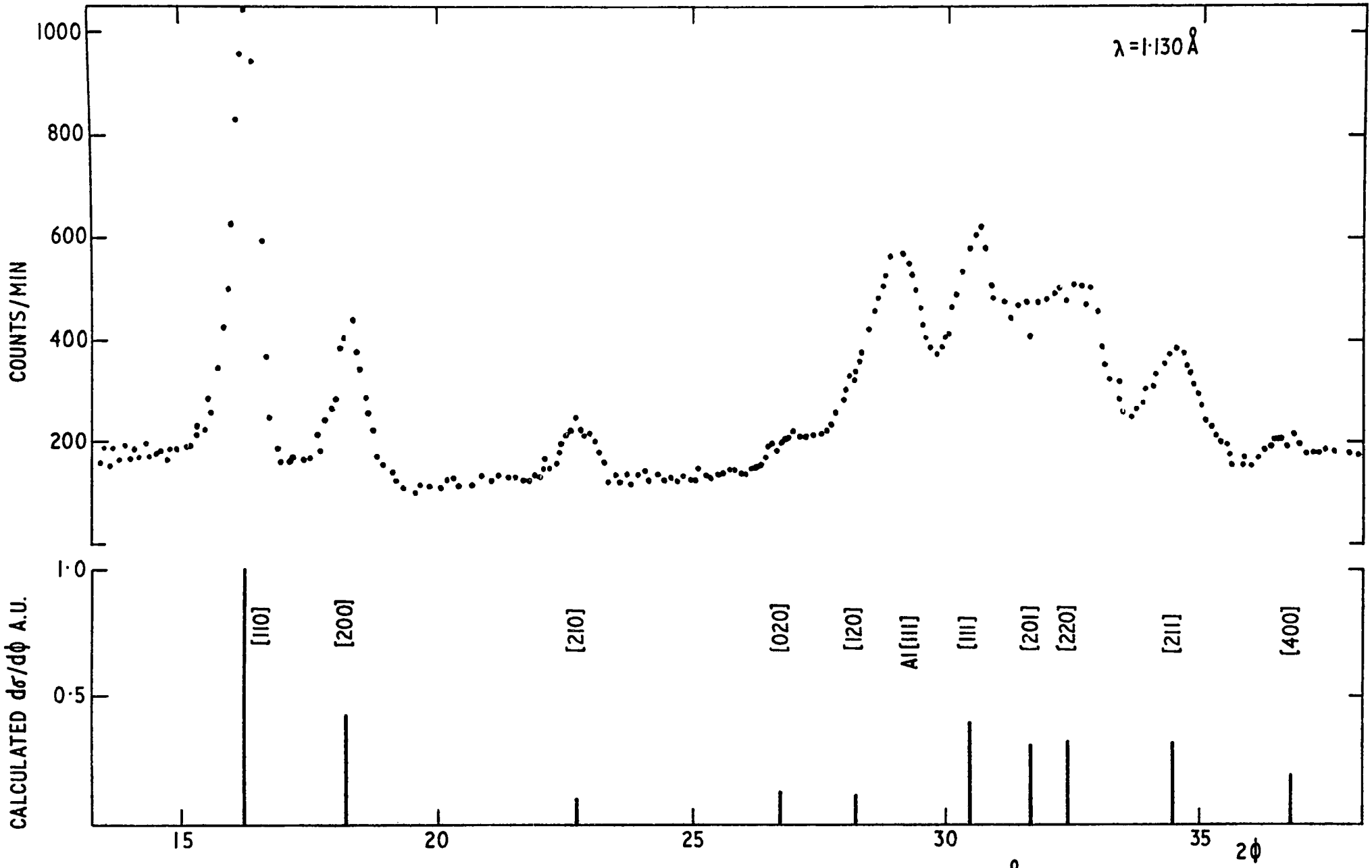

Fig. 6·1 Neutron diffraction data and calculated elastic structure factors for polycrystalline D.P.E. at 77°K

$$a = 7.155 \qquad b = 4.899 \qquad c = 2.547 \qquad \theta = 48^{o}$$

where the chain setting angle is again defined with respect to the bc plane as in Fig. 5.1. The room temperature data were in general agreement with the early X-ray diffraction work of Bunn [3] and yielded the same lattice parameters

$$a = 7.40 \qquad b = 4.93 \qquad c = 2.54$$

However a notable feature of the higher temperature data was the suppression in intensity of the [200] reflexion. At $77^{o}K$ the experimental intensity ratio [110]:[200] is 2.85 which compares favourably with the calculated value of 2.50. The proximity in $\vec{Q}$ of these two reflexions suggests that such a comparison should be independent of any arbitrary influence in the experimental intensity as a function of scattering angle. At $298^{o}K$ the ratio changes to 3.70 and since the other reflexions are relatively unchanged, the only reasonable explanation is a large increase in Debye Waller factor for molecular motion in the a-direction at the higher temperature. This is quite consistent with the thermal expansion data which shows a marked anisotropy perpendicular to the chains, the a-coefficient being 4.4 times that for the b-direction. On this basis the molecular vibrational amplitudes are expected to be greater in the a-polarization and this would be reflected by an increased α_{hoo} Debye Waller factor. Such an anisotropy in the Debye Waller factors coupled with the poor $\vec{Q}$ resolution and high incoherent background prevented a full analysis of the room temperature data to establish the chain setting angle. Higher resolution neutron diffraction studies of fully oriented D.P.E. are necessary and such work is planned.

6.4 Deuteropolyethylene time-of-flight spectroscopy

Time-of-flight spectra of D.P.E. in the powder and moulded form at 77, 117 and $298^{o}K$ were measured using the 4H5 and 6H cold neutron spectro-

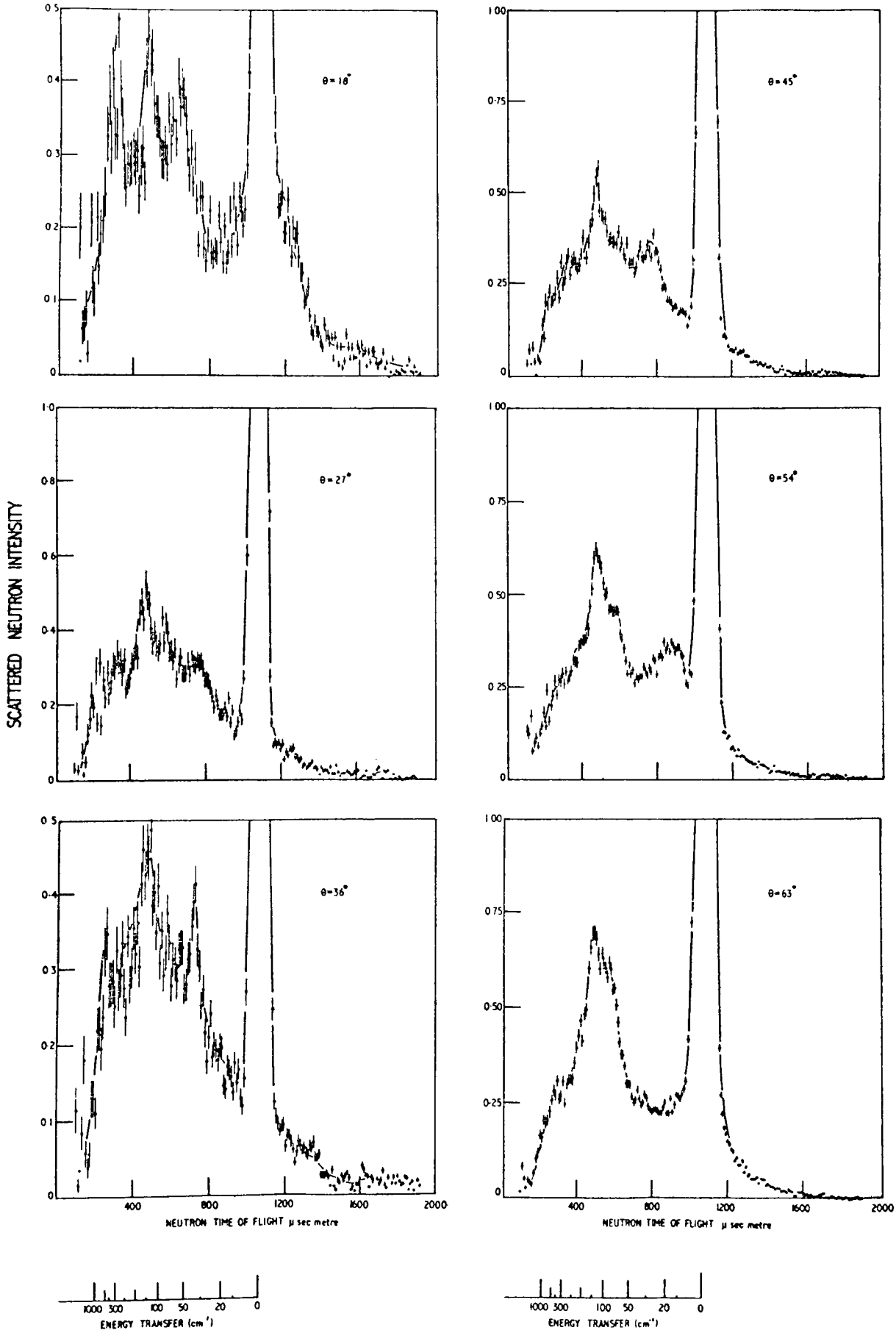

Fig. 6·2 Time-of-flight spectra of polycrystalline D.P.E. at six scattering angles to the incident 4·22 Å neutron beam at 298°K.

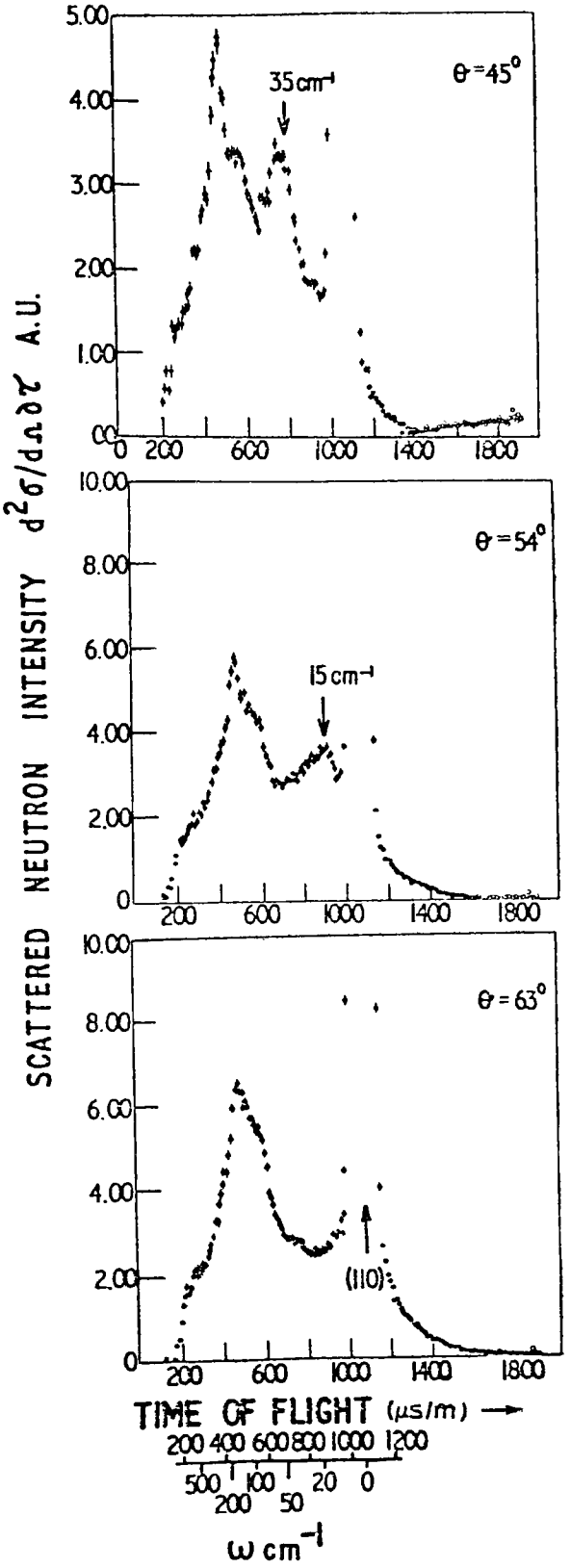

Fig. 6·3 Time-of-flight spectra of moulded D.P.E. at 45°, 54° and 63° to the incident 4·22 Å neutron beam at 298°K

meters at A.E.R.E. Harwell. The samples were contained in aluminium foil and mounted at an angle of 45° to the incoming beam. Sufficient D.P.E. to scatter 10% of the incident beam was employed. Experiments were performed using neutron wavelengths of 4.22, 4.86, 5.12 and 5.90 Å. Powder data obtained using 4.22 Å neutrons on the 6H spectrometer are shown in Fig. 6.2 for six scattering angles. Similar data from moulded D.P.E. are shown in Fig. 6.3. The intensity is proportional to the differential cross section (4.12) and the energy scale is in the very non linear time-of-flight units of μsec/metre.

Spectra are seen to contain an intense feature at the incident time-of-flight corresponding to elastically scattered neutrons together with a series of inelastic excitations corresponding to neutron energy gain from the sample. Most remarkable among these features is the sharp peak which traverses the inelastic spectrum with increasing scattering angle and finally disappears into the elastic peak at 63°. Its disappearance corresponds to a sharp accentuation of the elastic peak from coherent Bragg scattering off the [110] planes. By way of contrast the other singularities do not shift with scattering angle. Thus two sorts of information are provided in these spectra and it is appropriate that they be discussed separately.

[a] Coherent scattering

The inelastic feature just referred to shifted with both scattering angle and incident wavelength so that the peak energy was a clear function of the momentum transfer $\vec{Q}$ to the sample. Data collection at constant scattering angle θ infers a rather complicated relationship between the momentum and energy transfer, as set forth in (4.8). For polycrystals the direction of $\vec{Q}$ is not defined in the sample framework and it is customary to refer to $|\vec{Q}|$. The located singularities are then best presented on the instrumental $(|\vec{Q}|,\omega)$ track or 'dispersion curve' shown in Fig. 6.4 where their $|\vec{Q}|$ dependence is clearly illustrated for one wavelength. Such a

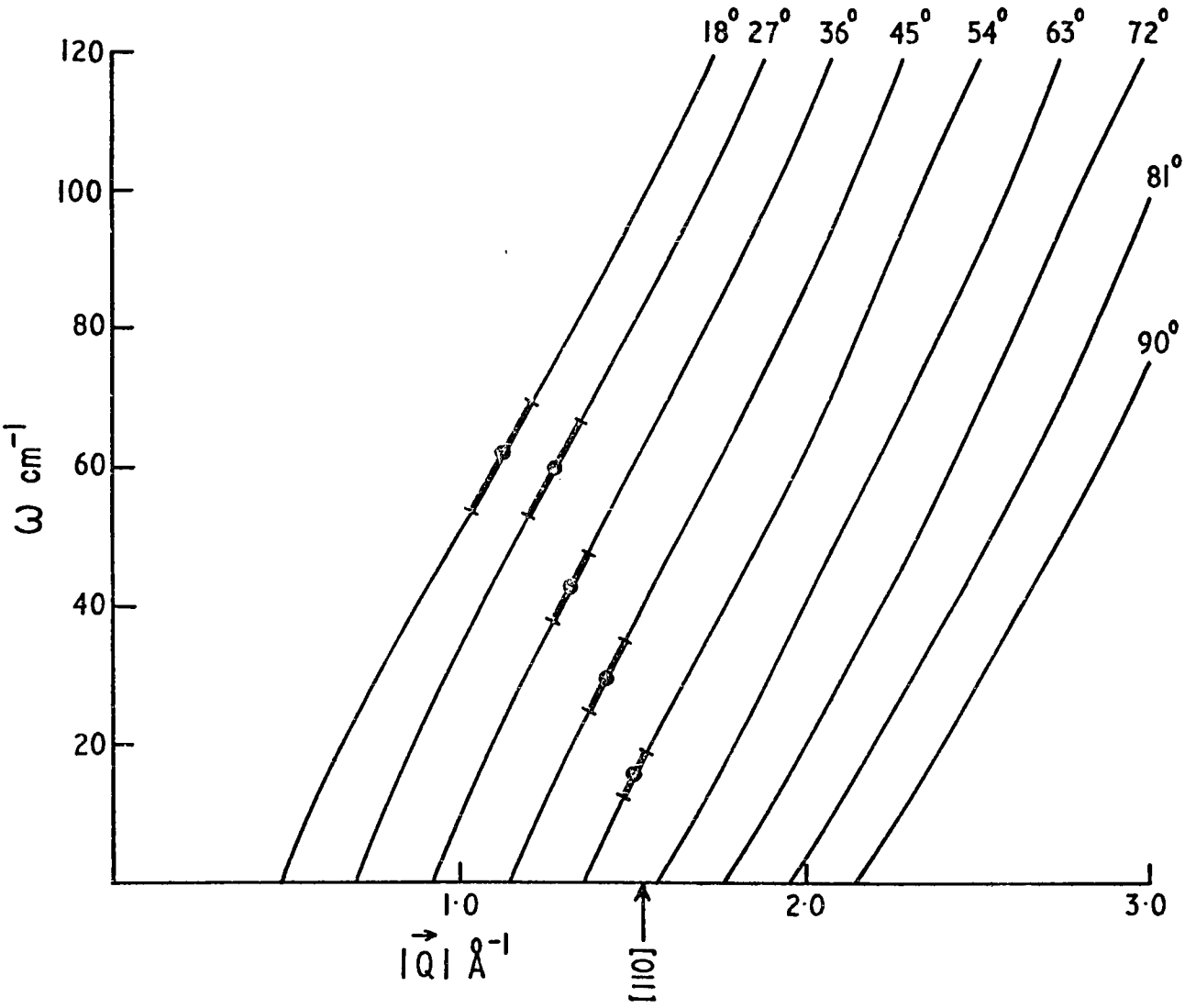

Fig. 6·4 Coherent inelastic singularities in the time-of-flight spectra of D.P.E. at 298°K assembled on the instrumental dispersion curves for 4·22 Å incident neutrons.

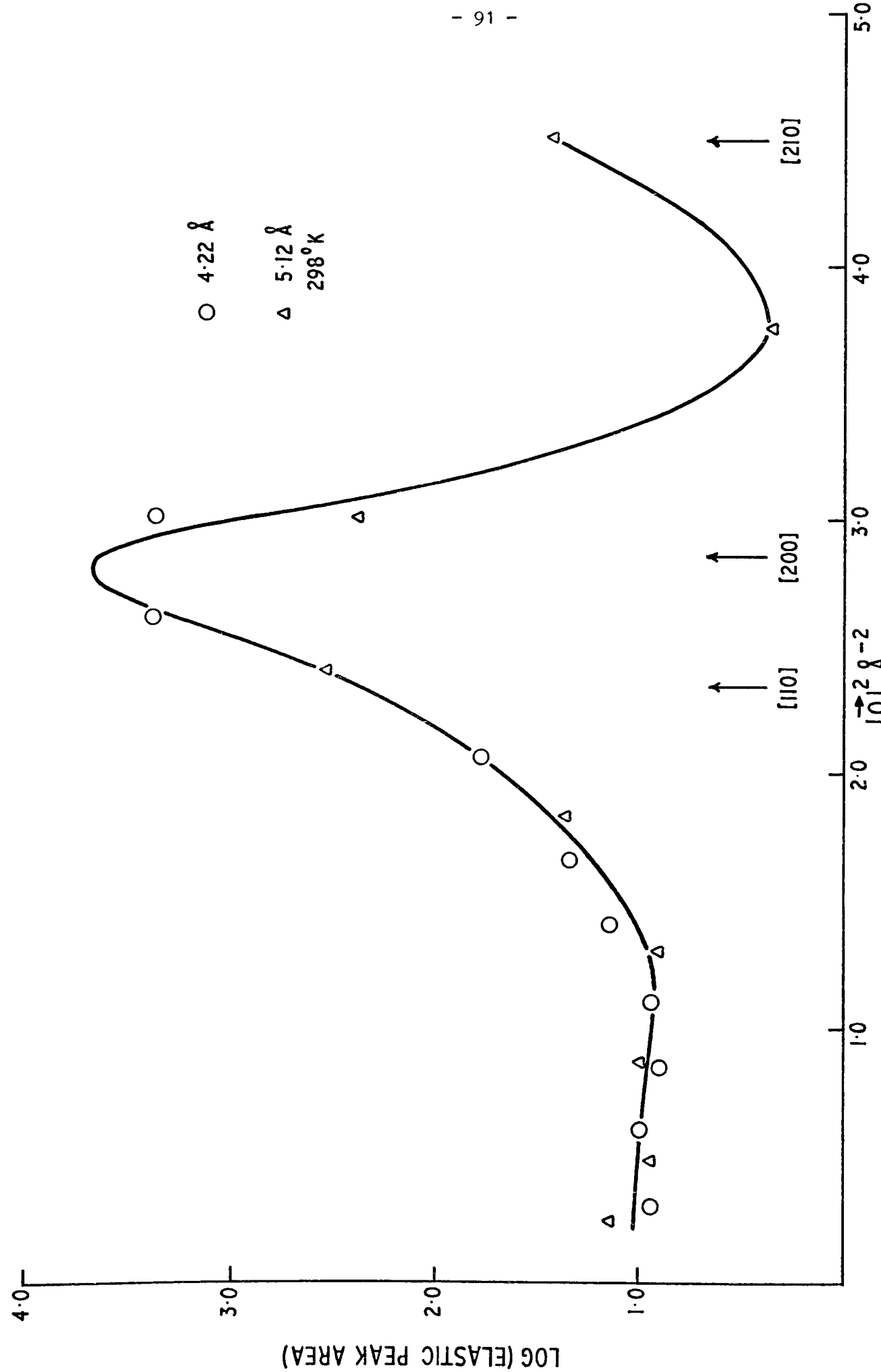

Fig. 6·5 Debye Waller plot for polycrystalline D.P.E.

phenomenon arises from the momentum conservation condition peculiar to coherent scattering (3.36) where the observed frequencies are a function of the instrumental dispersion curve, which must satisfy both energy and momentum transfer delta functions simultaneously. From Fig. 6.4 it is evident that these coherent inelastic features have a well defined acoustic dispersion relationship $\omega(|\vec{Q}|)$ which approaches zero as $|\vec{Q}|$ increases to $2\pi|\vec{\tau}|$ for [110] planes.

Parallel to this behaviour of the inelastic spectrum, the elastic peak shows a sudden upward jump in intensity as illustrated in the Debye Waller Plot of Fig. 6.5, where corrections for multiple scattering have not been made. The overall decrease in elastic peak intensity with increasing Q is typical of incoherent elastic scattering where the Q dependence is $\exp(-\alpha Q^2)$ and α is the isotropic Debye Waller Factor. The sharp increase above 1.5 $\mathring{A}^{-1}$ is caused by supplementary coherent elastic scattering from the [110] and [200] reflexions.

Data for the four wavelengths are assembled in Fig. 6.6. The error bars are projected onto the instrumental tracks and their fluctuation in size reflects the peak definition which is poorer at higher energy. An immediate conclusion from the data is that the information presented in Fig. 6.6 pertains to external i.e. interchain vibrations. This follows from the already existing measurements of intrachain [00ζ] phonons which show a much greater acoustic slope then can be obtained from Fig. 6.6. Moreover since the phonon groups are excited so near in $|\vec{Q}|$ to [110] it is reasonable to suppose that the dynamical structure factors are enhanced in the vicinity of such a strong Bragg peak. An average phonon wavevector $|\vec{q}|$ may be defined such that

$$\omega(|\vec{q}|) = \omega(2\pi|\vec{\tau}_{110}|-|\vec{Q}|)$$

and both $|\vec{q}|$ and $|\vec{Q}|$ are used as abscissa in Fig. 6.6. Cocking [9] makes a similar definition in his analysis of coherent inelastic excitations in

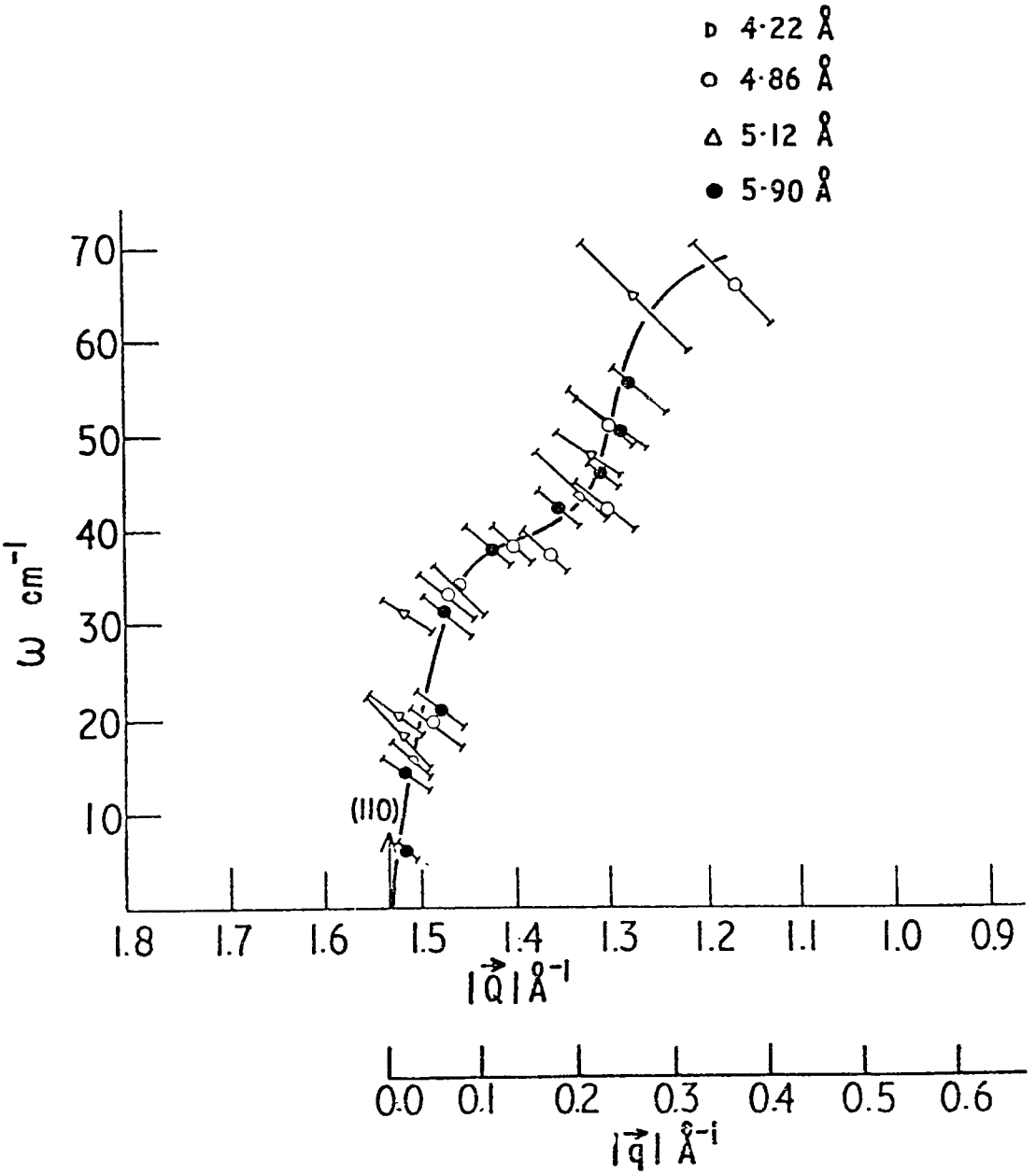

Fig. 6·6 Coherent inelastic singularities for isotropic D.P.E. at 298°K assembled as a function of $|\vec{Q}|$ and $|\vec{q}|$.

polycrystalline and liquid Sn at low $|\vec{Q}|$ and refers to the "average dispersion curve". In general the isotropically averaged dynamical structure factors derived for coherent phonon excitations in a polycrystal show no sharp peak in the frequency or time-of-flight distribution. The appearance of such a peak indicates the predominance of some strongly anisotropic contribution within the isotropically averaged inelastic cross section and this is confirmed in the next chapter by calculations of the dynamical structure factors. Further discussion along these lines is now postponed for reasons that will become shortly evident.

A prominent characteristic of the data on Fig. 6.6 is the inflexion in $\omega(|\vec{q}|)$ at about 40 cm^{-1}. Since 21% of the scattering from D.P.E. is incoherent, all the coherent singularities are observed in coincidence with the incoherent inelastic spectrum. Consequently some difficulty arises in the location of the coherent peaks because there is no way of exactly determining the incoherent background, which is strongly angle dependent. Scrutiny of the higher angles in Figs. 6.2 and 6.3 gives an indication of the purely incoherent singularities since the coherent inelastic contribution has ceased to be important. It became clear that the shoulder at 40 cm^{-1} observed in these high angle counters was responsible for the inflexion in $\omega(|\vec{q}|)$ i.e. the location of the coherent inelastic singularity is imperfect in this region as there is no satisfactory procedure for subtracting the important incoherent background.

The later assignment of this peak to the lowest frequency translatory lattice vibrations of c-polarization suggested a new experiment which promised a better analysis of these acoustic excitations. The interference from incoherent scattering at 40 cm^{-1} should disappear in experiments on c-oriented D.P.E. with the $\vec{Q}$ vector perpendicular to the chains, which are otherwise randomly oriented. Such experiments on an effectively two dimensional polycrystal should yield a similar coherent inelastic spectrum whilst removing the complication of a c-polarized incoherent singularity

at low frequency.

Summarising the principal suggestions of this section:

[1] Coherent inelastic excitations are observed in the neutron time-of-flight spectrum of D.P.E. An acoustic dispersion curve can be assembled which is suggestive of important information about the external chain vibrations of polyethylene.

[2] Extraction of this information is hindered by the incoherent inelastic contribution to the spectra. Similar experiments on c-oriented D.P.E. are suggested as a possible solution to this problem.

[b] Incoherent scattering

In the frequency region above 60 cm^{-1} the principal singularities observed in the D.P.E. spectra do not shift in frequency as a function of scattering angle and their intensity variation is typical of an incoherent scatterer. Consequently a density of states extrapolation to zero Q was performed in the incoherent approximation to give the one phonon frequency function $Z(\omega)$ of (3.42). Such functions are reproduced in Fig. 6.7 for the high temperature data and lines have been drawn in to underline features that are statistically significant after allowing for the resolution. Data below 60 cm^{-1} were left untreated on account of the strong coherent inelastic features which affected the extrapolation procedure. All the singularities appearing in these distributions occur in the original data. For the 77^{o}K experiment the low angle data were of especially low intensity on account of the adverse Boltzman Factor for upscattering amd so the extrapolation process was erratic. High angle data at 81^{o} are alone presented in Fig. 6.7 as a plot of corrected counts (4.12) against frequency from which the van Hove singularities can be picked out. There are three prominent features in all spectra at about 50, 100 and 150 cm^{-1} together with a weak shoulder around 220 cm^{-1} (see Table 6.1). The lowest feature is in the region discussed earlier, for which the extrapolation

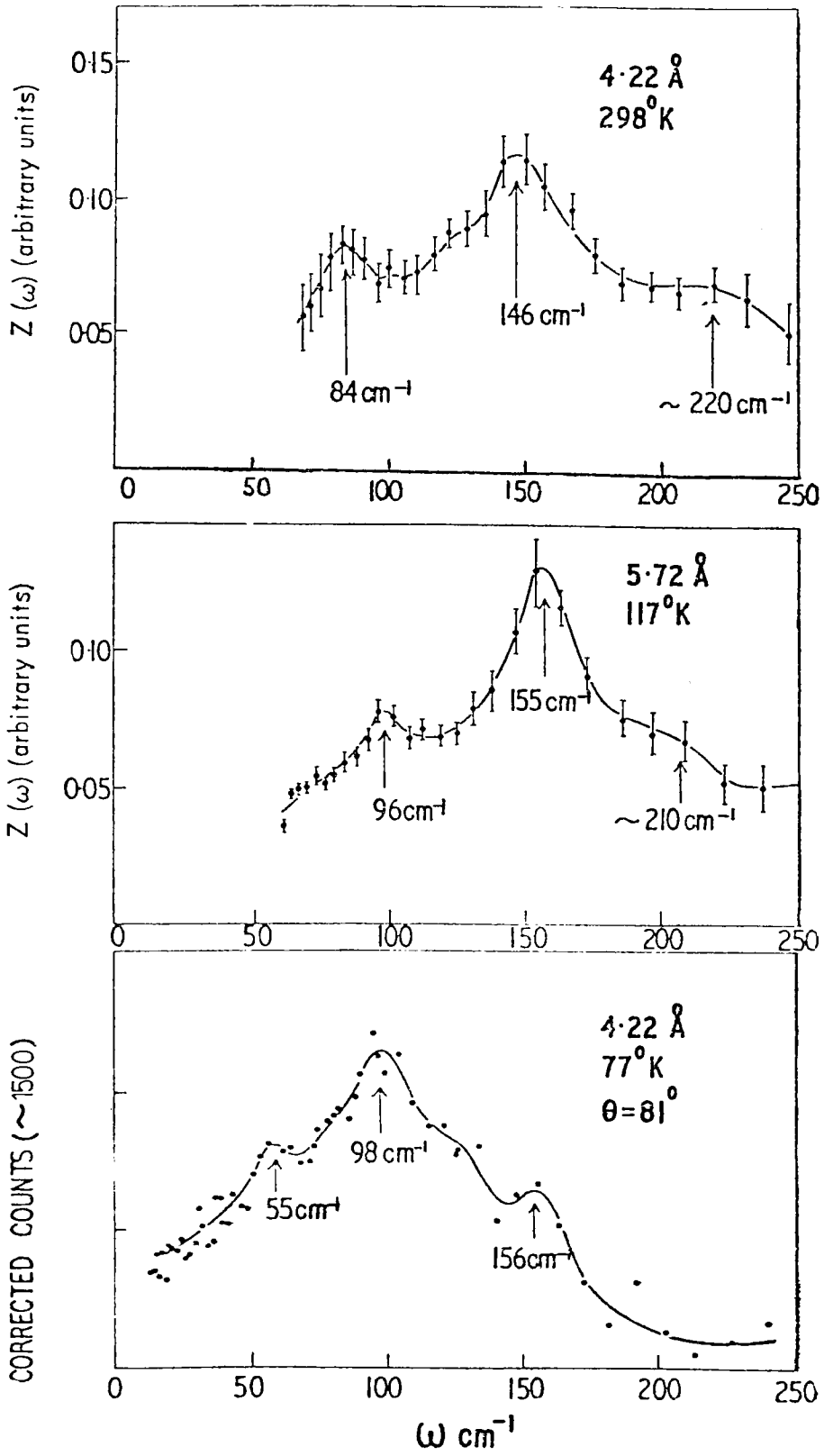

Fig. 6·7 Amplitude weighted density of phonon states, Z(ω), and neutron spectrum for D.P.E. at 77°, 117° and 298°K.

procedure is invalid on account of the coherent inelastic contributions. The peak position is established from the high angle data as mentioned previously (see Fig. 6.3). An upward shift of about 15 cm^{-1} on cooling to 77°K is observed for the two lowest peaks which is typical of external vibrational frequencies in molecular crystals. The 77°K data also agree with that of Lynch, Summerfield, Feldkamp and King [1] for down-scattering from D.P.E. Their peaks at 105 and 165 cm^{-1} compare reasonably with the present frequencies of 98 and 156 cm^{-1} but Lynch et al. do not resolve the important contribution at 55 cm^{-1}. Assignment of the experimental singularities is postponed until the data from normal polyethylene have been considered.

6.5 Normal polyethylene time-of-flight spectroscopy

Time-of-flight spectra of N.P.E. in various isotropic forms have been measured on the 6H spectrometer at 77 and 298°K. The samples were contained in aluminium foil and scattered 10% of the incident neutrons. For the ambient temperature measurements both moulded Rigidex 2 and chain extended material were used. Density of states extrapolations were performed as before in the one phonon incoherent approximation and only for the room temperature data. The spectra obtained differed little and so the Rigidex $Z(\omega)$ is reproduced in Fig. 6.8 as this had the best counting statistics (sample 1). Four peaks are discernible at 46, 112, 140 and 186 cm^{-1}, all poorly defined with the exception of the latter. At 77°K measurements were made on the isotropic single-crystal mats and chain extended material, samples 2 and 3 respectively. Data for high angle counters are also reproduced in Fig. 6.8 for both samples. Lowering the temperature sharpens the observed singularities and four clear peaks at 62, 94, 123 and 190 cm^{-1} are evident (see Table 6.1). The proximity of these peaks has defied their resolution by down-scattering techniques to date and is undoubtedly responsible for the poor definition of the spectra measured at room temperature where the pronounced effects of anharmonicity and

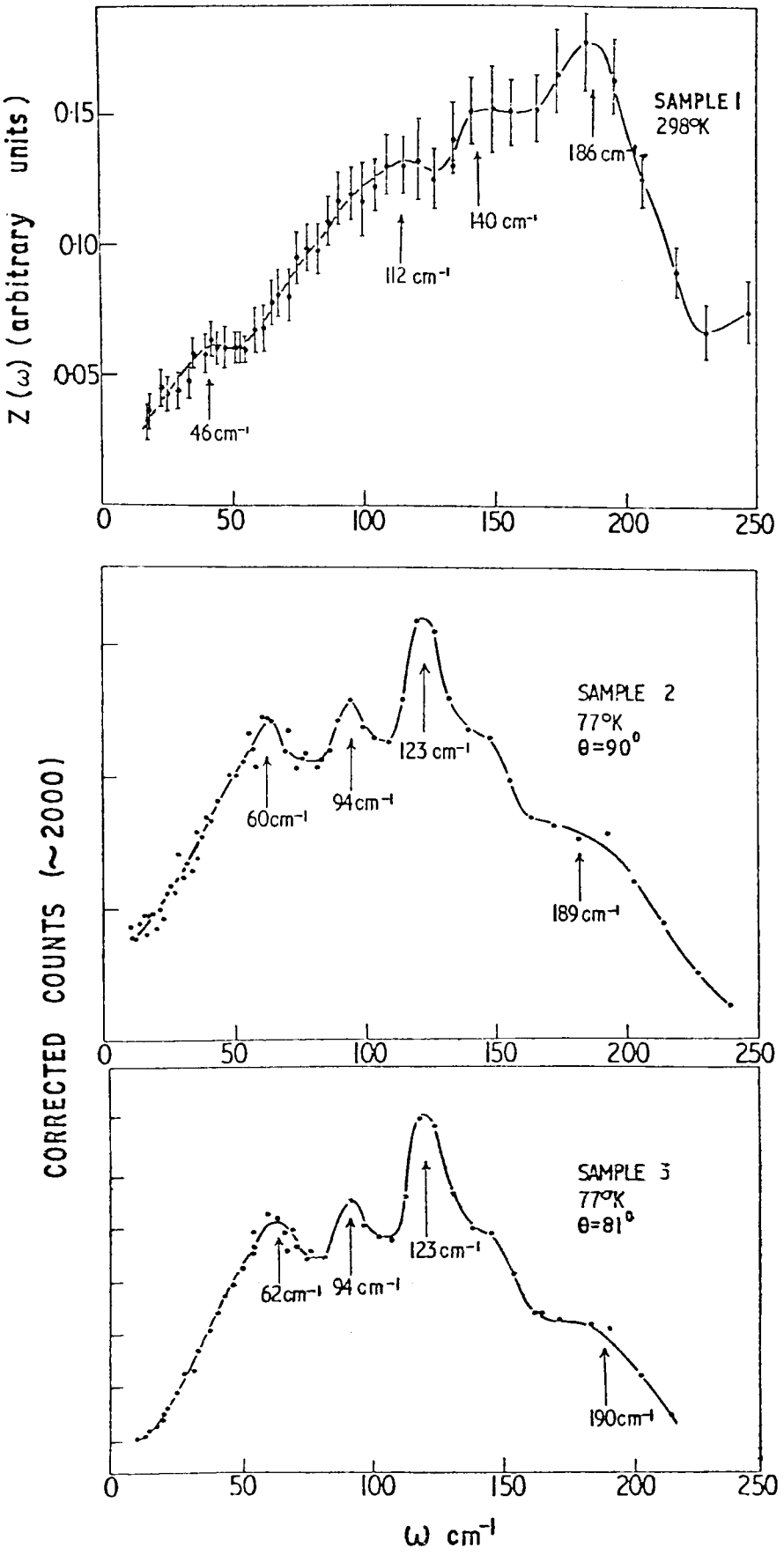

Fig. 6·8 Amplitude weighted density of phonon states, $Z(\omega)$, and neutron spectra for N.P.E. at 77° and 298°K

multiphonon scattering processes smear out these features. Also evident is the greater simplicity of the D.P.E. spectra which is highly suggestive and of prime importance in the assignments of the next section.

6.6 Assignment of singularities in the incoherent neutron spectra of normal and deuteropolyethylene

Only the lowest frequency ν_5 and ν_9 intrachain vibrations are definitely assigned in the neutron spectrum to date. Lower frequency singularities have been observed but assignments have been on the whole tentative, relying on calculated zone centre frequencies which are only in part responsible for the singularities observed in the neutron spectrum (see 5.3.4). In discussing the data presented in this chapter full reference is made to the contributions of Myers and Randolph [7] and Lynch, Summerfield, Feldkamp and King [1] who have employed down-scattering techniques complementary to this work to the same problem. Interpretation of the results begins with the low temperature data. It is common experience that room temperature spectra of relatively low melting point molecular crystals are broadened and obscured by anharmonicity effects and multiphonon processes. Certainly this is the case for polyethylene.

At 77°K the ν_5 chain stretching vibrations are insufficiently activated to contribute to the energy gain spectrum which tails off sharply around 250 cm^{-1}. However the sharp cut-off and distribution peak characteristic of the ν_9 chain torsional vibrations is clearly evident in all spectra. Peaks at 190 and 156 cm^{-1} for N.P.E. and D.P.E. respectively at 77°K are in excellent agreement with the prominent feature in all calculated frequency distributions (see Table 6.1). Although the neutron spectra are weighted by the atomic amplitudes, recent work on naphthalene and p-dichlorobenzene has justified the assumption that singularities in the amplitude weighted frequency distribution are common to the true density of states and this assumption is made here in comparisons effected between calculated frequency distributions and experimental neutron spectra [10].

Table 6.1 Comparison of singularities in the neutron spectra and calculated density of states of polyethylene and deuteropolyethylene at 77 and 298°K

POLYETHYLENE SINGULARITIES				
77°K	77°K		298°K	298°K
Calculated ω cm^{-1}	Neutron data ω cm^{-1}	Assignment	Neutron data ω cm^{-1}	Calculated ω cm^{-1}
210[a]	210 ± 12	Chain torsional cut-off	205 ± 12	205[a]
195	190 ± 10	Chain torsional peak	186 ± 10	200
150	123 ± 6	Hindered rotatory lattice mode	(140)	140
90	94 ± 4	a,b-translatory lattice mode	(112)	90
60	62 ± 3	c-translatory lattice mode	46 ± 2	60

DEUTEROPOLYETHYLENE SINGULARITIES

77°K	77°K		298°K	298°K
Calculated ω cm^{-1}	Neutron data ω cm^{-1}	Assignment	Neutron data ω cm^{-1}	Calculated ω cm^{-1}
170[a]	177 ± 9	Chain torsional cut-off	170 ± 9	-
160	156 ± 8	Chain torsional peak	146 ± 7	-
120	98 ± 4	Hindered rotatory, a,b-translatory lattice modes	84 ± 4	-
75	55 ± 3	c-translatory lattice mode	40 ± 2	-

[a]From Kitagawa [13, 14]

In the lower frequency region three peaks are resolved in N.P.E. at 62, 94 and 123 cm^{-1} and two in D.P.E. at 55 and 98 cm^{-1} for the 77°K data. From all the calculations it appears that the lowest frequency lattice vibrations are c-polarized and contribute to a peak in the density of states. That this is the proper assignment for the 55 and 62 cm^{-1} peaks in D.P.E. and N.P.E. is clearly demonstrated in the next chapter where the incoherent contribution to the neutron spectrum in this frequency region disappears in the experimental configuration with $\vec{Q}$ perpendicular to the defined chain axis. Cold neutrons give particularly good resolution and scattered intensity in this frequency region and so although Myers resolves a shoulder at 48 cm^{-1} in the 77°K spectrum of N.P.E. [7], such a singularity is not resolved at all for D.P.E. [1] on account of the inferior resolution of down-scattering techniques in this region. Myers confirmed the c-polarization of this feature in his dichroism studies using oriented N.P.E. The discrepancy in frequency of 14 cm^{-1} with the value obtained here is a likely consequence of the poor resolution of this feature in down-scattering studies where it is seen as a weak shoulder on a steeply rising spectrum (see Fig. 5.3). Myers suggests that the peak coincides with a zone centre critical point corresponding to the antiparallel translation of the chains along the c-axis with A_u symmetry. There are in fact six critical points associated with lattice vibrations of this polarization and consequently no such simple assignment is possible [12].

The peaks at 94 and 123 cm^{-1} in N.P.E. and at 98 cm^{-1} in D.P.E. correspond reasonably to the values of 97, 125 and 104 cm^{-1} respectively from the earlier contributors. They are more clearly resolved in the present up-scattering data as is illustrated by comparison of Fig. 6.8 with the data of Fig. 5.3. Myers and Randolph assign the 94 cm^{-1} peak to the B_{2u} zone centre singularity associated with antiparallel translation of the chains along the a-axis. A more tentative assignment of the 125 cm^{-1} peak to the B_{3g} zone centre singularity corresponding to the in phase

overall rotatory motion of the two molecules in the unit cell is also suggested on the basis of calculations by Tasumi and Krimm [11]. Lynch et al. assign the 104 cm^{-1} peak in D.P.E. to the same critical point.

As has been stressed earlier in this thesis, the density of states and related frequency functions have critical points at a variety of sites within the Brillouin Zone. Marsh and Martin [12] have evaluated these singularities for some of the existing interchain force fields. They show that there is little correlation between the zone centre frequencies and the position of peaks and inflexions in calculated frequency distribution functions. However it is possible to characterize these features using the associated eigenvectors and Kitagawa distinguishes three regions where the density of states has a peak arising from interchain vibrations [13, 14]. At 77°K peaks at 60, 90 and 150 cm^{-1} in N.P.E. are calculated for c-translatory, a, b-translatory and overall rotatory motion of the chains respectively. Such a qualitative assignment is realistic and has already been achieved for c-translatory lattice vibrations on purely experimental grounds. From the calculations two more lattice modes are expected in the density of states and the correct association with remaining experimental peaks, two in N.P.E. and one in D.P.E., becomes clear from two empirical considerations:

[1] The B_{1u} and B_{2u} zone centre frequencies have been observed in the far infrared spectrum at 79.5 and 109.5 cm^{-1} for N.P.E. at 2°K (see 5.2.2 and 9.4.4.1). From Marsh and Martin [12] it appears that the single peak in the calculated density of states associated with molecular translations in the ab plane is more in correspondence with a zone boundary singularity than with either of the critical points corresponding to B_{1u} and B_{2u} symmetry zone centre frequencies. This singularity was located in frequency between the two zone centre points in all the models examined and so it is reasonable to set low and high frequency limits on the position of the expected distribution peak for ab translatory motion corresponding

to the experimental B_{1u} and B_{2u} frequencies. Assignment of the 94 cm^{-1} peak in N.P.E. to such vibrations is consistent with these considerations and in especially good agreement with the 90 cm^{-1} peak calculated by Kitagawa [13].

[2] Comparison of N.P.E. and D.P.E. spectra reveals the greater simplicity of the latter in the frequency region under discussion. As the force field should not be affected on deuteration, any differences between D.P.E. and N.P.E. should be explicable in terms of changes in mass and inertia which will affect the translatory and rotatory frequencies. Changes in the latter are more dramatic since the moment of inertia about the c-axis is increased much more than the total mass on deuteration. Deuteration shifts of 22 and 6% are calculated for rotatory and translatory vibrations respectively. Assignment of the 123 cm^{-1} peak in N.P.E. to overall rotatory vibrations suggests an analogous D.P.E. feature at 98 cm^{-1} in excellent agreement with experiment. In contrast the translatory vibrations would be shifted from 94 to 88 cm^{-1}. And so without speculation as to the critical points implied by the distribution peak at 123 cm^{-1} in N.P.E., a clear assignment to overall rotatory chain motion can be made on the basis of the greater simplicity of the D.P.E. spectrum in which this peak has shifted to a frequency close enough to the translatory vibrations to escape instrumental resolution. Further corroboration of this assignment is provided in Chapter 10 by the confirmation of the A_g rotatory mode frequency at 111(137) cm^{-1} in D.P.E. (N.P.E.) at 77°K. From the work of Marsh and Martin this singularity would be expected to provide an upper limit to the frequency distribution peak for rotatory motion and is consistent with the proposed assignment.

A summary of these assignments is provided in Table 6.1 with the calculated density of states singularities of Kitagawa for comparison. The agreement for N.P.E. data at 77°K is good except for the rotatory peak calculated at 150 cm^{-1} and observed at 123 cm^{-1}. Tasumi and

Shimanouchi [15] do not calculate the density of states but give B_{3g} and A_g zone centre frequencies of 139 and 172 cm^{-1} which are clearly too high in the light of these experimental data and those of Chapter 10, especially since their calculation is for the room temperature structure. For D.P.E. agreement with Kitagawa is poorer since he does not resolve the ab- and c-translatory contributions but calculates one peak at 75 cm^{-1} for translatory modes and another at 120 cm^{-1} for rotatory modes. On the whole Kitagawa's force field gives a better fit to the low temperature singularities than the stronger force field of Tasumi and Shimanouchi, although both are defective in their predictions of the overall rotatory frequencies.

The high temperature data are less easily treated as the singularities are broadened and obscured by anharmonicity and the contribution of multi-phonon scattering processes to the spectra. For D.P.E. the broadening has less severe consequences than for N.P.E. where the distribution peaks are more numerous and closely adjacent. The 98 cm^{-1} peak at 77°K in D.P.E. shifts to 84 cm^{-1} at 298°K, a change typical of the lattice vibrations of many molecular crystals and mostly reflecting the increase in unit cell dimensions at the higher temperature. Similarly the c-polarized translatory lattice mode shifts from 55 to 40 cm^{-1} at 298°K. In N.P.E. there are two broad features at 110 and 140 cm^{-1} which are not simply assigned together with a peak at 46 cm^{-1} which may be related to the 62 cm^{-1} feature in the 77°K data. The ν_9 torsional peak and cut-off are prominent at all temperatures (see Table 6.1). Shoulders observed at 240 cm^{-1} in N.P.E. and 220 cm^{-1} in D.P.E. have been seen also by Myers and Lynch et al. who noted their transverse polarization and assigned them to two phonon processes. Kitagawa [13] has calculated the contributions expected from such processes and predicts a broad peak in this region from a combination of the ν_9 torsion and the overall rotatory mode which for D.P.E. would be at about 230 cm^{-1} in good agreement with the observed

peak at 220 cm^{-1} for the data at 298°K. An explanation of the room temperature N.P.E. data must await refinements in the force field since the severe effects of anharmonic broadening and multiphonon processes on the low frequency lattice singularities are hard to evaluate without a correct model for the one phonon spectrum.

A final point should be made about the contribution of the amorphous regions to the observed spectra. Neutron scattering from highly amorphous polyethylene has been reported and the spectra show no singularities but only a continuous decline in intensity from low frequency [16]. On this account the absence of features distinctive of the amorphous regions in the spectra reported here is not unreasonable.

6.7 Summary

Time-of-flight spectra of polycrystalline D.P.E. and N.P.E. are reported at 77 and 298°K. Coherent inelastic excitations are observed in the D.P.E. spectra and an acoustic dispersion curve assembled. This curve suggests potentially anisotropic information about the external chain vibrations but extraction of such information is hindered by the incoherent inelastic contribution to the spectrum. Experiments on c-oriented D.P.E. are recommended as a solution to this problem.

The incoherent contribution to the D.P.E. and N.P.E. spectra are examined and found to provide information that complements the earlier down-scattering work by resolving the lowest frequency singularity. Regions of the spectra are assigned to c-translatory, ab-translatory and overall rotatory motion of the chains on the basis of information available from far infrared studies and a comparison of the D.P.E. and N.P.E. data. Experimental singularities agree more closely with the calculations of Kitagawa than those of Tasumi and Shimanouchi although an overestimate in the frequency of rotatory lattice modes is common to both force fields. The temperature dependence of the lattice vibrations is noted but assignment

of the room temperature data is confused by both anharmonicity and the contribution of multiphonon scattering processes, some of which are identified.

References

[1] J.E. Lynch Jr., G.C. Summerfield, L.A. Feldkamp and J.S. King, J. Chem. Phys., 48, 912 1968.

[2] W.L. Carrick, R.W. Kluiber, E.F. Bonner, L.H. Wartman, F.M. Rugg and J.J. Smith, J.A.C.S., 82, 3883 1960.

[3] C.W. Bunn, Trans. Far. Soc., 35, 482 1939.

[4] R. Chiang and P.J. Flory, J.A.C.S., 83, 2857 1961.

[5] P.R. Swan, J. Poly. Sci., 56, 403 1962.

[6] P.W. Teare, Acta Cryst., 12, 294 1959.

[7] W.R. Myers and P.D. Randolph, J. Chem. Phys., 49, 1043 1968.

[8] G.E. Bacon, 'Neutron diffraction', Oxford 1962.

[9] S.J. Cocking, D.Phil. thesis, London University 1968.

[10] G.S. Pawley, P.A. Reynolds, J.K. Kjems and J.W. White, Solid State Commun., 9, 1351 1971.

[11] M. Tasumi and S. Krimm, J. Chem. Phys., 46, 755 1967.

[12] D.I. Marsh and D.H. Martin, J. Phys. C., 5, 2309 1972.

[13] T. Kitagawa, D.Sc. thesis, Osaka University 1968.

[14] T. Kitagawa and T. Miyazawa, Jap. Polym. J., 1, 471 1970.

[15] M. Tasumi and T. Shimanouchi, J. Chem. Phys., 43, 1245 1965.

[16] K. Doi, M. Sakamoto, M. Iizumi, N. Masaki and H. Motohashi, Nippon Genshiryoku Kenkyusho Kenkyu Hokoku, JAERI 1197, p. 109 1970.

Chapter 7

NEUTRON SCATTERING STUDIES OF UNIAXIALLY ORIENTED DEUTEROPOLYETHYLENE

7.1 Introduction

The measurements reported here are in historic sequence since they were stimulated by the first results from polycrystalline D.P.E. and the problems encountered in locating the coherent inelastic singularities. In this chapter experiments on c-oriented D.P.E. are described with particular reference to the nature and origin of these acoustic phonon groups. Dynamical structure factors are calculated from an Urey-Bradley force field and used to interpret the observations. Some comments are made about the extraction of anisotropic dynamical information from isotropic systems by coherent neutron scattering and the general applicability of this technique to partially oriented materials is assessed. Finally the results for D.P.E. are used in a criticism of the available force fields for the room temperature structure and comparison with data for intrachain acoustic phonons is effected to give a clear demonstration of the anisotropy of the polyethylene force field.

7.2 Sample characteristics

The c-oriented specimen was prepared in collaboration with Dr. C.P. Buckley of the Oxford Engineering Department. Deuteropolyethylene powder from Merck was moulded at 160°C by repeated application of pressure on a 10 ton hand press. Air bubbles were removed by transferring the molten polymer to a vacuum oven for a short period before quenching in cold water. The moulded specimen with dimensions 3.4 x 2.0 x 0.33 cm^3 was drawn in air at 120°C to 4.0 times the initial length. Drawing was essentially uniaxial since the ratio of relative contraction in width to thickness was only 1.5. The drawn specimen was dried under vacuum for 18 hours at 55°C.

In appearance the specimen was light brown indicating a small amount of degradation. Since the source D.P.E. is chemically pure and without deoxidants, such degradation is to a large extent inevitable, although every effort was made to prevent direct exposure of the molten material to air. Infrared spectra of moulded films produced from this specimen showed a very weak carbonyl peak.

The sample density was measured and found to be 1.076 gm ml^{-1} at 25°C compared to X-ray and amorphous densities of 1.149 and 0.975 respectively estimated for D.P.E. in the last chapter. A mass fraction crystallinity of 62.0% was calculated from these figures although this will be an underestimate on account of voids and other sample defects that will lower the observed density.

Wide angle X-ray diffraction pictures were taken for various sample orientations and suggested a well defined c-axis along the draw direction but no preferred orientation perpendicular to this direction. Neutron diffraction confirmed a c-mosaic of 10° FWHM and an isotropic distribution of a- and b-poles in the basal plane of the polymer. The calculated lattice parameters agreed exactly with Bunn's room temperature values discounting any change in the structure of the crystalline regions arising from the inclusion of carbonyl degradation products for example. Neutron diffraction data collected in the ab plane of the polymer are shown in Fig. 7.1. Again the [110] and [200] reflexions predominate in the $\vec{Q}$ region investigated by cold neutrons, however the collimation is relaxed and peaks are poorly resolved in these data. The asymmetry of the [110]-[200] doublet is attributed to scattering from the amorphous regions which peaks in $\vec{Q}$ just below [110]. Despite the appreciable contribution from incoherent and amorphous diffuse scattering, the [110] peak intensity is still about ten times the background level.

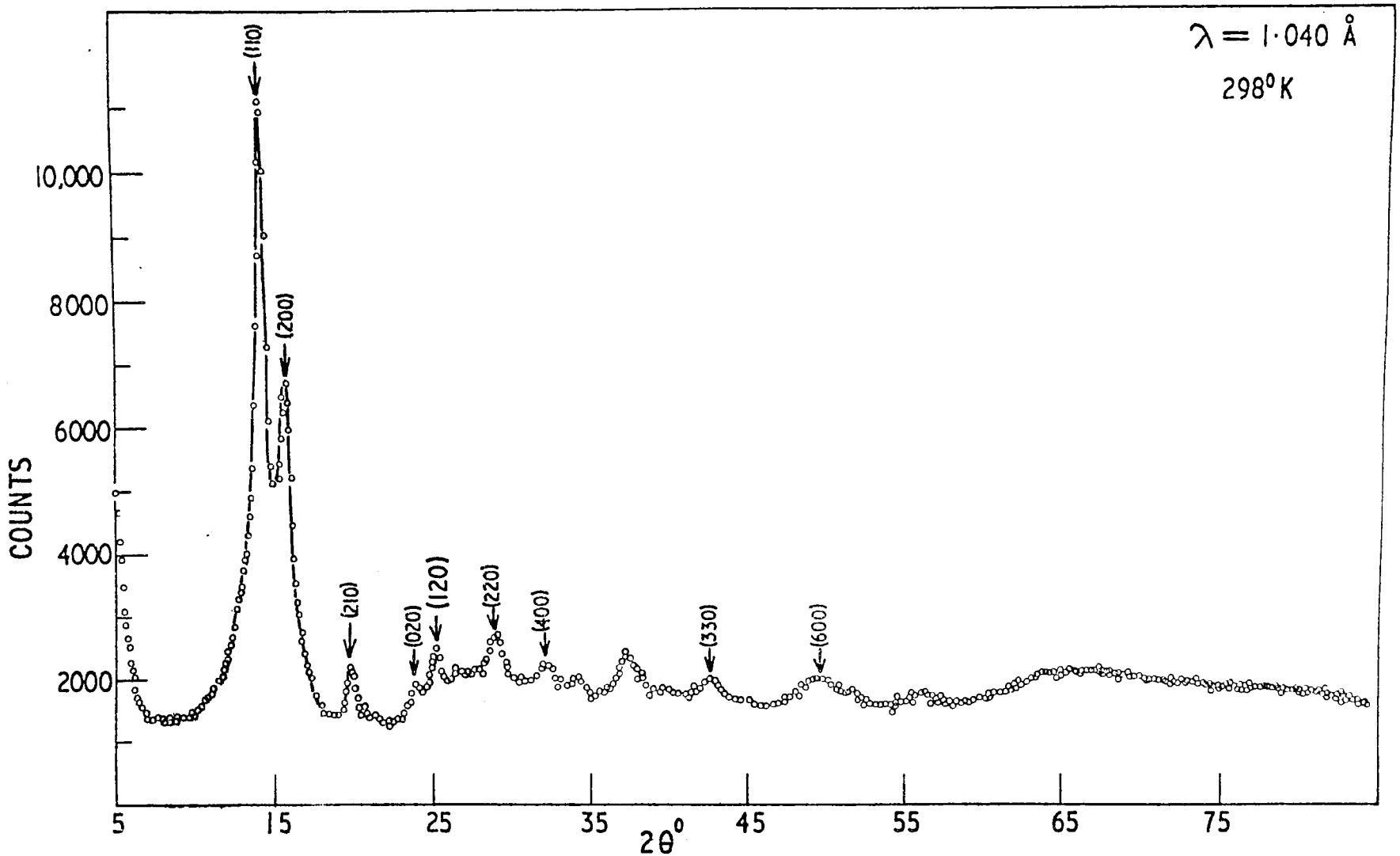

Fig. 7·1 Neutron diffraction data collected in the basal plane of uniaxially oriented D.P.E.

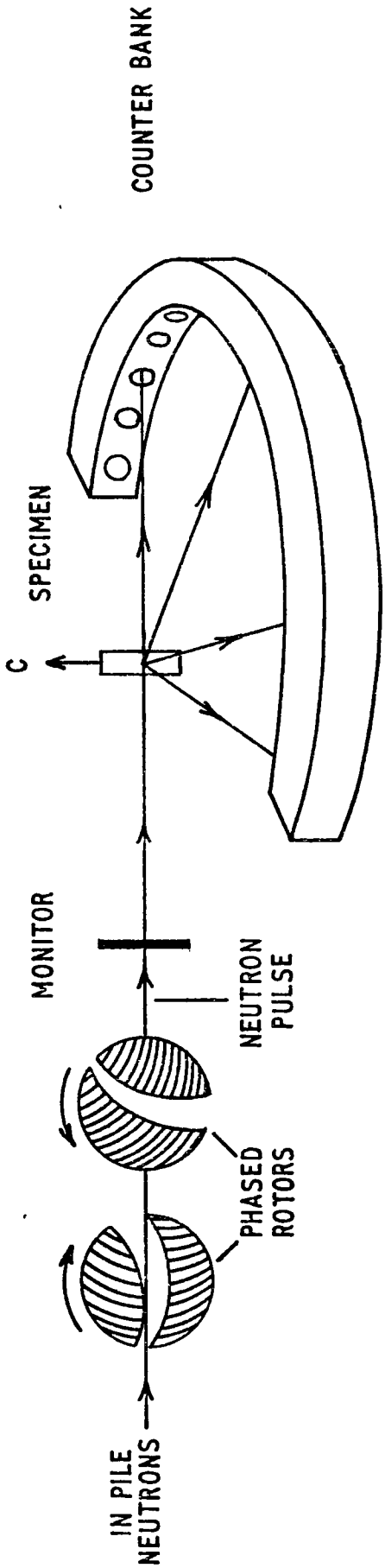

Fig. 7·2 Schematic illustration of the 7H time-of-flight spectrometer showing the sample orientation with respect to the phonon arc.

7.3 Time-of-flight spectroscopy

Time-of-flight spectra of c-oriented D.P.E. were obtained by use of the 7H phonon arc at A.E.R.E. Harwell described in 4.3.1. In these experiments the sample was mounted in an aluminium frame so that the c-axis was vertical. Neutrons were incident perpendicular to this axis and the scattered neutrons detected by an array of counters set at 2^{o} intervals in a horizontal arc as illustrated in Fig. 7.2. The counters subtended an angle at the sample within a vertical plane which was less than the c-mosaic. Counting statistics were poorer than for the polycrystalline data because of this small solid angle of detection and experiments took three or four times longer in consequence.

Neutron wavelengths between 2.70 and 3.90 Å were employed in these studies and the scattering angle ranged from 11 to 69^{o}. In Fig. 7.3 time-of-flight spectra for 3.10 Å neutrons are presented for four adjacent He^{3} counters. A well defined low energy peak is seen to propagate across the time-of-flight spectrum, disappearing into the elastic peak at 41^{o}. As in the earlier data the elastic peak is enhanced by Bragg scattering from [110] at this stage. The coherent inelastic singularities are easily located and Fig. 7.4 shows the 3.10 Å data assembled on the instrumental $(|\vec{Q}|,\omega)$ plot.

Because of the large number of counters dispersion of the coherent inelastic feature is well mapped and Fig. 7.4 shows a roughly linear dispersion relationship which extrapolates in $|\vec{Q}|$ to the [110] reciprocal lattice vector, as for the polycrystal. The absence of an incoherent singularity at 40 cm^{-1} in the higher angle counters where the coherent contribution has disappeared confirms the suspected c-polarization of this singularity, extensively discussed in the last chapter. It also explains the sharp contrast between these data and the polycrystalline data. The removal of the incoherent singularity in the vital frequency region by restricting $\vec{Q}$ to the basal plane of a c-oriented specimen

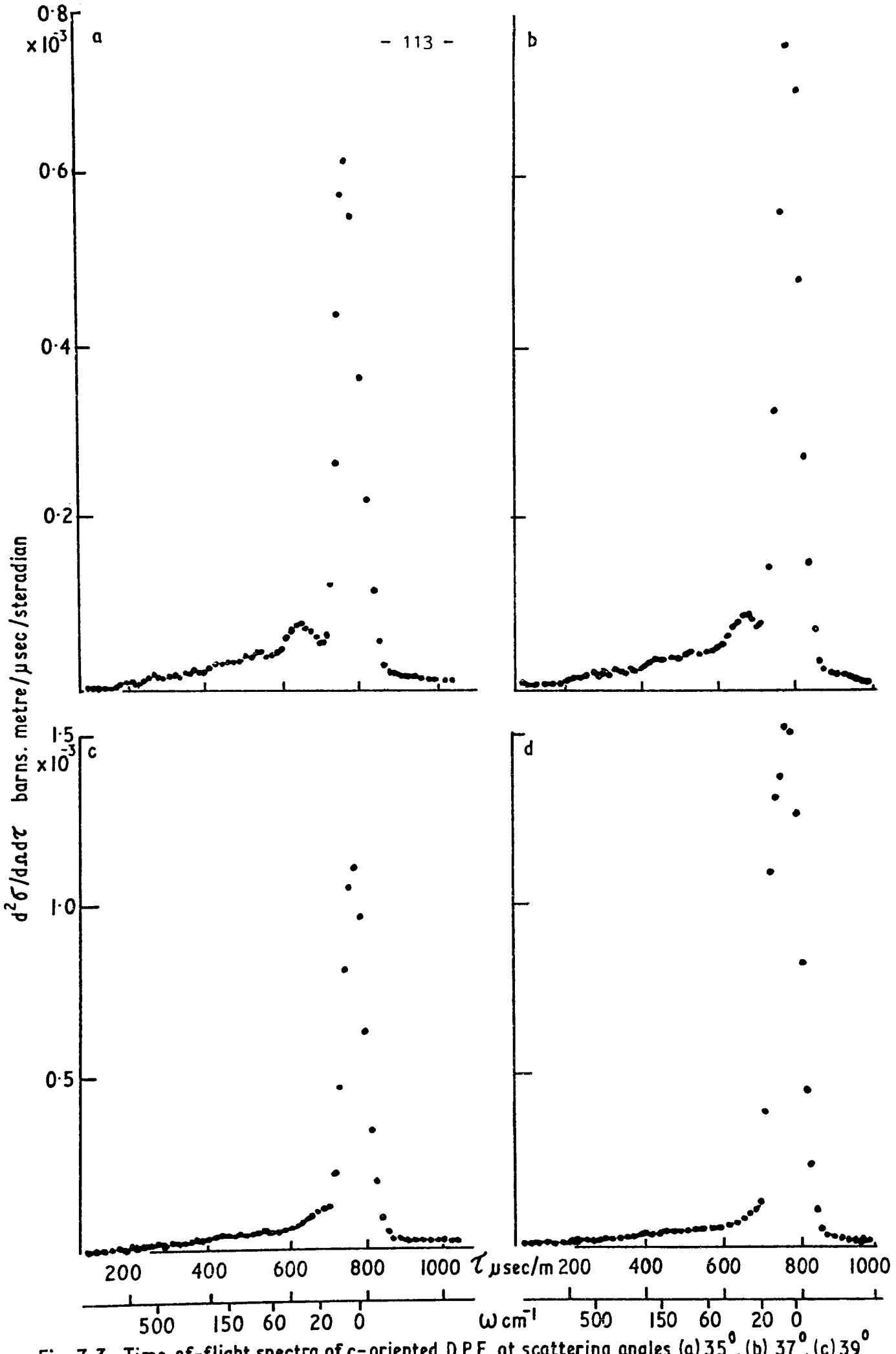

Fig. 7·3 Time-of-flight spectra of c-oriented D.P.E. at scattering angles (a) 35°, (b) 37°, (c) 39° and (d) 41° to the incident 3·1 Å neutron beam at 298°K

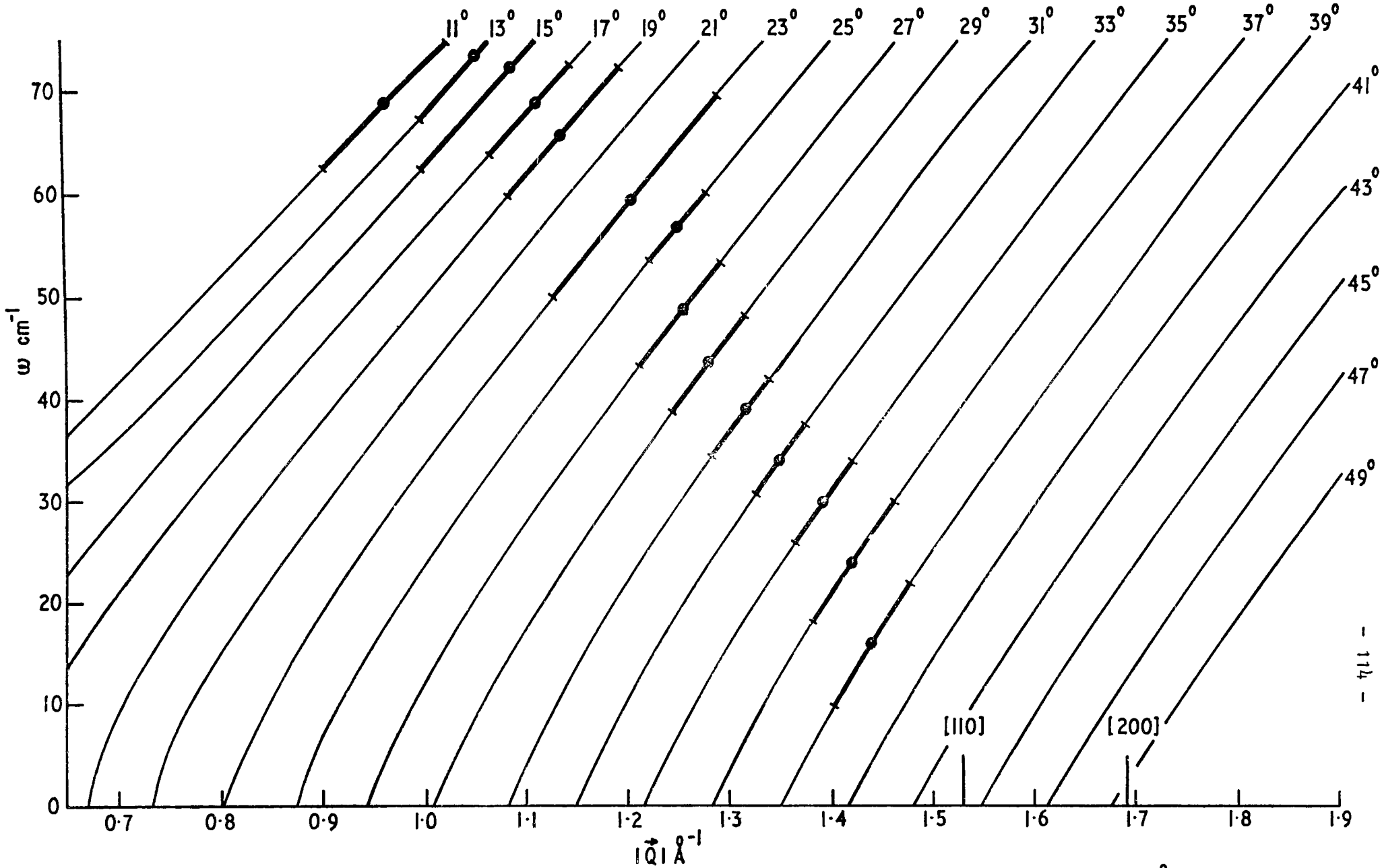

Fig. 7·4 Coherent inelastic singularities for c-oriented D.P.E. assembled on the instrumental dispersion curves for 3·1 Å incident neutron.

facilitates unambiguous location of the coherent features and the distortion in the first dispersion curve is removed.

The excellent definition of acoustic phonon groups in the time-of-flight spectra of an isotropic system is remarkable and suggests a strongly anisotropic contribution to the isotropically averaged dynamical structure factors. The ab-polarization of these groups infers that they contain information about acoustic phonons propagating perpendicular to the chains. Extraction of such information requires some knowledge of the dynamical structure factors and this can only be afforded by calculations based on a model force field.

7.4 Calculation of dynamical structure factors

The coherent inelastic cross section for single phonon excitation by a neutron is calculable once the frequencies and amplitudes of atomic motion are provided by a suitable model. The derived cross section is a sensitive function of the orientation of $\vec{Q}$ upon the reciprocal lattice on account of the momentum conservation condition operative in the case of coherent scattering. The dynamical structure factor for a single phonon excitation has been expressed in (3.37)

$$g_j(\vec{Q}) = \sum_\nu \left(\frac{\hbar}{2M_\nu \omega}\right)^{1/2} \bar{b}_\nu . \vec{Q} . \vec{\zeta}_{\nu j}(\vec{q}) . e^{-W_\nu} e^{i\vec{Q}.\vec{\alpha}_\nu} \qquad (7.1)$$

An intimate relationship between the elastic and inelastic structure factors is readily inferred from (7.1). Only the eigenvector product truly distinguishes the particular force model employed in a calculation of $g_j(\vec{Q})$. Moreover provided the eigenvectors have the correct symmetry properties, certain trends in the dynamical structure factors will persist for a variety of model force fields. For example in acoustic phonons the atomic eigenvectors $\vec{\zeta}_{\nu j}(\vec{q})$ will have the same polarization or sign. Such phonons will be most readily seen when excited from a strongly reflecting reciprocal lattice point in which the geometric factors $e^{i\vec{Q}.\vec{\alpha}_\nu}$ will be of the same phase or sign and when multiplied by the eigenvectors will add

up constructively.

Deficiencies in model force fields are rarely subtle enough to disguise the characteristic influences of symmetry upon the dynamical structure factors and so provided the model at least imposes the correct symmetry restrictions upon the atomic vibrations, it will provide a useful guide to the observed intensities.

Initial calculations on polyethylene utilized the rigid chain Urey-Bradley force field of Tasumi and Shimanouchi [1]. A dynamical matrix for external chain vibrations based on the Set 1 force field was made available by Dr. D.I. Marsh and Professor D.H. Martin of Queen Mary College, London [2]. As a consequence of the rigid chain approximation, the eigensolutions of this matrix characterize phonons with wave vector confined to the basal plane of the polymer.

Interpretation of the coherent inelastic features in the neutron spectra of polycrystalline and c-oriented D.P.E. required calculation of $g_j(\vec{Q})$ for $\vec{Q}$ values on concentric circles in the basal [hk0] plane of the reciprocal lattice using (7.1). Constant $|\vec{Q}|$ scans were simulated because calculations along the instrumental $(|\vec{Q}|,\omega)$ track proved expensive in computing time. Up to 200 orientations of $\vec{Q}$ on a 90° arc in the reciprocal lattice were used to construct the averaged frequency spectrum at constant $|\vec{Q}|$. The neutron scattering cross section is related to the square of the modulus of $g_j(\vec{Q})$ computed for all orientations of $\vec{Q}$ and summed over all normal modes weighted by a thermal occupation factor as in (3.36). The computed structure factors are found to be strongly dependent upon the relative orientation of $\vec{Q}$ and the reciprocal lattice with the acoustic modes predominating. Most intense contributions come from the highest frequency longitudinal acoustic (LA) mode which shows a pronounced polarity in $|g_j(\vec{Q})|^2$ with a well defined maximum for the co-linear configuration of $\vec{Q}$ and the [110] lattice vector. A subsidiary contribution arises from transverse acoustic (TA) vibrations in which the molecules move perpendicular to the phonon wavevector and in the ab plane. The third acoustic

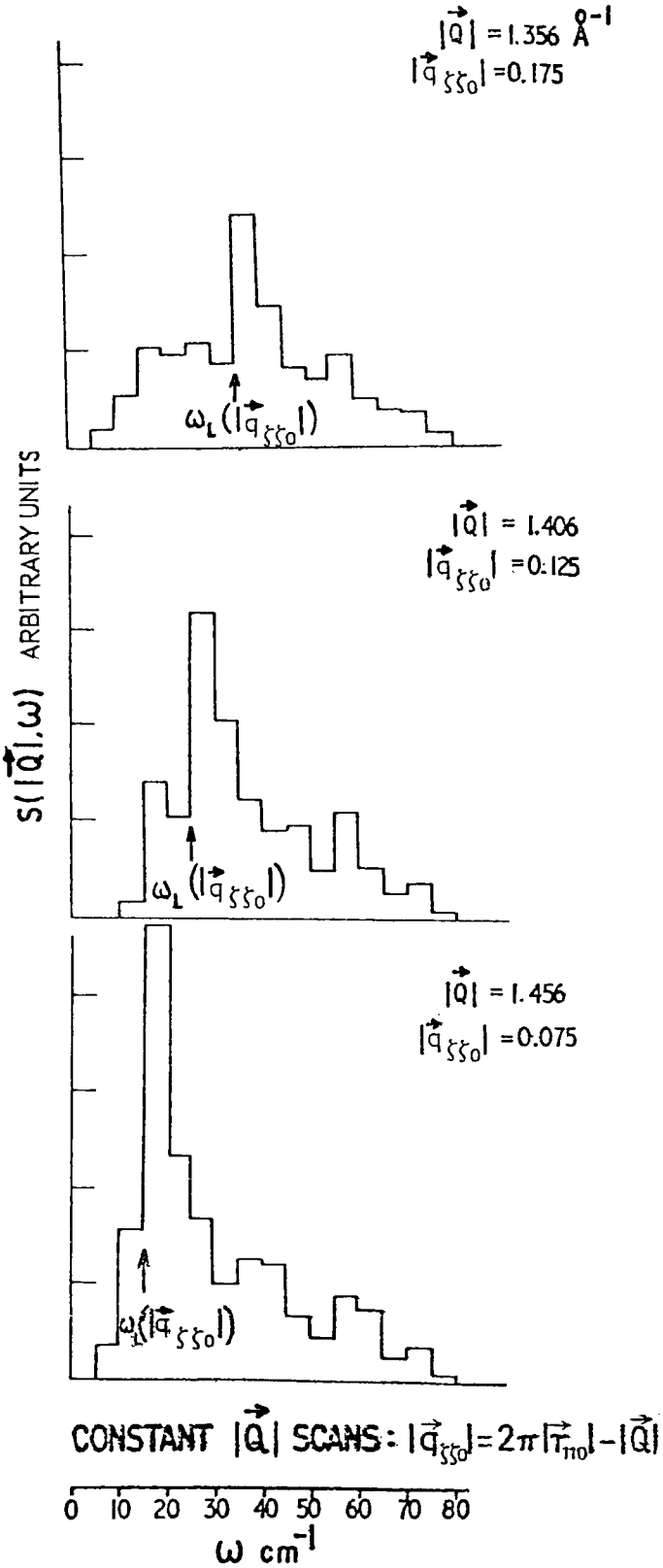

Fig. 7·5 Coherent inelastic spectra for constant $|\vec{Q}|$ scans in the basal plane of c-oriented D.P.E. calculated from the force field of Tasumi and Shimanouchi.

mode of lowest frequency and with c-polarized molecular eigenvectors is not selected in the configuration with $\vec{Q}$ restricted to the basal plane.

Frequency histograms $S(|\vec{Q}|,\omega)$ derived from (3.36) for three constant $|\vec{Q}|$ values are shown in Fig. 7.5. A strong parallel with the experimental data is shown by the behaviour of the prominent peak which shifts to lower frequency as $|\vec{Q}|$ aproaches the [110] reflexion. The low frequency edge of this feature labelled $\omega_L(|\vec{q}_{\zeta\zeta 0}|)$ in Fig. 7.5 corresponds to the strong contribution just described for LA phonons propagating along $[\zeta\zeta 0]$ with wavevector

$$|\vec{q}_{\zeta\zeta 0}| = 2\pi|\vec{\tau}_{110}| - |\vec{Q}| \qquad (7.2)$$

corresponding to a co-linear orientation of $\vec{q}$, $\vec{Q}$ and $2\pi\vec{\tau}$.

From these results a new approach to the experimental data is suggested. This is exemplified by Fig. 7.6 where the full room temperature data are assembled as a plot of frequency in cm^{-1} against $|\vec{q}_{\zeta\zeta 0}|$ derived from (7.2). A rigorous approach to the location of the predicted low frequency edges was abandoned because of the poor statistics and persistent uncertainty about the form of the incoherent background. In general the peak centre was taken but the error bars in Fig. 7.6 are sufficiently generous to cover such location errors and their fluctuation in size reflects the peak definition which is poorer at higher energy where the structure factors are lower. There is evidence of a slight distortion around 35 cm^{-1} which would arise from a residual contribution of the c-polarized incoherent singularity, possibly on account of the 10^{o} mosaic. A line was drawn giving greater weight to the observations above 35 cm^{-1} and a sound velocity established from the data with an estimated error of ±10%.

An elastic constant of $15\pm3\times10^{10}$ dyne cm^{-2} for LA deformations along $[\zeta\zeta 0]$ was evaluated from the measured slope of $3.6\pm0.4\times10^{5}$ cm/sec and a crystal density of 1.149 gm cm^{-3} at $298^{o}K$.

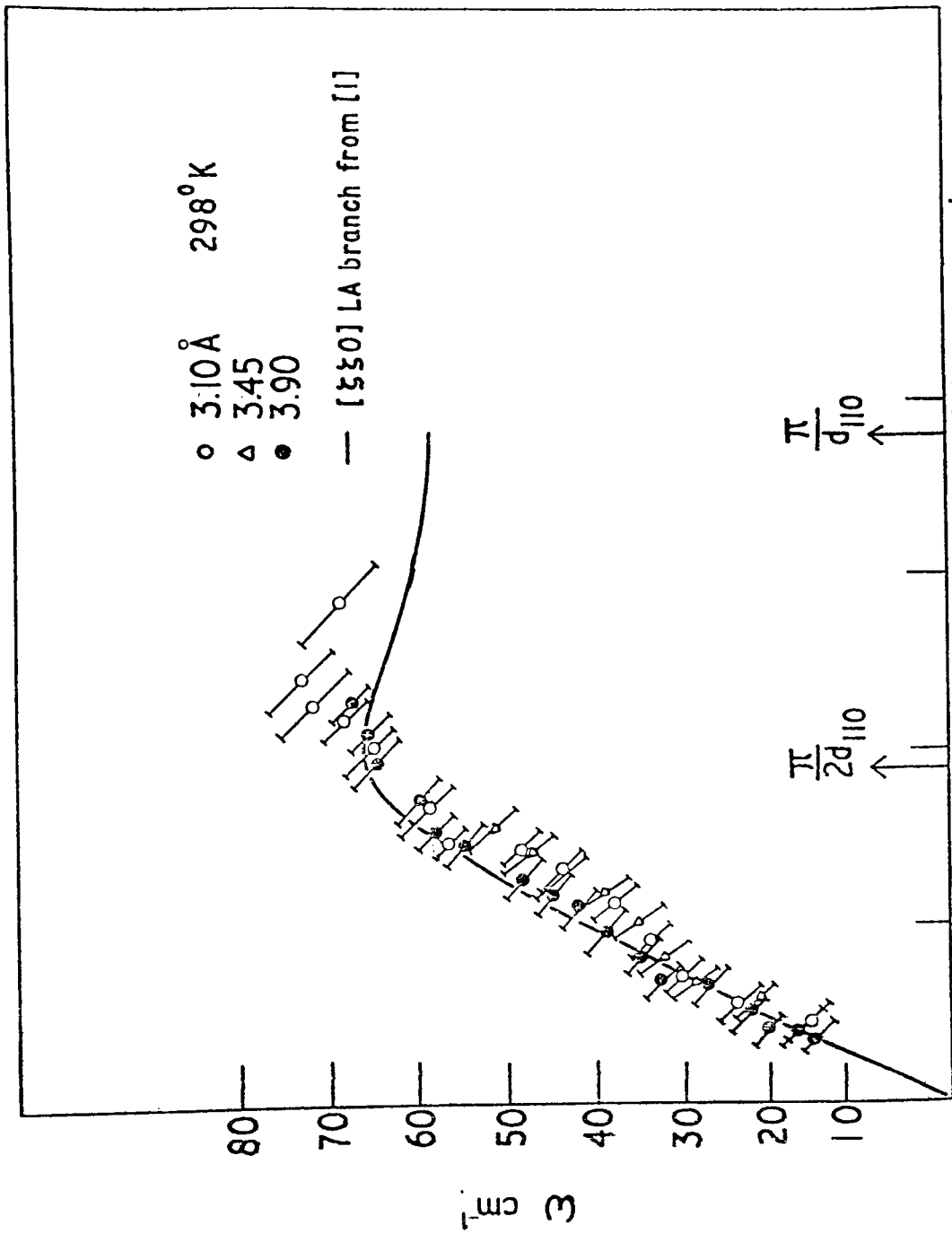

Fig. 7·6 Experimental LA phonon dispersion curve along [ξξ0] constructed from coherent inelastic singularities in the neutron spectra of c-oriented D.P.E. together with the calculated dispersion curve from [1].

7.5 Coherent scattering by polycrystals - a general appraisal

The results reported in this chapter could be seen as a historical prelude to the experiments on fully oriented D.P.E. which have yielded the most exciting information about the interchain force field to date. But this would be a great oversight. The definition of anisotropic excitations in the time-of-flight spectrum of an isotropic material is a remarkable development which deserves a closer scrutiny so that further applications of such studies may be evaluated. Moreover the limited anisotropy of available specimens makes the extension of such experiments on polymers an attractive proposition. As the potential applications of this method are an important aspect of this chapter it is expedient to examine them now before commenting on the specific experimental conclusions.

For a cubic monatomic crystal the dynamical structure factor (7.1) is simplified because there is no atomic basis and the exponential term vanishes. The cross section for coherent single phonon excitations becomes [3]

$$S(\vec{Q},\omega) = K \sum_j \frac{|\vec{Q}.\vec{\alpha}_j|^2 e^{-2W}}{\omega \sinh(\frac{\hbar\omega}{2kT})} \delta(\vec{Q}\pm\vec{q}-2\pi\vec{\tau}) \; \delta(\omega-\omega_j) \qquad (7.3)$$

where K is a constant and $\vec{\alpha}_j$ the eigenvector which now has no atomic label. From (7.3) it is clear that the scalar product term will now completely determine the relative intensities of longitudinal and transverse polarized phonons. For a polycrystalline experiment at constant $|\vec{Q}|$ the average of (7.3) may be computed by considering all possible orientations of the reciprocal lattice vectors $2\pi\vec{\tau}$ with respect to $\vec{Q}$ in the scattering diagram of Fig. 7.7 [a]. A range of phonon wavevectors $\vec{q}$ are then excited subject to the momentum conservation condition in (7.3). Of the three acoustic branches of the dispersion curves, one will have longitudinal and two will have transverse polarization with respect to the direction of $\vec{q}$. The intensities of each will be determined by the angle θ between $\vec{q}$ and $\vec{Q}$ in Fig. 7.7(a) where

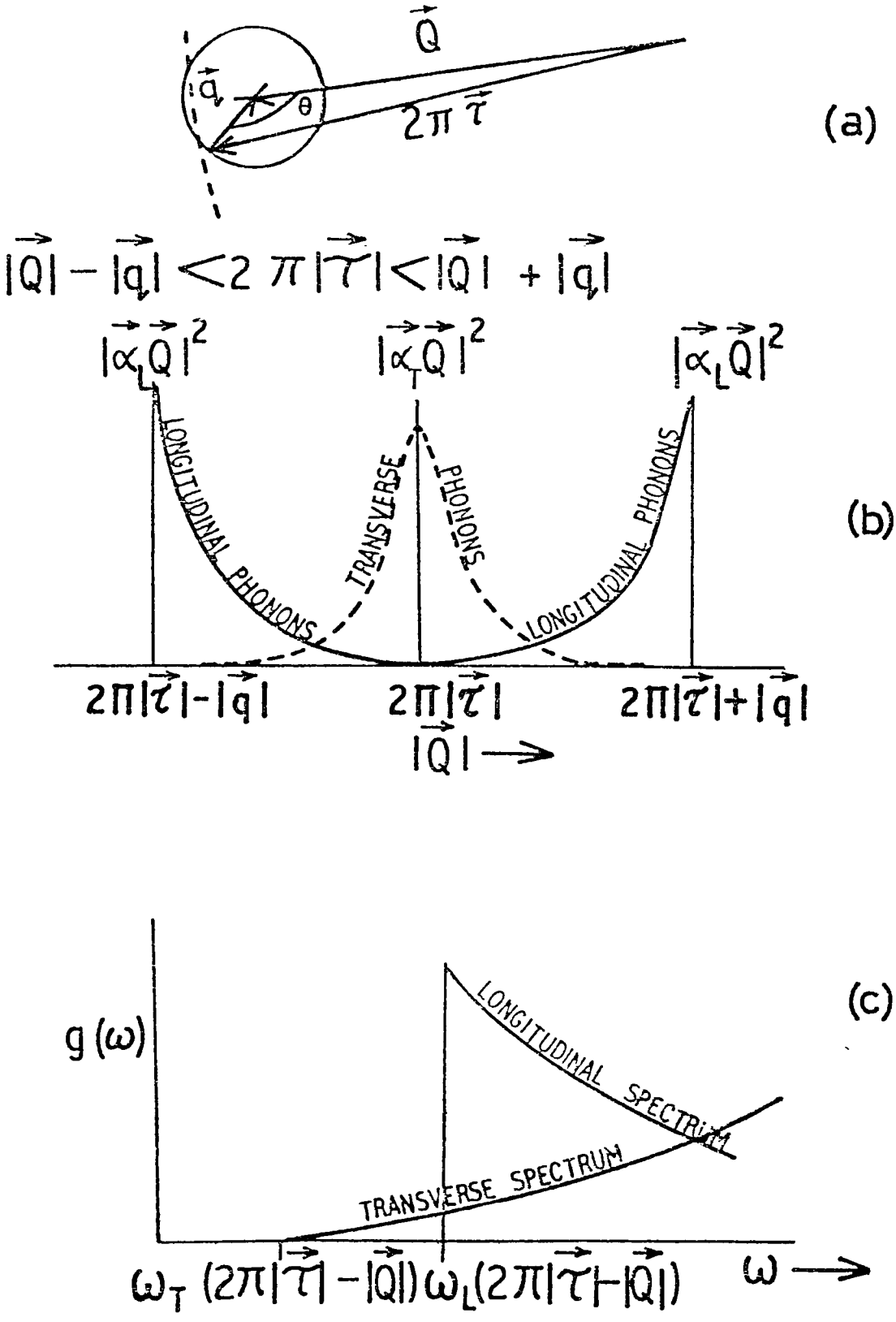

Fig. 7·7 Phonon excitations in a cubic monatomic polycrystal: (a) scattering diagram; (b) dynamical structure factors at constant $|\vec{q}|$ for LA and TA modes; (c) frequency spectra at constant $|\vec{Q}|$ for LA and TA modes.

$$\cos^2\theta = \frac{(2\pi|\vec{\tau}|)^2 - |\vec{Q}|^2 - |\vec{q}|^2}{2|\vec{Q}||\vec{q}|} \tag{7.4}$$

For longitudinal phonons the cross section will be proportional to $|\vec{Q}|^2\cos^2\theta$ and for transverse phonons, $|\vec{Q}|^2\sin^2\theta$. The $\cos^2\theta$ factor at constant $|\vec{q}|$ has a sharp cut-off at $|\vec{Q}|$ values

$$|\vec{Q}| = 2\pi|\vec{\tau}| \pm |\vec{q}| \tag{7.5}$$

whereas the $\sin^2\theta$ factor has a broad peak at

$$|\vec{Q}| = ((2\pi|\vec{\tau}|)^2 - |\vec{q}|^2)^{1/2} \simeq 2\pi|\vec{\tau}| \tag{7.6}$$

since $|\vec{q}|$ is usually much less than $2\pi|\vec{\tau}|$ (see Fig. 7.7(b)).

The implications for the energy spectrum of excited phonons are as follows. For constant $|\vec{Q}|$ the minimum value of $|\vec{q}|$ allowed in the neighbourhood of a particular lattice point is $2\pi|\vec{\tau}| - |\vec{Q}|$ for $|\vec{Q}| < 2\pi|\vec{\tau}|$. The transverse phonons have zero structure factor for this value of $|\vec{q}|$ since $\sin^2\theta$ is zero. As $|\vec{q}|$ increases on rotating $2\pi|\vec{\tau}|$ from the co-linear configuration (see Fig. 7.7(a)) the frequency and intensity of the transverse contribution to the spectrum increases continuously since $\omega_T(|\vec{q}|)$ is a rising function of $|\vec{q}|$ for acoustic vibrations. In contrast the longitudinal phonons have a maximum contribution at minimum $|\vec{q}|$ in the co-linear configuration which falls as $|\vec{q}|$ increases. The resulting frequency distribution derived at constant $|\vec{Q}|$ for a cubic monatomic polycrystal is shown in Fig. 7.7(c). Only one inelastic singularity is observed in the vicinity of each Bragg peak and this is the low frequency cut-off for LA phonons at which the direction of the phonon wavevector is defined since it is co-linear with the reciprocal lattice vector.

Such singularities have been observed by Cocking and Gurer in the time-of-flight spectra of polycrystalline tin and lead, both cubic systems [4, 5]. Full phonon dispersion curves were in fact available for both these systems since single crystals are readily obtained and the interest

of these authors was directed more towards the liquid phase in which the cut-offs were observed to persist.

In describing the coherent inelastic neutron spectrum of the simplest polycrystal a strong analogy with polyethylene has emerged. From the preceding analysis it appears that the LA contribution predominates in the averaged phonon spectrum because of the simple form of cross section expected for a monatomic lattice, in which the geometric phase factors do not appear. The persistence of the same phenomenon in a crystal such as polyethylene with twelve atoms in the unit cell may then be attributed to the high symmetry of the molecular basis. That is, it would appear from the calculations that the geometric factor in (7.1) does not interfere with the eigenvector product in its selection of LA modes. At the same time this 'elastic' part of the dynamical structure factor serves to enhance the intensity of acoustic phonons in the vicinity of a strong Bragg reflexion. And so the calculations indicate that the two primary components of the dynamical structure factor operate independently to the extent that the expression (7.1) could be regarded as a convolution of the elastic structure factor with the scalar product term in the eigenvectors. It is then a particular advantage to work in a $\vec{Q}$ region within the reciprocal lattice where the elastic structure factor is large at one point only as in this case the LA singularities can be clearly assigned. This condition is most readily achieved by the use of long wavelength neutrons.

What sort of systems can be profitably investigated by this technique? It is clearly of little profit to examine materials which can be obtained as single crystals since they can be fully investigated by triple axis spectrometry. For polymers this is rarely the case and frequently no more than one axis, the chain axis, can be defined in a bulk specimen. The advantages of time-of-flight techniques in their application to such specimens are twofold. The use of large solid angle detector banks is

particularly appropriate for neutron scattering studies of partially oriented materials. Moreover the long wavelengths employed are of the same magnitude as the interchain separation, which means that the Bragg reflexions associated with the lateral packing of the chains are prominent in the experimental $\vec{Q}$ region.

The choice of polymer for such studies is affected by the following considerations

[1] There must be a predominantly coherent cross section which restricts attention to deuterated or halogenated polymers.

[2] The symmetry of the molecular basis will be an important factor determining the prominence of singularities in the coherent spectrum, by analogy with polyethylene. Helical polymers, with an almost cylindrical distribution of atoms around the lattice points, will be particularly suitable.

[3] The presence of a suitable Bragg reflexion in the experimental $\vec{Q}$ region is a prime requisite.

[4] Specimens with a preferred chain orientation should be available.

Of readily accessible materials satisfying these points deuterated polyoxymethylene, polytetrafluoroethylene and polychlorotrifluoroethylene are immediate suggestions. For all of these polymers there is as yet no experimental information about phonons which propagate perpendicular to the chains, primarily because of the unavailability of fully oriented specimens. Investigation of these polymers by the technique described in this chapter should prove a fruitful enterprise and some significant results for polytetrafluoroethylene are reported in Chapter 11.

7.6 Discussion

The measurement of part of the LA branch in the [$\zeta\zeta$0] polarization at 298^{o}K provides the first anisotropic information about the interchain dispersion curves of polyethylene. It facilitates a demonstration of the anisotropy of the forces in a polymer crystal. This is provided by Fig. 7.8

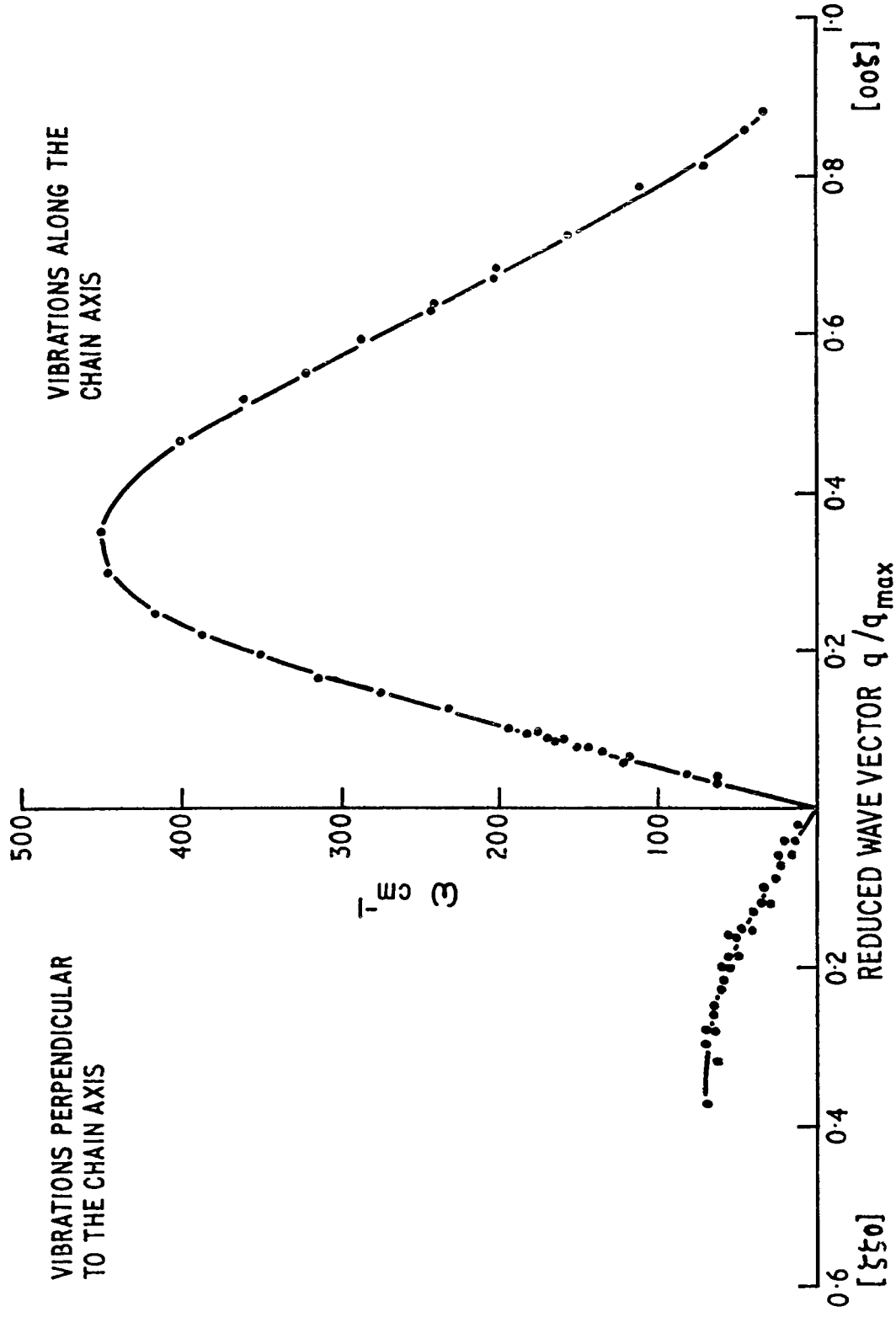

Fig. 7·8 Experimental dispersion curves for LA phonons propagating along [7] and perpendicular to the chain axis of D.P.E. at 298°K.

in which a comparison between these data and those reported earlier for intrachain phonons of [00ζ] polarization is effected [6, 7]. Both sets of data are for LA phonons and the reduced wave vector abscissa is used for clarity of presentation. A comparison of the acoustic velocities can be made from Fig. 7.8 after scaling down the left hand slope by a factor of 1.62. Elastic constants of 15 and 250×10^{10} dyne cm^{-2} for the [ζζ0] and [00ζ] directions at 298°K demonstrate the pronounced anisotropy of the force field in this polymer.

For orthorhombic polyethylene there are nine independent elastic constants and the constant measured here is in fact a compound of four of these (see 9.4.4.2). Since the experimental parameter is defined within an error of ±20% it is rather difficult to make conclusive comparisons with the various model predictions. Moreover the only room temperature model for which the relevant elastic constant is available is that of Tasumi and Shimanouchi used in the dynamical structure factor calculation. This figure of 17×10^{10} dyne cm^{-2} is within the experimental error (see Fig. 7.6). By contrast the model of Kitagawa and Miyazawa [8] based upon the 77°K structure predicts a value of 11.9×10^{10} dyne cm^{-2} which, as an upper limit for the room temperature constant, is well below the experimental figure.

Comparison of the elastic constant derived here with crystalline bulk moduli is again hampered by the fact that the latter reflects a total of nine such constants. However tensile elastic moduli are mostly dependent upon the magnitude of the elastic constants which relate to LA deformations (see 2.7) and so such a comparison although crude is not altogether insensitive. Bulk moduli measurements on polyethylene were discussed in 5.2.2 and the highest value of 8×10^{10} dyne cm^{-2} [9] for an 'average' tensile elastic modulus in the ab plane at 77°K is significantly lower than the neutron figure of 15×10^{10} dyne cm^{-2} measured at 298°K. The bulk figure is derived as a crystalline modulus by assuming a simple model [10] of the

composite polymer in which distinct amorphous and crystalline phases 'sandwich' and using this to interpret viscoelastic phenomena in c-oriented polyethylene. Since elastic constants from inelastic neutron scattering unambiguously characterize the microcrystal the discrepancy just noted may have some bearing upon the applicability of this model. More microscopically derived elastic constants are required before any definite conclusions are possible on this issue, which is further discussed in 10.4.1.

7.7 Summary

Neutron scattering studies of c-oriented D.P.E. in which the momentum transfer vector was restricted to the basal plane of the specimen are reported. Coherent inelastic singularities in the time-of-flight spectra are located and an acoustic dispersion curve assembled. Calculation of the dynamical structure factors illustrates the predominant contribution of LA phonons with [ζζ0] polarization in the isotropically averaged phonon spectrum. An elastic constant of $15\pm3\times10^{10}$ dyne cm^{-2} is derived from the acoustic slope at $298^{o}K$ providing the first anisotropic information about the interchain dispersion curves of a polymer from neutron scattering.

The physical basis of such observations is discussed and a simple analogy drawn. The persistence of anisotropic contributions within the isotropically averaged phonon spectrum is seen as a remarkable consequence of the anisotropy of the polyethylene unit cell and the high symmetry of the molecular basis therein, both of which act to simplify the dynamical structure factors. The extension of this technique to other partially oriented materials is discussed and some general principles established to aid in the choice of suitable systems.

Comparison of the [ζζ0] data with earlier measurements along [00ζ] is used to highlight the anisotropy of the force field of polyethylene. Further comparisons of the measured acoustic slope with calculated

dispersion curves are used to test the existing models. Finally the elastic constant obtained is contrasted with crystalline moduli derived from mechanical measurements and found to be at least twice as large.

References

[1] M. Tasumi and T. Shimanouchi, J. Chem. Phys., 43, 1245 1965.

[2] D.I. Marsh, Ph.D. thesis, University of London 1971.

[3] P.A. Egelstaff, 'Thermal neutron scattering', Academic Press 1965.

[4] S.J. Cocking and Z. Gurer, 'Neutron Inelastic Scattering', IAEA, Vienna, 1, 237 1963.

[5] S.J. Cocking, D.Phil. thesis, University of London 1967.

[6] L.A. Feldkamp, G. Venkataraman and J.S. King, 'Neutron Inelastic Scattering', IAEA, Copenhagen, 2, 159 1968.

[7] L.A. Feldkamp, Ph.D. thesis, University of Michigan 1969.

[8] T. Kitagawa and T. Miyazawa, Jap. Polym. J., 1, 471 1970.

[9] C.P. Buckley, D.Phil. thesis, Oxford University 1972.

[10] M. Takayanagi, K. Imada and T. Kajiyama, J. Poly. Sci. C, 15, 263 1966.

Chapter 8

PREPARATION AND CHARACTERIZATION OF FULLY ORIENTED DEUTEROPOLYETHYLENE

8.1 The quest for bulk anisotropy

The quality and extent of mechanical and spectroscopic studies of polyethylene have long been impaired by the unavailability of bulk specimens reflecting the full anisotropy of the unit cell. Uniaxial orientation of the crystallites is easily attained as in the last chapter where a c-oriented specimen was prepared by hot drawing. Some three dimensional orientation can be achieved by the application of biaxial stress to the isotropic polymer, as in rolling. Here the c-axes orient in the direction of maximum tensile stress and crystallographic a and b poles become defined, although invariably in a twinned configuration.

In a detailed wide angle X-ray diffraction study of the effect of rolling on sample texture, Hay and Keller have shown that polyethylene films actually achieve a full single crystal texture under the rollers, which transforms reversibly to the twin on release of pressure [1, 2]. Related studies of low density, branched polyethylene by the same authors indicate that a similar texture is instituted on annealing the biaxially oriented material [1]. In this work drawn polyethylene films were rolled in the draw direction and annealed between mica plates over a wide temperature range causing a series of textural changes. At first twinning relaxes to give a single crystal texture but at higher temperatures the a and c axes randomize about b, prior to a complete loss of orientation at the melting point. A contraction of the specimen length also occurs with increase of temperature, causing a loss of c-axis orientation in the early stages and particularly in the fully anisotropic texture.

This aspect was considered by Bowden and Young who developed a special procedure for the annealing [3, 4]. Rhodes and Stein [5] had annealed

oriented specimens with a constraint on the length, which reduced crystallite reorientation and the former authors employed such constraints in the preparation of single crystal texture polyethylene without loss of c-orientation. Biaxially oriented polyethylene was prepared by extrusion, shaped into discs and contained within a pyrophylite washer in a die. Annealing just below the melting point at very high pressures (about 4 kbar) produced a specimen of single crystal texture in which a and b poles were defined with a mosaic of around 20° FWHM in the basal plane. The undoubted secret of this method is the pyrophylite washer which acts as a pressure-tight seal, constraining the specimen shape and so eliminating the loss of c-orientation observed in earlier work. In the final specimen crystallographic a-axes orient perpendicular to the disc and the chains lie in the plane (along Z in Fig. 8.4).

Low angle X-ray diffraction and electron microscopy [3] indicate that the lamellae are oriented approximately perpendicular to the chain direction in the bc plane of these specimens and tilt by angles of up to 30° in the ac plane (Fig. 8.1). Fracture studies show that cleavage in the bc plane is much easier than in any other direction [3, 4]. Bowden and Young proceeded to identify the fold direction as [100] on the basis of these observations, in agreement with the conclusions of Bank and Krimm for bulk crystallized polyethylene [6]. In Fig. 8.1 the model proposed for the lamellar crystal structure is illustrated, where it becomes clear that fraction in other than the bc plane involves cleavage of the carbon chains and will be impeded [3].

In this work deuteropolyethylene specimens of single crystal texture were produced for employment in neutron scattering studies. The method of Bowden and Young was developed by varying the conditions of temperature and pressure to optimize the mosaic spread, which was a critical factor affecting the extraction of anisotropic dynamical information.

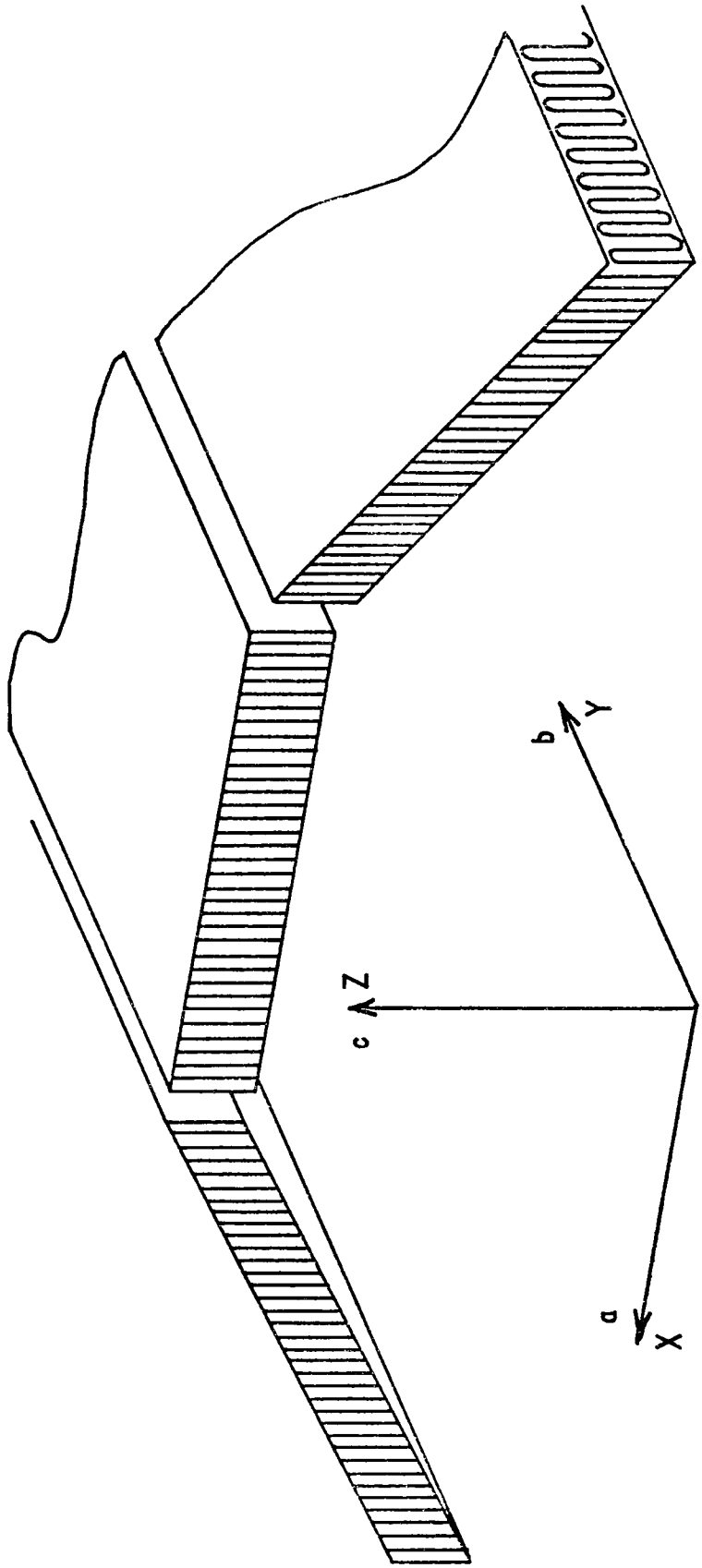

Fig. 8·1 Lamellar structure of single crystal texture polyethylene [3]

8.2 Experimental method

The preparation of fully oriented D.P.E. was facilitated by Dr. J.S. King, Nuclear Engineering Department, University of Michigan who provided the specimen of stretch-oriented D.P.E. on which the measurements of acoustic chain phonons were performed [7]. This specimen was prepared by stretching 500% under infrared heat and neutron diffraction from [002] indicated a c-mosaic of 8° FWHM. An isotropic distribution of a and b poles was also inferred.

For the annealing process two dies were constructed from mild steel to withstand pressures of up to 3 kbar. In design they consisted of a $1\frac{1}{2}$" diameter cylinder recessed to contain a closely fitting cylindrical piston of 1" diameter, through which the pressure was applied to the sample. The die set was held between heated plattens on a hydraulic press capable of applying loads of up to 200 tons. Copper-constantan thermocouples were attached to the dies through base plates so that the sample temperature could be measured and controlled to $\pm 2^{\circ}$C.

Sample treatment was in two stages each of which contributed to the final orientation. First a three dimensional orientation was induced by application of biaxial stress. This was accomplished by rolling the stretch-oriented D.P.E. with the direction of advance in the draw direction. Specimen thicknesses were reduced from 0.017" to 0.012", a reduction of 30%. Further rolling caused crazing and general deterioration of the sample. Characterization by X-ray diffraction revealed a twin texture for the a,b poles and a slight increase in c-mosaic. A series of 0.9" diameter discs were cut out of the rolled specimen in preparation for annealing. These discs were taken in pairs and placed inside a circular pyrophylite clay washer within the lower die, as outlined in Fig. 8.2. The dieset was then compressed to the required pressure (<3 kbar) and heated to a temperature below the melting point at that pressure. After annealing the pattern assembly was cooled by water injection with

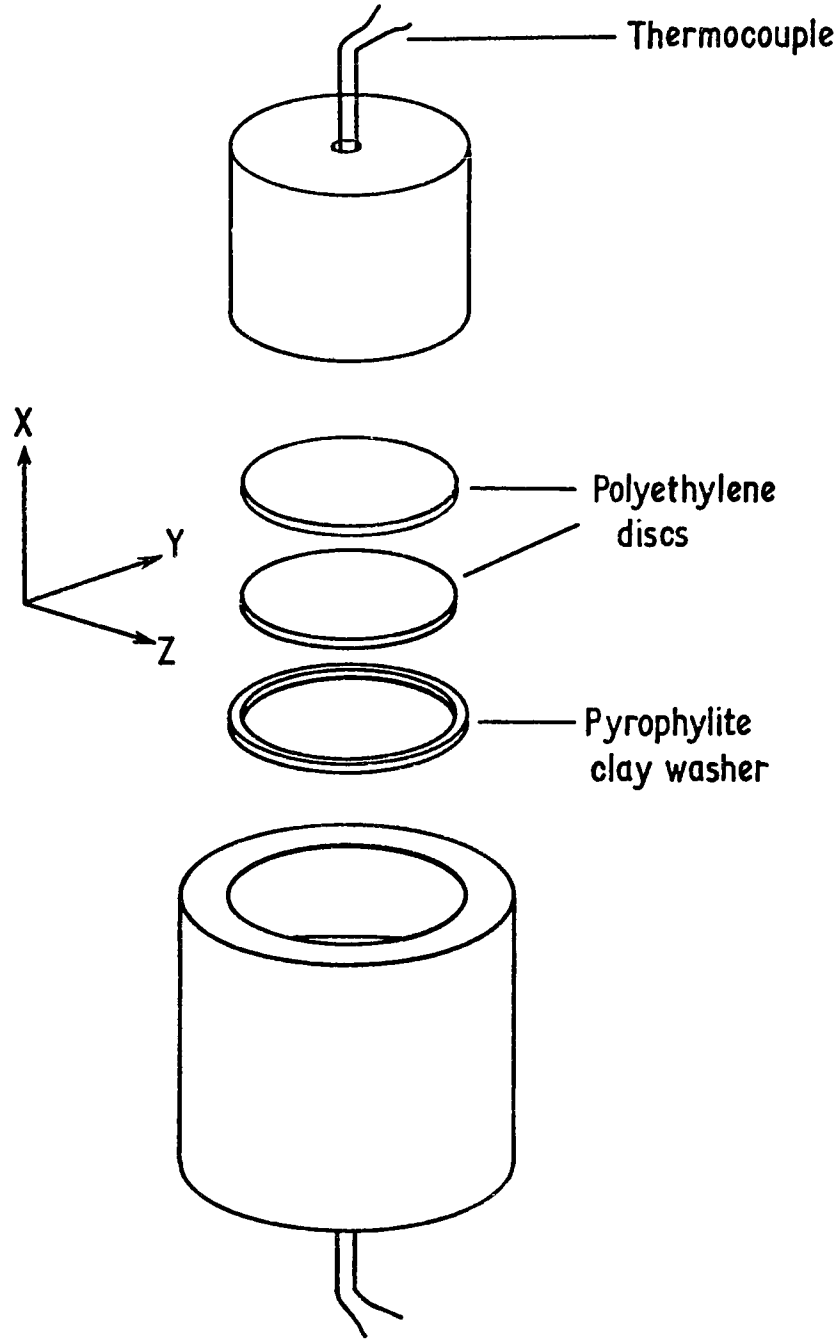

Fig. 8·2 High pressure annealing assembly

the pressure maintained and the die set opened to recover the oriented specimen.

The three variables - temperature, pressure and annealing time - were systematically varied to optimise the mosaic spread of a and b poles in the product, characterized by flat plate X-ray photographs. Temperature proved to be the most difficult factor since chance melting with complete loss of orientation cost much in time and labour. A load of 11 tons was finally chosen, corresponding to a pressure of 2.1 kbar on the 0.9" diameter disc. Annealing at 185±3°C for 15 minutes gave the best results with a sample mosaic in the basal plane of as low as 14° FWHM. At this pressure the melting point was 190±3°C which is in good agreement with a value of 191°C found by Baer and Kardos [8] for N.P.E., implying that the pressure on the sample has been correctly estimated from the load and disc area. The final orientation was increased as the temperature of annealing approached the melting point and so the ultimate choice of temperature was the highest value possible, short of actually melting the specimen.

Specimen densities were measured by weighing in ethanol and found to be around 1.10 gm ml^{-1} which corresponded to a crystallinity χ_M of about 75%. In appearance the discs were yellowish to light brown, although comparison with the drawn starting material showed that very little additional degradation had occurred on annealing. A sample volume of about 1 ml is desirable for triple axis spectrometry and so the annealing process was repeated several times with a view to assembling the oriented discs into a suitable specimen.

8.3 Characterization by X-ray and neutron diffraction techniques

As the crystal structure of polyethylene is well known, information about the orientational distribution of crystallites in a bulk specimen is readily derived by diffraction methods. In this work three techniques

were applied at different stages. Initial development of the annealing process was assisted by taking X-ray flat plate photographs, which gave a rapid albeit qualitative indication of the anisotropy achieved. Later studies of the optimal specimens employed four-circle X-ray diffractometry to give the full polar distribution of crystallite orientations. Finally a two axis neutron diffractometer was used in the assembly and characterization of a sample with dimensions suitable for triple axis neutron spectrometry.

8.3.1 X-ray flat plate diffractometry

In this method monochromatic X-rays are diffracted by the specimen and recorded on a flat photographic plate as illustrated schematically in Fig. 8.3. In the reciprocal space formalism the condition for Bragg reflexion is

$$\vec{k}' - \vec{k} = \vec{Q} = 2\pi\vec{\tau} \qquad (8.1)$$

where $\vec{k}$ and $\vec{k}'$ are the incident and outgoing wave vectors, $\vec{Q}$ is the momentum transfer and $2\pi\vec{\tau}$ is a vector in the reciprocal lattice. The range of $\vec{k}$ and $\vec{k}'$ is restricted in a flat plate experiment by the fixed sample and detector orientation and so for a single crystal (8.1) will not be satisfied for most lattice vectors.

For a polycrystal all possible relative orientations of $\vec{Q}$ and $2\pi\vec{\tau}$ are present, so that each point on the reciprocal lattice becomes a sphere. Now a very useful property of the reciprocal lattice is its relationship to the diffraction pattern which is its spatial Fourier transform. The transform of a point lattice is another point lattice and the transform of a set of spheres is a set of circles. Hence whereas a single crystal gives layer lines of discrete point reflexions, the diffraction pattern of a polycrystal is a series of concentric circles, the so-called Debye-Scherrer rings. Here outgoing X-rays fall on cones which are projected

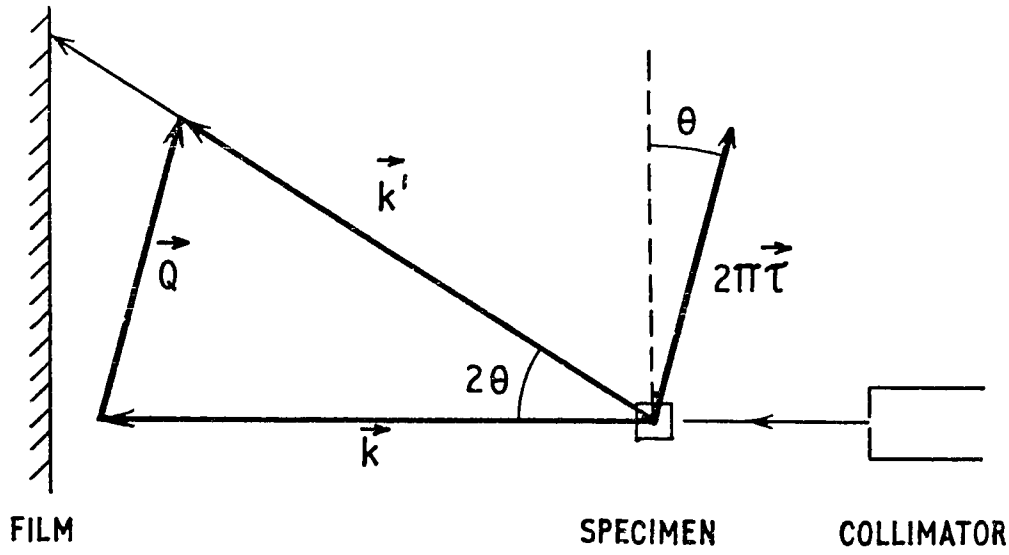

Fig. 8·3 Debye-Scherrer X-ray camera (schematic)

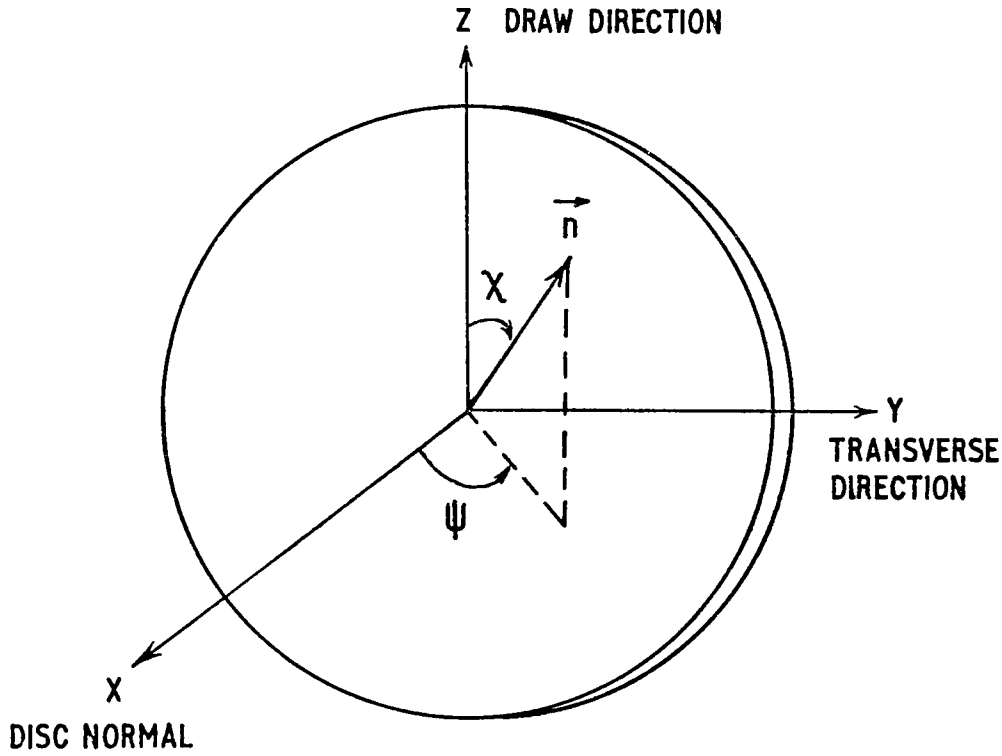

Fig. 8·4 Specification of an arbitrary vector in the sample framework.

onto the flat detector plate as concentric rings with radii characteristic of the reflecting planes.

In partially oriented polymers the reciprocal lattice points are usually delocalized to the extent that incomplete Debye-Sherrer rings appear for several reflexions. When the mosaic is large enough sufficient information is available from two or three flat plate photographs to define the sample anisotropy. The locus of $\vec{Q}$ can be inferred from Fig. 8.3 and it is clear that the directional spread of reciprocal lattice vectors perpendicular to $\vec{k}$ will in large part determine the reflexions observed. Intensity distribution on Debye-Scherrer rings will be related to the radial distribution of planes which are almost parallel to $\vec{k}$, inclined by their respective Bragg angles which must be small compared with the mosaic spread. When this condition applies, qualitative information about the sample anisotropy can be obtained from the changes in the diffraction pattern with sample orientation. In polyethylene Hay and Keller have shown that photographs taken in three orthogonal directions are sufficient to define the bulk texture and give a qualitative estimate of the mosaic spread [1].

Diffraction pictures were obtained using an Euraf T.N.20 X-ray generator which provided a point collimated beam of nickel filtered CuK_{α} radiation. Exposure times were between two and four hours and the photographic film was mounted 5 cm behind the sample. It is convenient to define a set of axes with respect to the macroscopic sample so that X is perpendicular to the disc and Y in the plane of the disc perpendicular to Z, the draw direction. An arbitrary vector $\vec{n}$ in the sample framework can then be specified by the polar angles ψ and χ as in Fig. 8.4. X-ray photographs for the uniaxially oriented starting material and the annealed product taken with $\vec{k}$ along the macroscopic X and Z directions are shown in Fig. 8.5.

For the drawn starting material with the beam along Z, Debye-Scherrer rings for [110] and [200] are observed showing that the crystallites are

[a] DRAWN STARTING MATERIAL

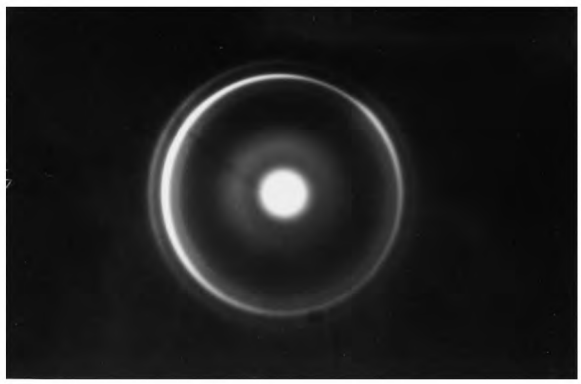

$\vec{k}$ along Z

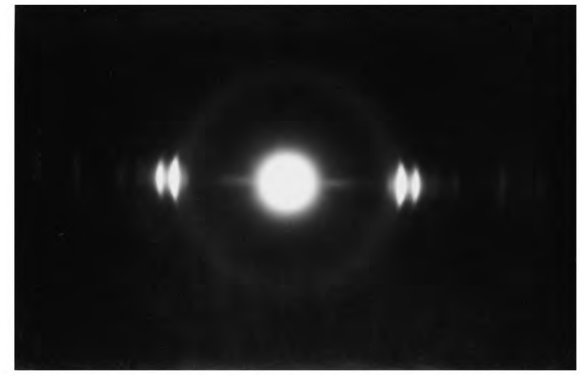

$\vec{k}$ along X

[b] HIGH PRESSURE ANNEALED MATERIAL

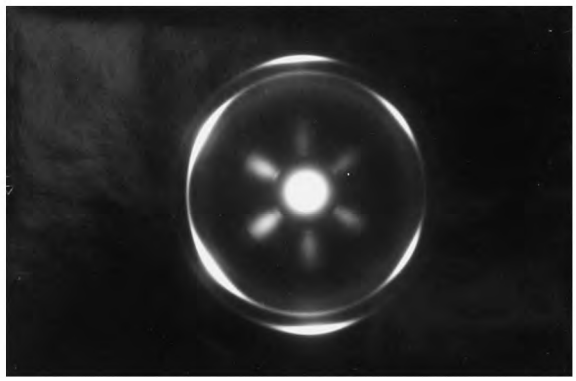

$\vec{k}$ along Z

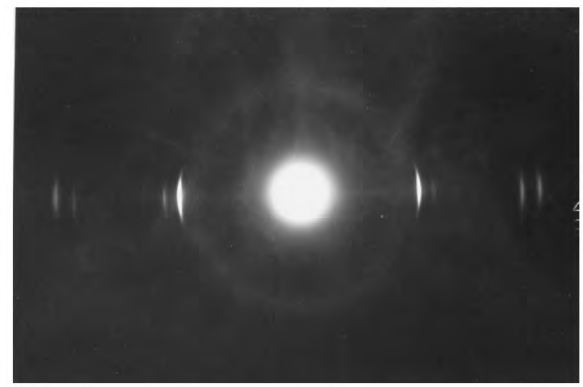

$\vec{k}$ along X

Fig. 8·5 X-ray flat plate photographs taken with $\vec{k}$ along the X and Z directions of the original drawn D.P.E. and the high pressure annealed material of single crystal texture.

randomly oriented in the basal plane of the specimen. The observed deviations from a completely uniform polar intensity distribution in Fig. 8.5(a) are attributable to the differing flight paths through a rectangular specimen. In the perpendicular configuration these reflexions are distributed on arcs which represent the distribution of [110] and [200] poles about the draw direction, previously determined as 8° FWHM. The relative intensity of [110] and [200] resembles the 4:1 ratio found in the polycrystal (see 6.3).

On rolling some preferred orientation of the [hk0] planes about the c-axis is achieved. Although the flat plate pictures closely resemble those for the drawn material there is evidence of anisotropy in the intensity distribution on the Debye-Scherrer rings obtained with $\vec{k}$ along Z for [110] and [200] planes. This is confirmed by the X-ray four-circle diffractometry reported in the next section, which establishes a hexagonal distribution of these two poles in the basal plane from quantitative intensity measurements (Fig. 8.7(b)). Hay and Keller interpret this as the result of twinning in which each a-pole has two related poles at $\pm 60^{\circ}$ to the original direction.

Annealing the biaxially oriented material at 185°C and 2.1 Kbar for 15 minutes completes the process of orientation. Comparison of Fig. 8.5(a) and 8.5(b) highlights the success of the annealing operation which induces full anisotropy. The Debye-Scherrer rings are reduced to arcs, two for [200] and [020] and four for [110] in the configuration with $\vec{k}$ along Z. These arcs qualify the mosaic in the basal plane. Furthermore the [200] reflexion is completely suppressed when $\vec{k}$ is along X, which could only be the case if the beam is actually looking along the a-direction. The observed reduction in intensity and breadth of [110] in this configuration is caused by the anisotropy perpendicular to the chains which reduces the number of crystallites satisfying the geometric conditions for Bragg reflexion onto the flat plate, illustrated in Fig. 8.3. When the beam is incident along

Y (not shown in Fig. 8.5), [110] and [200] arcs appear with equal intensity and [020] disappears in the diffraction pattern of the annealed specimen. Since $\vec{Q}$ moves mainly in the XZ plane here, [200] will be enhanced, [110] suppressed and [020] should disappear altogether, in agreement with the observations.

Characterization of sample texture by taking X-ray flat plate photographs greatly accelerated the process of optimizing the conditions for annealing. Single crystal texture was readily distinguished by a four point pattern for [110] with $\vec{k}$ along Z and the absence of [200] in the configuration with $\vec{k}$ along X. A qualitative indication of the mosaic sufficient for comparative purposes was also provided by the size of the Debye-Scherrer arcs. As previously stated the mosaic in the basal plane decreased as the annealing temperature approached the melting point. The quality of biaxial orientation, i.e. in the twinned form, proved to be another important factor determining the final mosaic after twinning was removed. For this reason rolling was continued until the specimen reached the stage of imminent physical deterioration. The best samples possessed a mosaic spread of 10-20^{o} FWHM for a and b poles in the basal plane, achieved with minimal relaxation of the c-orientation which was still defined within 10^{o} FWHM.

8.3.2 Four-circle X-ray diffractometry

A full polar distribution for [hkl] planes can be obtained only when the Bragg condition is satisfied for all sample orientations and the intensities recorded. Practically this is achieved by setting the Bragg angle and rotating the sample over a sphere. This is equivalent to rotating the $\vec{Q}$ vector in the sample framework and measuring intensities $I_{hkl}(\psi,\chi)$ for the whole range of ψ and χ with $\vec{k}$ and $\vec{k}'$ fixed. Intensity contours are then constructed for [hkl] which are related to the polar distribution of crystallites in the macroscopic specimen.

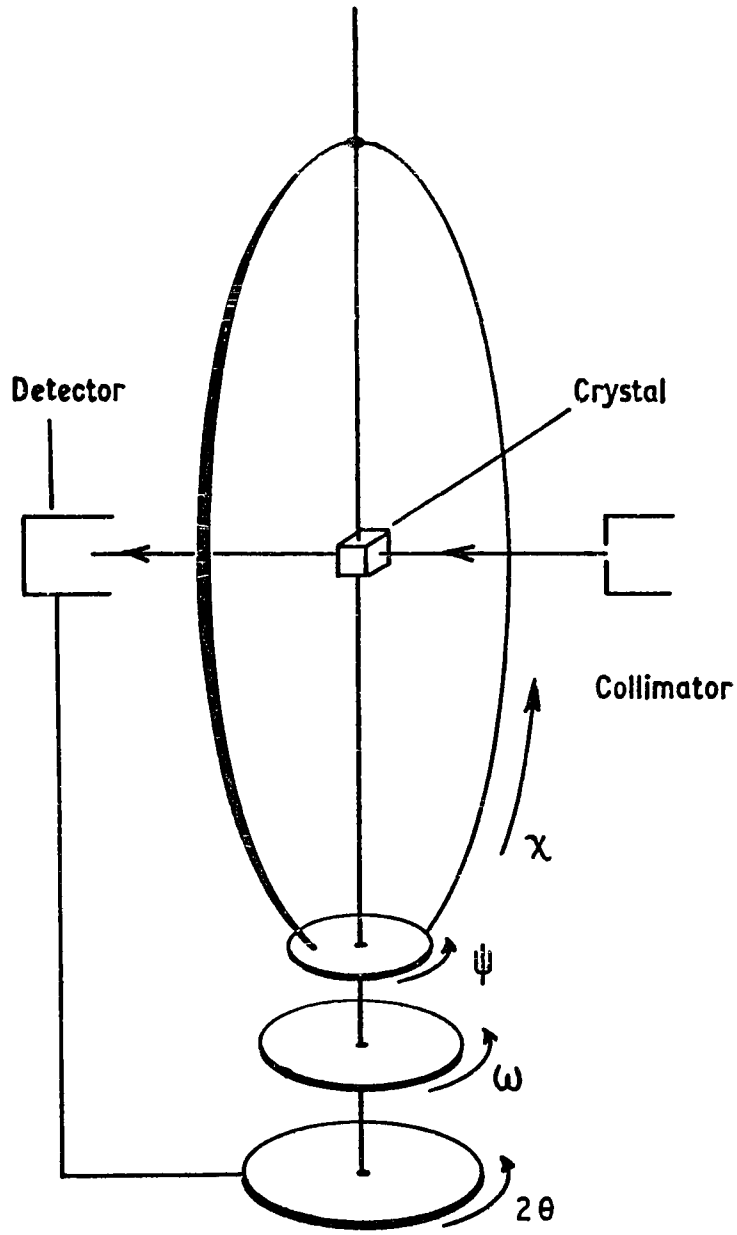

Fig. 8·6 Schematic illustration of the four-circle x-ray diffractometer.

Pole figures were obtained using a Hilger Watts computer controlled four-circle diffractometer available in the Chemical Crystallography Laboratory, Oxford University [9]. Incident CuK_α X-radiation was diffracted from a mobile specimen and detected by a scintillation counter. The specimen was mounted on a goniometer which could be automatically rotated about three axes at the command of an on-line PDP8 computer. Four angular variables defined the relative orientation of $\vec{k}$, $\vec{k}'$ and the specimen, as shown schematically in Fig. 8.6. Of the four allowed circles of rotation, θ and ω were coincident and in the scattering plane, whereas ψ and χ defined the goniometer orientation with respect to this plane. As the polyethylene specimens were always mounted with the draw direction vertical, ψ and χ take on the same meaning as they have in Fig. 8.4.

Cubic specimens of 1 mm edge were cut from the annealed material, attached by amorphous glue to the end of a glass fibre and mounted on the goniometer with the chain axes vertical. Zero values of ψ and χ were determined by identifying two strong reflexions, usually [200] and [020], and rocking the angles to maximize the scattered intensity. Pole figures were derived by programming the PDP8 to step ψ and χ in increments $0<\psi<360^\circ$, $0<\chi<90^\circ$ with θ and ω set to the Bragg angle for [hkl] planes. In this way the vector $\vec{Q}$ was constrained to move in a spiral about a hemisphere in the reciprocal lattice with radius equal to $2\pi\vec{\tau}$ for the reflexion [hkl]. Scattered intensity was then directly related to the polar distribution of [hkl] in real space and could be used to construct a contour map as a function of ψ and χ [10].

Pole figures for drawn, rolled and annealed D.P.E. are shown in Figs. 8.7 and 8.8 and were obtained with the assistance of Dr. R.W. Gray, Oxford University Engineering Department. Intensity contours represent percentages of the maximum intensity of the given reflexion. Projections of the spherical distribution onto a flat surface are presented for convenience. As the c-orientation is so good, pole figures over the full range of χ group

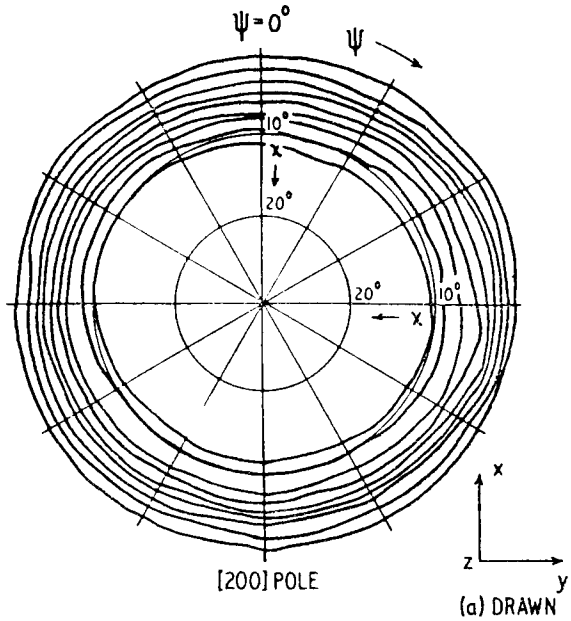

[200] POLE

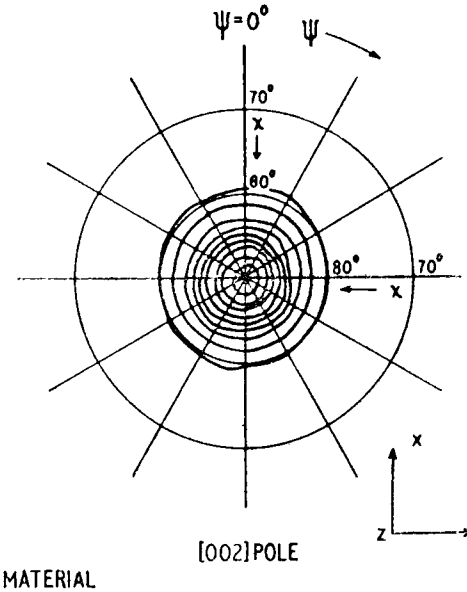

[002] POLE

(a) DRAWN STARTING MATERIAL

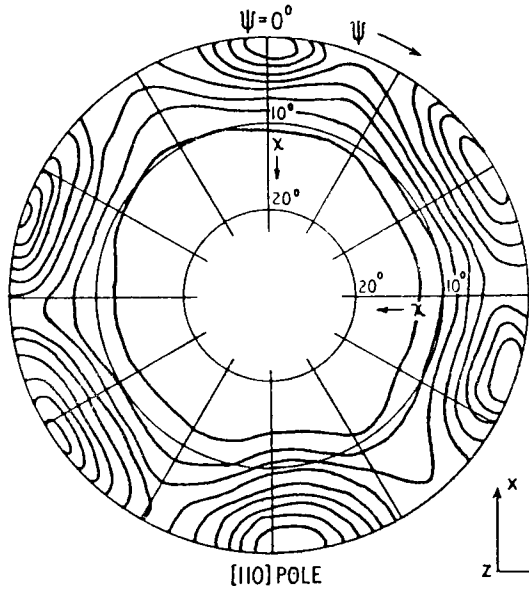

[110] POLE

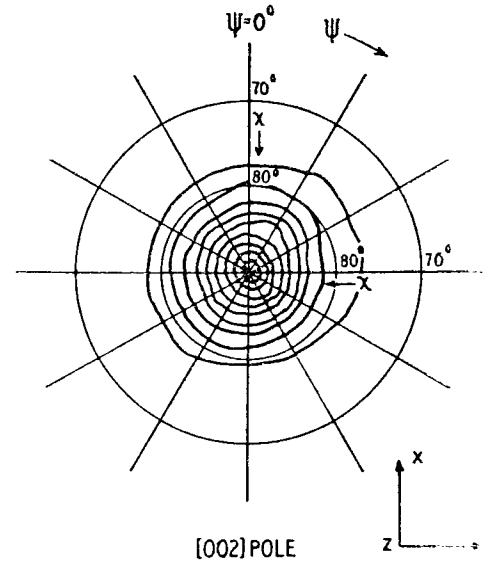

[002] POLE

(b) BIAXIALLY ORIENTED ROLLED MATERIAL

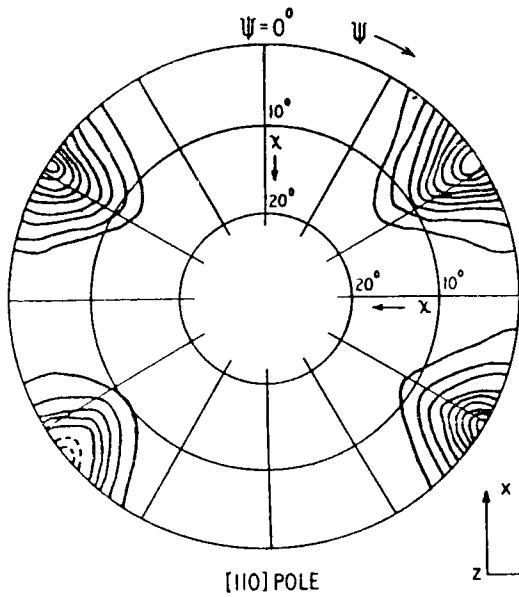

[110] POLE

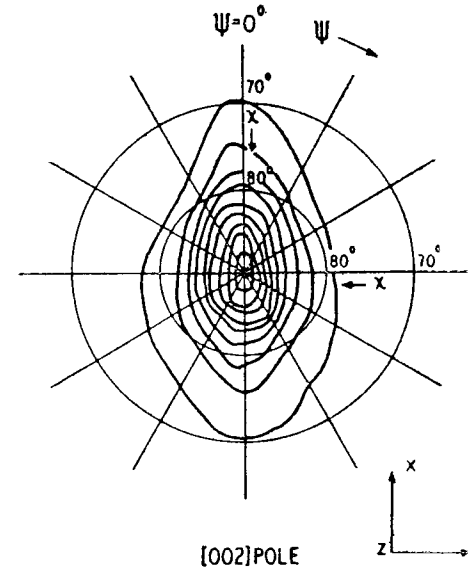

[002] POLE

(c) HIGH PRESSURE ANNEALED MATERIAL OF SINGLE CRYSTAL TEXTURE

Fig 8·7 POLE FIGURES FOR DRAWN, ROLLED AND ANNEALED D.P.E. SHOWING THE DEVELOPMENT OF ORIENTATION ALONG AND PERPENDICULAR TO THE CHAIN DIRECTION.

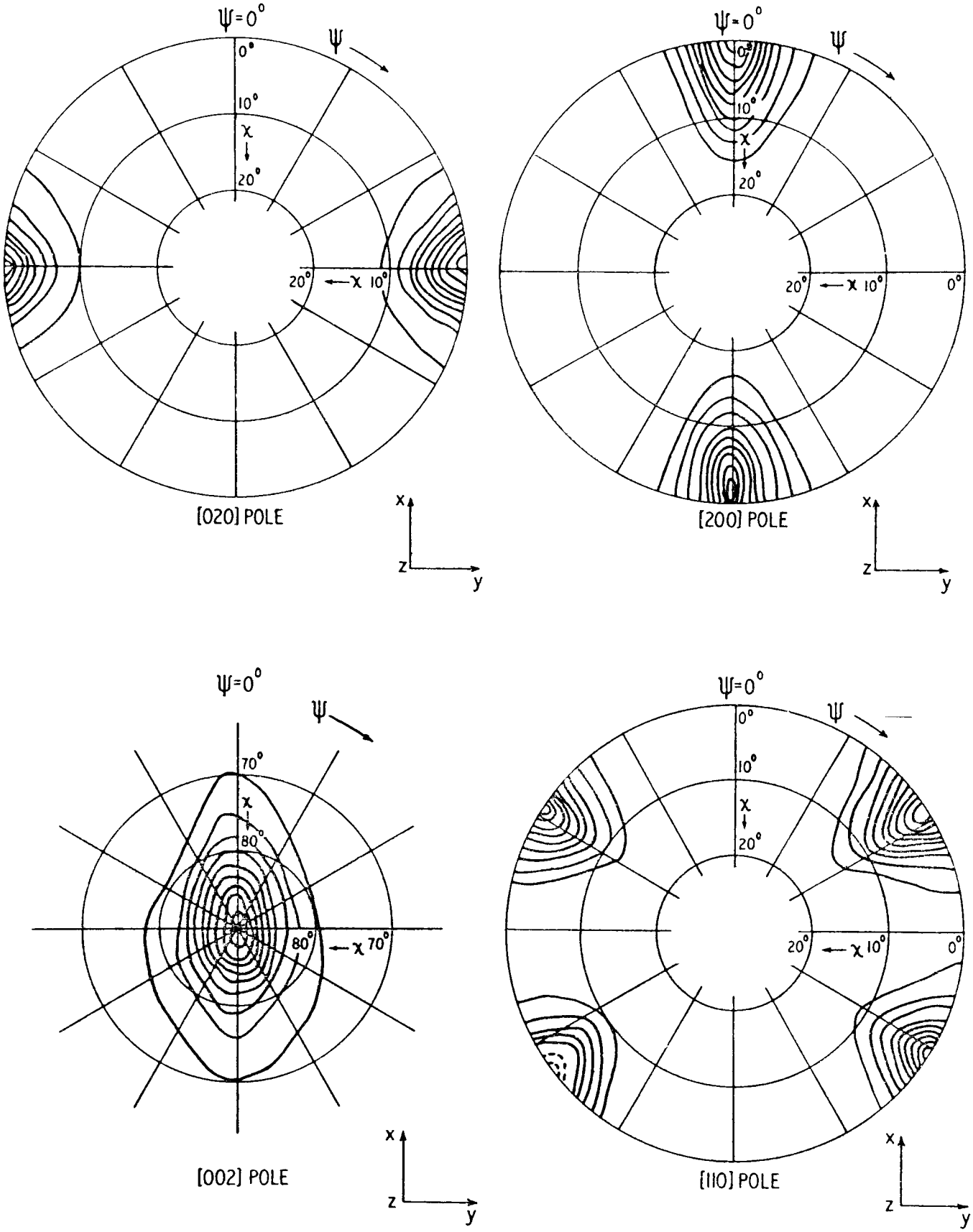

Fig. 8 8 POLE FIGURES FOR ANNEALED D.P.E. OF SINGLE CRYSTAL TEXTURE

the contours too closely and so only a limited portion of the reflexion sphere is projected. The contours are plotted from 10% to 90% of the maximum intensity and a good estimate of the mosaic FWHM is obtained from the dimension of the 50% contour. In Fig. 8.7 the three stages of orientation are unambiguously characterized. For the drawn material [hk0] planes show no preferred orientation perpendicular to the chain axis, rather giving rise to a series of concentric rings on the pole figure as shown in Fig. 8.7(a) for [200]. By contrast [002] poles are aligned about the Z axis within 8° FWHM. Rolling has little effect upon the [002] pole figure but substantially changes the orientation perpendicular to Z as is evident from Fig. 8.7(b). A six point pattern emerges for [110] superimposed upon a still sizeable isotropic component, which explains the persistence of a Debye-Scherrer ring in the flat plate picture. This hexagonal polarity is common to all [hk0] reflexions and it is well established that it arises from twinning of a single crystal texture so that each set of planes has a twin relative at $\pm 60^{\circ}$ to the original direction [1, 2, 3]. Twinning is removed on annealing and the full single crystal texture of Figs. 8.7(c) and 8.8 is achieved. A close analogy with Fig. 8.5(b) emerges with [110] adopting four poles and [200] and [020] two opposite poles in the basal plane. Scrutiny of the [002] pole figure infers that there are two preferred chain orientations 4° apart in the XZ plane. This doublet profile has a FWHM of 12° compared to 8° for the orientation function in the YZ plane, which indicates some overall loss in chain alignment on annealing. An average c-mosaic of 10° may be compared with the figure of 8° for the starting material. By contrast the mosaic of [hk0] poles in the basal plane is 14° as derived from the 50% contours. These parameters varied from disc to disc and the data of Figs. 8.7 and 8.8 represent about the best orientation achieved.

Four-circle diffractometry provided an excellent quantitative description of the crystallite orientation in single crystal texture D.P.E. However the information obtained applied to only a $1mm^3$ volume of the bulk specimen, and since samples were far from homogeneous the

texture varied across the specimen. In selecting the best discs for triple axis experiments the technique of neutron diffraction was preferred since by sampling over the whole specimen a better estimate of the overall orientation was achieved.

8.3.3 Two-axis neutron diffractometry

Neutron diffraction data were obtained using the Tas IV two-axis neutron diffractometer at A.E.K. Risø, Denmark. Wavelength and zero angle calibration were achieved by a least squares fit to the observed peak positions in the diffraction pattern of alumina. In the experiments on D.P.E. an incident neutron wavelength of 2.35 Å was provided by a zinc monochromator.

The choice of annealed discs for inclusion in the final specimen was affected by two criteria:

[1] The mosaic of [hk0] reflexions in the basal plane

[2] The intensity of Bragg reflexions in a particular sample compared with the level of background scattering.

Both these parameters were quantified for each disc by setting the scattering angle for reflexion from [hk0] and rocking the specimen in the scattering plane with the Z axis vertical. In Fig. 8.9 such data are shown for [110] as a plot of normalized counts against polar angle ψ, from which the mosaic and peak to background ratios can be estimated. The most striking feature about the two sets of data presented is the different background level observed when the peaks are normalized to the same intensity. Integration of these peaks less the background gave an estimate of the 'single crystal content' of the bulk specimens when compared to the total integrated intensity for $0<\psi<360^{\circ}$. A parameter α can be defined as

$$\alpha = 400 :: \frac{\text{Integrated peak area}}{\text{Total area}} \%$$

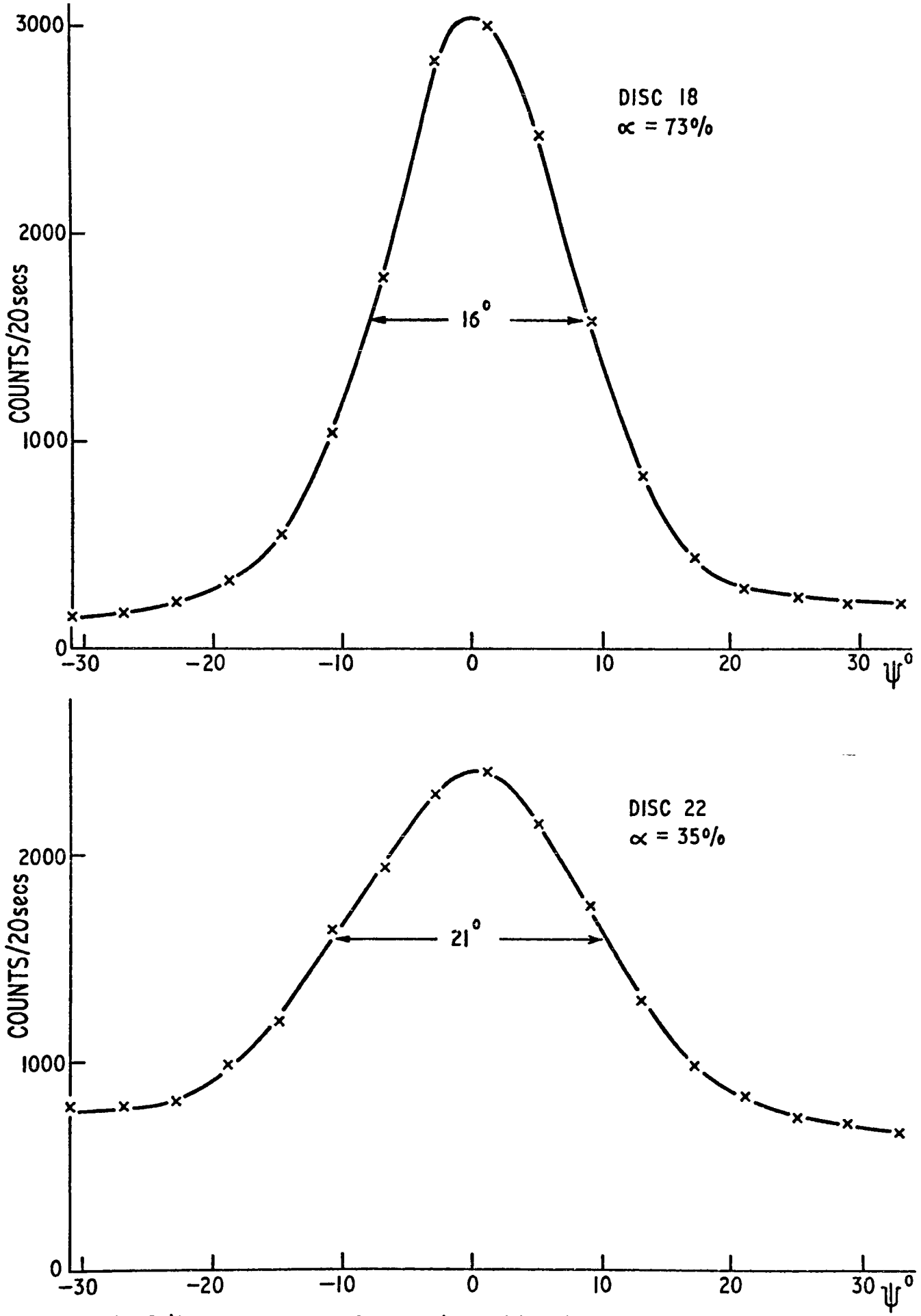

Fig. 8·9 [110] ψ – rocking curves for superior and inferior specimens of high pressure annealed D.P.E.

where, in the case of [110], there are four poles for $0<\psi<360^{o}$.

Any factor which induces an isotropic contribution to the diffraction pattern will cause a reduction in α. Since 25% of all the samples was amorphous a sizeable proportion of isotropic scattering is expected, both from the amorphous regions and from the incoherent component of the total scattering cross section. This contribution should be roughly constant since density variations from sample to sample were minimal, and an upper limit to α of about 75% is expected. Hence the value of 73% for the 'single crystal content' of the superior disc in Fig. 8.9 represents about the highest attainable figure.

What factors then determine the observed variation of this parameter, which in the case of the inferior disc reduces to a proportion of one third? The answer lies in the pronounced $\vec{Q}$ dependence of the background level in this case. It becomes clear from this that a large fraction of the crystallites are in fact still randomly oriented in some of the discs. Such samples behave as a compound of 'single crystal', 'polycrystal' and 'amorphous' phases and in the construction of the final specimen it was necessary to consider not only the mosaic quality, but also the proportion of the first phase in each disc.

Four discs were selected on this basis and assembled in an aluminium frame. The relative orientation of the component discs was adjusted to align the chain axes. This was effected by maximizing the scattered neutron intensity from [110] in a systematic manner. Final sample characteristics are related to the properties of the component discs in Table 8.1. Mosaic spread was 10^{o} FWHM about the chain axis and 17^{o} FWHM in the basal plane. The final value of α was 72%, which was very satisfactory considering the size of the amorphous content. Although the sample weighed only half a gram the count rate from [110] on the triple axis spectrometer was 4,500 c.p.s., which was deemed sufficient for phonon measurements.

Table 8.1 Characteristics of the annealed discs selected for assembly into the final sample of single crystal texture D.P.E.

Disc	Mosaic	α	Weight
1	16.6°	66%	0.117 gm
2	15.5	80	0.100
3	16.8	73	0.133
4	17.8	65	0.134
Total	17.0	72	0.484

References

[1] I.L. Hay and A. Keller, J. Mat. Sci., 1, 41 1966.

[2] idem, ibid., 2, 538 1967.

[3] R.J. Young, 'Deformation mechanisms in crystalline polymers', D.Phil. thesis, Cambridge 1972.

[4] R.J. Young, P.B. Bowden, J.M. Ritchie and J.G. Rider, J. Mat. Sci., 8, 23 1973.

[5] M.B. Rhodes and R.S. Stein, J. Appl. Phys., 32, 2344 1961.

[6] M.I. Bank and S. Krimm, J. Appl. Phys., 39, 4951 1968.

[7] L.A. Feldkamp, G. Venkataraman and J.S. King, 'Neutron Inelastic Scattering', IAEA Copenhagen, Vol. 2, 159 1968.

[8] E. Baer and J.L. Kardos, J. Poly. Sci. A3, 2827 1965.

[9] U.W. Arndt and B.T.M. Willis, 'Single Crystal Diffractometry', Cambridge University Press, 1966.

[10] R.W. Gray, private communication.

Chapter 9

MODEL CALCULATIONS OF THE INTERCHAIN PHONON DISPERSION CURVES FOR POLYETHYLENE

9.1 Introduction

Dynamical models for external vibrations in molecular crystals are presently restricted to the few systems for which experimental data about the phonon dispersion curves are available. Deuterohexamethylenetetramine (DHMT) is the most extensively treated system in the literature [1-3]. Phonon measurements along principal symmetry directions have been made and a variety of models constructed. Dolling, Pawley and Powell [3] have successfully employed an atom-atom potential parameter (AAPP) model whereas earlier calculations fitted up to twelve intermolecular force constants using the observed dispersion curves. For other systems the latter procedure is hard to justify since the number of parameters involved frequently exceeds the quantity of experimental data. Here the AAPP method with its empirical basis from structural and thermodynamic data is particularly preferred in the calculation of dispersion curves for external vibrations. Such calculations have been performed for naphthalene and anthracene assuming rigid molecules and reasonable agreement with the sparse experimental data attained [4-7]. More recently Reynolds, Kjems and White [8] have measured phonon dispersion curves for β-phase p-dichlorobenzene along the [ζ00] and [0ζ0] symmetry directions and performed an AAPP calculation using experimentally derived potential parameters. Experimental frequencies were reproduced within an average error of 17% by the calculation [9]. From this work it is clear that acoustic phonon frequencies are more closely reproduced than the higher frequency optical branches of the phonon dispersion curves. In view of the assumption of rigid molecules such a result is not surprising since any coupling between internal and external modes will have the greatest effect on the higher frequency external vibrations [5].

Summarizing the present state of dynamical calculations for molecular crystals, four observations are relevant:

[1] Available experimental data are limited in quantity and a clear assessment of the dynamical models is consequently impaired.

[2] The rigid molecule approximation appears to have a much greater effect upon the fits obtained than the approximations peculiar to the AAPP method such as that of pairwise additivity.

[3] Of the systems studied DHMT and p-dichlorobenzene both involve three types of atom and so potential parameters are defined with greater difficulty and approximation.

[4] To date the most refined potential parameters are those for the hydrocarbon system and they have scarcely been used at all in dynamical calculations.

In this chapter phonon dispersion curves for interchain vibrations in polyethylene are to be derived using the potential parameter method. The only published dispersion curves are those of Kitagawa and Miyazawa [10] and Marsh and Martin [11], both sets being based on Urey-Bradley force fields for hydrogen-hydrogen interactions as described in 5.2. An AAPP calculation is long overdue, especially on account of [4]. Moreover the planning of triple axis experiments requires a suitable model for the prediction of dynamical structure factors and the deficiencies of the present models in their prediction of the density of states encourages a new approach.

9.2 Choice of pseudopotential

Several potential parameter sets are available in the literature [12-15]. All are derived by a fitting procedure from experimental data available for the hydrocarbon system and it is the choice of these data that distinguishes them. In principle the more experimental parameters employed in the fitting process the better the definition of the pseudopotential with the underlying assumption that the force field is transferable

among all the systems chosen. Williams [14-19] has derived seven different parameter sets from structural and thermodynamic data for aromatic and aliphatic systems. Properties such as crystal lattice parameters, heats of sublimation and elastic moduli are used to establish a series of observational equations and potential parameters are defined by a least squares fitting procedure using these equations, subject to the limitations discussed in 1.3. Only six parameters are actually employed in the fitting process since the exponent coefficients C_{ij} of (1.4) are fixed to values consistent with calculations of the compressibility of graphite in the case of C .... C interactions and the repulsion between two hydrogen molecules in the case of H .... H. A geometric mean combining law is invoked to give the C .... H exponent from these two figures. Of the seven sets of parameters two were chosen for this work on the basis of their successful reproduction of the structure of polyethylene. Set IV were obtained from 108 observational equations from both aliphatic and aromatic crystal structures whereas Set VII incorporated 31 equations for aliphatic systems only. Observational equations for polyethylene include four parameters sensitive to the intermolecular potential, two lattice parameters a and b [20], the setting angle θ of the chains [21] and the heat of sublimation [22] all for the low temperature structure. Six-exp potential parameters for the two models are given in Table 9.1.

9.3 Structure calculations for polyethylene

Eigensolutions for harmonic molecular motion are related to the curvature of the crystal potential with respect to various structural parameters at its minimum value. Dynamical calculations proceed then in two stages. Firstly the pseudopotentials just described are used to calculate the equilibrium structure, which should be a close approximation to the observed low temperature structure in each case. Secondly derivative properties of the potential are calculated at the theoretical minimum and from these the normal modes of external chain vibrations, their frequencies,

Table 9.1 Potential parameter sets employed in model calculations [15]

Pseudopotential	A_{CC} [1]	B_{CC} [2]	C_{CC} [3]	A_{CH}	B_{CH}	C_{CH}	A_{HH}	B_{HH}	C_{HH}	Observables
Williams set IV	568	83,630	3.60	125	8,766	3.67	27.3	2654	3.74	108
Williams set VII	505	61,900	3.60	128	11,000	3.67	32.3	2629	3.74	31

[1] Kcal Å^6 [2] Kcal [3] Å^{-1}

amplitudes and other properties relevant to this thesis are estimated.

Structural calculations proceeded with two constraints common to the procedures used in evaluating the potential constants themselves:

[1] Molecules were assumed to be rigid with an imposed coincidence of the chain axis and the crystallographic c-direction.

[2] Symmetry of the crystal space group was preserved.

After these considerations only three variables remained, crystallographic a and b lattice parameters and the setting angle θ between the chains. In the calculation molecules of local D_{2h} symmetry were placed on the orthorhombic lattice with two orientations as illustrated in Fig. 5.1. These orientations are related by the crystal space group operations summarized for polyethylene in Table 9.2. Here each symmetry operation $\vec{R}_n$ is expressed as an operation $\vec{\alpha}_n$ of the D_{2h} factor group combined with a non-primitive translation vector $\vec{\tau}_n$ as in (2.19). For example

$$\begin{bmatrix} x \\ y \\ z \end{bmatrix}_D = \begin{bmatrix} -1 & 0 & 0 \\ 0 & 1 & 0 \\ 0 & 0 & -1 \end{bmatrix} \begin{bmatrix} x \\ y \\ z \end{bmatrix}_E + \begin{bmatrix} 0.5 \\ 0.5 \\ 0 \end{bmatrix} \tag{9.1}$$

shows the transformation of molecules at site E(0,0,0) to site D (0.5,0.5, 0) by the improper rotation C_2^b. Labelling the atoms according to their chemical nature, the crystal potential can be written as a sum over three types of intermolecular interaction

$$\begin{aligned} 2\Phi = & -A_{CC} \sum_{C-C} r_{CC}^{-6} + B_{CC} \sum_{C-C} \exp(-C_{CC} r_{CC}) \\ & -A_{CH} \sum_{C-H} r_{CH}^{-6} + B_{CH} \sum_{C-H} \exp(-C_{CH} r_{CH}) \\ & -A_{HH} \sum_{H-H} r_{HH}^{-6} + B_{HH} \sum_{H-H} \exp(-C_{HH} r_{HH}) \end{aligned} \tag{9.2}$$

At equilibrium the potential derivatives with respect to a, b and θ disappear to define the theoretical crystal structure where

Table 9.2 Symmetry operations of the Pnam (D_{2h}^{16}) crystal space group of orthorhombic polyethylene

$\vec{R}_n$	$\vec{\alpha}_n$	$\vec{\tau}_n$
E	$\begin{bmatrix} 1 & 0 & 0 \\ 0 & 1 & 0 \\ 0 & 0 & 1 \end{bmatrix}$	(0,0,0)
C_2^a	$\begin{bmatrix} 1 & 0 & 0 \\ 0 & -1 & 0 \\ 0 & 0 & -1 \end{bmatrix}$	(0.5,0.5,0.5)
C_2^b	$\begin{bmatrix} -1 & 0 & 0 \\ 0 & 1 & 0 \\ 0 & 0 & -1 \end{bmatrix}$	(0.5,0.5,0)
C_2^c	$\begin{bmatrix} -1 & 0 & 0 \\ 0 & -1 & 0 \\ 0 & 0 & 1 \end{bmatrix}$	(0,0,0.5)
i	$\begin{bmatrix} -1 & 0 & 0 \\ 0 & -1 & 0 \\ 0 & 0 & -1 \end{bmatrix}$	(0,0,0)
σ(bc)	$\begin{bmatrix} -1 & 0 & 0 \\ 0 & 1 & 0 \\ 0 & 0 & 1 \end{bmatrix}$	(0.5,0.5,0.5)
σ(ac)	$\begin{bmatrix} 1 & 0 & 0 \\ 0 & -1 & 0 \\ 0 & 0 & 1 \end{bmatrix}$	(0.5,0.5,0)
σ(ab)	$\begin{bmatrix} 1 & 0 & 0 \\ 0 & 1 & 0 \\ 0 & 0 & -1 \end{bmatrix}$	(0,0,0.5)

$$\frac{\partial\Phi}{\partial a}, \frac{\partial\Phi}{\partial b}, \frac{\partial\Phi}{\partial\theta} = 0 \qquad (9.3)$$

Minimization of (9.2) proceeded by Powell's method of steepest descent [23] which searched the function Φ along a, b and θ tracks generating conjugate search directions to speed the location of the minimum. Several starting values were used for the variables in a bid to avoid the possibility of having found a false minimum. The computer program POLYPOT written for this purpose defined the crystal potential minimum for a given set of potential parameters with an accuracy of 0.01% in the structural variables. In summing the intermolecular potential defined by (9.2) separate summation limits were used for each type of atom pair

$$r_{HH} < 5.0 \quad r_{CH} < 5.5 \quad r_{CC} < 6.0 \text{ Å} \qquad (9.4)$$

which were chosen by Williams to reproduce 80% of the observed heat of sublimation. Since the number of pairs within these limits changes as the structural parameters vary, this number was fixed initially to avoid producing discontinuities in the potential function. Consequently an exact reproduction of Williams's calculated structures was not possible, although the results are very close to these.

Calculated structures for Williams's set IV and VII pseudopotentials are described in Table 9.3 together with the number of atom pairs considered and the sublimation energies. Experimental data for the 77°K structure are also reproduced from Swan [20], together with skeletal structural parameters derived for $C_{36}H_{74}$ by Teare [21] and the experimental sublimation energy [22]. From Table 9.3 it is clear that these three potentials enjoy considerable success, reproducing the observed lattice parameters within an error of at most 0.2%. For the setting angle θ, defined with respect to the b-axis in Fig. 5.1, agreement is poorer although there is still much controversy about the experimental value. Smith [24] quotes 48° from his analysis of X-ray diffraction data from the n-paraffins and

Table 9.3 Calculated and observed crystal structures of polyethylene

Structural parameter	Williams set IV calculated structure	Williams set VII calculated structure	Experimental† structure 77°K
a Å	7.139	7.140	7.155
b Å	4.874	4.889	4.889
θ deg.	46.53	46.45	42.3
ε kcal/mole	-1.465	-1.458	-1.838
Number of pairs	182	186	-
c Å	2.540	2.540	2.547
∠HCH deg.	104.0	106.0	106.0
∠CCC deg.	113.1	113.1	112.3
r_{C-H} Å	1.04	1.04	1.10
r_{C-C} Å	1.522	1.522	1.533

† [20], [21], [22]

Shearer and Vand [25] quote 48.6° for monoclinic $C_{36}H_{74}$. In contrast Bunn [26] reports a figure of 41.3° and the value of Teare [21] given in Table 9.3 is 42.3°. Further experimental work is clearly required. For the moment it is very hard to dispute the calculated values, all of which lie around 46.5°.

9.4 Model calculations for the external vibrations of polyethylene

9.4.1 Dynamical formalism for a molecular crystal

After the approximations suggested for dynamical calculations on molecular crystals some adaptation of the general treatment described in 2.4 is required. In particular the Hamiltonian for molecular vibrations is now broken into two parts pertaining to intra- and intermolecular motion and the former is ignored in the rigid molecule approximation. Furthermore the kinetic and potential energy are to be expressed in terms of rigid molecular translations and rotations with harmonic restoring forces. Consequently the application of Lagrange's equation is helped by the choice of an inertial coordinate system, for which the kinetic energy assumes a diagonal form. The equations of motion for a molecule at $\vec{x}(^{l}_{k})$ then separate into two groups

$$m\ddot{u}_{\alpha}(^{l}_{k}) = -\sum_{l'k'\beta} \Phi_{\alpha\beta}(^{l-l'}_{kk'})u_{\beta}(^{l'}_{k'}) \qquad (9.5)$$

$$I_{\alpha}\ddot{u}_{\alpha+3}(^{l}_{k}) = -\sum_{l'k'\beta} \Phi_{\alpha+3\beta}(^{l-l'}_{kk'})u_{\beta}(^{l'}_{k'}) \qquad (9.6)$$

where $u_{\alpha}(^{l}_{k})$, $u_{\alpha+3}(^{l}_{k})$, $\alpha = 1,3$ correspond to molecular translations and rotations about the inertial axes and I_{α}, $\alpha = 1,3$ are the moments of inertia of molecules mass m about the same axes. Terms on the right of (9.5) and (9.6) represent the forces and couples on molecule k in the l-th cell caused by rotational and translational displacements of neighbour molecules and the coefficients are intermolecular force constants. Solution of these equations proceeds by writing the

translation-rotation of each molecule in the form of a travelling wave

$$u_\alpha(^1_k) = \frac{1}{m_\alpha^{1/2}} U_{k\alpha}(\vec{q}) \exp(i\vec{q}.\vec{x}(^1_k) - i\omega t) \qquad (9.7)$$

Substitution of (9.7) into (9.5) and (9.6) gives the dynamical matrix for external molecular vibrations

$$\omega^2 U_{k\alpha}(\vec{q}) = \sum_{k'\beta} D_{\alpha\beta}(^{\vec{q}}_{kk'}) U_{k'\beta}(\vec{q}) \qquad (9.8)$$

where

$$D_{\alpha\beta}(^{\vec{q}}_{kk'}) = \frac{1}{(m_\alpha m_\beta)^{1/2}} \sum_1 \Phi_{\alpha\beta}(^1_{kk'}) \exp(-i\vec{q}.(\vec{x}(^0_k) - \vec{x}(^1_{k'}))) \qquad (9.9)$$

and

$$\begin{aligned} m_\alpha &= m \text{ for } \alpha = 1,3 \\ I_\alpha &\text{ for } \alpha = 4,6 \end{aligned} \qquad (9.10)$$

Since all molecules in the crystal are related by symmetry it is sufficient to derive a 6 x 6 dynamical matrix for one molecule in the zeroth cell at $\vec{x}(^0_k)$ and to build the full 6n x 6n Hermitian matrix for the n molecules in the basis using the symmetry operations of the space group. Diagonalization of the full dynamical matrix for input wave vector $\vec{q}$ gives the phonon frequencies $\omega_j(\vec{q})$ and amplitudes $U^j_{k\alpha}(\vec{q})$ for each normal mode.

9.4.2 Computation of phonon dispersion curves using CRISS-CROSS

Phonon dispersion curves were calculated from the analytical pseudo-potentials described earlier using a suitably amended version of the computer program CRISS-CROSS kindly lent by Dr. G.S. Pawley of Edinburgh University. This program was originally designed for the calculation of external lattice vibrational frequencies of rigid centrosymmetric molecules in crystal structures with two molecules in the unit cell and as such was

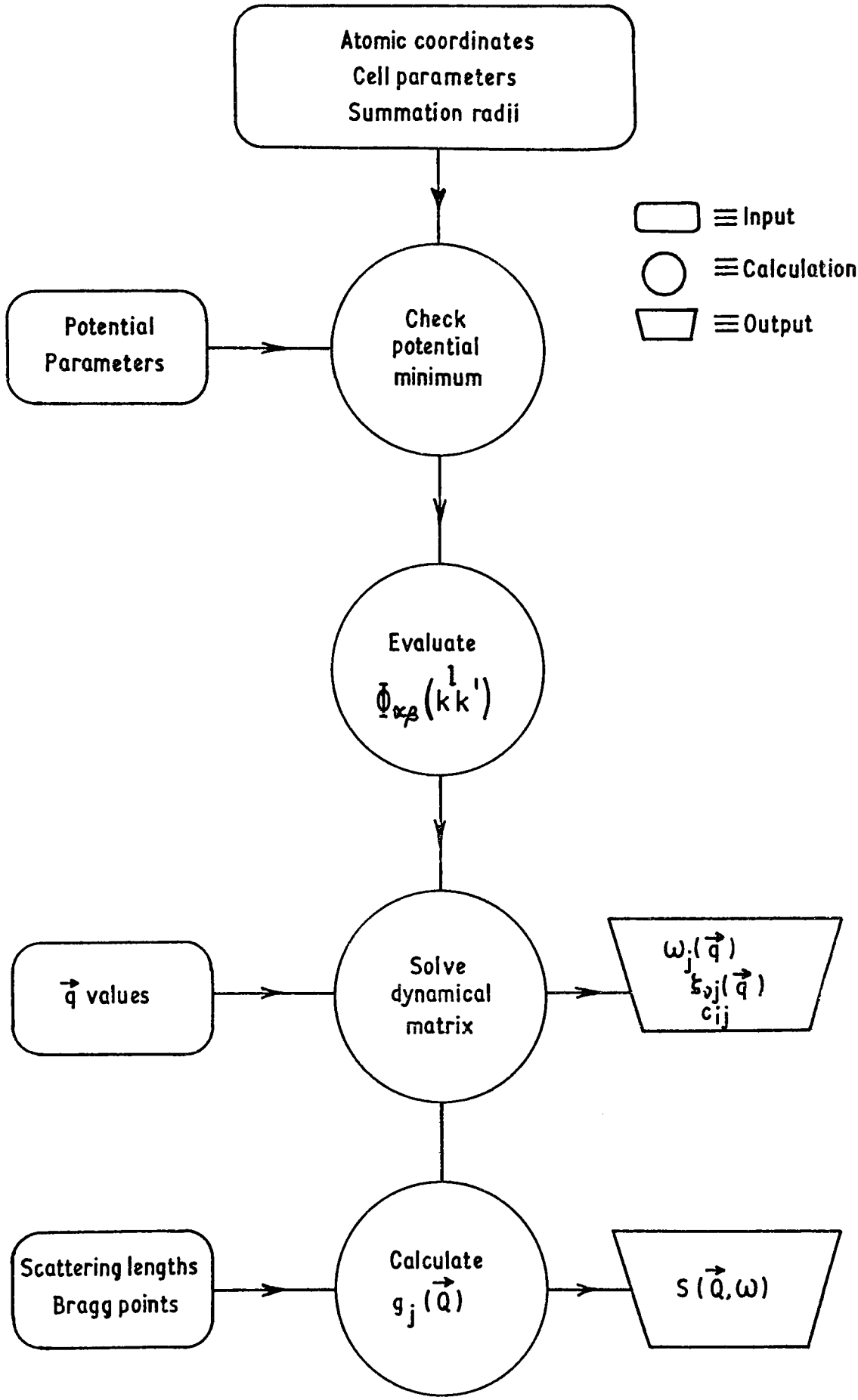

Fig. 9·1 Flowchart showing the logical construction of CRISS-CROSS.

ideally applicable to polyethylene [4, 9]. A logical outline of this program is reproduced in Fig. 9.1. The sequence of calculation can be categorized under four headings:

[1] Reproduction of the molecular geometry and unit cell parameters corresponding to the pseudopotential minimum obtained in the structure calculation.

[2] Calculation of intermolecular force constants by differentiation of the crystal potential at its minimum value.

[3] Construction and solution of the dynamical matrix to give phonon frequencies and molecular amplitudes.

[4] Computation of required properties such as dynamical structure factors and elastic constants from the eigensolutions of the dynamical matrix.

As in the structure calculation distances between nonbonded atoms on neighbouring molecules were sorted to define the three types of interaction in (9.4) and the number of pairs within a chosen summation limit. Intermolecular potentials were then calculated from the analytical form for the pseudopotential

$$\Phi\left(\begin{smallmatrix}1\\ kk'\end{smallmatrix}\right) = \tfrac{1}{2} \sum_{\mu} \sum_{\nu} \bar{\Phi}\left(\begin{smallmatrix}1\\ k\mu k'\nu\end{smallmatrix}\right) \qquad (9.11)$$

where the summation extends over the chosen atomic pairs. Functional differentiation of (9.11) with respect to changes in the spacing of nonbonded atoms on molecules k and k' generated by molecular displacements α gave the force constants in (9.9). In this way force constant tensors were established for interactions between a molecule at the origin and its symmetry related neighbours. To complete the information required for the evaluation of (9.9) the coefficients relating forces and couples on the centre molecule to its own displacements were required. These 'self terms' were derived from the conditional invariance of the crystal potential to overall translations and rotations of the lattice whereby

$$-\sum_{1}\sum_{k'}\Phi_{\alpha\beta}\begin{pmatrix}1\\kk'\end{pmatrix} = 0 \qquad \alpha,\beta = 1,3 \tag{9.12}$$

for translational invariance, since an arbitrary displacement of all the molecules produces no net force. From (9.12) the translational self terms can be written

$$\Phi_{\alpha\beta}\begin{pmatrix}0\\kk\end{pmatrix} = -\sum_{1}\sum_{k'}{}'\Phi_{\alpha\beta}\begin{pmatrix}1\\kk'\end{pmatrix} \tag{9.13}$$

where the sum prime indicates the exception of the left hand term. Similar expressions can be derived for the rotational self terms [27]. Such summations were readily achieved after the force constant tensors had been calculated.

For a centrosymmetric molecule dynamical matrix elements constructed using (9.9) are either purely real or purely imaginary since the translational and rotational components of the motion are 90^{o} out of phase [28]. Centrosymmetry was exploited in CRISS-CROSS by the reduction of the Hermitian matrix to a real symmetric form which is more quickly diagonalized. Furthermore in evaluating the force constant tensors only half the required complement of intermolecular interactions were considered since there was inversion symmetry about the centre molecule.

9.4.3 Qualification of the dynamical treatment for orthorhombic polyethylene

Crystalline polyethylene belongs to the nonsymmorphic space group D_{2h}^{16} or Pnam shown in Table 9.2. Each C_2H_4 unit possesses inversion symmetry i and all atoms in the bimolecular basis may be generated from the asymmetric CH_2 unit by application of the space group operations. $\vec{R}_n$, defined by (2.19). Interpretation of the eigensolutions of the dynamical matrix is facilitated when the $\vec{q}$ group has been established and the symmetry and degeneracies of the several normal modes defined. For these purposes symmetry points and lines in the orthorhombic zone of polyethylene will be labelled using the nomenclature of Slater [29] as in

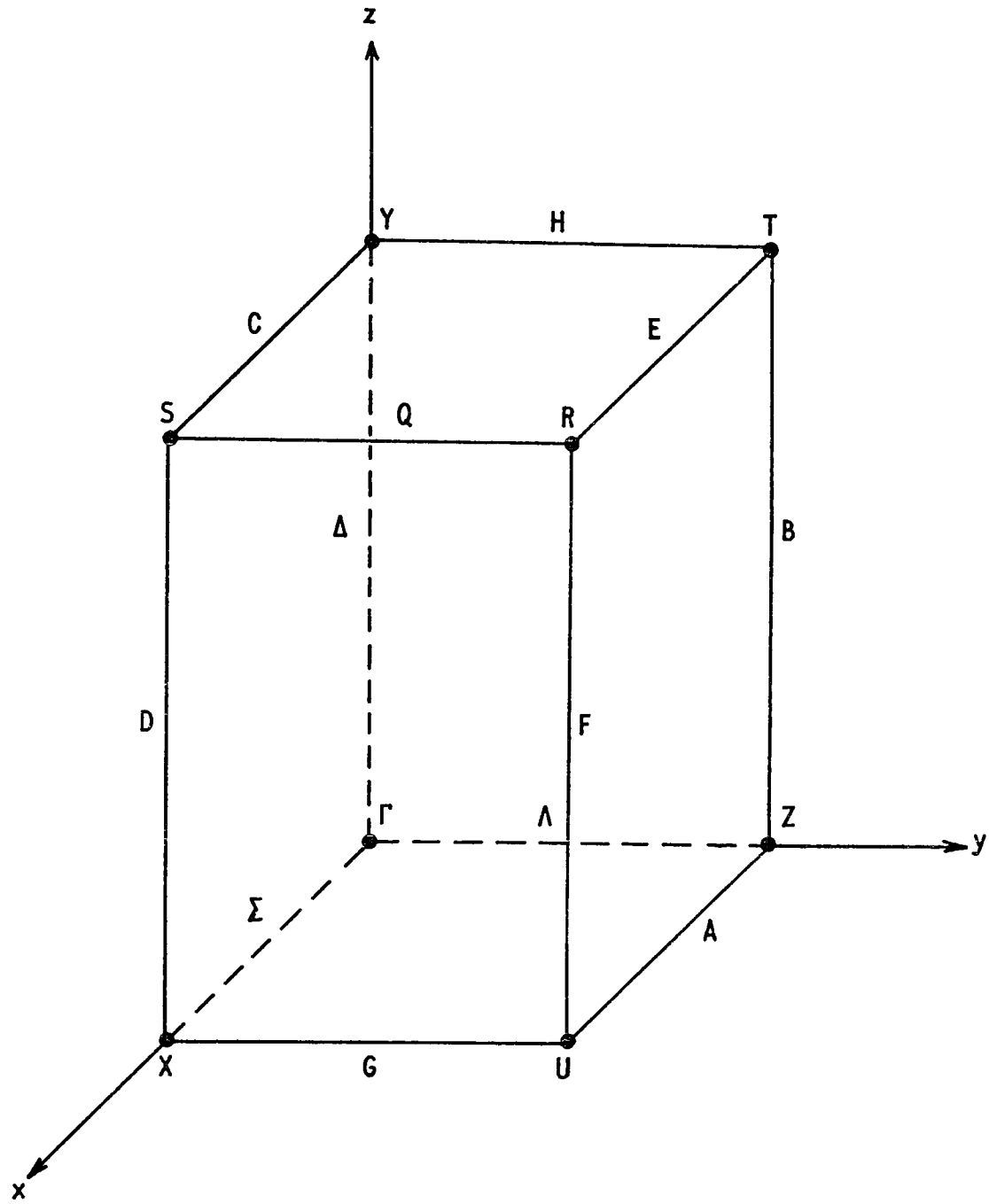

Fig. 9·2 Symmetry points and lines in the Brillouin zone of orthorhombic polyethylene labelled after [29].

Fig. 9.2, where crystallographic a, b and c axes correspond to the x, y and z axes. Highest symmetry points lie at the zone corners where D_{2h} symmetry is adopted by the $\vec{q}$ group. Lower symmetry groups belong to points on the faces of the zone and for an arbitrary position of $\vec{q}$ virtually no symmetry remains at all. Kitagawa and Miyazawa [30] have derived compatibility relationships for the eigensolutions around the zone and their results will be used in the next section for the labelling of the normal modes.

For a crystal containing two molecules in the unit cell a total of twelve external lattice modes are normally expected. Polyethylene is effectively a two-dimensional molecular crystal since one of the crystallographic axes coincides with the axis of an extended molecular chain. Consequently the four 'external' normal modes involving librations about the a and b axes are in fact intrachain deformations, reducing the number of genuine external chain modes to eight. Such internal chain stretching and bending modes have been observed around 1000 cm^{-1} by Raman and infrared techniques and are essentially decoupled from the lower frequency interchain librations.

In the external mode calculation using CRISS-CROSS it is necessary to treat the chain as being discontinuous at the cell boundary and to assume that dynamical properties derived for a single C_2H_4 unit are valid for a continuous chain. Essentially this infers that the potential derivatives in (9.9) are scaled by the same factor as the mass and inertial terms for all chain lengths

$$\lim_{i\to\infty} \left(\frac{\bar{\Phi}_i}{m_i}\right) = \frac{\bar{\Phi}_1}{m_1} \qquad (9.14)$$

where $\bar{\Phi}_i$ are intermolecular force constants $\bar{\Phi}_{\alpha\beta}(^{1}_{kk'})$ derived for adjacent $C_{2i}H_{4i}$ units and m_i are terms $(m_\alpha m_\beta)^{1/2}$ for the i-th unit. This assumption can of course be tested by repeating the calculations for several chain lengths and comparing the resulting frequencies. To implement such a

simplification the inertial axes for $C_{2i}H_{4i}$ segments are redefined to take account of their incorporation within an infinite chain. In CRISS-CROSS this was achieved by introducing two dummy atoms of very large mass at displacements above and below each C_2H_4 unit upon the crystallographic c-axis. Calculation of the inertia tensor proceeded with the inclusion of these atoms and on diagonalizing the principal axes of inertia were defined along and perpendicular to the chain axis. Moreover dynamical matrix elements for the librations forbidden on a rigid chain model disappeared then since the inertial denominators in (9.9) become very large for rotations about the a and b axes. Although strictly terms in (9.9) go to infinity for the intrachain distortions the essential decoupling of these four modes was most simply achieved by shifting them to zero frequency. In this limit the dynamical matrix requiring solution reduced in dimensions from 12 x 12 to 8 x 8.

9.4.4 Results

Phonon dispersion curves for interchain vibrations in deuteropolyethylene were calculated for the two potential parameter sets used in the structure calculations. Structural parameters derived for the pseudopotential minimum in POLYPOT and summarized in Table 9.3 were used as input for CRISS-CROSS, which also contained the accommodations just described for polyethylene. Calculations were repeated for chain lengths up to $C_{20}D_{40}$ and confirmed the reasoning of the last section in that the derived phonon frequencies were insensitive to the length of segment chosen for the calculation. Additional routines were written to calculate elastic constants and dynamical structure factors from the eigensolutions of the dynamical matrix.

CRISS-CROSS establishes the force constant tensors from the molecular geometry and input potential parameters and scarcely employs the many elements of symmetry proper to both the molecules and the unit cell. Consequently when the dynamical matrix factorizes on solution at a symmetry

point or along a line of symmetry, the irreducible representations of the solutions are not explicitly presented and must be derived by hand from the eigenvectors using the crystal space group elements. For polythene this is a relatively simple task since the $\vec{q}$ vector is restricted to the ab plane by the assumption of rigid molecules and the irreducible representations of the $\vec{q}$ groups have been tabulated by Kitagawa and Miyazawa [30].

Frequency solutions (cm^{-1}) are shown in Fig. 9.3 for the Williams set VII pseudopotential as a function of $[\delta_a \delta_b 0]$ where

$$\delta_a = a\, q_a \qquad \delta_b = b\, q_b \qquad \delta_c = c\, q_c \tag{9.15}$$

As presented the solutions are for $\vec{q}$ values along the zone edges defined by symmetry lines Σ, G, A and Λ described in Fig. 9.2 and following the nomenclature of Slater for orthorhombic lattices [29]. General principles affecting the construction of such curves have already been described in 2.5. In Fig. 9.3 normal modes are labelled according to their irreducible representation in the local $\vec{q}$ group after reference [30]. For an arbitrary point $[\delta_a \delta_b 0]$ there are at least two symmetry operations which leave $\vec{q}$ invariant, the identity operator E and the reflexion plane σ(ab) described in Table 9.2 and constituting the C_s $\vec{q}$ group. Consequently translatory modes polarized along the c-axis belong to an irreducible representation which is always different to those for modes polarized in the ab plane at all points $[\delta_a \delta_b 0]$ in the zone. From [30] it is clear that on moving away from the zone centre $\vec{q}$ group symmetry is reduced from D_{2h} to C_s in all but the $[\delta_a 00]$ and $[0\delta_b 0]$ directions for which C_{2V} symmetry is preserved. Along $\Sigma[\delta_a 00]$ and $\Lambda[0\delta_b 0]$ there are four representations, two of which attach to antiparallel translations of the chains along the c-direction and cross over the remaining ab polarized modes. Of the remaining six modes two involve librations of differing phase about the chain axis and the rest involve molecular translations along the a and b axes. Since all these modes belong to the two remaining representations of the C_{2V} $\vec{q}$ group they

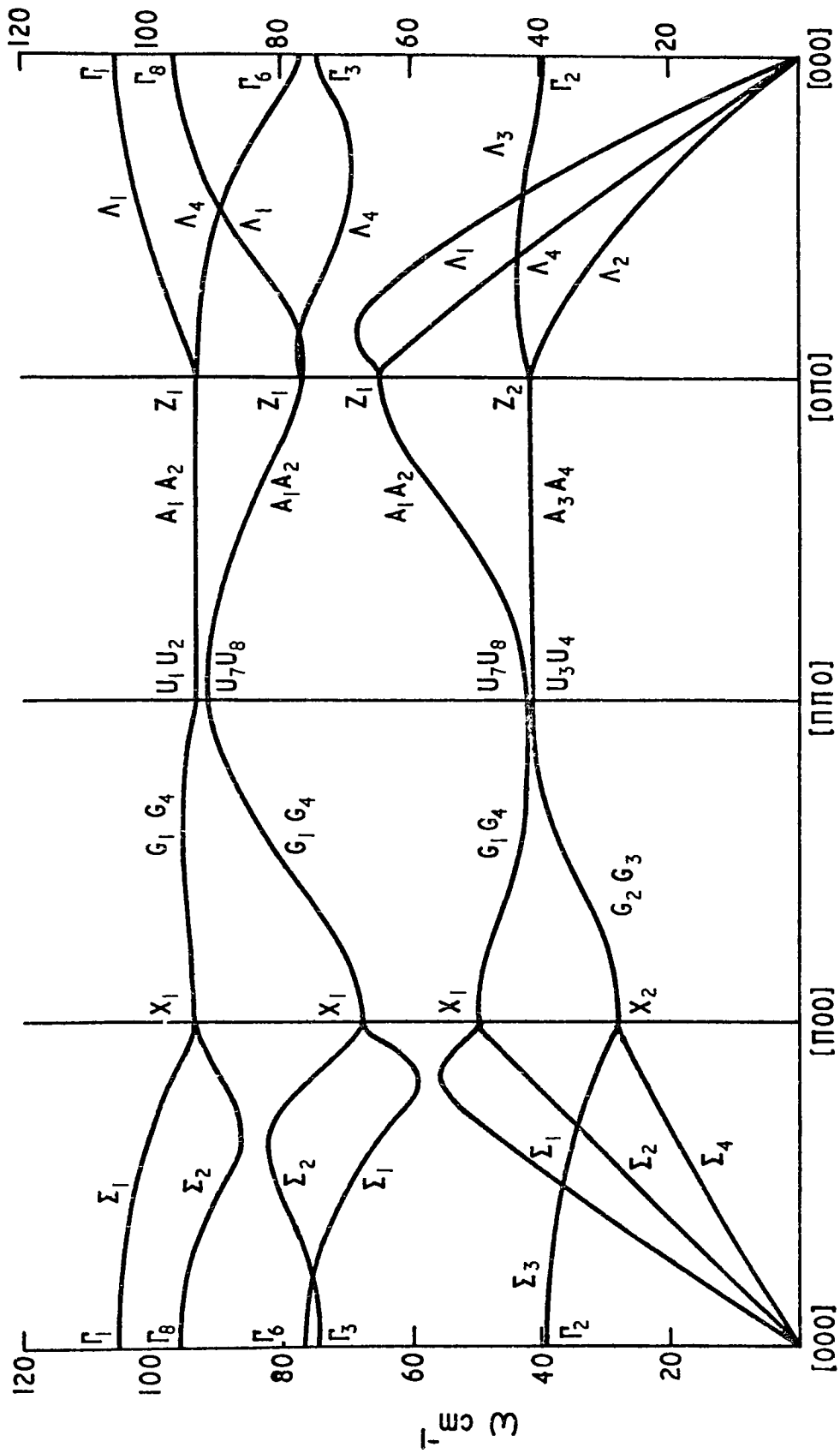

Fig. 9·3 Interchain phonon dispersion curves for D.P.E. calculated for rigid molecules using Williams set VII potential parameters.

mix extensively (see Fig. 9.3). Degeneracies at [π00] and [0π0] are a consequence of the continuity principle described in 2.5 and persist for arbitrary points [$\pi\delta_b 0$] and [$\delta_a \pi 0$] around the zone edges by virtue of the time reversal degeneracy discussed by Kitagawa and Miyazawa [30].

Specific aspects of the derived dispersion curves are now to be discussed under three headings of relevance to the experimental section:

9.4.4.1 Zone centre solutions

At the zone centre Γ[000] point the $\vec{q}$ group attains its highest symmetry of D_{2h}, the factor group of the crystal space group D_{2h}^{16}. Five external normal modes of polyethylene have non zero intercepts at the zone origin and are summarized in Table 9.4 for the two potential models. Their irreducible representations are derived from the transformation properties of the eigenvectors under D_{2h} group operations. In Fig. 9.4 the eigenvectors are explicitly represented and the distinction between modes of translatory and rotatory character is made clear. Of the five modes two are infrared active, Γ_6 and Γ_8, corresponding to antiparallel translation of the chains in the b and a directions with B_{1u} and B_{2u} symmetry respectively. Another two modes, Γ_1 and Γ_3, correspond to external librations about the c-axis with A_g and B_{3g} symmetry and both are Raman active. The remaining $\Gamma_2(A_u)$ vibrations are inactive in both the infrared and Raman spectrum and involve antiparallel motion of the two chains in the cell along the c-axis. From Table 9.4 it is evident that the two pseudopotentials of Williams yield lattice frequencies in close agreement, as might be expected from their nearly identical reproduction of the crystal structure (Table 9.3). Further comment on the numbers in Table 9.4 is postponed until the next chapter.

9.4.4.2 Acoustic slopes and elastic constants

Orthorhombic polyethylene possesses nine independent elastic (stiffness) constants c_{ij} as defined in Table 9.5.1 together with the related compliance

Table 9.4 Calculated zone centre interchain modes for D.P.E.

Mode	Frequency cm^{-1}		Activity	Description
	set IV	set VII		
$\Gamma_1(A_g)$	105.7	105.1	Raman	Antiphase libration of adjacent chains about the c-axis
$\Gamma_8(B_{2u})$	96.6	96.1	infrared	Antiphase translation of adjacent chains along the a-axis
$\Gamma_6(B_{1u})$	75.0	76.8	infrared	Antiphase translation of adjacent chains along the b-axis
$\Gamma_3(B_{3g})$	73.9	74.7	Raman	In phase libration of adjacent chains about the c-axis
$\Gamma_2(A_u)$	40.7	39.8	Inactive	Antiphase translation of adjacent chains along the c-axis

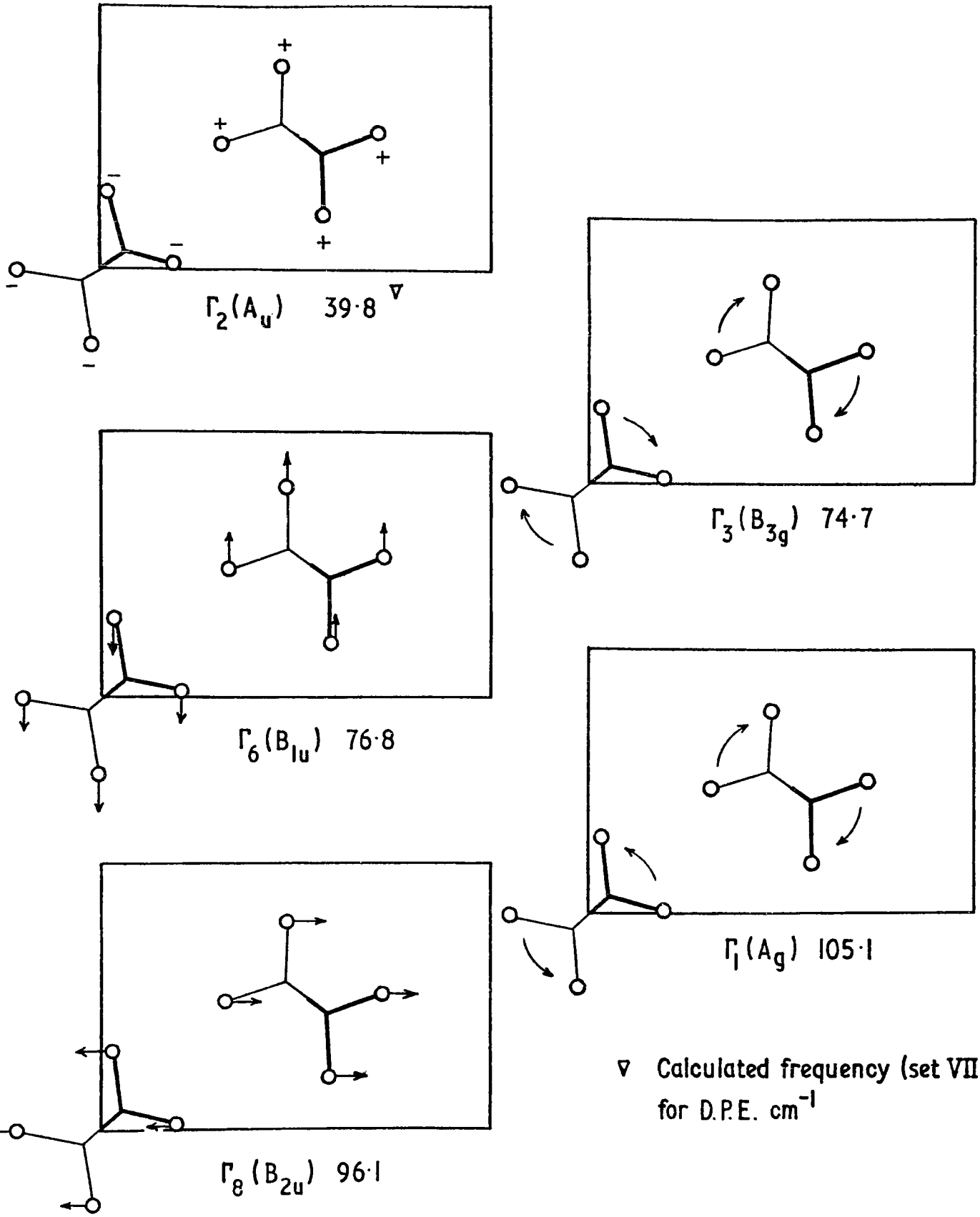

∇ Calculated frequency (set VII) for D.P.E. cm^{-1}

Fig. 9·4 Explicit representation of the eigenvectors for normal modes at the zone centre Γ point of orthorhombic polyethylene.

Table 9.5.1 Elastic constant matrix for orthorhombic polyethylene

	e_1	e_2	e_3	e_4	e_5	e_6
S_1	c_{11}	c_{12}	c_{13}	0	0	0
S_2	c_{12}	c_{22}	c_{23}	0	0	0
S_3	c_{13}	c_{23}	c_{33}	0	0	0
S_4	0	0	0	c_{44}	0	0
S_5	0	0	0	0	c_{55}	0
S_6	0	0	0	0	0	c_{66}

Table 9.5.2 Compliance matrix for orthorhombic polyethylene

	S_1	S_2	S_3	S_4	S_5	S_6
e_1	s_{11}	s_{12}	s_{13}	0	0	0
e_2	s_{12}	s_{22}	s_{23}	0	0	0
e_3	s_{13}	s_{23}	s_{33}	0	0	0
e_4	0	0	0	s_{44}	0	0
e_5	0	0	0	0	s_{55}	0
e_6	0	0	0	0	0	s_{66}

matrix elements of Table 9.5.2 [31]. All of these can in principle be determined from the velocities of long wavelength acoustic phonons travelling in special directions in the crystal as discussed in 2.7. Odajima and Maeda [32] have compiled a secular equation which greatly facilitates the identification of these constants from acoustic slopes. Based on the discussion of 2.7 the long wavelength frequency solutions ω^2 of (9.9) for acoustic phonons at $[\delta_a \delta_b 0]$ can be derived from the secular equation

$$\begin{bmatrix} \frac{c_{11}}{a^2}\delta_a^2 + \frac{c_{66}}{b^2}\delta_b^2 - \rho\omega^2 & \frac{(c_{12}+c_{66})\delta a \delta b}{ab} & 0 \\ \frac{(c_{12}+c_{66})\delta a \delta b}{ab} & \frac{c_{66}}{a^2}\delta_a^2 + \frac{c_{22}}{b^2}\delta_b^2 - \rho\omega^2 & 0 \\ 0 & 0 & \frac{c_{55}}{a^2}\delta_a^2 + \frac{c_{44}}{b^2}\delta_b^2 - \rho\omega^2 \end{bmatrix} = 0 \qquad (9.16)$$

where the column eigenvectors contain, in vertically descending order, elastic displacements along the a, b and c axes.

Only six of the nine elastic constants can be reproduced by the rigid chain model employed here, although the large size of c_{33} compared to all the other constants supports this approximation by reducing the significance of c_{13} and c_{23} in the calculation of interchain moduli. Five of the calculable elastic constants can be obtained from the frequency solutions along the symmetry directions $\Sigma[\delta_a 00]$ and $\Lambda[0\delta_b 0]$ as shown in Table 9.6. Along these directions symmetry demands that the eigenvectors adopt purely longitudinal or transverse polarizations with respect to the phonon wave vector. The sixth constant c_{12} is determinable from acoustic slopes in an arbitrary direction $[\delta_a \delta_b 0]$. Elastic constants were derived for the Williams set IV and set VII pseudopotentials from acoustic slopes determined at phase angles of 0.01π along $[\delta 00]$, $[0\delta 0]$ and $[\delta\delta 0]$. Results are summarized in Table 9.7

Table 9.6 Acoustic slopes along $[\delta_a \delta_b 0]$ and their relationship to the elastic constants

Direction	Symmetry	Slope†	Eigenvector polarization
$[\delta 00]$	Σ_1	c_{11}/a^2	a-direction
	Σ_2	c_{66}/a^2	b-direction
	Σ_3	c_{55}/a^2	c-direction
$[0\delta 0]$	Λ_1	c_{22}/b^2	b-direction
	Λ_2	c_{44}/b^2	c-direction
	Λ_4	c_{66}/b^2	a-direction
$[\delta\delta 0]$	Ω_1 }	$\frac{1}{2}[c_{11}/a^2+c_{22}/b^2+c_{66}(1/a^2+1/b^2)$	
	Ω_1 }	$\pm\{(c_{11}/a^2+c_{66}/b^2-c_{22}/b^2-c_{66}/a^2)^2$	ab-plane
		$+4(c_{12}+c_{66})^2/a^2b^2\}^{1/2}]$	
	Ω_2	$c_{55}/a^2+c_{44}/b^2$	c-direction

† $\rho(\omega/|\vec{q}|)^2$

Table 9.7 Elastic constants for polyethylene calculated from the potential parameter models assuming rigid molecules

Model	c_{11}	c_{22}	c_{12}	c_{44}	c_{55}	c_{66}
Williams set IV	12.5†	10.9	6.2	3.6	2.3	5.7
Williams set VII	12.4	11.1	6.3	3.3	2.2	5.5

† units 10^{10} dyne cm^{-2}

which again demonstrates the virtual equivalence of the two parameters sets in the prediction of dynamical properties.

Elastic moduli E_a and E_b for compression along the a and b axes were derived from the compliance matrix elements s_{11} and s_{22} as in 2.7

$$E_a = (s_{11})^{-1} \tag{9.17}$$

$$E_b = (s_{22})^{-1} \tag{9.18}$$

and were estimated at 8.9 (8.8) and 7.8 (7.9) x 10^{10} dyne cm^{-2} respectively for the set IV (VII) potential. These figures are rightly lower than the values 13.7 and 11.9 x 10^{10} dyne cm^{-2} calculated directly from the potential function by Williams without allowing for reorientation of the chains during tensile compression [15, 33].

As a final check the significance of the omission of c_{13}, c_{23} coefficients in the calculation of s_{11} and s_{22} was tested using Kitagawa's complete set of elastic constants and found to shift E_a and E_b by less than 1% from the values he quotes [34]. This is a consequence of the magnitude of c_{33} which is known experimentally to be almost two orders of magnitude greater than c_{11} and c_{22} (see Fig. 7.8).

9.4.4.3 Dynamical structure factor calculations

Calculation of the coherent inelastic neutron cross section for single phonon excitations and the employment of these calculations in the interpretation of triple axis data was a major function of the dynamical model described in this chapter. Starting with the frequencies and cartesian atomic displacements generated by CRISS-CROSS for particular $\vec{q}$ values, the dynamical structure factors $g_j(\vec{Q})$ of (3.37) were constructed and used to calculate the total coherent inelastic cross section by summation over the instrumental $(\vec{Q},\omega)$ track. Further accommodation for the mosaic of the specimen was provided by treating the reciprocal lattice points as arcs representing a Gaussian intensity distribution with FWHM equal to the

observed angular mosaic of 17^{o} in the basal plane. As demonstrated in Fig. 10.5 a particular constant $\vec{Q}$ scan on the reciprocal lattice then involves a whole sequence of $\vec{q}$ values all of which are to be summed to produce the cross section (3.36)

$$\frac{d^2\sigma}{d\Omega dE}_{coh} = (2\pi)^3 \sum_{\vec{q}j} \frac{k'}{k} \delta(\hbar\omega \pm \hbar\omega_j(\vec{q})) \times \sum_{\vec{\tau}} \delta(\vec{Q} \pm \vec{q} - 2\pi\vec{\tau})(n_{\vec{q}j} + \tfrac{1}{2} \pm \tfrac{1}{2}) |g_j(\vec{Q})|^2 \qquad (9.19)$$

Two sorts of experimental scan were simulated in this way: zone centre scans at Bragg points and longitudinal scans in the vicinity of certain strongly reflecting reciprocal lattice points. The results are best discussed in the context of the experimental data which they illuminate.

References

[1] B.M. Powell, 'Neutron inelastic scattering', IAEA, Copenhagen, 2, 185 1968.

[2] G. Dolling and B.M. Powell, Proc. Roy. Soc., A319, 209 1970.

[3] G. Dolling, G.S. Pawley and B.M. Powell, Proc. Roy. Soc., A333, 363 1973.

[4] G.S. Pawley, Phys. Stat. Sol., 20, 347 1967.

[5] G.S. Pawley and S.J. Cyvin, J. Chem. Phys., 52, 4073 1970.

[6] G.S. Pawley and E.A. Yeats, Sol. Stat. Comm., 7, 385 1969.

[7] V.A. Lutz and W. Halg, Sol. Stat. Comm., 8, 165 1970.

[8] P.A. Reynolds, J.K. Kjems and J.W. White, 'Neutron inelastic scattering', IAEA, Grenoble, 195 1972.

[9] P.A. Reynolds, D.Phil. thesis, Oxford University 1972.

[10] T. Kitagawa and T. Miyazawa, Jap. Polym. J., 1, 471 1970.

[11] D.I. Marsh and D.H. Martin, J. Phys. C, 5, 2309 1972.

[12] A.I. Kitaigorodskii and K.V. Mirskaya, Soviet Physics-Cryst., 6, 408 1961.

[13] A.I. Kitaigorodskii, J. Chim. Phys., 63, 6 1966.

[14] D.E. Williams, J. Chem. Phys., 45, 3770 1966.

[15] idem, ibid., 47, 4680 1967.

[16] idem, ibid., 43, 4424 1965.

[17] idem, J.A.C.S., 91, 1243 1968.

[18] idem, Acta Cryst. A25, 464 1969.

[19] idem, ibid. A27, 452 1971.

[20] P.R. Swan, J. Poly. Sci., 56, 403 1962.

[21] P.W. Teare, Acta Cryst., 12, 294 1959.

[22] F.W. Billmeyer Jr., J. Appl. Phys., 28, 1114 1957.

[23] M.J.D. Powell, Comput. J., 7, 155 1964.

[24] A.E. Smith, J. Chem. Phys., 21, 2229 1953.

[25] H.M. Shearer and V. Vard, Acta Cryst., 9, 379 1956.

[26] C.W. Bunn, Trans. Far. Soc., 35, 482 1939.

[27] G.S. Pawley, Phys. Stat. Sol., 49, 475 1972.

[28] W. Cochran and G.S. Pawley, Proc. Roy. Soc., A280, 1 1964.

[29] J.C. Slater, 'Quantum theory of molecules and solids', vol. 2, McGraw-Hill, N.Y. 1965.

[30] T. Kitagawa and T. Miyazawa, Bull. Chem. Soc. Jap., 43, 372 1970.

[31] J.F. Nye, 'Physical properties of crystals: their representation by tensors and matrices', Oxford 1957.

[32] A. Odajima and T. Maeda, Rep. Prog. Poly. Phys. Jap., 8, 33 1965.

[33] G. Wobser, D.Sc. thesis, Stuttgart University 1971.

[34] T. Kitagawa, D.Sc. thesis, Osaka University 1968.

Chapter 10

NEUTRON SCATTERING STUDIES OF FULLY ORIENTED DEUTEROPOLYETHYLENE

10.1 Instrumental details

Experiments were performed on the TAS II triple axis spectrometer at A.E.K. Risø described in 4.4. Since measurements on a specimen with mosaic as high as 20° had never been attempted before, careful consideration of the dynamical structure factors for phonon excitations in such a system was an essential preliminary to experiment. Once the limitations of mosaic became clear from the calculations and the possibility of obtaining useful experimental information emerged, attention was diverted to the design of the spectrometer. The major problem arising was the rate of data collection which can become prohibitive for specimens with mosaic of this order. For this reason pyrolytic graphite was employed in the monochromation and analysis of incident and scattered neutrons respectively to provide an additional factor in the count rate. This factor arose both from the high transmission of graphite and from the choice of specimens with appreciable mosaic, 0.5 and 1.2° respectively. Further enhancement of the count rate was achieved by relaxing the collimation within limits determined by the associated deterioration in energy resolution. Relaxation in the energy resolution had the most severe consequence in the observation of low energy phonon excitations since such contributions to the inelastic cross section were then overshadowed by the resolution broadened elastic peak.

Resolution characteristics were calculated from experimental parameters using the computer program RESOL developed by D.H. Saunderson, A.E.R.E. Harwell and based upon the formulae of Cooper and Nathans [1, 2]. In most experimental scans the collimators C2 and C3 of Fig. 4.5 were removed and the collimation developed a dependence upon sample orientation in consequence,

so that

$$C_2 = \tan^{-1}\left\{\frac{d_M\left|\cos\theta_M\right| + d_S\left|\cos(\psi-\psi_o)\right|}{2D_{M-S}}\right\} \qquad (10.1)$$

$$C_3 = \tan^{-1}\left\{\frac{d_S\left|\cos(\phi-\psi+\psi_o)\right| + d_A\left|\cos\theta_A\right|}{2D_{S-A}}\right\} \qquad (10.2)$$

where d_M, d_A and d_S are the monochromator, analyser and sample widths respectively. All angles are defined in Fig. 4.5 and ψ_o corresponds to a perpendicular orientation of the planar sample face to the incident beam (i.e. $\vec{k}$ along [ζ00]). From the collimation parameters C_1, C_2, C_3, C_4 and the monochromator and analyser mosaics the resolution ellipsoid (4.22) was constructed. The energy resolution could then be calculated by making suitable projections of the ellipsoid onto the energy axis (see Fig. 4.6) and was found to be in good agreement with the experimental widths. For elastic scattering these widths were between 10 and 14 cm^{-1} FWHM decreasing for neutron energy loss processes to as low as 8 cm^{-1} and increasing to around 20 cm^{-1} on the energy gain side in the experimental region.

Using the experimental configuration described above, i.e. with C2 and C3 absent the count rate for the strongest Bragg peak [110] was 4500 c.p.s. and for the best phonon group 30 c.p.m. above background.

10.2 Acoustic phonon measurements

Phonon groups were observed by the method of 'constant $\vec{Q}$' in the vicinity of several strongly reflecting Bragg points in the reciprocal lattice. From the dynamical structure factors it was apparent that the effects of mosaic were more acute at high $\vec{Q}$ and this is demonstrated well in Fig. 10.1 which shows the blurring of the reciprocal lattice due to the specimen mosaic of 17° FWHM. On this account longitudinal scans were performed in the vicinity of low $\vec{Q}$ Bragg points with high elastic structure factor, i.e. [110], [200], [210], [020], [120] and [310] as shown in Fig. 10.1. The direction of these scans was occasionally limited by

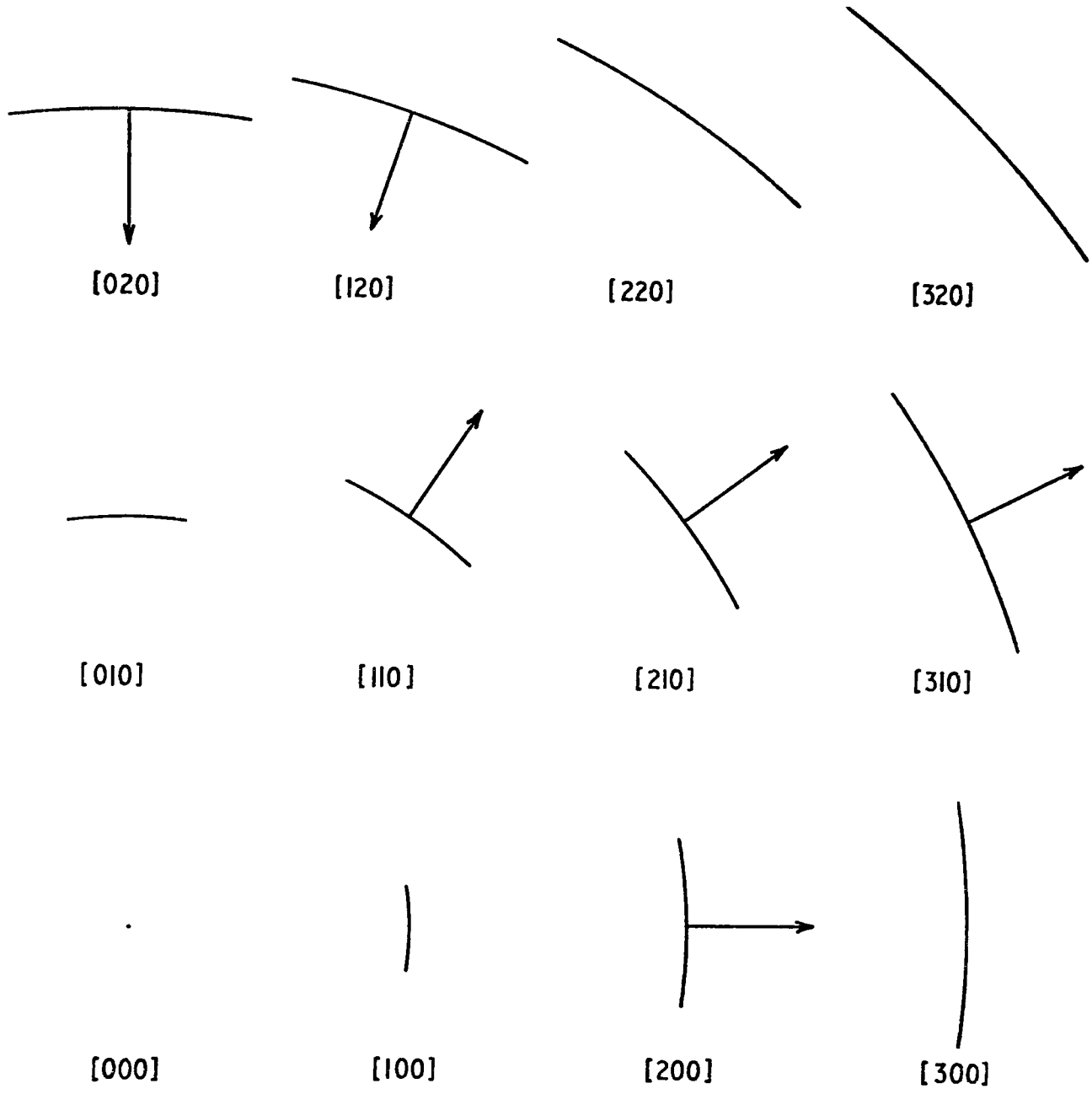

Fig. 10·1 Reciprocal lattice for D.P.E. crystal with mosaic 17^0 FWHM in the basal plane showing the loci of constant $\vec{Q}$ tracks for LA phonons.

interference from neighbouring lattice points as in the case of [020] and [120]. In general scans in a direction away from [000] were preferred on account of the Q^2 dependence of the scalar product term in (3.36) but this was not always possible for the reason mentioned.

Experiments were performed at 77°K and 298°K although more attention was given to the low temperature data in a bid to minimize the effects of anharmonicity and multiphonon contributions to the neutron spectrum. After an exhaustive series of scans around the Bragg points listed above two conclusions were reached:

[1] Acoustic phonons could be measured only in the longitudinal [110], [200] and [020] directions.

[2] Scans for transverse phonons were foiled by the smearing of the reciprocal lattice points as expected from the calculations.

Once these limitations of the mosaic were realised attention was diverted to the measurement of LA phonons in the [ζζo], [ζ00] and [0ζ0] polarizations. Typical constant $\vec{Q}$ scans with neutron energy loss are illustrated in Figs. 10.2 and 10.3 for the last two of these directions. The energy range of phonon measurements was very restricted. At low energies (<15 cm^{-1}) the elastic scattering makes a large contribution to the spectrum disguising any inelastic excitations which at best appeared as shoulders on the elastic peak as in Fig. 10.2. This could be offset to some extent by improving the energy resolution although at some cost to the count rate. High energy (>35 cm^{-1}) measurements were hampered by the lower intensity and greater width of phonon groups well away from the zone centre. Consequently phonon measurements generally spanned a third of the zone and were in most cases only sufficient to define an acoustic slope.

Much attention was given to the problem of extracting the phonon groups from the background which came mainly from incoherent elastic scattering. Various analytical forms were employed to describe both the phonon group and the residual scattering in attempts at a deconvolution of the two contributions

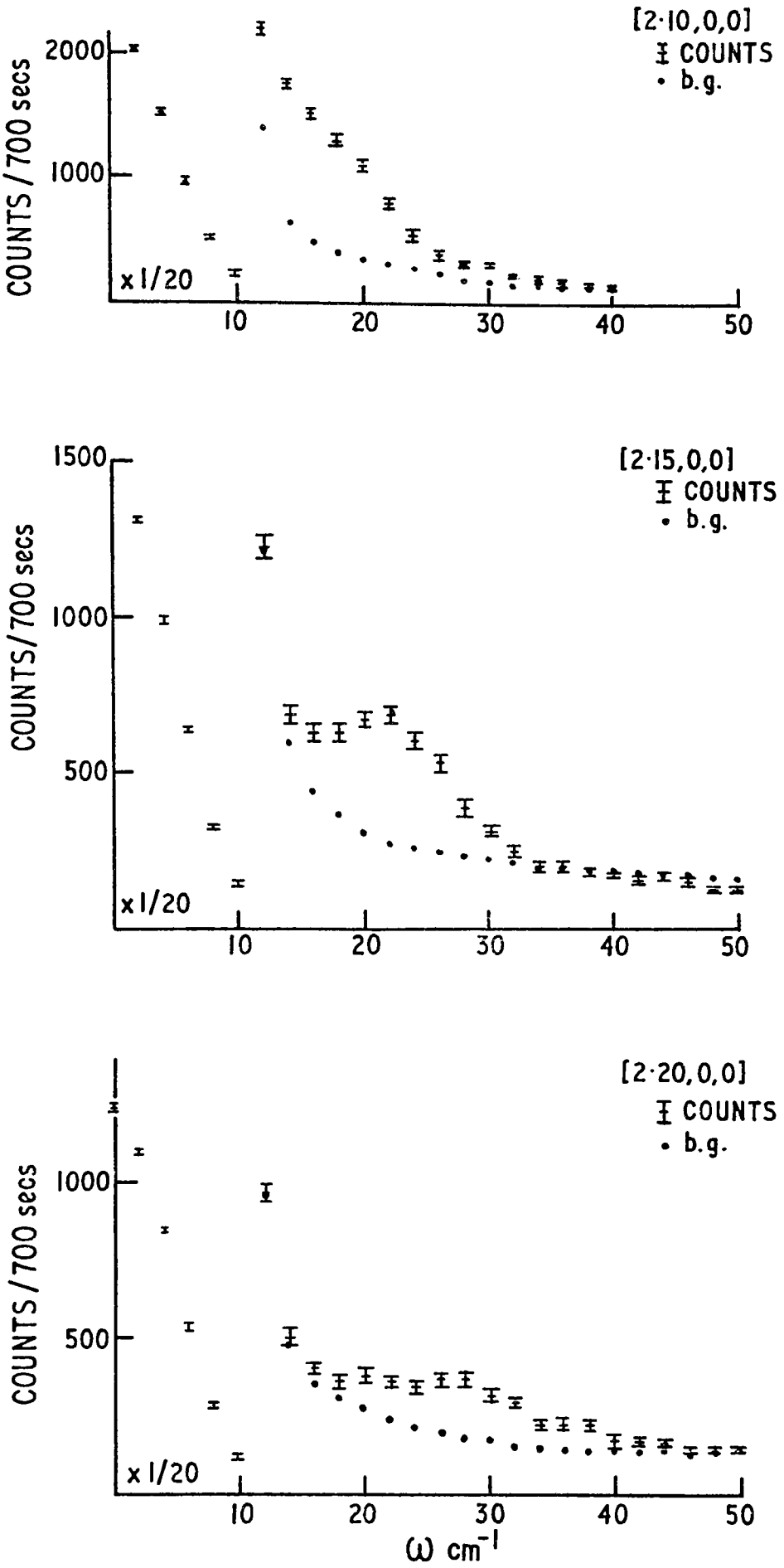

Fig. 10·2 Neutron energy loss spectra at constant $\vec{Q}$ sites along [ξ00] for single crystal texture D.P.E. at 77°K.

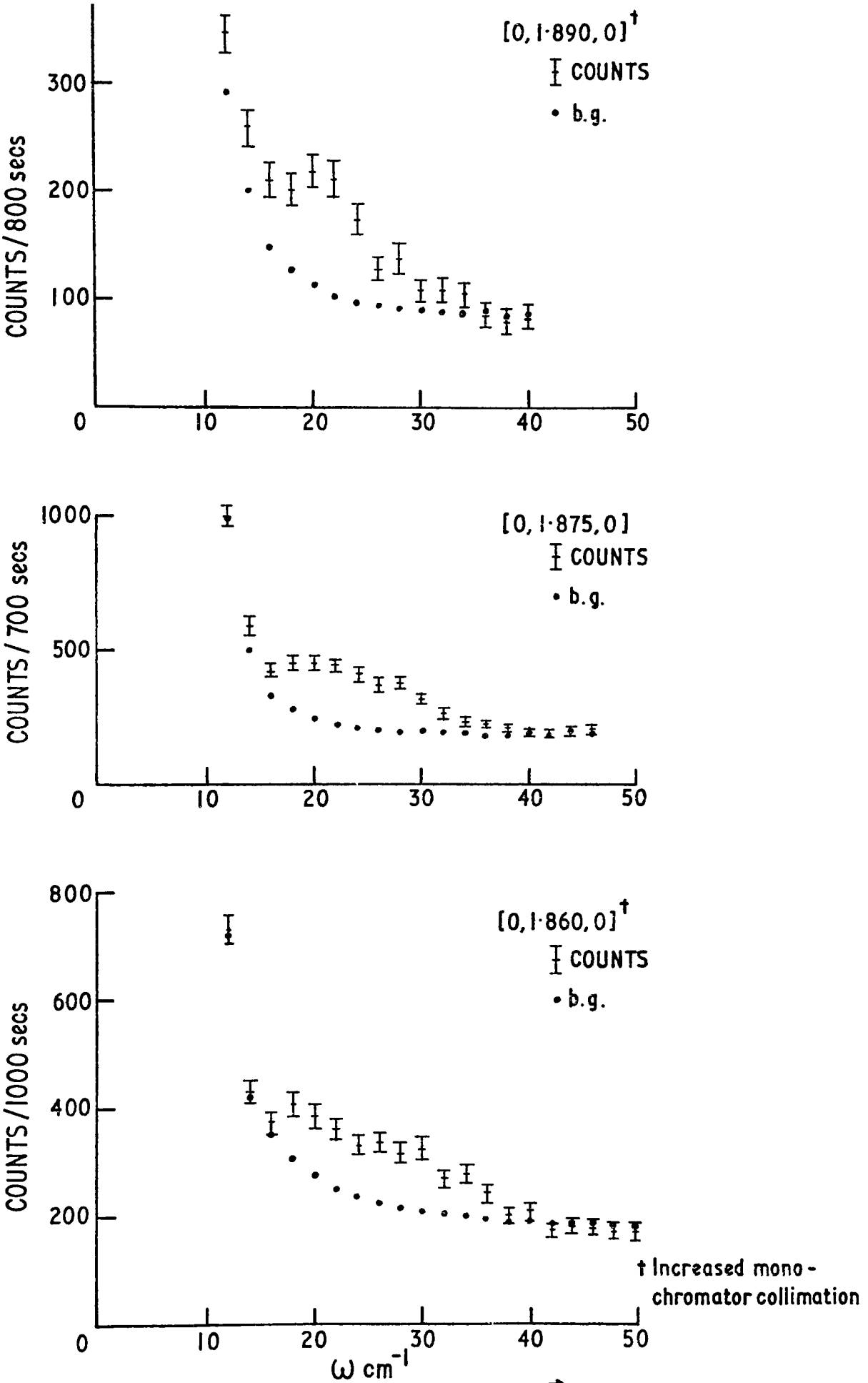

Fig. 10·3 Neutron energy loss spectra at constant $\vec{Q}$ sites along [0ξ0] for single crystal texture D.P.E. at 77°K

by fitting to the total energy spectrum. Normally the phonon shape can be equated to the energy resolution profile and a fitting procedure involving parameters of two Gaussians and a sloping background is sufficient to reproduce the spectrum. Mosaic introduces additional parameters in any fitting procedure related to the shape of the phonon group. Since the shape of the excitation is an experimental unknown such fitting procedures become very sensitive to the analytical form employed for the phonon group. Provided that the functional description of the background is known to be accurate and contains but few parameters it is likely that a fitting procedure could discriminate between different analytical forms for the phonon. Unfortunately the Gaussian description of the elastic scattering component of the background was found to be inadequate since the examination of constant $\vec{Q}$ scans performed well away from the zone centre where the phonon contribution had disappeared revealed an additional component in the low energy spectrum. This component could be accommodated only by increasing the number of parameters in the background formula to allow for the aspect of the elastic peak which introduces a sizeable wing extending out to four standard deviations. Physically the origin of such a quasielastic contribution is obscure but it may possibly be associated with the amorphous regions of the polymer which account for 30% of the sample. At any rate this phenomenon introduced a complication which proved too much for the fitting procedures. Although several analytical forms were tried, including various leaning Gaussian functions for the phonon group and several polynomials for the background, it was concluded that the amount of experimental data available in a typical scan was insufficient to define the relevant functional parameters in a unique sense. Thus for a set of data such as in Fig. 10.2 which shows a continuous shift of the inelastic excitation to higher energy the fitted backgrounds, peak widths and positions gave a poor reflexion of this continuity. Consequently this procedure was abandoned and a different approach to the formulation of the background adopted. It

was assumed that the shape of the background scattering profile was constant for a series of constant $\vec{Q}$ scans along a line in reciprocal space, after the subtraction of a linear function. In this approximation the background counts B(E) could be constructed from the renormalized energy spectrum C'(E) taken at a point so distant from the reciprocal lattice point that the phonon contribution had disappeared

$$B(E) = \alpha B'(E) + \beta E + \gamma \tag{10.3}$$

where

$$B'(E) = C'(E) - \beta' E - \gamma' \tag{10.4}$$

and the parameter α is derived from the ratio of the elastic peak heights

$$\alpha = (C(0)-\gamma)/(C'(0)-\gamma') \tag{10.5}$$

Backgrounds calculated in this way are reproduced in Figs. 10.2 and 10.3. Peak positions derived on this basis are in much better agreement with the limits that can be set by inspection than the values obtained previously by fitting procedures.

Experimental phonon groups located in this manner are assembled in Fig. 10.4 as plots of phonon frequency against phase angle (9.15) along the [0ζ0], [ζζ0] and [ζ00] directions. There are several noteworthy features which appeal to the calculations for elucidation. Firstly the data cover at most only half the zone. In parallel with the sharp fall in intensity there is a marked broadening in the widths of the observed groups across the zone, which is reflected by the increased amplitude of the error bars in Fig. 10.4. In the case of the [0ζ0] data this broadening is suggestive of a splitting into two separate contributions (see Fig. 10.3) although on account of the poor statistics obtained in the region of interest no definite conclusion can be made on this issue. Furthermore the [ζ00] data show a rather sudden departure from a linear dispersion relationship around the half zone mark, which suggests the emergence of a contribution secondary to the LA component of the experimental phonon group and at lower frequency.

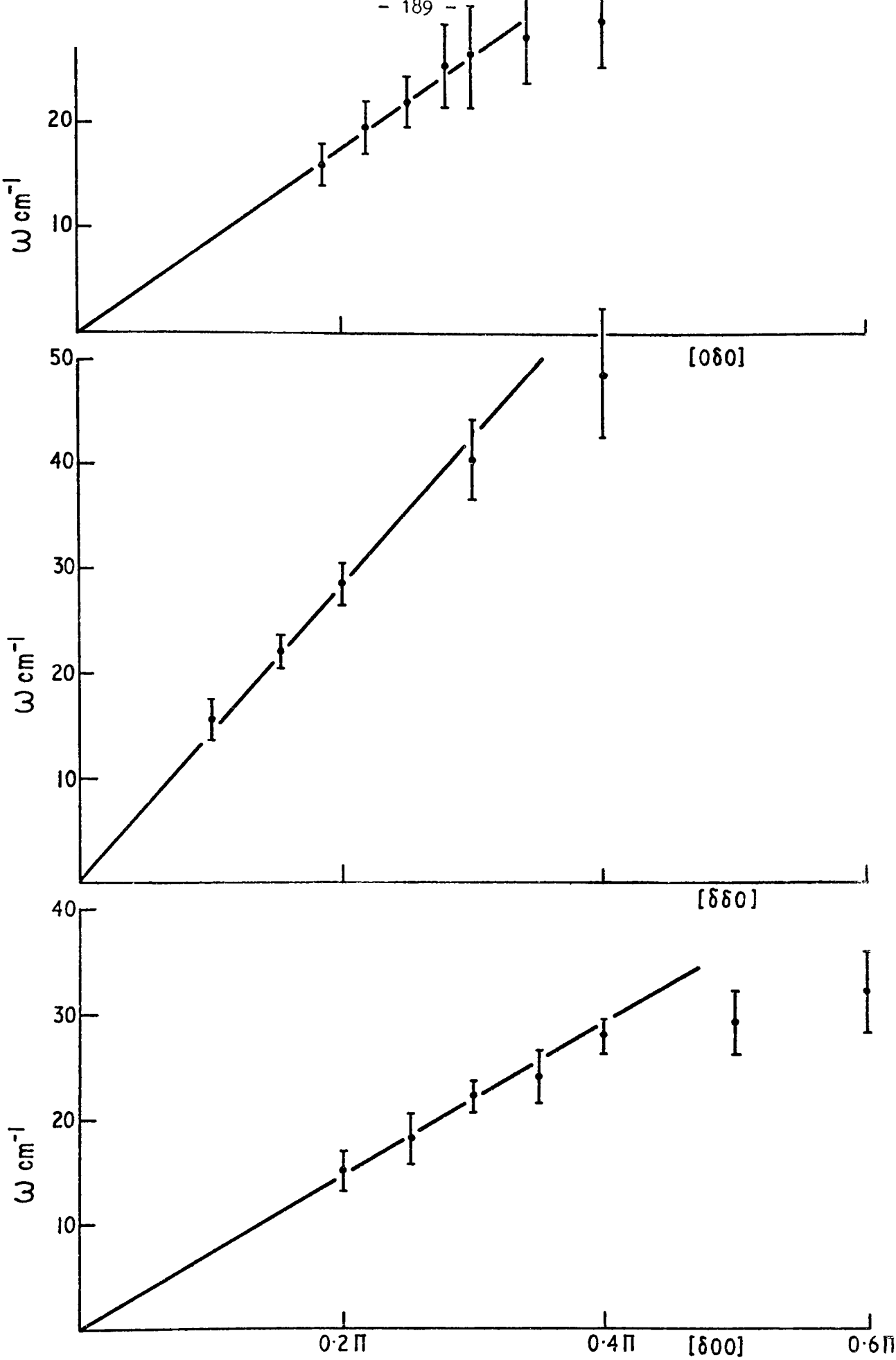

Fig. 10·4 Experimental phonon groups parametrised by the phase angle $[\delta_a \delta_b 0]$ derived from the geometry of the co-linear configuration of $\vec{Q}$, $\vec{q}$ and $2\Pi\vec{\tau}$ in Fig. 10·5 [a].

Calculations of the mosaic broadened phonon excitations based on the potential parameter model provide an insight into these effects. The total coherent inelastic cross section must be written as a sum over the configurations illustrated in Fig. 10.5[a]. From such summations it appears that the $\vec{q}$ components inclined to $\vec{Q}$ about the arc defined by the lattice vectors can in some circumstances contribute towards a singularity in the total cross section supplementary to the expected term from LA modes excited parallel to $\vec{Q}$. Such contributions arise from the generally termed transverse acoustic (TA) mode which is always of lower frequency than its longitudinal counterpart at a particular $\vec{q}$ value and involves the shearing of [hk0] planes in the basal plane of polyethylene. The relative contribution of these components is very sensitive to the choice of reciprocal lattice point for phonon scans. In Figs. 10.5[b] and 10.5[c] the calculated structure factors for longitudinal (LA) and transverse (TA) ab polarized normal modes excited in the vicinity of [110] and [020] Bragg points are shown for the series of $\vec{q}$ values parametrized by the mosaic angle θ of Fig. 10.5[a]. The function $F_j(\theta)$ is defined from (3.36) as

$$F_j(\theta) = G(\theta)\left|g_j(\vec{Q})\right|^2(n_{\vec{q}j}+1)\delta(\vec{Q}+\vec{q}-2\pi\vec{\tau})_\theta \qquad (10.6)$$

where $G(\theta)$ is a triangular approximation to a Gaussian function of FWHM equal to the mosaic spread of 17^o

$$G(\theta) = 1.0-|\theta|/17 \qquad -17<\theta<17^o \qquad (10.7)$$

which weights the structure factors of the configurations defined in Fig. 10.5[a] as a function of θ. The relative importance of LA and TA phonon contributions can be assessed from the areas enclosed in Figs. 10.5[b] and 10.5[c]. Frequency distributions derived by summing $F_j(\theta)$ for all θ and j, folding the resulting histogram with the resolution function and multiplying by an arbitrary constant are shown in Fig. 10.6 together with the observed groups for comparison. It appears from Fig. 10.6 that the calculations

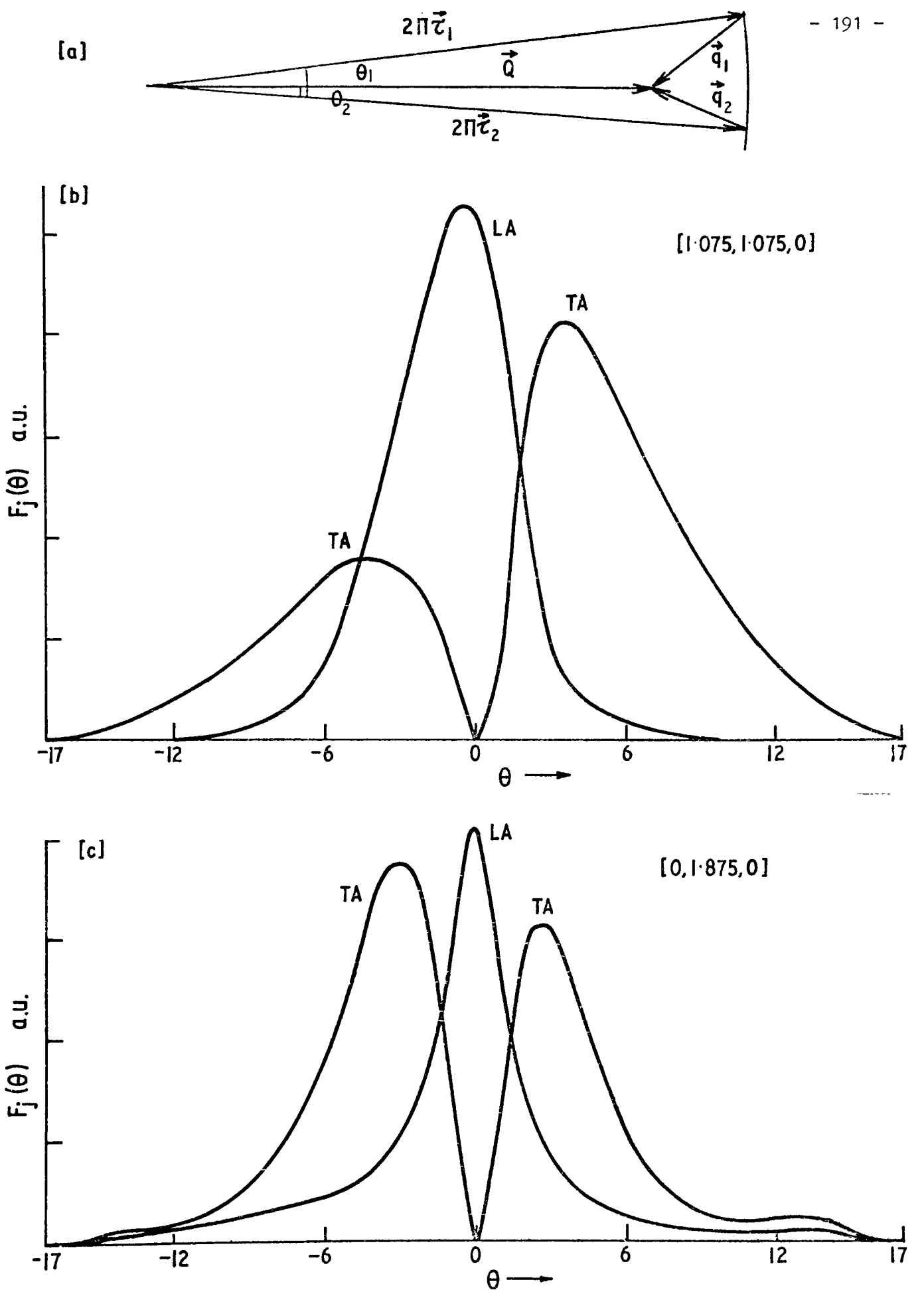

Fig. 10·5 [a] Scattering diagram illustrating the range of $\vec{q}$ vectors generated at constant $\vec{Q}$ by the mosaic spread of $2\pi\vec{\tau}$

[b] Polar variation of $F_j(\theta)$ for LA and TA modes excited at [1·075, 1·075, 0]

[c] Polar variation of $F_j(\theta)$ for LA and TA modes excited at [0, 1·875, 0]

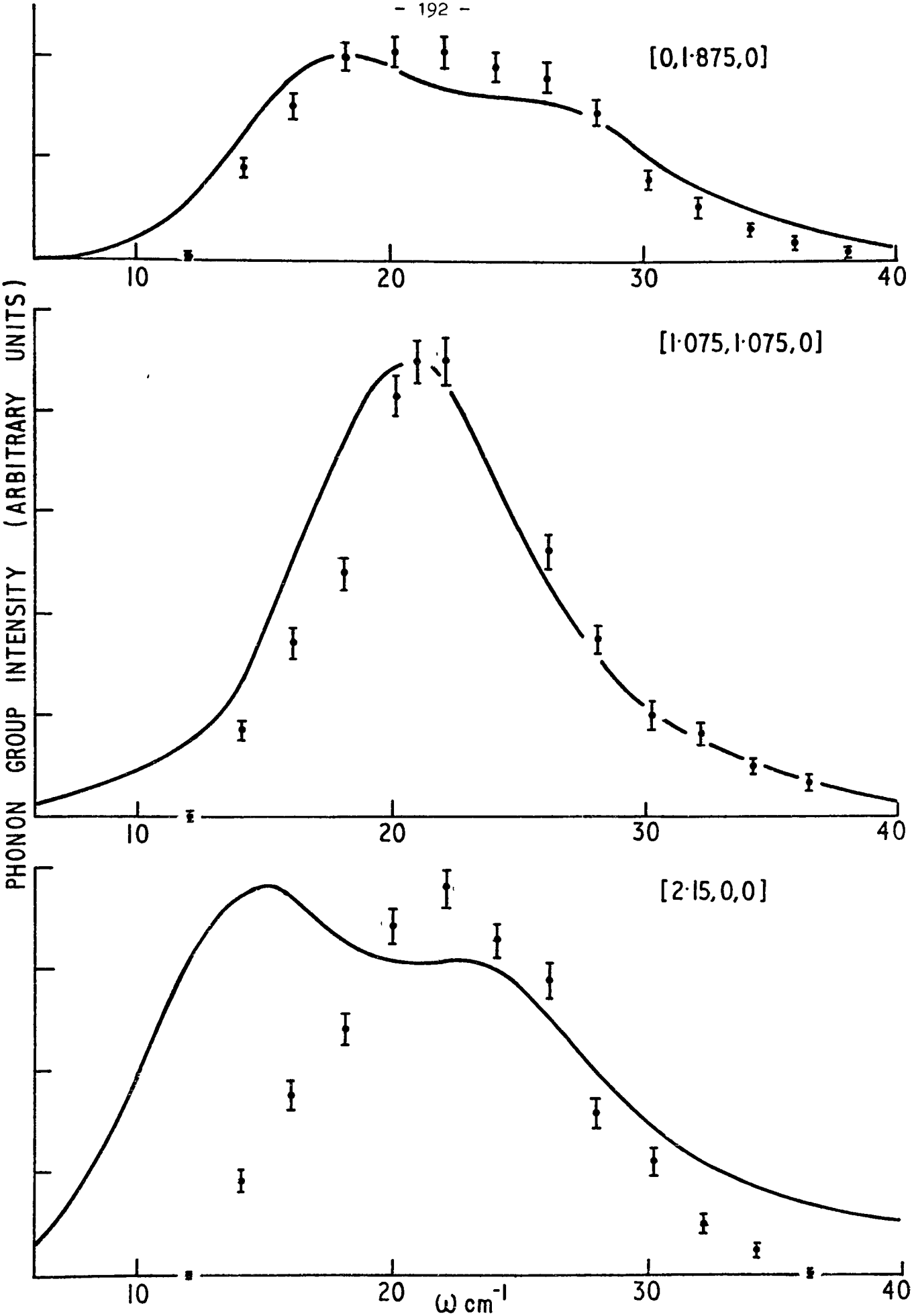

Fig. 10·6 Calculated (—) and observed (⊺) phonon groups for D.P.E. with basal plane mosaic 17° FWHM.

enjoy some success in the reproduction of [0ζ0] and [ζζ0] experimental groups. The large widths of [0ζ0] groups are then explicable since the calculations predict that [ζζ0] TA and [0ζ0] LA phonons contribute to the total cross section with about equal weight to give broad doublets, suggested to some extent by the experimental data of Fig. 10.3. Again the [ζζ0] data are very closely reproduced by the calculations which confirm that the LA component predominates in the total cross section. For the [ζ00] data there is a serious discrepancy between the observed peak and the calculated profile, which is much broader and shifted to lower frequency. The balance between TA and LA components is very delicate along [ζ00] with the calculated width a sensitive function of $\vec{q}$ as the dominant contribution changes from the higher energy (LA) to the lower energy (TA) mode. From the discrepancy between calculation and experiment it would appear that the calculations fail in their prediction of the exact site along [ζ00] at which the TA mode begins to contribute significantly. Experimental widths for the [ζ00], [ζζ0] and [0ζ0] groups are plotted as a function of energy in Fig. 10.7. Clearly the widths group into two categories of which the narrower type most likely characterize pure LA excitations whereas the broader group pertain to mixed LA-TA excitations. In the case of [ζ00] groups the widths increase gradually up to [2.25,0,0] where there is a sudden jump from 14 to 20 cm^{-1}. This discontinuity is reflected in Fig. 10.4 by a sharp departure from the linear dispersion relationship at [2.25,0,0]. On this basis it is reasonable to postulate that the [ζ00] groups retain their LA character up to this point and thereafter become a synthesis of TA and LA modes with a consequent downward shift in the peak centre frequency and increase in peak width.

Summarizing there are three acoustic slopes definable from the experimental data at 77°K. Two of these can be related to single branches of the interchain dispersion curves although the third must be seen as a combination of two such branches in equivocal ratio. Elastic constants of 11.5 and

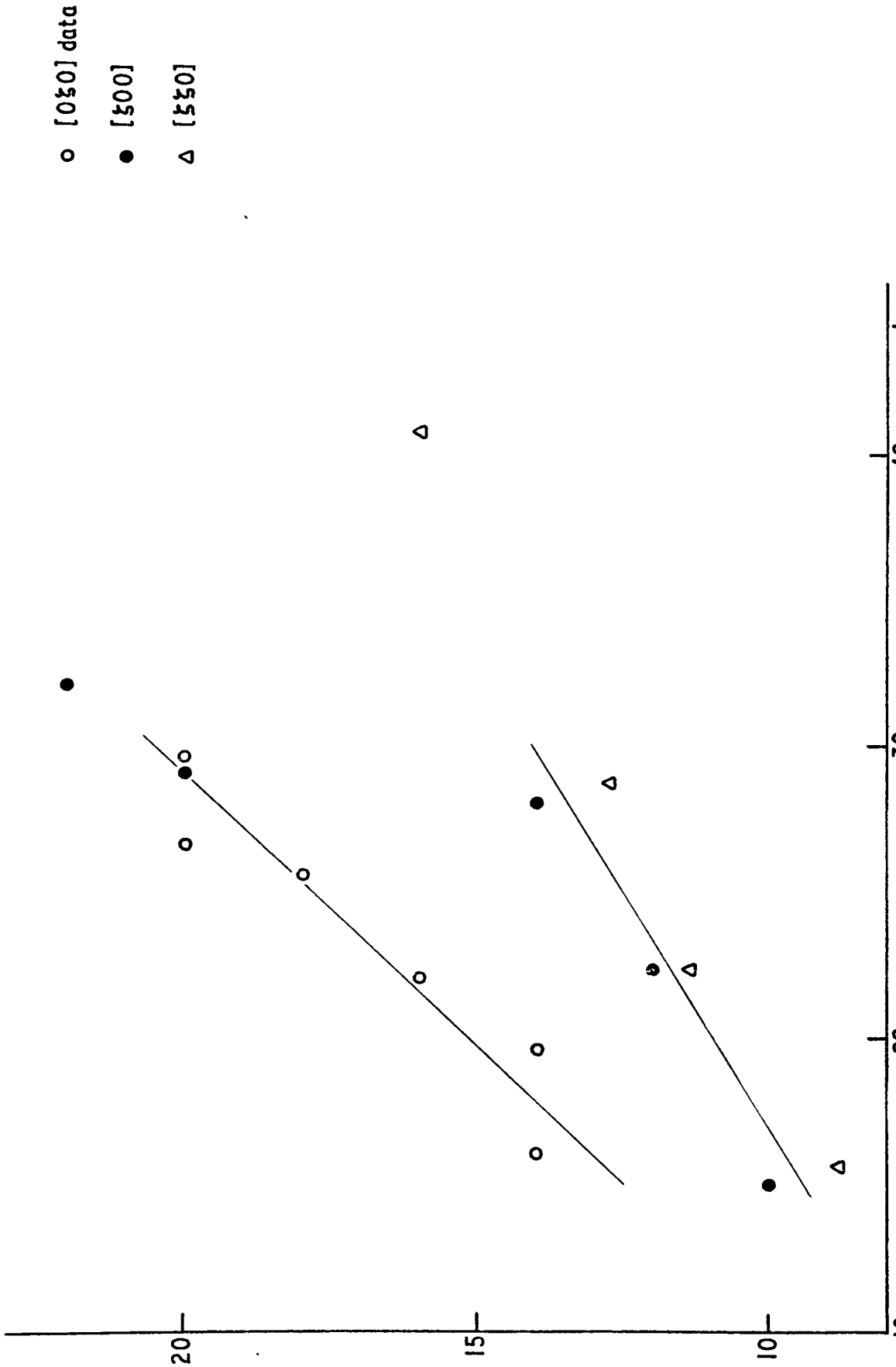

Fig. 10·7 Experimental phonon group widths assembled as a function of their energy for [ξ00], [ξξ0] and [0ξ0] groups.

14.2×10^{10} dyne cm^{-2} were determined from the calculated slopes along the [ζ00] and [ζζ0] directions at 77°K, with an error of 6% representing a 3% estimated error in the acoustic slope determination. An elastic constant of 6.5×10^{10} dyne cm^{-2} was derived from the [0ζ0] data with the assumption that the observed phonons represented an exact mean of the [0ζ0] LA and [ζζ0] TA branches employed in defining a mean phonon wave vector.

Finally experimental data at room temperature for [ζζ0] LA phonons are reproduced in Fig. 10.8 together with the singularities reported in Chapter 7 and obtained from the uniaxially oriented D.P.E. As can be seen the two sets of data are in good agreement, defining moduli of 13.5±0.8 and $15\pm3\times10^{10}$ dyne cm^{-2} respectively at 298°K. This lends support to the arguments used in Chapter 7 for the assignment of the singularities observed in polycrystalline and uniaxially oriented D.P.E.

10.3 Zone centre mode investigation

Zone centre normal modes were investigated by a series of constant $\vec{Q}$ scans at reciprocal lattice points [hko] in the basal plane of the polymer. Dynamical structure factors were calculated at various lattice points so that constant $\vec{Q}$ scans enhancing particular modes could be selected. Since all the normal modes in question approach the zone centre with zero slope the effects of sample mosaic are much less severe than those obtained in the last section for acoustic phonons. Table 10.1 assembles dynamical structure factors calculated for zone centre scans at some of the Bragg points chosen for experimental investigation. The region of $\vec{Q}$ space suitable for such scans is limited on the low $\vec{Q}$ side by the small Bragg angles, which lead to contamination of the scattered counts by the straight through beam, and on the high $\vec{Q}$ side by the increasing significance of sample mosaic. Consequently although the B_{2u} mode appears in strength only at [100] this lattice point is inaccessible to the experiment for the first reason. Of the remaining ab-polarized modes, B_{3g}, B_{1u} and A_g are enhanced at the [300], [010] and [120] Bragg points respectively.

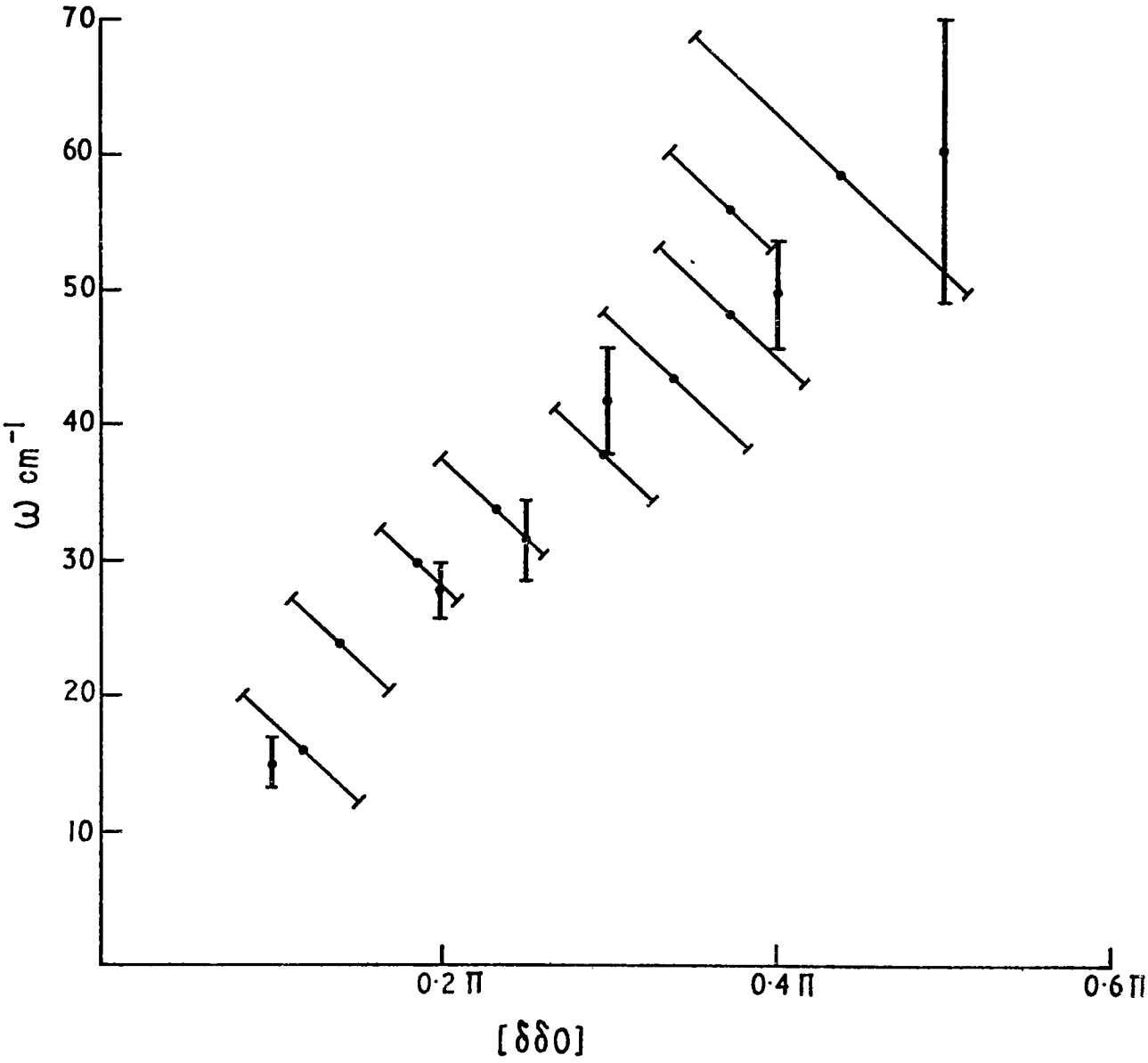

Fig. 10·8 Experimental LA phonon groups along [ζζ0] from time-of-flight experiments (↖↘) on c-oriented D.P.E. compared with those derived from triple axis constant $\vec{Q}$ scans (I) on single crystal texture D.P.E., both at 298°K

Table 10.1 Calculated dynamical structure factors for zone centre scans at [hkO] in D.P.E.

Mode	ω † cm^{-1}	$\lvert g_j(\vec{Q})\rvert^2 (n_{oj}+1)$		
		[010]	[300]	[120]
B_{3g}	74.7	183	1947	310
B_{1u}	76.8	1308	0	25
B_{2u}	96.1	0	474	2
A_g	105.1	0	0	2488

†Calculated Williams set VII.

From the calculations and results of infrared and Raman spectroscopy these four modes are expected to lie in the region 50-120 cm^{-1} in D.P.E. at 77°K. Choice of a suitable wavelength presents some difficulty. Basically there is an option of down-scattering from short (1.5-2.0 Å) wavelength neutrons or of upscattering neutrons with lower incident energy (~2.5 Å) to attain the energy transfers just mentioned. Two factors enter the deliberations: resolution and higher order contamination. Neutron energy gain processes always involve some defocusing of the resolution ellipsoid with respect to the dispersion surface, so that neutron energy loss is the preferred technique when possible. However since the energy resolution deteriorates as the incident energy increases both options seem to be open. The deciding factor resides in the wavelength selectivity of the filters available for removing higher order contamination from the incident beam. On this basis up-scattering from 2.40 Å neutrons was preferred since this is the wavelength at which a pyrolytic graphite filter operates most efficiently (see 4.4.1).

Zone centre constant $\vec{Q}$ scans taken at [120], [010] and [300] with neutron energy gain are illustrated in Figs. 10.9 and 10.10. Lines have been drawn in to guide the eye by underlining statistically significant singularities. The sharp rise in intensity above 90 cm^{-1} in the [010] scan can be attributed to a contribution from unscattered neutrons which increases as the counter approaches the straight-through beam position. Unfortunately there is no justifiable method for constructing the backgrounds to these scans, all of which are appreciable. Three singularities are clearly evident in the data exhibited. They lie at 72, 96 and 111 cm^{-1} in the [010], [300] and [120] scans respectively. According to the calculated structure factors of Table 10.1 prominent features are expected from B_{1u}, B_{3g} and A_g modes in these respective zone centre scans. On this basis it is reasonable to make assignments using the model predictions since there appears to be only one strong feature in both the calculated and experimental

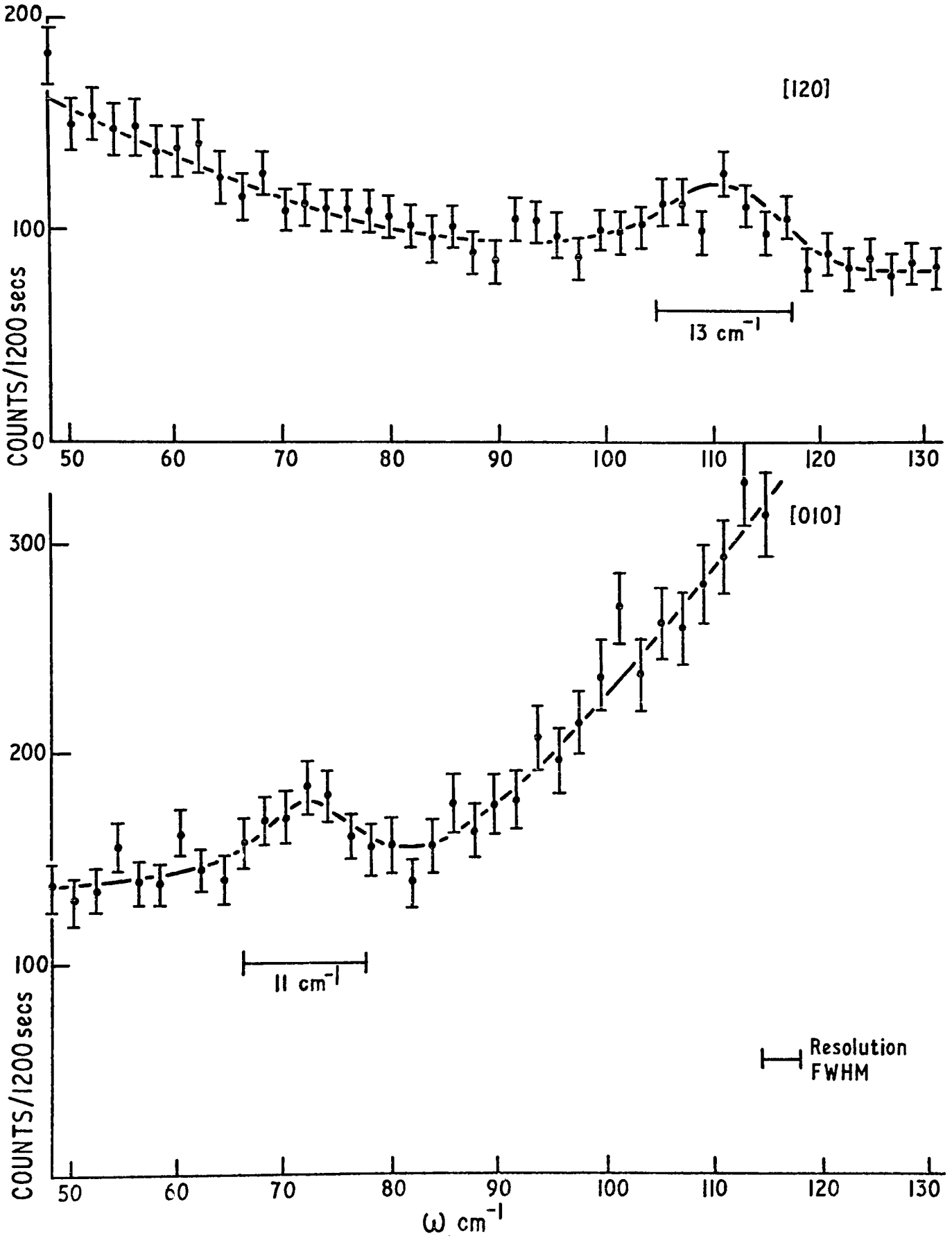

Fig. 10·9 Zone centre constant $\vec{Q}$ scans taken at [120] and [010] with neutron energy gain from D.P.E. at 77°K

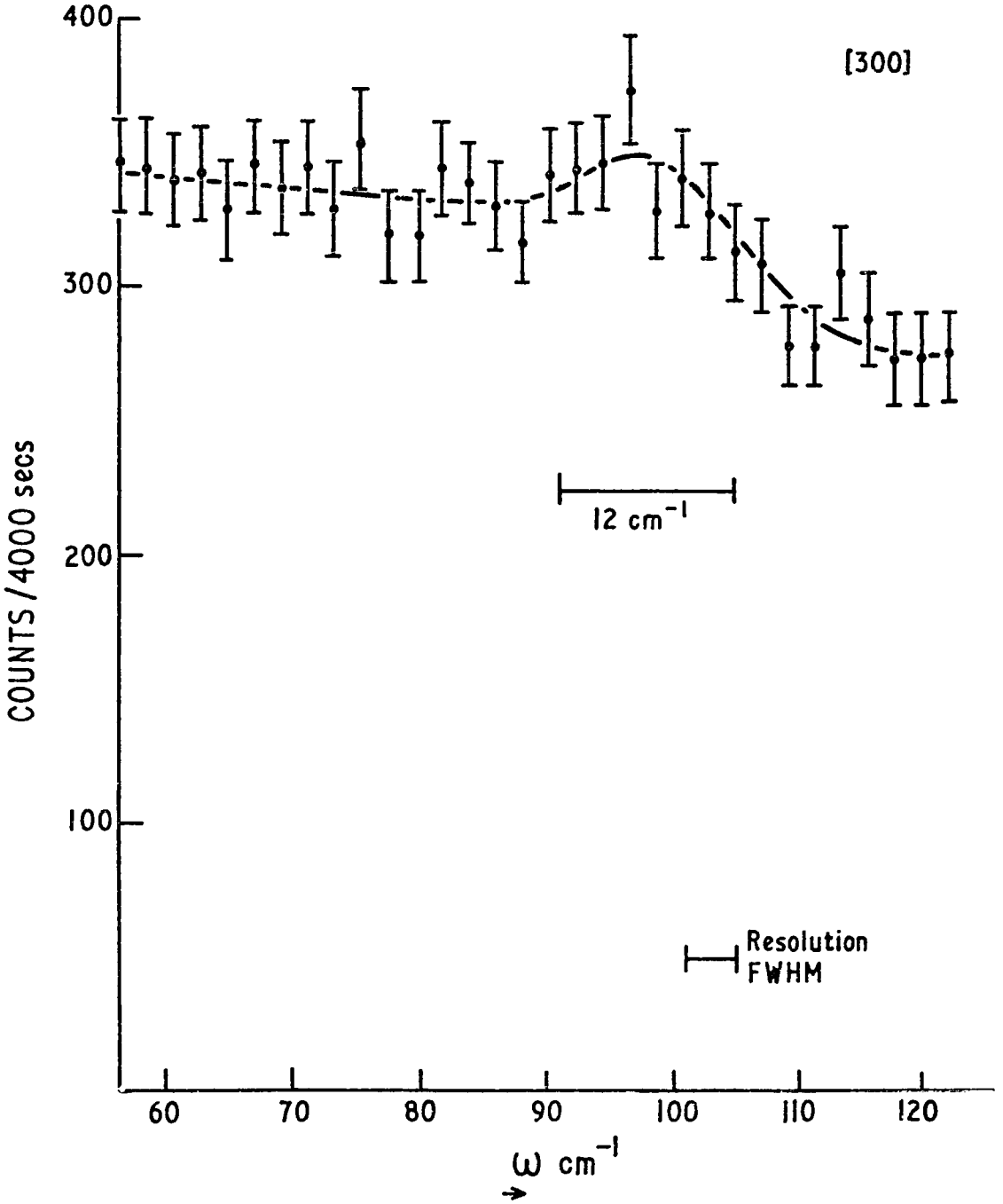

Fig. 10·10 Zone centre constant $\vec{Q}$ scan taken at [300] with neutron energy gain from D.P.E. at 77°K.

scans. Moreover the b-translatory B_{1u} mode has been observed in N.P.E. already by far infrared spectroscopy and so a comparison may be effected after scaling down the frequency [3]. A figure of 75 cm^{-1} ($2^{o}K$) may be contrasted with the value of 72 cm^{-1} ($77^{o}K$) obtained here, which is very satisfactory considering the temperature difference and the inferior resolution (11 cm^{-1} FWHM) of the latter measurement. The assignment of the 111 cm^{-1} mode to the rotatory A_g mode was followed up by the author in conjunction with Harley and Hayes [4] as discussed in 5.2.2. Laser Raman spectroscopy on single crystal textured N.P.E. prepared by the author revealed a band at 136.5 cm^{-1} ($77^{o}K$) with a polarization indicative of A_g symmetry. A figure of 110 cm^{-1} ($77^{o}K$) for D.P.E. can be derived from this measurement, again giving excellent confirmation of the neutron value. This work clears up some of the experimental controversy described in 5.2.2. Finally the 96 cm^{-1} singularity in Fig. 10.10 requires consideration. Assignment to the lower frequency B_{3g} rotatory mode is suggested by the calculations. This would be equivalent to a mode at 119 cm^{-1} in N.P.E. and compares with a figure of 108 cm^{-1} obtained in [4]. Both these figures are lower than earlier claims [5] although they differ by an appreciable increment. Since the Raman work is reasonably conclusive about the B_{3g} assignment on the basis of the observed dichroism some scrutiny of the neutron data is necessary. In particular the B_{2u} translatory mode has been discussed in 5.2.2 and is thought to be around 100 cm^{-1} in D.P.E. from both far infrared studies and the calculations. Table 10.1 indicates that B_{3g} and B_{1u} modes contribute to the [300] spectrum in the ratio 4:1. Since the observed neutron singularity corresponds exactly with the calculated B_{1u} frequency (96.6 cm^{-1}) which has some empirical corroboration, it is evident that more experimental information is required before the postulated assignment of the neutron peak to B_{3g} can be deemed definitive. Such information could be achieved by following the evolution of this singularity into the zone and is yet to be obtained. On this account there is no strong case for challenging the

Raman data which infers a singularity at 87 cm^{-1} (77°K) for the B_{3g} mode in D.P.E.

In summary two zone centre modes have been observed and assigned at 72 (B_{1u}) and 111 (A_g) cm^{-1} for D.P.E. at 77°K. These figures are in excellent agreement with those derived from far infrared and Raman studies of N.P.E. [3, 4]. Furthermore the value of 111 (137) cm^{-1} for the higher frequency rotatory mode in D.P.E. (N.P.E.) is more consistent with the density of states peak at 98 (123) cm^{-1} reported in Chapter 6 and associated with external chain librations [6] than earlier figures of up to 137 (167) cm^{-1} quoted for this mode from Raman data.

10.4 Conclusions

10.4.1 Elastic constants and moduli of polyethylene

Experimental difficulties associated with the mosaic have prevented a complete determination of the elastic constants of polyethylene from acoustic velocities. However the three experimental parameters determined in this work can be compared with the predictions of various models and used to select the optimum set of elastic constants from the calculations. Such a comparison was attempted in 7.6 using the one room temperature elastic constant derived there and seemed to indicate that the force field of Kitagawa was too weak in this context. Apart from the dynamical models constructed in this thesis using Williams set IV and VII pseudopotentials, there are two force fields provided in the literature for the 77°K crystal structure, those of Kitagawa and Miyazawa [7] and Tasumi and Krimm [8]. Both were discussed in 5.2.3 and interchain dispersion curves calculated on a rigid chain model from these two force fields were kindly provided by Dr. D.I. Marsh and were in good agreement with the published data of these authors.

Elastic constants for these models were derived from the acoustic slopes as described in 9.4.4.2 and those relevant to the experimental data are assembled in Table 10.2. The parameters C^{L}_{110} and C^{T}_{110} are the constants

Table 10.2 Calculated and experimental elastic constants for D.P.E. at 77°K

Source	c_{11}	c_{110}^{L}	c_{110}^{T}	$\bar{c}$	c_{22}	E_a	E_b
Kitagawa and Miyazawa [7]	8.1†	11.9	3.2	6.6	11.4	6.7	9.4
Tasumi and Krimm [8]	15.3	19.8	6.0	12.1	20.3	13.5	17.9
Williams set IV	12.5	14.1	3.0	6.3	10.9	8.9	7.8
Williams set VII	12.4	14.0	2.9	6.3	11.1	8.8	7.9
Experimental	11.5	14.2	-	[6.5]	-	-	-

†Units 10^{10} dyne cm^{-2}

obtained from longitudinal and transverse acoustic slopes along [ζζ0]

$$C^{L}_{110} = \frac{d_{110}^{2}}{2}\left\{\frac{c_{11}}{a^2} + \frac{c_{22}}{b^2} + \frac{c_{66}}{a^2} + \frac{c_{66}}{b^2} + \left[\left(\frac{c_{11}}{a^2} + \frac{c_{66}}{b^2} - \frac{c_{22}}{b^2} - \frac{c_{66}}{a^2}\right)^2 + 4\left(\frac{c_{12} + c_{66}}{a^2b^2}\right)^2\right]^{1/2}\right\} \qquad (10.8)$$

$$C^{T}_{110} = \frac{d_{110}^{2}}{2}\left\{\frac{c_{11}}{a^2} + \frac{c_{22}}{b^2} + \frac{c_{66}}{a^2} + \frac{c_{66}}{b^2} - \left[\left(\frac{c_{11}}{a^2} + \frac{c_{66}}{b^2} - \frac{c_{22}}{b^2} - \frac{c_{66}}{a^2}\right)^2 + 4\left(\frac{c_{12} + c_{66}}{a^2b^2}\right)^2\right]^{1/2}\right\} \qquad (10.9)$$

where d_{110} is the spacing of [110] planes in angstroms.

Comparison of the experimental elastic constants derived from the [ζ00] and [ζζ0] data with calculated constants is straightforward as they correspond to c_{11} and c^{L}_{110} respectively. Since the [0ζ0] groups are found to be a compound of [0ζ0] LA and [ζζ0] TA phonons the derived acoustic slope will be intermediate between c_{22} and c^{T}_{110}. The exact nature of this synthesis is an experimental unknown since the two components are not resolved in the data of Fig. 10.3. However the centres of the calculated groups (Fig. 10.6) are generally midway between the two component peak centres and so a mean elastic constant

$$\bar{c} = \frac{1}{4}\left((c^{T}_{110})^{1/2} + (c_{22})^{1/2}\right)^2 \qquad (10.10)$$

can be defined from the models and used in comparisons with the experimental parameter on at least a qualitative basis.

From Table 10.2 it is clear that the best agreement between experiment and model is obtained for the potential parameter calculations which reproduce the experimental constants within little more than the experimental error. It appears that the force fields of Kitagawa and Miyazawa [7] and Tasumi and Krimm [8] are too weak and too strong respectively. Moreover in supporting the potential parameter force field the experimental data are suggestive of a greater isotropy in the interchain forces than has been

suggested by the calculations, as can be seen by comparing c_{11} and c_{22} or E_a and E_b in Table 10.2. Tensile elastic moduli of 9 and 8 x 10^{10} dyne cm^{-2} for compression along the a and b axes are suggested compared with figures of 13.5 and 18 x 10^{10} dyne cm^{-2} derived from the force field of Tasumi and Krimm.

Comparison of these figures with the interchain bulk crystal modulus of 8 x 10^{10} dyne cm^{-2} obtained by Buckley at 77°K shows an exceptional agreement [9]. As explained in 5.2.2 this value was obtained as a mean tensile modulus in the ab plane. Buckley interpreted his experimental data using the model of Takayanagi, Imada and Kajiyama [10] which relates dynamical moduli from creep studies to a tensile elastic modulus perpendicular to the draw direction of an uniaxially oriented specimen. This model assumes that bulk polyethylene contains alternate layers of crystal and amorphous regions which provide component strains inversely proportional to their characteristic modulus when a stress is applied. Such a 'sandwich' model was justified by Buckley on morphological grounds for his specimen which contained planar lamellae stacked along the draw direction and linked by tie molecules, which can be viewed as the amorphous regions (see 5.1.3). The agreement obtained here between the interchain moduli of the microcrystal confirmed by neutron scattering and the bulk crystal modulus of Buckley lends impressive support to such a two phase model of polyethylene from a source quite distinct from the morphological evidence.

10.4.2 Model force fields for polyethylene

It is appropriate to extend the analysis of the last section to cover the model predictions of all the experimental parameters available for the interchain potential, both elastic constants and zone centre frequencies. There are seven such parameters in total from neutron scattering, far infrared and Raman spectroscopy. Of these the B_{2u} translatory mode frequency is taken from [11] and awaits confirmation by dichroism studies and the quantity $\bar{c}$ is

by origin an approximate description of the experimental parameter. The full set of parameters is assembled in Table 10.3 together with the predictions of the four models employed in the last section. All of the figures refer to D.P.E. at 77°K. Strictly the pseudopotential predictions are for the absolute zero structure but in practice lattice frequencies change very little over the temperature range 0-77°K. It is useful to define a function representing the mean percentage deviation of calculated frequencies and elastic constants from the experimental values

$$\prod = \frac{100}{N} \sum_{k}^{N} \frac{|p_k^c - p_k^o|}{p_k^o} \qquad (10.11)$$

where p_k^c and p_k^o are the k-th calculated and observed parameter respectively. Sums restricted to the zone centre frequencies or elastic constants only are labelled $\prod_\omega$ or $\prod_e$ and the latter are constructed from acoustic velocities since they are the actual observables. Values of $\prod$, $\prod_\omega$ and $\prod_e$ are given in Table 10.3 for the potential parameter and Urey-Bradley force models. The predictions of the analytical pseudopotentials are evidently much closer to the experimental situation than those of Kitagawa and Miyazawa [7] although if attention is restricted to just the zone centre frequencies both models give a good fit. The two Urey-Bradley force fields might be expected to reproduce the zone centre frequencies more closely than the elastic constants since they are both fitted to the experimental B_{1u} mode frequency (see 5.2.3). Of these two force fields the best overall fit (9%) is obtained using that of Kitagawa and Miyazawa which is based upon a variety of experimental data. The force field of Tasumi and Krimm is evidently far too strong, calculating parameters on average 19% greater than the experimental values. By contrast the potential parameter models, which do not incorporate any dynamical information at all, reproduce the experimental data of Table 10.3 with an average error of 5%.

Only one experimental parameter seriously conflicts with these calculations, the B_{3g} rotatory mode. This parameter was taken from the Raman data of Harley, Hayes and Twisleton [4] and scaled down for D.P.E. One possible

Table 10.3 Calculated and experimental parameters of the interchain force field of D.P.E. at 77°K

Source	Zone centre mode frequency cm^{-1}				Elastic constant 10^{10} dyne cm^{-2}			Mean error functions %		
	B_{1u}	B_{3g}	B_{2u}	A_g	c_{11}	c_{110}^{L}	$\bar{c}$	Π_ω	Π_e	Π
Experimental	72	87	103	111	11.5	14.2	[6.5]	-	-	-
Williams set IV	75	74	97	106	12.5	14.1	6.3	7.4	2.1	5.1
Williams set VII	77	75	96	105	12.4	14.0	6.3	8.2	2.1	5.6
Kitagawa and Miyazawa [7]	66	96	87	116	8.1	11.9	6.7	9.7	8.7	9.3
Tasumi and Krimm [8]	75	109	104	143	15.3	19.8	12.1	14.8	25.1	19.2

source of error in this work is the near coincidence of this mode (108.0 cm^{-1}) with the infrared active B_{2u} mode which has been assigned at 109.5 cm^{-1} in N.P.E [11]. Translatory and rotatory modes can be readily distinguished by their deuteration shift as in 6.6 and ideally the Raman spectrum of D.P.E. would provide an unambiguous assignment of this mode. Unfortunately the deuterated samples used here were unsuitable for Raman studies since they fluoresced extensively. Until this experiment succeeds an element of doubt will remain about the assignment of the B_{3g} mode.

Experimental data for the zone centre and LA phonon frequencies are assembled in Fig. 10.11 for [ζ00] and [ζζ0] polarizations, together with the phonon dispersion curves calculated from Williams set VII potential parameters. Although experimental measurements are very incomplete, they are evidently in good agreement with the pseudopotential model. On the basis of this agreement it is tempting to make some predictions on the assumption that the model is corroborated as a whole. An isotropy of the modulus for compression perpendicular to the chains is one such prediction discussed in the last section and it is to be hoped that the experimental corroboration of this dynamical model will prove useful in other fields.

Considering the quantity of experimental information available it is rather difficult to speculate upon the importance of the assumptions enumerated in 1.3 as basic to the pseudopotential approach. One significant feature however is the poorer reproduction of the zone centre frequencies (8%) compared to the excellent fit derived for the elastic constants (2%) by the pseudopotential models. Possibly this is a reflection of the approximation of molecular rigidity. Pawley and Cyvin [12] show that this approximation has the greatest effect upon the highest frequency external modes. Moreover Reynolds, Kjems and White [13, 14] obtain the same effect in p-dichlorobenzene where their atom-atom potential gives a close reproduction of the experimental data for acoustic modes but is less successful for the optical branches. Even with this reservation the pseudopotential

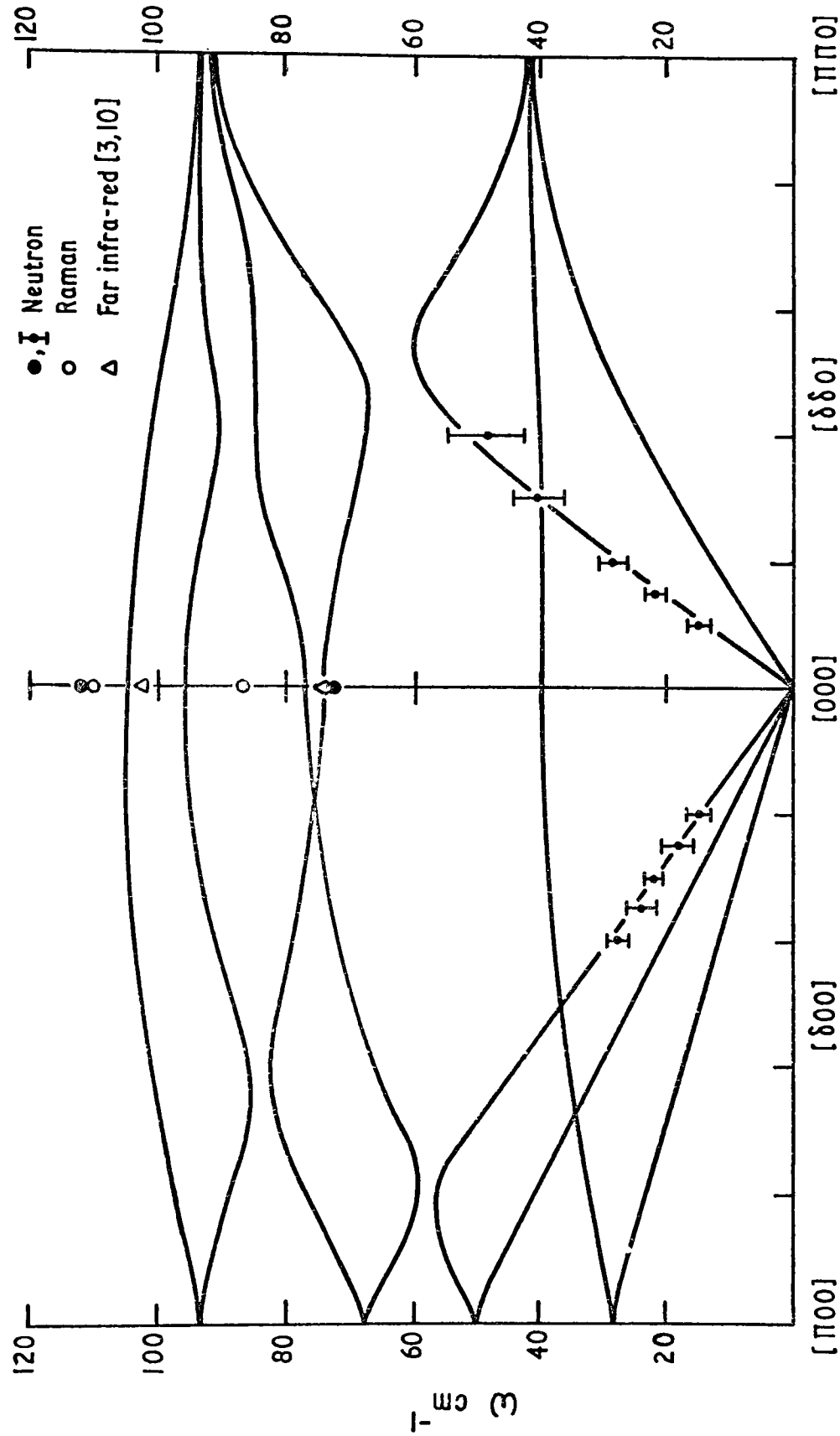

Fig. 10·11 Phonon dispersion curves for D.P.E. along [ξ00] and [ξξ0] calculated from Williams set VII potential parameters together with the available experimental data at 77°K.

predictions are undoubtedly more substantiated by experiment than those of the Urey-Bradley force fields. Since the latter models actually rely upon some dynamical information for their construction it is especially significant that the pseudopotentials should provide the better fit, a fit that extends back from the dynamics to a whole range of structural and thermodynamic parameters.

References

[1] D.H. Saunderson, A.E.R.E. rep. USS/P.21 1971.

[2] M.J. Cooper and R. Nathans, Acta Cryst., 23, 357 1967.

[3] S. Krimm and M.I. Bank, J. Chem. Phys., 42, 4059 1965.

[4] R.T. Harley, W. Hayes and J.F. Twisleton, J. Phys. C 6, 167 1973.

[5] R.F. Shaufele, private communication to T. Kitagawa.

[6] J.F. Twisleton and J.W. White, 'Neutron Inelastic scattering', IAEA, Grenoble, p. 301 1972.

[7] T. Kitagawa and Miyazawa, Jap. Polym. J., 1, 471 1970.

[8] M. Tasumi and S. Krimm, J. Chem. Phys., 46, 755 1967.

[9] C.P. Buckley, D.Phil. thesis, Oxford University 1972.

[10] M. Takayanagi, K. Imada and T. Kajiyama, J. Poly. Sci. C, 15, 263 1966.

[11] G.D. Dean and D.H. Martin, J. Chem. Phys. Lett., 1, 415 1967.

[12] G.S. Pawley and S.J. Cyvin, J. Chem. Phys., 52, 4073 1970.

[13] P.A. Reynolds, J.K. Kjems and J.W. White, 'Neutron inelastic scattering', IAEA, Grenoble, 195 1972.

[14] P.A. Reynolds, D. Phil. thesis, Oxford University 1972.

Chapter 11

NEUTRON SCATTERING STUDIES OF POLYTETRAFLUOROETHYLENE

11.1 Introduction

Polytetrafluoroethylene (P.T.F.E.) is a well characterized relative of polyethylene possessing many properties of commercial and scientific interest which have already been contrasted with those of polyethylene. Among these properties the high melting point and low coefficient of friction have attracted most attention and are responsible for the widespread applications of the polymer under the brand name 'Fluon' and its American relative 'Teflon'. Before cataloguing the structural and dynamical information at present available for P.T.F.E. it should be noted that the carbon and fluorine atoms possess almost wholly coherent neutron cross sections, making this polymer an attractive system for neutron scattering studies of the type just described for deuteropolyethylene [1].

Wide angle X-ray diffraction studies [2-6] confirm the helical structure of the P.T.F.E. molecule. Three phases have been identified. Below 19°C the chains possess a repeat unit of 13 CF_2 units coiled in six turns of a helix. However there is considerable controversy about the crystal structure of this phase. Triclinic, monoclinic and hexagonal unit cells containing one chain molecule have been predicted by different workers from the analysis of X-ray diffraction data [2, 3, 5]. More recently a monoclinic structure with two chains in the unit cell was suggested on the basis of the far infrared spectrum [7] and some observed splittings of assigned intrachain modes in the Raman spectrum of this phase [8]. The debate continues. In a first order transition at 19°C the helix untwists slightly from 13/6 to 15/7 and the X-ray diffraction spots become more diffuse. The crystal structure is known to be hexagonal with one chain molecule in the unit cell [2, 5]. Although the helix is well defined there is some disorder about the chain axis so that the setting angle about this

axis has not been defined. This explains the broadening of lines in the diffraction pattern. Above 30°C the helices become gradually disordered but the hexagonal stacking of the chains apparently persists up to and even into the melt.

Many of the unique properties of P.T.F.E. can be attributed in some way to the rod-like shape of a helical fluorocarbon chain which contrasts with the planar zig-zag conformation adopted in the long chain hydrocarbon system. Projections along and perpendicular to the axis of the 13/6 helix are illustrated in Fig. 11.1 and demonstrate the almost cylindrical shape of P.T.F.E. molecules. Moreover electron micrography [9] has confirmed that P.T.F.E. crystallizes to give straight chain segments of length between 2,000 and 10,000 Å in sharp contrast to the spherulitic growth from the melt common to most hydrocarbon polymers, in which chain folding plays an important role. A popular explanation for this behaviour resides in the unusual stiffness of fluorocarbon chains, confirmed by conformational calculations which also highlight the nonbonded fluorine-fluorine interactions as a principal factor determining the helical structure [2, 10-12]. Consequently P.T.F.E. melts are thought to contain 'bundles' of extended chain molecules which encourage the growth of larger crystals and explain the low entropy of fusion and high melting point [13].

Much attention has been given to dynamical aspects of the two phase transitions. Clark and Muus [5] have proposed a mechanism for dynamic disorder based upon X-ray diffraction and nuclear magnetic resonance [14] studies of the three phases in both isotropic and uniaxially oriented P.T.F.E. The observed molecular disorder in the middle phase is attributed to torsional oscillations of large amplitude about the chain axis with the mean atomic positions still ordered on a 15/7 helix. At the second transition complete loss of this order and the onset of translational motion in the chain direction are predicted. No information about the potential barriers for hindered rotatory or translatory displacements is derived in

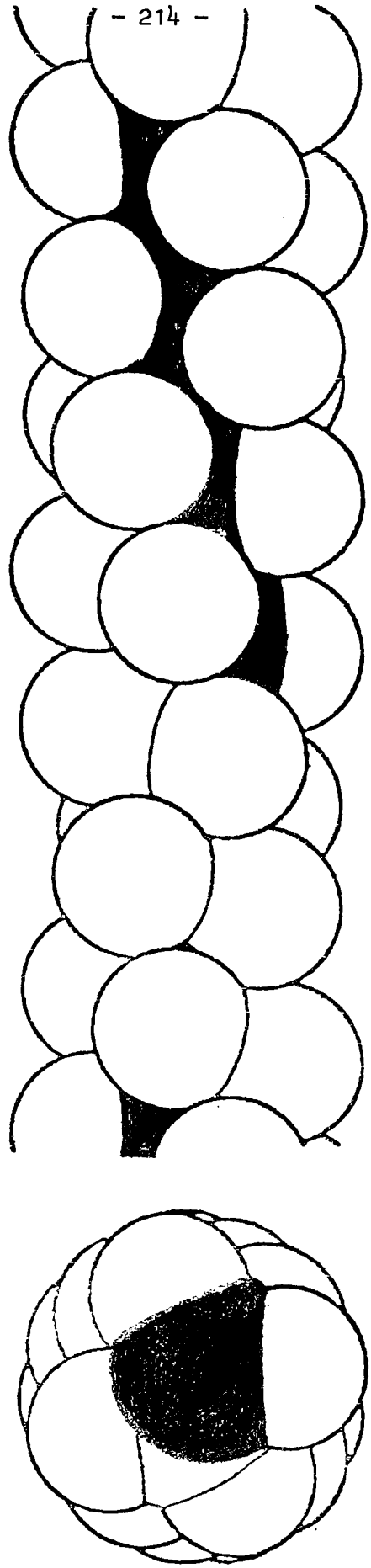

Fig. II·1 Projections along and perpendicular to the axis of a P.T.F.E. molecule in the low temperature phase. Shaded and unshaded regions correspond to carbon and fluorine atoms respectively assembled on a 13/6 helix.

their qualitative analysis. Recent neutron diffraction studies of Teflon fibres [6] suggest that there is appreciable static disorder perpendicular to the chain axes in all three phases of P.T.F.E. in addition to the dynamic disorder inferred from N.M.R. for the two high temperature phases [14].

Spectroscopic studies of P.T.F.E. have so far been mainly restricted to the intrachain modes. Infrared and Raman data [15-17] have been assigned with the assistance of normal mode calculations for an isolated chain [18-22]. There is still considerable confusion about the assignments mainly because the number of peaks observed exceeds the number predicted on the basis of the selection rules for electromagnetically induced transitions derived for an isolated chain. The extra peaks have been attributed to defect-induced transitions [20] and crystal field effects were recently invoked to explain some of the observed multiplet excitations in the low temperature phase [8]. This explanation involved the postulate of a unit cell containing two chains and has been contested by Piseri, Powell and Dolling [22]. They suggest that the different symmetries of chain molecules and the proposed unit cells are sufficient to relax the isolated chain selection rules without the postulate of a bimolecular basis. Finally Johnson and Rabolt [7] have observed four lines in the far infrared spectrum of P.T.F.E. below 100 cm^{-1} which they assign to lattice modes. These data are peculiar to the low temperature phase and have been used to support the two-chain unit cell.

Neutron time-of-flight spectra of moulded P.T.F.E. have been reported by Safford and Naumann [23]. In this work many singularities are located and the coincidence of a fraction of these with some singularities derived from an early model of the isolated chain dynamics is noted. Since the singularities are regarded as part of the incoherent spectrum and the model is based on a planar chain skeleton the suggested assignments are very questionable. Lagarde, Prask and Trevino [24] have measured part of the LA chain mode of P.T.F.E. in the hexagonal phase at 25°C by applying triple

axis techniques to Teflon fibres in work analogous to that of Feldkamp et al. described earlier for D.P.E. [25]. This measurement encouraged a refinement in the intrachain force field [19]. More recently Piseri, Powell and Dolling [22] extended these measurements on the uniaxially oriented material at 25°C and found poor agreement between the observed phonon structure factors and those calculated from an isolated chain model. From these discrepancies they concluded that the interchain force field must be taken into account in deriving selection rules for both electromagnetic and neutron spectroscopy. A model for the chain phonons was constructed with the inclusion of an interchain potential and the dynamical structure factors were recalculated. Changes in the structure factors were in the right direction but too small to give a satisfactory explanation of the observed neutron scattering data. However the interchain potential used had a rather weak empirical basis [12] and it is possible that a more realistic force field used in conjunction with the present intrachain potential function could provide better agreement with their experimental data.

It appears that structural and dynamical studies of P.T.F.E. although extensive to date have raised more questions than they have answered. Most spectroscopic attention has been given to the intrachain vibrations but it is clear that the interpretation of Raman and infrared data is hazardous without unambiguous knowledge of the crystal structure. Moreover even for the hexagonal phase there is still no satisfactory explanation of the observed selection rules for Raman, infrared and neutron scattering spectroscopy, although the interchain force field is expected to play an important role in determining them. In this chapter neutron scattering techniques analogous to those used in Chapters 6 and 7 are applied to P.T.F.E. following the suggestions of 7.5. Time-of-flight spectra of polycrystalline and fibrous P.T.F.E. are reported for several incident neutron wavelengths in an extension of the work of Safford and Naumann [23] who reproduce data at constant scattering angle and wavelength. Coherent

acoustic groups are observed and used in the construction of a dispersion curve for interchain vibrations. These data provide the first anisotropic information about the interchain force field of P.T.F.E. and are contrasted with the complementary data for intrachain phonon excitations [22, 24].

11.2 Sample characteristics

Polytetrafluoroethylene was investigated in the powder and fibre forms produced commercially. 'Fluon' powder G163 was supplied by Mr. H.A. Willis, I.C.I., Welwyn Garden City. Commercial manufacture starts from chloroform and follows the scheme

$$CHCl_3 \xrightarrow{F_2} \underset{g}{CHF_2Cl} \xrightarrow{\text{pyrolysis}} \underset{g}{C_2F_4} \xrightarrow{\text{catalyst}} \underset{s}{(CF_2)_n}$$

Fluon in its original form is a white powder of high crystallinity which can be sintered i.e. melted and recrystallized to give the familiar commercial product. Since the crystallinity reduces from about 95% to around 70% on sintering experiments were performed on the unsintered material. The extensive presence of voids restricts the accuracy of crystallinity measurements on P.T.F.E. since a simple two phase model is inadequate for this polymer. In particular the density method for determining crystallinity using (6.1) works only for void-free specimens. Direct measurements of the crystalline and amorphous content by diffraction and infrared absorption techniques have been described however and lead to a figure of 95-7% for the crystallinity of unsintered Fluon [26].

Teflon fibres were supplied by Dr. H.W. Starkweather, E.I. du Pont de Nemours, Wilmington, U.S.A. A suitable specimen was prepared by tightly winding the fibres on a metal frame so that the adjacent threads were parallel and masking the ends with cadmium for neutron experiments. The resulting 2" x 1" sample weighed 30 gms and had a c-mosaic of 9° FWHM determined by neutron diffraction. Crystallinity was roughly estimated as 80% after comparison of diffraction data from this sample with the data for Fluon.

11.3 Neutron diffraction measurements

Neutron diffraction data for P.T.F.E. in fibre and powder form were obtained using the Badger 2 diffractometer at A.E.R.E. Harwell. Results for the powder and the fibres mounted vertically on the diffractometer are reproduced in Fig. 11.2. No preferred orientation perpendicular to the fibre axis was observed as is common for polymer specimens prepared by the application of uniaxial stress. Comparison of the two sets of data for the hexagonal phase at 25°C distinguishes the prismatic reflexions and the assignments in Fig. 11.2 were facilitated by structure factor calculations based upon the atomic coordinates of Iwasaki [11] and the lattice parameters of Clark and Muus [5]. Since there is known to be appreciable disorder about the chain axis in the hexagonal phase, structure factor calculations which preserve translational symmetry in the basal plane are an approximation, although the computed structure factors are very insensitive to the choice of chain setting angle about this axis as might be expected from Fig. 11.1. It was apparent from the calculations that the $[10\bar{1}n]$ reflexions have intensities which are very sensitive to the nature of the helix. For a 15/7 helix $[10\bar{1}7]$, $[10\bar{1}8]$ and $[10\bar{1}15]$ predominate and the first two of these were identified in the 25°C data thus characterizing the helix.

Experimental lattice parameters for the hexagonal phase at 25°C are

$$a = 5.66 \pm 0.05 \qquad c = 19.50 \pm 0.05 \qquad (11.1)$$

in exact agreement with Clark and Muus [5] for both powder and fibre data. Cooling below the 19°C transition caused some sharpening of the observed peaks and the appearance of several new features. A downward shift of 0.01 Å in the prismatic $[10\bar{1}0]$ d-spacing was resolved in agreement with earlier observations although it was not possible to make any definite conclusions about the crystal structure of the controversial lower temperature phase. Experiments on a recently prepared fully oriented specimen of

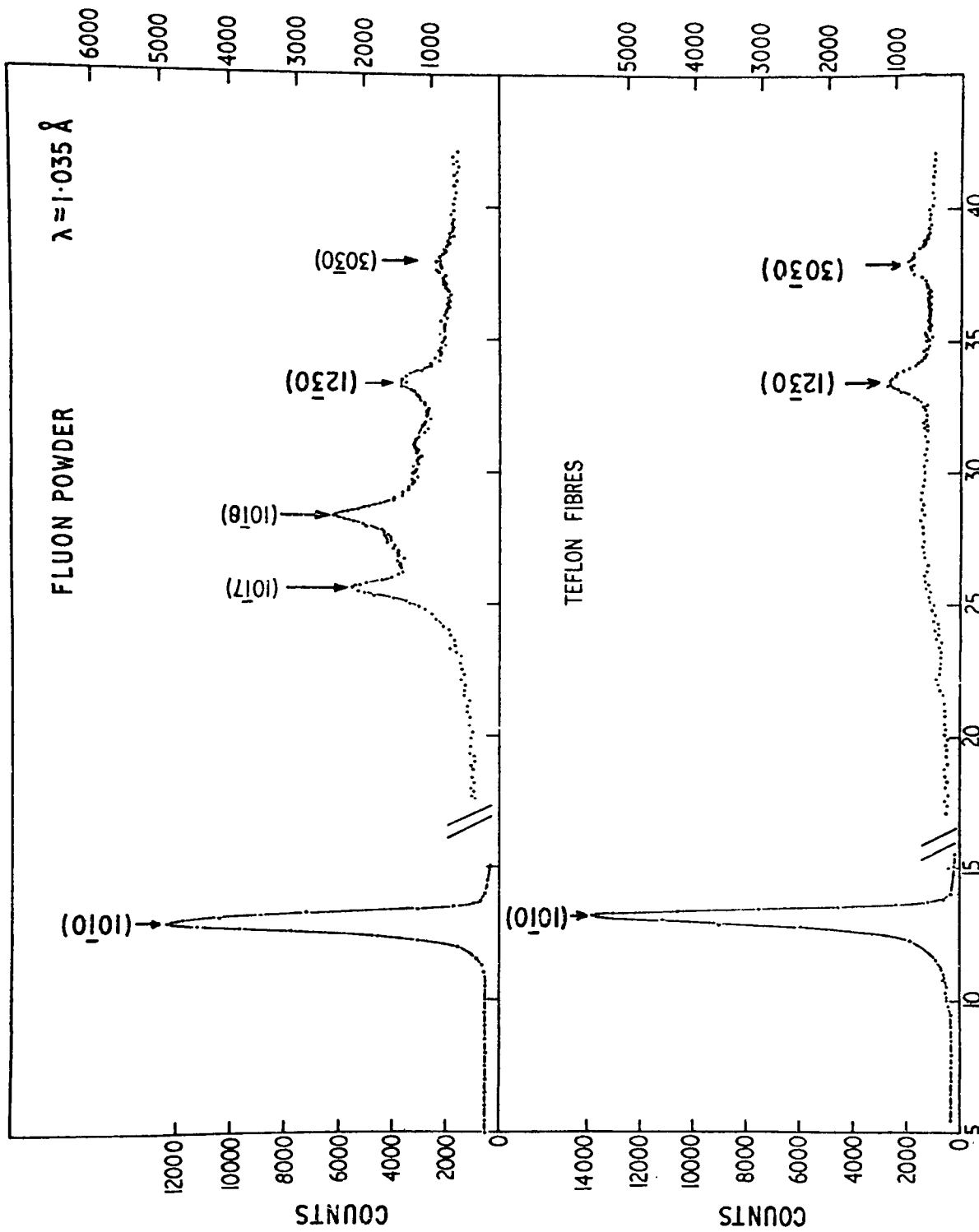

Fig. II·2 Neutron diffraction data for polycrystalline and fibrous P.T.F.E. in the hexagonal phase at 25°C

P.T.F.E. are in preparation and should help to resolve this problem. Above the 30°C transition there is a gradual shift of the [10$\bar{1}$0] peak as the hexagonal lattice expands and a blurring of the [10$\bar{1}$n] reflexions parallel to the loss of order along the chain direction [5]. Consequently only one lattice parameter could be defined, from the prismatic [10$\bar{1}$0] reflexion.

11.4 Time-of-flight spectroscopy

Time-of-flight spectra of P.T.F.E. in powder and fibre form were measured at several wavelengths over a wide temperature range, giving most attention to the well characterized hexagonal phase. Powder experiments were performed on the 4H5 and 6H spectrometers to exploit the large solid angle of detection. Fibre measurements were made on the 4H5 phonon arc with data collection in the basal plane of the polymer as in Fig. 7.2. Both fibre and powder spectra contained coherent acoustic phonon excitations in a strong parallel with the data reported earlier for deuteropolyethylene. In discussing the data obtained it is convenient to start with the acoustic phonon groups and to move on from there to a consideration of subsidiary aspects of the time-of-flight spectra and, in particular, the changes in the low frequency spectra observed on cooling below the 19°C phase transition.

11.4.1 Coherent acoustic phonon excitations

Powder data obtained for the hexagonal phase of P.T.F.E. at 25°C using the 6H spectrometer are reproduced in Fig. 11.3. Four spectra are presented to demonstrate the angular dependence of the inelastic spectrum for an incident neutron wavelength of 5.0 Å. One feature clearly dominates the low angle time-of-flight spectra and is seen to progress across the energy scale, finally disappearing into the elastic peak at a scattering angle of 63°. This behaviour is exactly analogous to that observed in D.P.E. although the singularity in question is very much more intense in the spectra of P.T.F.E. Since the scattering from P.T.F.E. is almost wholly coherent such effects will be enhanced here compared to in D.P.E. where 20%

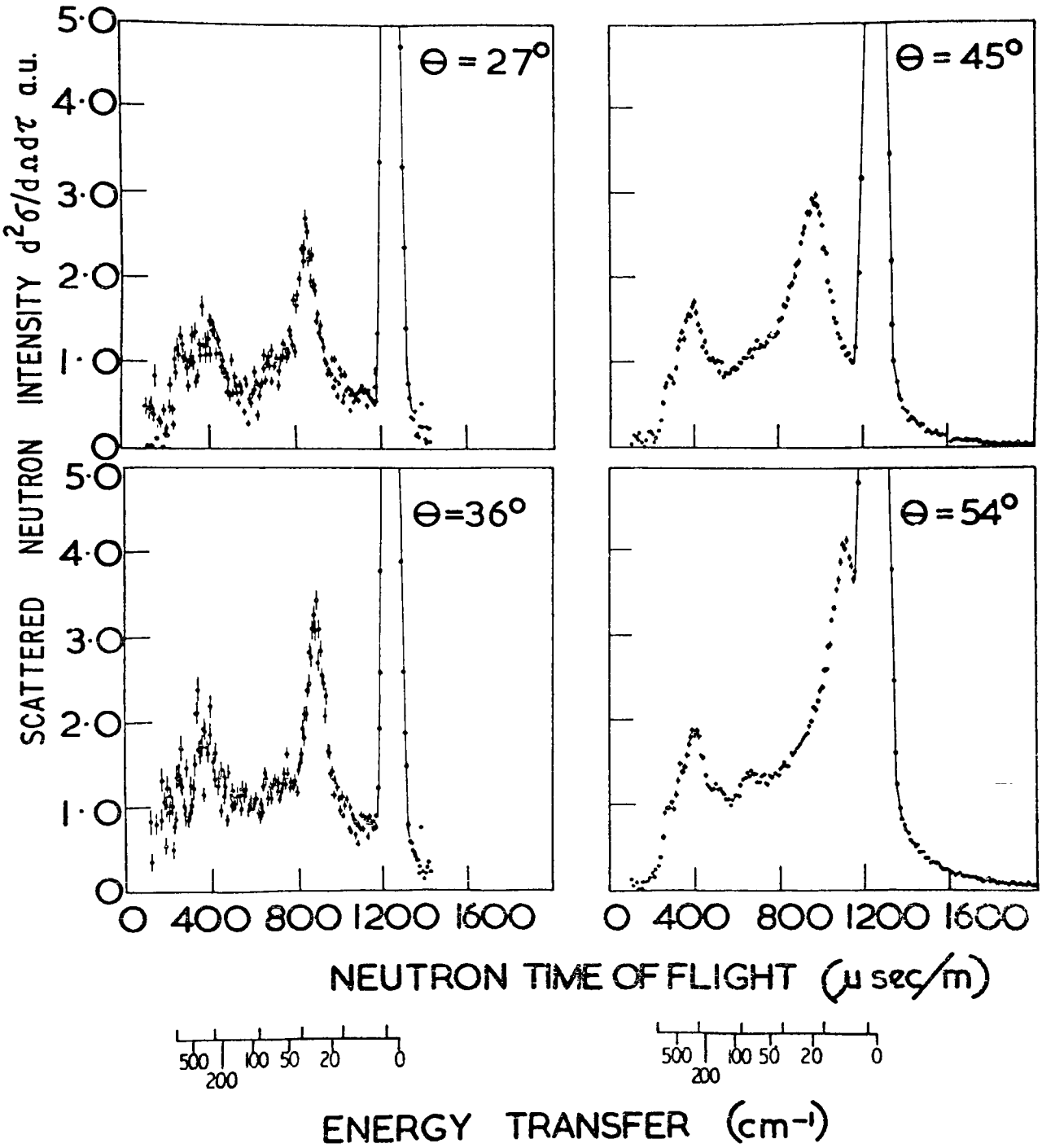

Fig. II·3 Time-of-flight spectra for polycrystalline P.T.F.E. in the hexagonal phase at four scattering angles to the incident 5·0 Å neutron beam at 25°C.

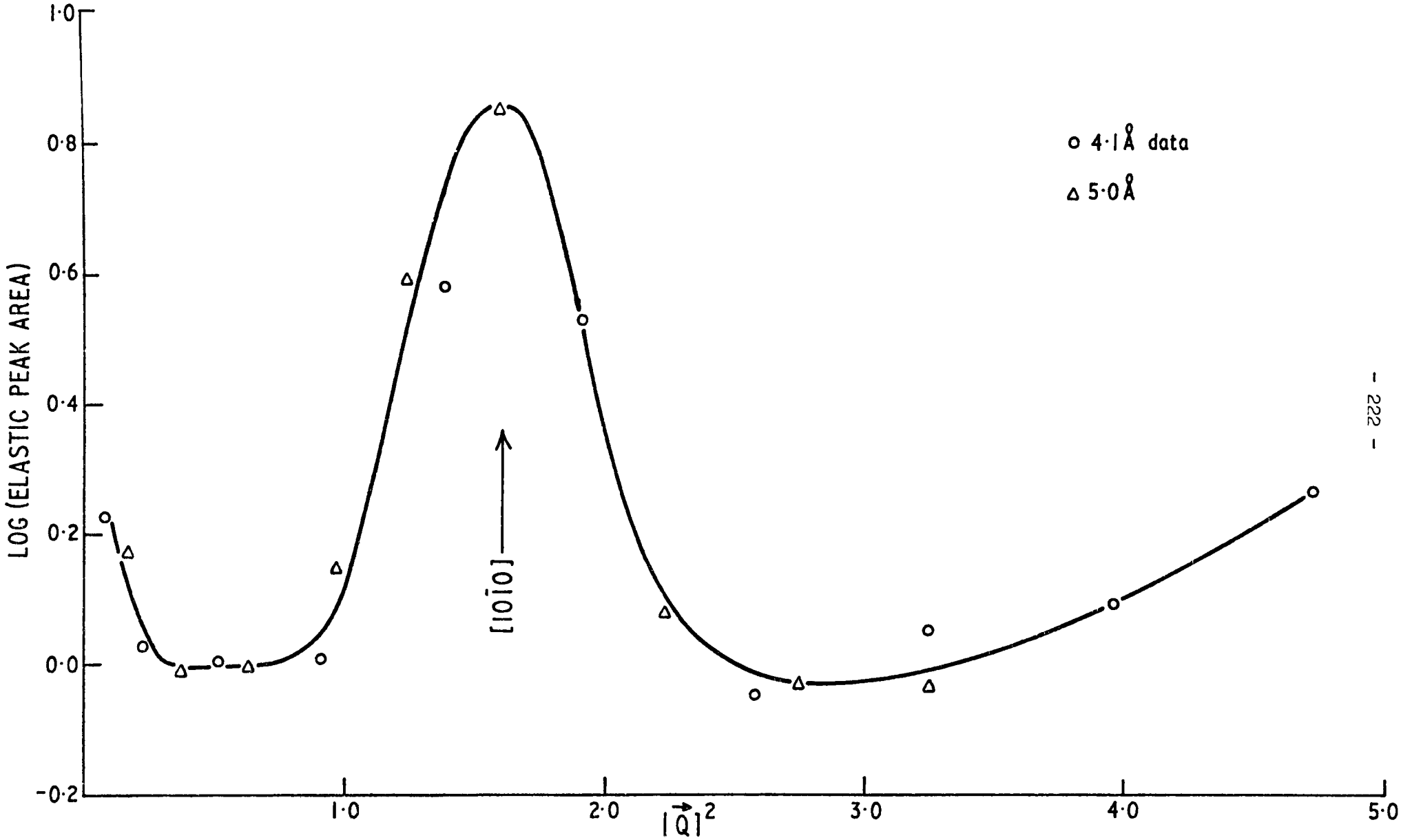

Fig. II·4 Debye Waller plot for polycrystalline P.T.F.E. in the hexagonal phase at 25°C.

of the total cross section is incoherent. In Fig. 11.4 the elastic peak intensities are reproduced as a function of $|\vec{Q}|^2$ in the so-called Debye Waller plot. The strong peak coincides with the $[10\bar{1}0]$ prismatic Bragg reflexion prominent in the diffraction picture of Fig. 11.2. As in D.P.E. this contribution emerges as the acoustic group disappears into the elastic peak and suggests the definition of a phonon group wave vector at the turning point of

$$|\vec{q}_{\zeta 0 \bar{\zeta} 0}| = 2\pi|\vec{\tau}_{10\bar{1}0}| - |\vec{Q}| \qquad (11.2)$$

In 7.5 the importance of the atomic distribution as a factor determining the sharpness of singularities in the polycrystal spectrum was stressed and it is clear from Fig. 11.1 that this distribution is highly isotropic when projected into the basal plane of P.T.F.E. In such circumstances the eigenvector product in 3.37 predominates giving rise to the LA singularities discussed in 7.5. Coherent acoustic groups for P.T.F.E. are assembled in Fig. 11.5 as a plot of frequency against $|\vec{Q}|$ and $|\vec{q}_{\zeta 0 \bar{\zeta} 0}|$ for data obtained at several wavelengths. Also entered on Fig. 11.5 are the singularities obtained from fibre experiments analogous to those described in Chapter 7 (see Fig. 7.2) only performed on the long wavelength 4H phonon arc described in 4.3.1. The coincidence of the fibre data obtained in the basal plane of P.T.F.E. with the polycrystalline results supports the postulated assignment of these groups to interchain LA phonons polarized along $[\zeta 0 \bar{\zeta} 0]$. Since the proportion of coherent scattering is so high in P.T.F.E. none of the interference from incoherent singularities observed in polycrystalline D.P.E. is present here.

Experimental data were collected at 12, 25 and 48°C so that acoustic slopes were defined for each of the three phases described in 11.2. In fact the three sets of data were coincident at least within the experimental error qualifying the derived acoustic slopes (10%). The onset of dynamic disorder about the chain axis at the first transition might be expected to have a dramatic effect upon external chain librations, but any shift in LA

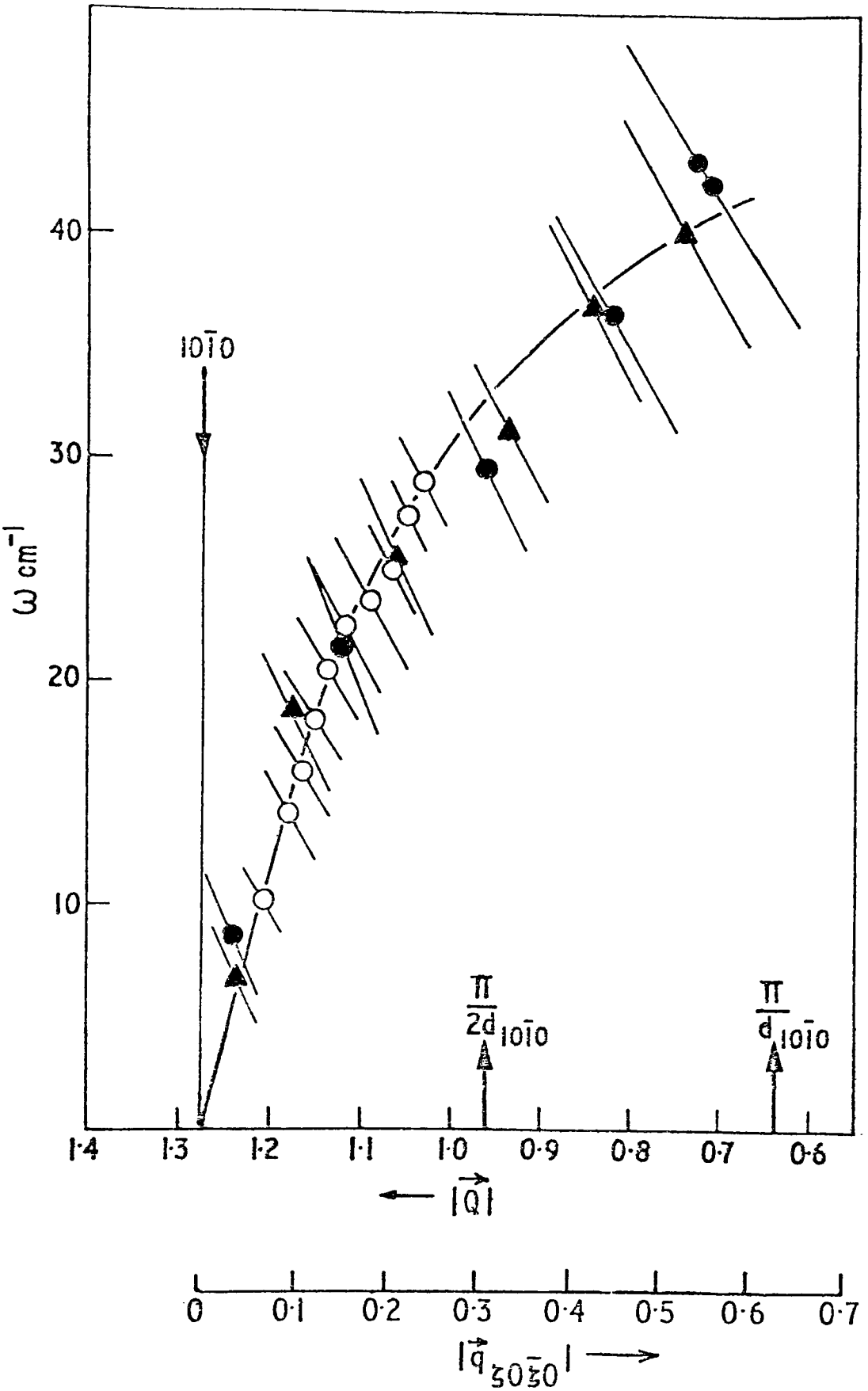

Fig. II·5 Coherent acoustic singularities for polycrystalline and fibrous P.T.F.E. in the hexagonal phase at 25°C assembled as a function of $|\vec{Q}|$ and $|\vec{q}_{50\bar{5}0}|$: ● 4·1 Å, ▲ 5·0 Å powder data; o 5·8 Å fibre.

phonon frequencies would arise principally from the associated lattice expansion. It appears that this increment (2%) is too small to shift the frequencies significantly. On the other hand the loss of translational symmetry perpendicular to the chain axes implies a reduction in phonon lifetime and consequent broadening in the energies of experimental groups. Such broadening is masked in the data reported here for polycrystalline P.T.F.E. by the spectrum of $\vec{q}$ values which contribute to the full profile of coherent acoustic groups.

Another implication of disorder concerns the elastic constant derivable from the data of Fig. 11.5. A molecule such as P.T.F.E. lacks any of the symmetry elements of a hexagonal lattice in either its 13/6 or 15/7 conformations. Only the near cylindrical shape of such molecules can explain the adoption of hexagonal stacking and to some extent the ease of static and dynamic disordering about the unique axes. For a hexagonal crystal LA slopes along $[\zeta 0\bar{\zeta}0]$ and $[0\zeta\bar{\zeta}0]$ are equal and define the same elastic constant, c_{11}. Scrutiny of the molecular symmetry of P.T.F.E. suggests that c_{11} and c_{22} should differ simply because a 60^{o} rotation of an array of P.T.F.E. molecules ordered on a hexagonal lattice does not reproduce the original array. However the whole concept of a crystal space group breaks down with the loss of translational symmetry perpendicular to the chain axis. When the chain setting angles are undefined c_{11} and c_{22} must be equal since the molecular bases are then randomly distributed about the lattice points and macroscopic measurements along $[\zeta 0\bar{\zeta}0]$ and $[0\zeta\bar{\zeta}0]$ will be equivalent.

From the data of Fig. 11.5 an acoustic slope of $2.8\pm0.3\times10^{5}$ cm/sec can be derived for LA phonon groups polarized along $[\zeta 0\bar{\zeta}0]$. The 10% error represents the 'loss' of information expected in experiments on isotropic material and is primarily caused by the necessarily approximate location of low frequency cut-offs in the observed phonon groups. This error is doubled in the elastic constant c_{11} which is estimated to be

$18\pm3\times10^{10}$ dyne cm^{-2} using a crystalline density of 2.302 gm ml^{-1} at $25^{o}C$. Full discussion of this result is postponed until 11.5.

11.4.2 Secondary aspects of the coherent inelastic spectrum

In addition to the coherent acoustic phonon groups just described there are several other subsidiary features of the time-of-flight spectra of P.T.F.E. which merit attention. All originate from coherent scattering events and so the simple parallel with the amplitude weighted density of states function valid for incoherent scattering is not strictly applicable. However there are certain singularities in the P.T.F.E. spectra which persist without appreciable shifts in frequency over the full range of scattering angle and for all incident wavelengths. One such peak is at 230 ± 20 cm^{-1}, clearly evident in Fig. 11.3 and observed also by Safford and Naumann [23]. This prominent singularity occurs in all three phases of P.T.F.E. and can be assigned with some certainty to the ν_8 intrachain stretching mode which has been measured across the zone by Piseri, Powell and Dolling [22]. As in polyethylene two prominent density of states peaks are expected for the ν_8 and ν_9 chain stretching and torsional modes and these have been predicted for P.T.F.E. at 200 and 20 cm^{-1} by Boerio and Koenig [21] on the basis of an isolated chain model. These peaks correspond to the calculated frequency maxima of the two normal mode dispersion curves along [000ζ]. Piseri et al. have measured the ν_8 branch in the hexagonal phase and obtain a maximum at 225 cm^{-1} (see Fig. 11.7) which is in excellent agreement with the singularity reported here. Hence it appears that the polycrystalline time-of-flight experiments sample a region of the ν_8 branch sufficient to define a singularity in close agreement with the expected density of states peak for the skeletal stretching motion.

From the predictions of Boerio and Koenig and by analogy with polyethylene a strong contribution to the density of states is expected at much

lower frequencies from the torsional motion of the P.T.F.E. chain. The low frequency time-of-flight spectra are very dependent upon both scattering angle and wavelength and are dominated largely by the coherent acoustic groups analysed in 11.4.1. This contribution disappears however when the $|\vec{Q}|$ value at the elastic peak is greater than $2\pi|\vec{\tau}_{10\bar{1}0}|$, as Fig. 11.5 demonstrates. At these higher scattering angles a broad peak emerges with a centre about 35 cm^{-1} and extending out to 70 cm^{-1}. Although the coherent origin of this peak precludes direct association with density of states singularities it seems very likely that the ν_9 chain torsional mode makes an important contribution to this feature, on the basis of the calculated frequency distribution [21]. In Fig. 11.6 scattering data collected at 90^{o} to an incident 4.1 Å neutron beam are shown for two temperatures above and below the $19^{o}C$ transition. A definite change in the time-of-flight spectrum involving an overall shift of the low frequency distribution towards the elastic peak is observed on transition to the disordered phase. Since the translatory modes are found to be virtually unaffected by the phase transition, at least along $[\zeta\bar{0}\zeta 0]$, it is reasonable to attribute this change to a downward shift in the external chain libratory frequencies parallel to the onset of dynamical disorder about the chain axis. The origin of the broad peak is then most likely threefold, including contributions from internal chain torsion and external libratory and translatory modes as suggested earlier. This apparent coupling of internal and external modes undermines the isolated chain description of the ν_9 mode and would seem to invalidate a rigid chain model for external vibrations of the type employed for polyethylene.

Finally some attention was given to changes in the elastic scattering arising at the transition. Elastic peak intensities as a function of $|\vec{Q}|^2$ for the data at $25^{o}C$ were illustrated in Fig. 11.4. The associated widths showed a $|\vec{Q}|^2$ dependence that mirrored the intensity plot i.e. the peak width decreased with $|\vec{Q}|^2$ on approaching $[10\bar{1}0]$, increased again and

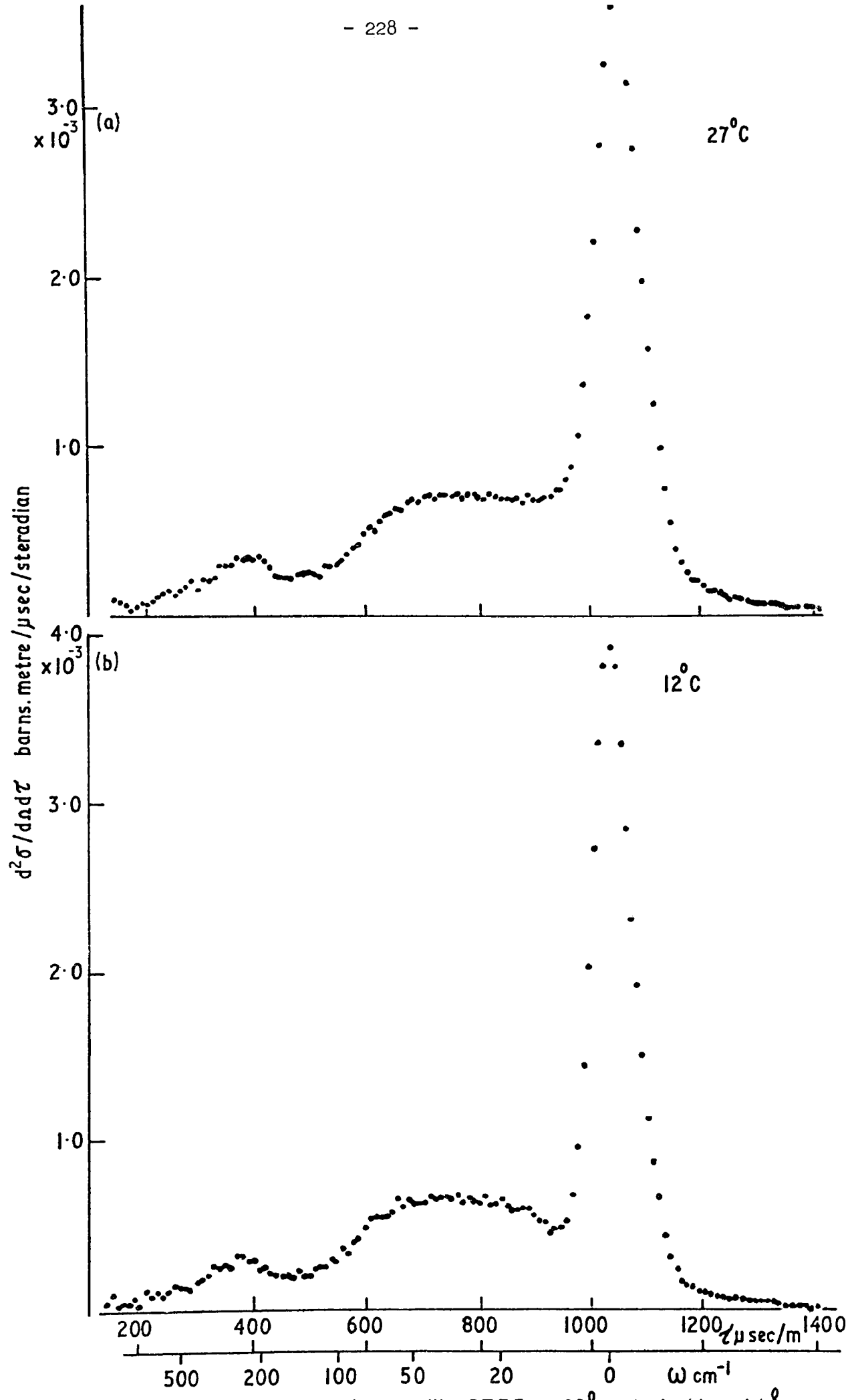

Fig. II·6 Time of flight spectra of polycrystalline P.T.F.E. at 90° to the incident 4·1 Å neutron beam above (a) and below (b) the 19°C phase transition.

decreased as $|\vec{Q}|$ approached the $[10\bar{1}n]$ Bragg reflexions. Such reciprocal behaviour of widths and intensities is typical of purely coherent elastic scattering from a solid and so although both parameters changed slightly at the 19°C transition it was not possible to make any conclusions about a possible quasielastic contribution to the spectrum of the disordered phase.

11.5 Discussion

Comparison of the interchain elastic constant c_{11} with the related intrachain parameter c_{33} is hampered by a disagreement between the two sets of neutron data for intrachain LA phonons. La Garde, Prask and Trevino [24] do not quote c_{33} although a figure of $220\pm10\times10^{10}$ dyne cm^{-2} can be estimated from their data. By contrast Piseri, Powell and Dolling [22] derive a figure of $150\pm10\times10^{10}$ dyne cm^{-2} for c_{33} and can make no definite conclusion about the evident discrepancy between their data and those of La Garde et al. The later work is however in best agreement with a dynamical model based upon the most recent assignment of infrared and Raman data for intrachain vibrations [22]. Moreover Sakurada, Ito and Nakamae [27] derive a chain modulus of 156×10^{10} dyne cm^{-2} from the change in [0015] plane spacing with applied stress along the axis of fibrous P.T.F.E. which is very close to the value of c_{33} obtained by Piseri et al. On these grounds a comparison with the later neutron data is preferred and Fig. 11.7 shows the $[\zeta 0\bar{\zeta}0]$ phonon measurements together with those along $[000\zeta]$ from [22] plotted with common abscissae in units of Å^{-1}. Acoustic velocities of 2.8 and 8.1×10^{5} cm/sec derived from Fig. 11.7 correspond to elastic constants c_{11} and c_{33} of 18 and 150×10^{10} dyne cm^{-2} at 25°C.

A ratio c_{33}/c_{11} of 8 compares with a figure of 22 for deuteropolyethylene derived from neutron scattering and highlights the greater anisotropy of the hydrocarbon force field (cf. Fig. 7.8). In fact the rigid chain approximation quite successfully employed in the interpretation of external

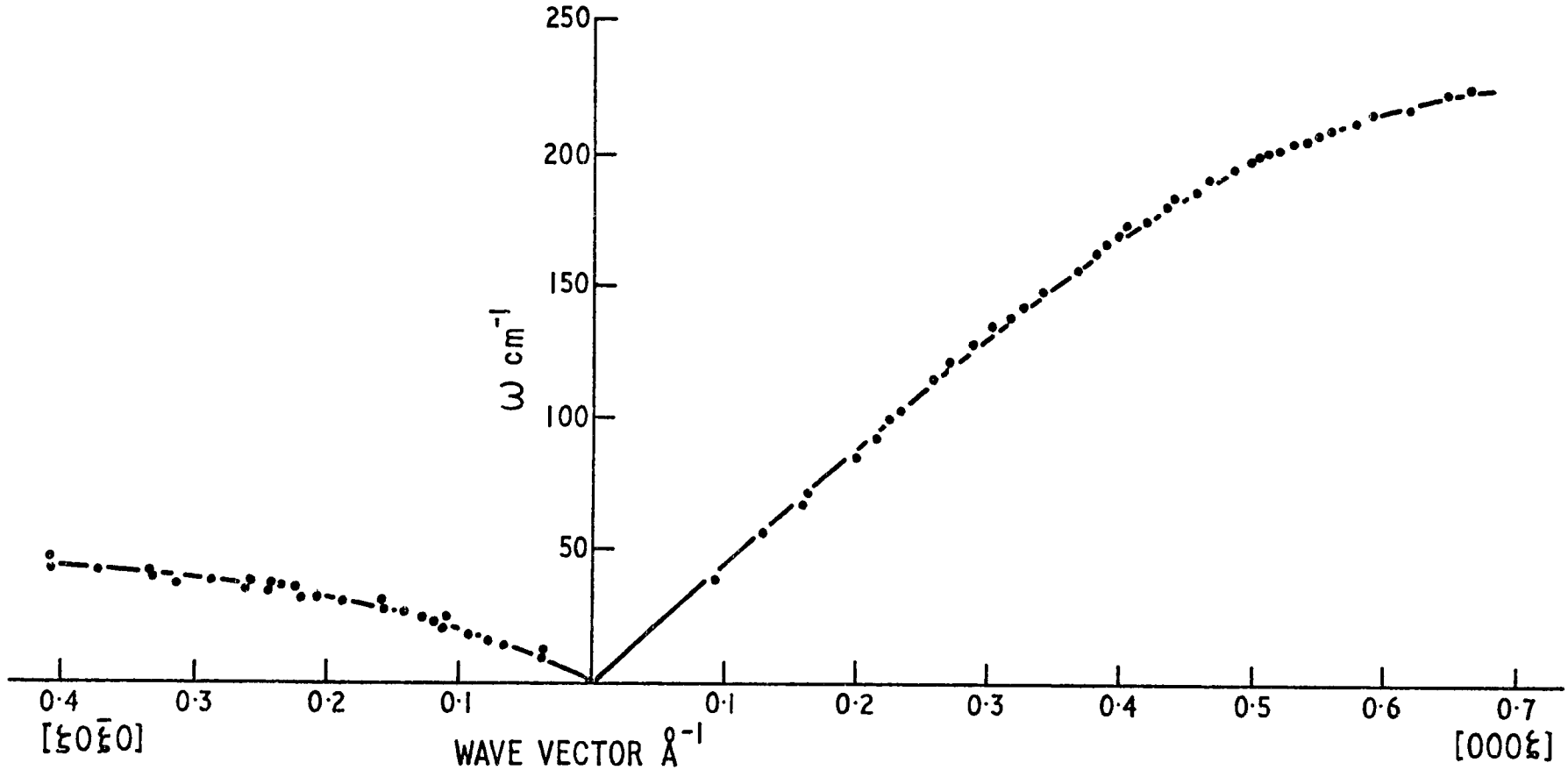

Fig. II·7 Experimental dispersion curves for LA phonons propagating along and perpendicular to the chain axis of P.T.F.E. in the hexagonal phase at 25°C.

chain vibrations of polyethylene is definitely inappropriate in P.T.F.E. The coupling of internal and external chain librational modes suggested from the time-of-flight spectra in 11.4.2 underlines this point. Unfortunately a calculation of the interchain dispersion curves of P.T.F.E. without the rigid chain approximation is prohibited at present by the size of the full dynamical matrix for a unit cell containing up to 45 atoms. The loss of translational symmetry perpendicular to the chains in the hexagonal phase and the unavailability of good F-F pseudopotentials are further impediments.

Despite these deterrents there are several aspects of the interchain force field which merit further experimental investigation. Recent preparation of fully oriented P.T.F.E. facilitates more extensive measurements of the interchain phonon dispersion curves and their behaviour at the 19 and 30°C transitions. Some changes in the low frequency time-of-flight spectra have already been noted for the polycrystal and attributed tentatively to a downward shift in external librational frequencies parallel to the onset of dynamic disorder at the 19°C transition. Full characterization of the libratory mode will be facilitated by triple axis spectroscopy of a P.T.F.E. single crystal and it should be possible to monitor the evolution of this mode across the two transitions. Experiments of this kind should provide invaluable insight into the nature of phase transitions in general since the restriction of dynamic disorder to one axis greatly simplifies the interpretation of such data.

11.6 Summary

Coherent inelastic features in the neutron time-of-flight spectra of polycrystalline and fibrous P.T.F.E. are assigned to acoustic phonon groups propagating in the basal plane of the polymer. Despite the range of phonon wave vectors associated with each group it is possible to identify a cut-off at which the wave vector becomes defined. Phonon excitations at

this point are longitudinally polarized along the [ζ0$\bar{\zeta}$0] symmetry direction. Experimental singularities located in this way define an acoustic slope for LA phonons from which the elastic constant c_{11} is derived to be $18\pm3\times10^{10}$ dyne cm^{-2} for the hexagonal phase of P.T.F.E. at 25°C. This measurement provides the first anisotropic information about the inter-chain force field of this polymer. Comparison with a figure of 150×10^{10} dyne cm^{-2} obtained earlier for c_{33} indicates that the force field of P.T.F.E. is less anisotropic than that of polyethylene.

Other features in the time-of-flight spectra are assigned to the intrachain stretching mode and to a combination of internal chain torsion and external chain libratory and translatory modes. Strong coupling between the lowest frequency intrachain mode and the external chain vibrations is suggested and the applicability of the isolated chain description of the internal vibrations of P.T.F.E. is questioned.

Changes in the low frequency time-of-flight spectrum of P.T.F.E. at the 19°C transition are attributed to the decrease in external librational frequencies parallel to the onset of dynamic disorder about the chain axis. By contrast no resolvable shifts in the LA phonon singularities are observed for data at 12, 25 and 48°C showing the relative insensitivity of these translatory lattice vibrations to the elements of molecular disorder introduced at the phase transitions.

References

[1] J.F. Twisleton and J.W. White, Polymer, 13, 40 1972.

[2] C.W. Bunn and E.R. Howells, Nature, 174, 549 1954.

[3] H.G. Kilian and E. Jenckel, Z. Elektrochem., 63, 308 1959.

[4] E.S. Clark and L.T. Muus, Z. Kristall., 117, 108 1962.

[5] idem, ibid., 119 1962.

[6] J.W. White, private communication.

[7] K.W. Johnson and J.F. Rabolt, J. Chem. Phys., 58, 4536 1973.

[8] F.J. Boerio and J.L. Koenig, J. Chem. Phys., 54, 3667 1971.

[9] C.W. Bunn, A.J. Cobbold and R.P. Palmer, J. Poly. Sci., 28, 365 1958.

[10] T. Miyazawa, J. Poly. Sci., 55, 215 1961.

[11] M. Iwasaki, J. Poly. Sci. A, 1, 1099 1963.

[12] T.W. Bates, Trans. Far. Soc., 63, 1825 1967.

[13] T.W. Bates and W.H. Stockmayer, Macromolecules, 1, 17 1968.

[14] D. Hyndman and G.F. Origlio, J. Appl. Phys., 31, 1849 1960.

[15] C.Y. Liang and S. Krimm, J. Chem. Phys., 25, 563 1956.

[16] F.J. Boerio and J.L. Koenig, J. Chem. Phys., 50, 2823 1969.

[17] C.J. Peacock, P.J. Hendra, H.A. Willis and M.E.A. Cudby, J. Chem. Soc. (Lond.) A, 2943 1970.

[18] M.J. Hannon, F.J. Boerio and J.L. Koenig, J. Chem. Phys., 50, 2829 1969.

[19] F.J. Boerio and J.L. Koenig, Bull. Amer. Phys. Soc., 14, 406 1969.

[20] idem, J. Chem. Phys., 52, 4170 1970.

[21] idem, ibid., 4826 1970.

[22] L. Piseri, B.M. Powell and G. Dolling, J. Chem. Phys., 58, 158 1973.

[23] G.J. Safford and A.W. Naumann, Adv. Poly. Sci., 5, 1 1967.

[24] V. La Garde, H. Prask and S. Trevino, Disc. Far. Soc., 48, 15 1969.

[25] L.A. Feldkamp, G. Venkataraman and J.S. King, 'Neutron Inelastic scattering', IAEA, Copenhagen, 2, 159 1968.

[26] 'Physical properties of polytetrafluoroethylene', I.C.I. Technical Service Note F12.

[27] I. Sakurada, T. Ito and K. Nakamae, J. Poly. Sci. C, 15, 75 1966.